CONTROLLED FABRICATION OF ALIGNED CARBON NANOTUBE ARCHITECTURES FOR MICROELECTRONICS PACKAGING APPLICATIONS

A Thesis
Presented to
The Academic Faculty

by

Lingbo Zhu

In Partial Fulfillment
of the Requirements for the Degree
Doctor of Philosophy in the
School of Chemical & Biomolecular Engineering

Georgia Institute of Technology
December 2007

CONTROLLED FABRICATION OF ALIGNED CARBON NANOTUBE ARCHITECTURES FOR MICROELECTRONICS PACKAGING APPLICATIONS

Approved by:

Dr. C. P. Wong, Advisor
School of Materials Science & Engineering
Georgia Institute of Technology

Dr. Sankar Nair
School of Chemical & Biomolecular Engineering
Georgia Institute of Technology

Dr. Dennis W. Hess, Advisor
School of Chemical & Biomolecular Engineering
Georgia Institute of Technology

Dr. Z. L. Wang
School of Materials Science & Engineering
Georgia Institute of Technology

Dr. William J. Koros
School of Chemical & Biomolecular Engineering
Georgia Institute of Technology

Date Approved: Oct. 24, 2007

To my parents

ACKNOWLEDGEMENTS

There are many who have contributed to my success in graduate school, and first among them are my Ph.D. advisors, Dr. C. P. Wong and Dr. Dennis W. Hess, who led me to a project well suited for my interests, gave me the freedom to direct my progress, and challenged me throughout this progress. I sincerely appreciate their trust and confidence. I am also indebted to my thesis committee members, Dr. William J. Koros, Dr. Sankar Nair, and Dr. Z. L. Wang for their involvement in my research, invaluable discussions and insights, and critical reading of my work.

I also wish to acknowledge the entire Wong research group and Hess research group at Georgia Tech and the Microelectronics Research Center cleanroom facilities. In particular, I wish to recognize the extraordinary contributions from the following individuals: Dr. Ding Yong, Mr. Yonghao Xiu, Mr. Hongjin Jiang, Dr. Kyoung-sik Moon, Dr. Jianwen Xu, Dr. Yangyang Sun, Dr. Zhuqing Zhang, Dr. Lianhua Fan, Mr. Gray Spinner, and Mr. Charlie Suh. I also want to express my gratitude to all graduate students and post-doc fellows who provided help in my thesis work. They are Dr. Myung Jin Yim, Ms. Jiongxin Lu, Ms. Yi Li, Mr. Wei Lin, Mr. Brian Bertram, Ms. Gusuel Yun, Mr. Rongwei Zhang, Dr. Shu Shu, Dr. Galit Levitin, Dr. Ashwini Sinha, Dr. Prahakar Tamirisa, Dr. Qian Luo, Dr. Ingu Song, Dr. Shantanu Pathak, Mr. Balamurali Balu, Ms. Fangyu Wu, Mr. Ashish Pande, and Dr. Hollie Reed.

I value the friendships I have made during my days at Georgia Tech, as they often eased the difficult time. Especially, I thank Dr. Jie Diao and Dr. Lan Wu, who always encouraged me and helped me when I first arrived at Georgia Tech, and Dr. Gary D.

Gray, who helped me get familiar with cleanroom work and was willing to listen when I complained.

Finally, I would like to thank my parents and my sister for their continuous support and encouragement. I thank my wife, Na Ding, for her patience and support.

TABLE OF CONTENTS

LIST OF TABLES

LIST OF FIGURES

SUMMARY

As IC performance increases, many technical challenges appear such as thermal management, electrical interconnects, and thermal-mechanical reliability. To address these problems, carbon nanotubes (CNTs) were proposed in IC packaging for electrical interconnects and thermal management, due to their excellent electrical, thermal, and mechanical properties. CNTs promise to bring revolutionary improvement in reducing the interconnect pitch size, increasing thermal conductivity, and enhancing system reliability.

This thesis is devoted to the fabrication of carbon nanotube structures for microelectronics packaging applications with an emphasis on fundamental studies of nanotube growth and assembly, wetting of nanotube structures, and nanotube-based composites. A CVD process is developed that allows controlled growth of a variety of CNT structures, such as CNT films, bundles, and stacks. Use of an Al_2O_3 support enhances the Fe catalyst activity by increasing the CNT growth rate by nearly two orders of magnitude under the same growth conditions. By introducing a trace amount of weak oxidants into the CVD chamber during CNT growth, aligned CNT ends can be opened and/or functionalized, depending on the selection of oxidants. By varying the growth temperature, CNT growth can be performed in a gas diffusion- or kinetics-controlled regime.

To overcome the challenges that impede implementation of CNTs in circuitry, a CNT transfer process was proposed to assemble aligned CNT structures (films, stacks & bundles) at low temperature which ensures compatibility with current microelectronics fabrication sequences and technology. Field emission and electrical testing of the as-assembled CNT devices indicate good electrical contact between CNTs and solder and a very low contact resistance across CNT/solder interfaces. For attachment of CNTs and

other applications (e.g. composites), wetting of nanotube structures was studied. Two model surfaces with two-tier scale roughness were fabricated by controlled growth of CNT arrays followed by coating with fluorocarbon layers formed by plasma polymerization to study roughness geometric effects on superhydrophobicity. Due to the hydrophobicity of nanotube structures, electrowetting was investigated to reduce the hydrophobicity of aligned CNTs by controllably reducing the interfacial tension between carbon nanotubes (CNTs) and liquids. Electrowetting can greatly reduce the contact angle of liquids on the surfaces of aligned CNT films. However, contact angle saturation still occurs.

Variable frequency microwave (VFM) radiation can greatly improve the CNT/epoxy interfacial bonding strength. Compared to composites cured by thermal heating, VFM-cured composites demonstrate higher CNT/matrix interfacial bonding strength, which is reflected in composite negative thermal expansion. The improved CNT/epoxy interface enhances the thermal conductivity of the composites by 26-30%.

CHAPTER 1

INTRODUCTION

Carbon is an extraordinary element, considering the diversity of the materials which it can form. From 3D insulating diamond, 2D semiconducting graphite, 1D metallic and semiconducting nanotubes, to 0D fullerenes, carbon shows many interesting properties. As a new form of carbon structures, carbon nanotubes (CNTs) are strongly related to other forms of carbon, especially to the crystalline 3D graphite, and to its constituent 2D graphene layers. The extraordinary properties of CNTs arise from the unusual properties of sp^2 graphite, as well as from the additional quantum confinement and topological constraints in the circumferential direction of the nanotube [1]. These constraints results in quantum confinement of the wave functions in the radial and circumferential directions, with plane wave motion occurring only along the nanotube axis corresponding to a large number of closely spaced allowed wave vectors. Thus, although CNTs are closely related to a 2D graphene sheet, the tube curvature and the quantum confinement in the circumferential direction lead to specific properties that are different from those of a graphene sheet.

In this chapter, first, a brief review of the graphite and related materials, such as graphite whiskers and carbon fibers, is presented for better understanding of CNTs, due to their close connection to the structure and properties of CNTs. Then some basic definitions relevant to the structure and properties of CNTs are provided. This information is followed by a review of various growth methods and mechanisms for nanotubes; chemical vapor deposition (CVD) method is particularly emphasized. The electrical properties of nanotubes are briefly discussed. This is followed by a review of the different categories of CNT defects and functionalization of CNTs that broadens the

nanotube's applications. Finally, the research challenges and objectives of this thesis are presented.

1.1 Remarkable Carbon Element

Carbon is a very important element for all living organisms. In the periodic table, carbon is the sixth element and has the lowest atomic number of any element in column IV. Each carbon atom has six electrons occupying $1s^2$, $2s^2$, and $2p^2$ atomic orbitals. The $1s^2$ orbital contains two strongly bound core electrons. The other four more weakly bound electrons occupy the $2s^2p^2$ valence orbitals. The electronic configuration of the carbon atom allows the formation of three different hybridized atomic orbitals, sp^3, sp^2 and sp, giving a variety of chemical bonds. In the crystalline phase, the valence electrons give rise to 2s, 2px, 2py, and 2pz orbitals that are important for forming covalent bonds in carbon materials. Since the s-orbital and p-orbitals of carbon's second electronic shell have very similar energies, compared with the binding energy of the chemical bonds, the electronic wave functions for these four electrons can easily mix with each other, thus changing the occupation of the 2s and 2p atomic orbitals to enhance the binding energy of the C atom with its neighboring. As a result, carbon can adapt to form chemical bonds with different geometries. The covalent bonds have directional properties. This in turn gives carbon the ability to adapt into various molecular and crystalline structures. The general mixing of 2s and 2p atomic orbitals is called hybridization, whereas the mixing of a single 2s electron with one, two, or three 2p electrons is called sp, sp^2, sp^3 hybridization, respectively. For instance, within diamond, one s-orbital and three p-orbitals undergo a sp^3 hybridization, so the geometry of the hybridized orbital is tetrahedral, while within graphite, one s-orbital and two p-orbitals undergo a sp^2 hybridization so that the geometry of the hybridized orbital is trigonal planar. This is the reason why each carbon atom within graphite has three nearest neighbors within the graphite sheets. One of the p-orbitals is left unaffected. This p-orbital overlaps with those from neighboring carbon

atoms, in a planar configuration to form the distributed π-bonds that reside above and below each graphite sheet. These hybridized atomic orbitals form chemical bonds to form diamond, graphite, and fullerenes. Figure 1.1 illustrates how the variety of the C-C bonding nature of carbon atoms leads to a large family of organic molecules and inorganic-like carbon materials [2].

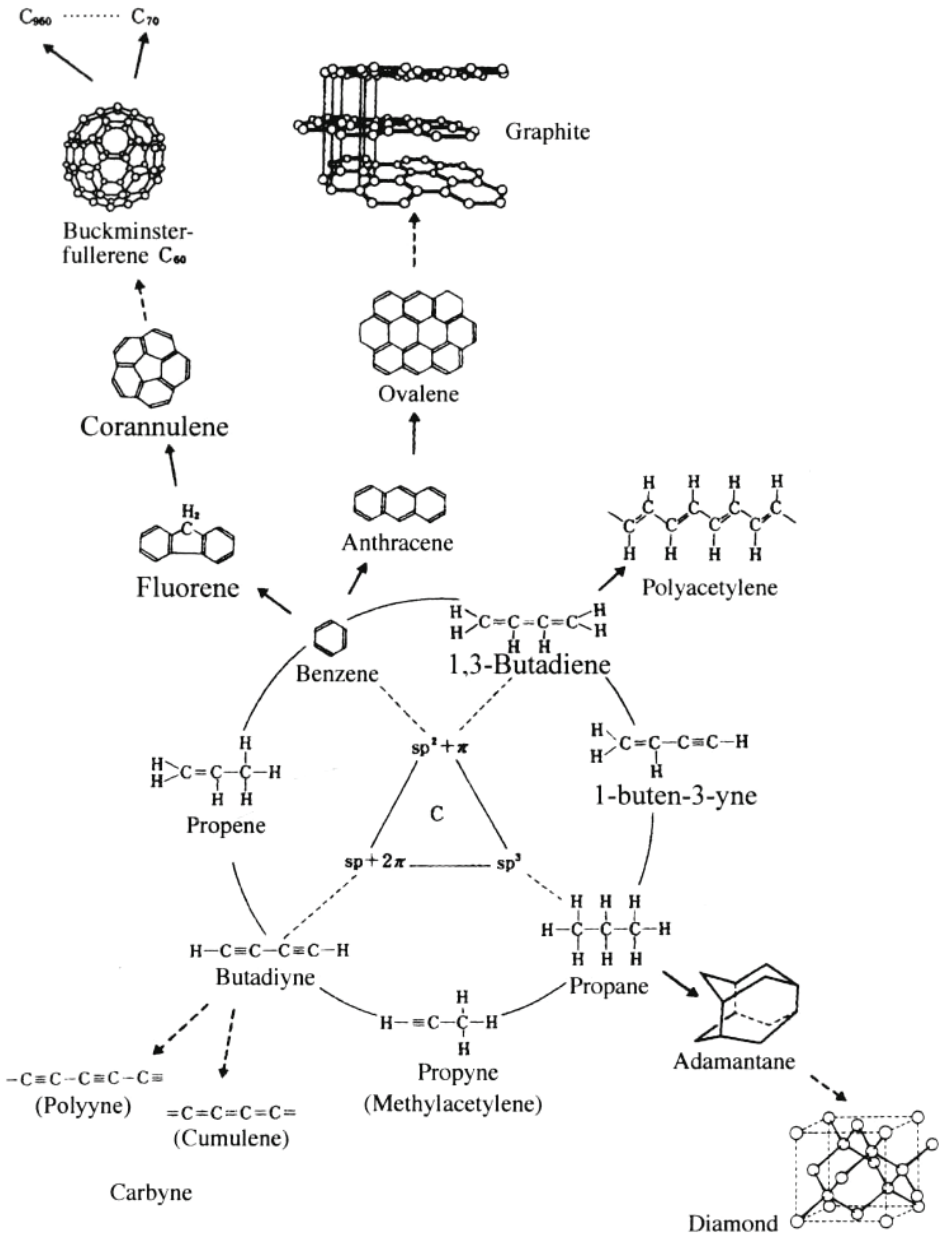

Figure 1.1 Examples of the enormous number of organic compounds based on carbon-carbon bonds using sp^3, sp^2 and sp hybrid orbitals and inorganic-like materials as their extension [2]. The dashed arrows simply indicate increasing complexity of the molecules.

1.2 Carbon Phase Diagram

The carbon phase diagram continues to guide the research in new forms of carbon. Figure 1.2 is a new version of the carbon phase diagram [3]. In Figure 1.2, A indicates commercial synthesis of diamond from graphite by catalysis; B is P/T threshold of very fast (less than 1 ms) solid-solid transformation of graphite to diamond; C is P/T threshold of a very fast transformation of diamond to graphite; D is the single crystal hexagonal graphite transformation to retrievable hexagonal-type diamond; E is the upper end of shock compression/quench cycles that convert hex-type graphite particles to hex-type diamond; F is the upper end of shock compression/quench cycles that convert hex-type graphite to cubic-type diamond; B, F, G signifies the threshold of fast P/T cycles that convert graphite or hexagonal diamond into cubic-type diamond; and H-I-J indicates a path along which a single crystal hex-type graphite compressed in the c-direction at room temperature loses some graphite characteristics and acquires properties consistent with a diamond-like polytype, but reverses to graphite upon release of pressure. This figure clearly shows that sp^2 bonded graphite is the stable phase under ambient conditions, while at higher temperatures and pressures, sp^3 bonded cubic diamond is stable.

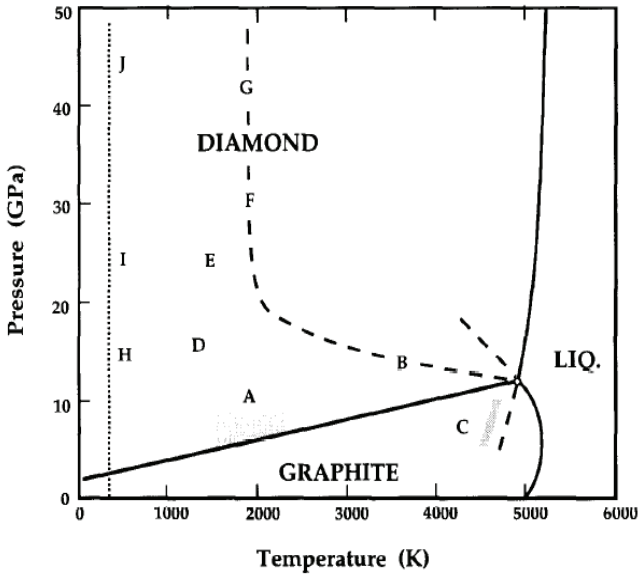

Figure 1.2 A new version of the phase and transition diagram for carbon [3]. Solid lines represent equilibrium phase boundaries.

1.3 Graphite and its Related Structures

This thesis focuses on the CVD growth, characterization and applications of carbon nanotubes (CNTs). However, due to the structural similarities, the carbon structures based on hexagonal networks of carbon atoms, i.e., graphite-related materials, are briefly reviewed in the following sections.

1.3.1 Graphite [1]

The carbon family with sp^2 bonding is represented by graphite, where a honeycomb network contains two atoms per unit cell, as shown in Figure 1.3a. The layers of hexagons of carbon atoms are stacked in parallel using π electron clouds with a regularity of ABAB, which is an ideal hexagonal crystal system. Figure 1.3b is a top-down view of graphite crystal structures. Neighboring graphene planes are colored differently (red and black). The in-plane C-C bonding length is 1.421 Å, the in-plane lattice constant is 2.462 Å, and the c-axis lattice constant is 6.708 Å with an interplanar distance of 3.354 Å. The interplanar spacing between CNTs is essentially the same as that of graphite (~3.4 Å). One consequence of the strong C-C bonding in graphite is that impurity species are unlikely to enter the covalently bonded lattice sites substitutionally, except for boron, but rather occupy interstitial positions between the graphene layer planes which are bonded by weak van der Waals forces. These arguments also apply to CNTs and explain why substitutional doping of CNTs with species other than boron is difficult.

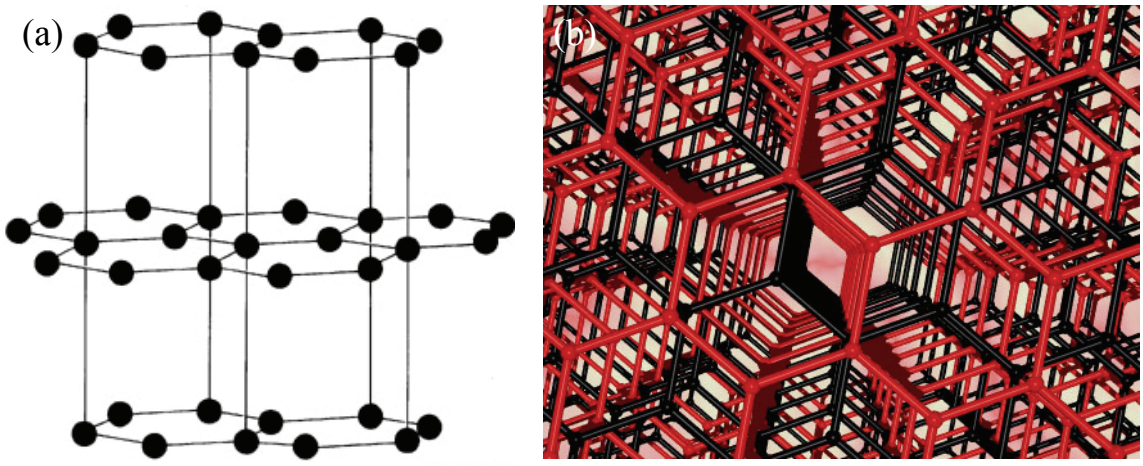

Figure 1.3 (a) The crystal structure of hexagonal single crystal graphite; (b) top-down view of graphite crystal structures. Neighboring graphene planes are colored differently (red and black).

However, most graphite materials are not structurally perfect, and parallel layers do not stack with perfect Bernal layer stacking. These stacking faults lead to a small increase in the interlayer distance from the value 3.354 Å to 3.440 Å [1]. At such a distance, the stacking of the individual carbon layers becomes uncorrelated with essentially no site bonding between carbon atoms between the two layers. Such structure of uncorrelated 2D graphene layers is called turbostratic graphite. The multi-walled CNTs (MWNTs) consist of an array of carbon honeycomb cylinders that are concentrically nested. The structural arrangement of MWNTs causes the carbon atoms on adjacent nanotubes to be uncorrelated, with a similar behavior to the graphene sheets in turbostratic graphite. Thus, perfect nanotube cylinders at large spatial separation from one another should be able to slide past one another easily.

The most commonly used high-quality graphitic materials is highly oriented pyrolytic graphite (HOPG), which is prepared by the pyrolysis of hydrocarbons at temperatures above 2000 °C. The resulting pyrolytic carbon is subsequently heat treated to higher temperatures to improve the crystalline order. When annealed above 3300 °C, the HOPG displays electronic, transport, thermal, and mechanical properties close to

those of single-crystal graphite, showing a very high degree of c-axis alignment. For the high temperature/stress-annealed HOPG, the crystalline order extends to ~1 μm within the basal plane and to ~ 0.1 μm along the c-direction [1].

1.3.2 Carbon Fibers

Carbon fibers represent an important category of graphite-related materials, whose structure and properties are closely related to CNTs. In terms of the difference of production process, the fibers can be divided into three categories: PAN (polyacrylonitrile)-, pitch-based or vapor-grown [2]. The PAN- or pitch-based carbon fibers are produced by the spinning of their precursors, followed by stabilization and carbonization at temperatures up to 1300 °C [2], while the vapor-grown carbon fibers are prepared by thermal decomposition of hydrocarbon precursors, where stabilization is not needed. The pitch-based carbon fibers are divided into isotropic-pitch-based and anisotropic mesophase-pitch-based carbon fibers, based on the precursors and the resulting material structure and properties. The commercially available mesophase-pitch-based fibers are exploited for their high bulk modulus and high thermal conductivity, while the commercial PAN (polyacrylonitrile) fibers are widely used for their high tensile strength. The high modulus of the mesophase pitch-based fibers is related to the high degree of c-axis orientation of adjacent graphene layers, while the structural defects inhibit the slippage of adjacent graphene planes relative to each other, and thus prevent the sword-in-sheath failure mode [1].

Although many precursors can be used to grow carbon fibers with different cross-sectional morphologies, the preferred orientation of the graphene planes is parallel to the fiber axis for all carbon fibers, which accounts for the high mechanical strength of the fibers [1]. In the 1970's and 1980's, carbon fibers with very small diameter were prepared by pyrolysis of hydrocarbons at high temperature (>1000 °C) in the presence of transition metal catalyst particles [4-8]. However, during these early years, no detailed

systematic studies of such very thin fibers were carried out. These fibers have various external shapes (tubular, twisted and irregular, and balloon-like) and contain a hollow cavity with a diameter ranging from 2 to more than 50 nm along the fiber axis. They consist of turbostratic stacks of carbon layers, parallel to the fiber axis, and arrange in concentric sheets. These fibers have two textures resulting from different growth processes: one is termed core region, and are made of long, straight and parallel carbon layers formed by catalytic growth; the other is termed external region, which results from a pyrolytic deposition during the secondary thickening growth process. The thickening process of the fibers occurs through an epitaxial growth process, in which the hydrocarbon gas is dehydrogenated at the ~1050 °C growth temperature, and the carbon deposit forms on the surface of the growing fibers. After heat treatment to about 2500 °C, the fibers bear a close resemblance to CNTs. After further heat treatment to about 3000 °C, the outer regions of the fibers form facets, and become more like graphite because of the strong interplanar correlations resulting from the facets.

1.3.3 Carbon Nanotubes

In 1991, Iijima of the NEC Laboratory reported the observation of multi-walled CNTs (MWNTs), collected from the carbon soot generated by an arc-discharge [9]. Figure 1.4 shows the HRTEM images of multi-walled CNTs observed by Iijima in 1991. Whereas Iijima's initial observation was for multi-walled CNTs, two years passed before single-walled CNTs were discovered [10, 11]. The theoretical studies predicted the extraordinary electronic properties of the nanotubes, and many experiments demonstrated a wide range of potential applications resulting from the unique structure and properties of CNTs. The most striking theoretical development was the prediction that CNTs could be either metallic or semiconducting, depending on their diameter and chiral angle [12-15]. Although predicted in 1992, it was not until 1998 that the prediction regarding the nanotube electronic properties was verified experimentally by STM [16, 17].

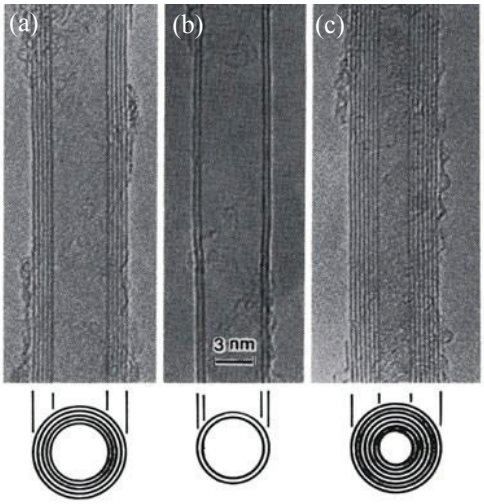

Figure 1.4 HRTEM images of multi-walled CNTs observed by Iijima in 1991 [9]: (a) 5-walled, (b) double-walled, and (c) 7-walled CNTs.

1.4 Carbon Nanotube Structures

The structure of a single-walled CNT is conveniently illustrated in terms of its 2D unit cell, defined by the vectors C_h and T, as shown in Figure 1.5 [12, 15]. The circumference of any carbon nanotube can be described in terms of the chiral vector Ch=nā1 + mā2, where ā1 and ā2 are unit vectors, and n and m are integers. The chiral angle, θ, is determined relative to the direction defined by ā1. Vector OB determines the fundamental one-dimensional translation vector T. The unit cell of the 1D lattice is the rectangle defined by the vectors Ch and T. For instance, in Figure 1.5a, the vector C_h has been constructed for (n, m) = (4, 2), and the unit cell of this nanotube is bounded by OAB'B. The formation of the nanotubes can be imagined by considering that this cell is rolled up so that O meets A and B meets B', and the two ends are capped with half of a fullerene molecule. Different types of carbon nanotubes have different values of n and m. Zigzag nanotubes correspond to (n, 0) or (0, m) and have a chiral angle of 0°, armchair nanotubes have (n, n) and a chiral angle of 30°, while chiral nanotubes have general (n, m) values and a chiral angle of between 0° and 30°. Examples are shown in Figure 1.6.

According to theory [12, 15], the (n, m) indices are crucial to the nanotube electronic structure. Specifically, SWNTs are metallic if |n-m|=3q and those for which |n-m|=3q±1 are semiconducting, where q is an integer, as shown in Figure 1.5b.

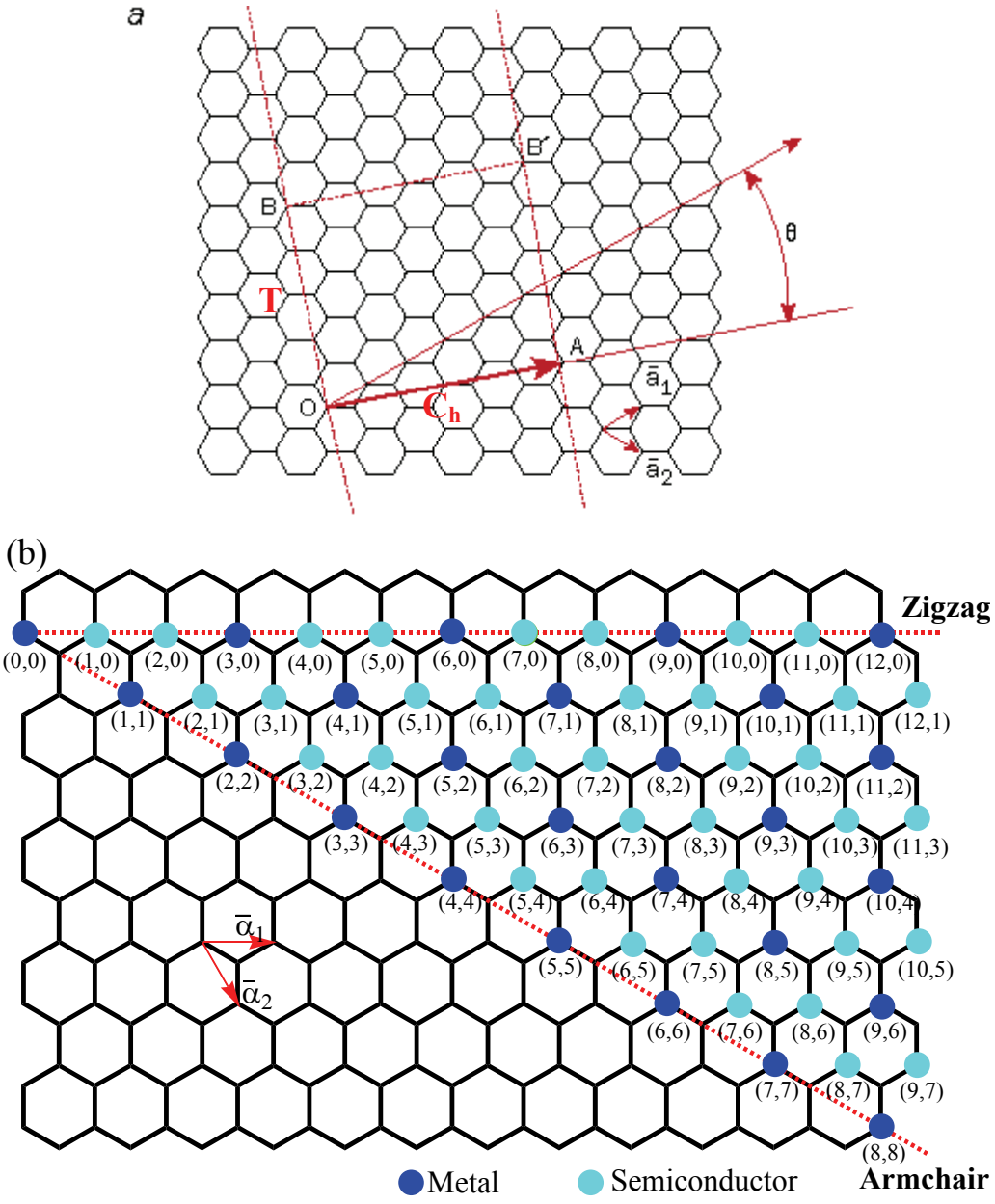

Figure 1.5 (a) Formation of a carbon nanotube by rolling up a two-dimensional graphene sheet into a cylinder and capping each end with half of a fullerene molecule; (b) chiral structures of nanotubes.

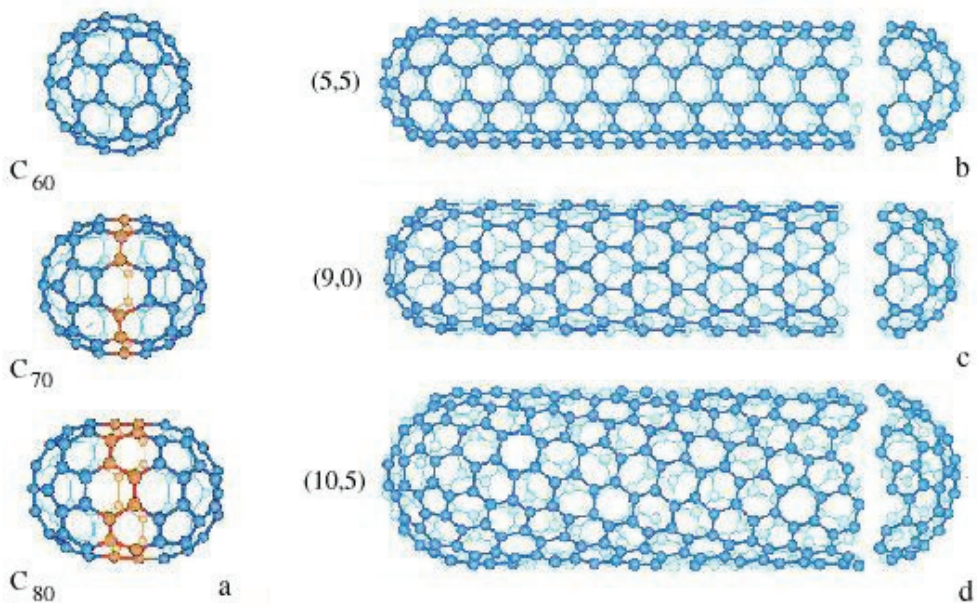

Figure 1.6 Each end of the CNT cylinder is capped with the hemisphere of a fullerene molecule.

The geometry of the graphene lattice and the chiral vector of the tube determine the structural parameters, such as diameter, unit cell, and number of carbon atoms. The diameter of the nanotube is given by

$$d = \frac{|C_h|}{\pi} = \frac{\sqrt{3}a_{c-c}\sqrt{n^2 + nm + m^2}}{\pi} \qquad \textbf{Equation 1.1}$$

where a_{c-c} is the C-C bond length (1.42 Å), while other parameters are summarized in Table 1.1.

Table 1.1 Parameters of carbon nanotubes [18, 19]

Symbol	Name	Formula	Value
a_{c-c}	Carbon-carbon bond length		1.42 Å
a	Length of unit vector	$\sqrt{3}a_{c-c}$	
$\bar{a}_1$, $\bar{a}_2$	Unit vectors		
$\mathbf{C_h}$	Chiral vector	$\mathbf{C_h}=\mathbf{n}\,\bar{a}_1+\mathbf{m}\,\bar{a}_2$	n, m are integers
L	Circumference of nanotubes	$L=a\sqrt{n^2+nm+m^2}$	
d	Diameter of the nanotube	$L=\frac{a\sqrt{n^2+nm+m^2}}{\pi}$	
θ	Chiral angle	$\cos\theta=\frac{2n+m}{2\sqrt{n^2+nm+m^2}}$	
T	Translational vector of 1D unit cell	$\mathbf{T}=t_1\,\bar{\mathbf{a}}_1+t_2\,\bar{\mathbf{a}}_2$ $t_1=\frac{2m+n}{\gcd(2n+m,2m+n)}$ $t_2=-\frac{2n+m}{\gcd(2n+m,2m+n)}$	gcd(m,n): the greatest common divisor of the two integers n and m
T	Length of **T**	$t_1=\frac{\sqrt{3}L}{\gcd(2n+m,2m+n)}$	
N	Number of hexagons per 1D unit cell	$N=\frac{2(n^2+n+m^2)}{\gcd(2n+m,2m+n)}$	

1.5 Carbon Nanotube Growth and Mechanism

The full potential applications of CNTs will not be realized until nanotube growth is optimized and well controlled. For composites applications, high quality CNTs are required at the kilogram or ton level, which requires the growth methods to be simple, efficient and cost-effective. For device applications, the layout of CNTs will rely on self-assembly or controlled growth strategies on substrates combined with micromachining technologies. In general, CNTs can be grown by arc-discharge, laser ablation and chemical vapor deposition (CVD) methods [1]. However, for device applications, the growth of CNTs by a CVD method is particularly attractive, due to the characteristic

CNT growth features, such as selective spatial growth, large area deposition capabilities, and aligned CNT growth.

1.5.1 Arc-Discharge and Laser Ablation Methods

An arc-discharge process has been developed to prepare high-quality multi-walled CNTs (MWNTs) and single-walled CNTs (SWNTs). In this process, carbon atoms are evaporated by a plasma of inert gas excited by high electric currents passing between an opposing carbon cathode and anode. Usually the carbon anode contains a small percentage of metal catalysts such as cobalt, nickel or iron. In 1992, Ebbesen and Ajayan adapted the standard arc-discharge technique for fullerene synthesis to synthesize MWNTs in a large scale under a helium atmosphere [20]. The results show that the purity and yield depend sensitively on the gas pressure in the reaction vessel. The length of the synthesized MWNTs is about several micrometers with diameters ranging from 2 to 20 nm. The nanotubes are highly oriented, indicating their high crystallinity. However, the synthesized CNTs are inevitably accompanied by the formation of carbon particles that are attached on the nanotube walls. A subsequent purification process is necessary to achieve high-purity nanotubes. In 1993, Bethune et al. reported the substantial production of SWNTs by an arc-discharge method using the carbon electrode incorporated with ~ 2 atom % cobalt metal [21]. At high temperature, the carbon and metal catalyst are co-vaporized in the arc, leading to the formation of carbon nanotubes with very uniform diameter (about 1.2 nm). However, fullerenes, the by-products of the arc-discharge process, form abundantly at the same time. In order to obtain high-purity SWNTs, a purification process is necessary.

In 1996, the Smalley group reported the synthesis of high-quality SWNTs with yields >70% using the laser ablation method [22]. This method utilized double pulse lasers to evaporate graphite rods doped with 1.2 atomic % a 50:50 mixture of Co and Ni powder, which was placed in a tube-furnace heated to 1200 °C in flowing argon at 500

Torr; this process was followed by heat treatment in vacuum at 1000 °C to sublime C_{60} and other small fullerenes. The synthesized SWNTs were very uniform with a diameter of ~1.38 nm which form ropes consisting of tens of individual SWNTs closely-packed into hexagonal crystal structures and stabilitzed through van der Waals forces.

The success in producing large quantities of high quality CNTs by arc-discharge and laser ablation offers wide availability of CNTs for fundamental studies and exploration of potential applications. However, there are several issues to be addressed in these two methods. First, both methods rely on evaporating carbon atoms from a solid carbon source at >3000 °C, which limits the scale-up of CNT production. Secondly, the CNTs synthesized by these methods are entangled, thereby making the purification, manipulation, and assembly difficult. Furthermore, the CNTs produced by these two methods are accompanied with by-products, including fullerenes, graphitic polyhedrons, and amorphous carbon in the form of particles or over-coats on the sidewalls of the nanotubes [23, 24].

1.5.2 Chemical Vapor Deposition (CVD)

For electronic device applications, chemical vapor deposition (CVD) methods are particularly attractive due to characteristic CNT growth features such as selective spatial growth, large area deposition capability and aligned growth. The CVD growth process involves heating the catalyst to a high temperature and introducing hydrocarbon gas or carbon monoxide (CO) into the tube reactor. The mechanism for CNT growth was generally assumed to be a dissociation-diffusion-precipitation process in which elemental carbon is formed on the surface of a metal particle followed by diffusion and precipitation in the form of cylindrical graphite [25, 26]. The main parameters in CVD growth of CNTs are the carbon precursors, catalysts, reactor chamber pressure, and growth temperatures. The effect of these process parameters on CNT growth has been investigated extensively in the literature, and these observations provide additional

insight into the nanotube growth mechanism. However, the exact nanotube growth mechanisms are still not understood well.

Influence of Temperature. Temperature has a significant effect on CNT formation and growth. Depending on the nanotube growth method, the CNT growth temperature can range from 400 °C [27, 28] to 3600 °C [29]. MWNTs are generally favored at temperatures between 500 to 1000 °C while SWNTs tend to grow at higher temperature, although recently the growth of aligned SWNTs at 750 °C has been reported [30, 31]. Lee et al. examined the temperature dependence of CNT growth from 800 °C to 1100 °C, and observed an increase of nanotube diameter and growth rate with increasing temperature, which was ascribed to the increased bulk diffusion rate of carbon in the metal catalyst particles [27].

Influence of Carbon Precursors. It was observed that CNTs can form from numerous carbon sources, including some hydrocarbon, polymer and organic compounds [32]. Hydrocarbons include methane, ethylene, acetylene, and some aromatic compounds, such as benzene and xylene. Favorable conditions for CNT growth for individual carbon precursors are highly dependent on the associated temperature, pressure, carrier gases, and choice of metal catalyst. The optimal recipe under one set of experimental conditions may be ineffective at different conditions.

Influence of Metal Catalyst. Iron, nickel, and cobalt are the most commonly used catalysts for CNT growth. Other metals have been reported for CNT growth, such as molybdenum [33, 34], tungsten [35], yttrium [36], and magnesium [37]; however these metals are generally used in combination with Fe, Ni, or Co. Fe, Ni, and Co nanoparticles, instead of smooth and continuous films, are often used as the catalysts. One of the reasons for choosing these metals as the catalyst for nanotube growth lies in the metal-carbon phase diagrams. At high temperature, carbon has finite solubility in these metals, which leads to the formation of metal-carbon solutions and precipitation of carbon atoms when supersaturated. The methods of implementing catalyst nanoparticles for nanotube

growth include solution-based catalyst preparation [38-42], physical evaporation for catalyst preparation [43-48], and floating catalyst approach [32, 49-51]. These methods differ in terms of the catalyst source, targeted applications, cost and final nature of the resulting CNT products, since CNT crystallinity, chirality, diameter, and growth rate are all influenced by the type of catalysts employed [52, 53].

Influence of support materials. The catalyst-support interactions not only determine the nanotube growth mode, but affect the CNT growth rate and quality. Prerequisites for a support material are thermal and chemical stability under the synthesis conditions. Other requirements include the surface area and porosity of the support materials. Hernadi et al. prepared supported Fe catalysts by different methods (impregnation and ion-adsorption precipitation) and by using various supports [54]. Iron on graphite showed low activity with low yield. Zeolite-supported catalysts prepared by ion-exchange were inactive in the formation of nanotubes, while the catalysts prepared by impregnation showed higher activity. The Fe/Y catalysts gave better results than Fe/ZSM-5. However, the Fe/silica catalysts led to even better results. Su et al. reported improved nanotube productivity using a novel aerogel supported Fe/Mo catalyst [24]. The nanotube productivity on Al_2O_3 supported catalysts is much higher than that on the SiO_2 supported catalysts with other conditions the same. Colomer et al. also found that the synthesis of SWNTs is more efficient for metal catalysts supported on alumina than on fumed silica [55]. Many other reports demonstrated that the coupling of catalysts and support has to be considered and that the support should be carefully chosen for different metals [56-59], since the metal-support interactions are critical in CVD processes for nanotube synthesis.

1.5.3 Nanotube Growth Mechanism

The catalyzed growth of CNTs by chemical vapor deposition (CVD) was discussed in detail, because it offers a promising route to bulk production of high-purity nanotubes that can be scaled-up to achieve commercialization. Composite materials research requires a ready supply of nanotubes with high purity in an easily dispersible form for applications of CNTs as conductive fillers or as reinforcing fibers [53, 60]. To optimize the CVD process, an understanding of nanotube growth mechanisms by CVD is necessary.

The formulation and growth of nanotubes is postulated to be an extension of known catalytic growth of carbon filaments on metals such as cobalt, nickel, and iron [61], since observation of the resulting CNTs indicated that catalyst particles were found on both ends of the CNTs, analogous to the case of carbon filament studies. Also it has been proposed that the form of the produced graphite is closely related to the physical dimensions of metal catalyst particles, based on a considerable volume of research conducted on the formation of graphitic carbon over various metals during the past three decades [62-66]. The appropriate metals have been consistently shown to be cobalt, nickel, and iron. The particular ability of these metals to form ordered carbon structures from decomposed hydrocarbon is presumably due to the following factors:

- Their catalytic activity for the decomposition of hydrocarbon
- Carbon has finite solubility in these metals
- They can form metastable carbides
- Carbon is able to diffuse through and over these metals rapidly.

These properties allow ordered carbon structures to be formed by a diffusion-precipitation mechanism. When the pyrolysis of hydrocarbons occurs over some transition metals, the metal could act as a solvent in which carbon dissolves to form a solid solution; graphite is then formed by crystallization. When the metal is present as nanoparticles, the carbon structure is formed as filaments with a similar diameter to that

of the catalyst particles. The metal particles can be supported on substrates or introduced as floating particles in the CVD chamber. A generally accepted mechanism for the growth of carbon filaments or nanotubes is the diffusion of carbon through the catalyst particles. The carbon deposited on the exposed surface of the particle dissolves in and diffuses through the catalyst particles [67]. However, the nature of the driving force for carbon diffusion through the catalyst particles is a subject of debate. The driving force could be temperature- [68-70] or concentration- gradient [71] within the particle. For CNT growth, the two mechanisms may be operative in parallel to describe CNT growth in various CVD environments.

Temperature-driven carbon diffusion mechanism. The key step in this mechanism was believed to be diffusion of carbon species through the particle from the hotter surface on which the exothermic pyrolysis of hydrocarbons occurs, to the cooler trailing surfaces on which carbon is precipitated (endothermic process) from the solid solution [62]. There is considerable experimental evidence to support this mechanism. For example, the measured activation energy of filament growth by olefin pyrolysis on nickel is 32±2 kcal/mol, a value in close agreement with the sum of the activation energy (20±2 kcal/mol) for diffusion of carbon through nickel in the temperature range 350-700 °C [72] and the enthalpy of solution of carbon in nickel (~10 kcal/mol) [73]. However, a temperature-driven dissolution-precipitation mechanism cannot provide a rational explanation for the endothermic pyrolysis of some hydrocarbons, e.g. methane decomposition.

Concentration-driven carbon diffusion mechanism [71]. Other than carbon diffusion driven by temperature, the only other possible driving force is concentration. This mechanism involves a concentration gradient across the catalyst particle in contact with hydrocarbon on one side and with a graphitic precipitation on the other side. Carbon growth involves a fast gas phase reaction (decomposition of hydrocarbon), carbon atom

dissolution in the metal, and carbon precipitation as graphitic structures at the opposite side of the catalyst particle.

Interaction between the metal catalyst particle and the support material is a key factor that influences the CNT growth mode. Figure 1.7 is a schematic representation of the two typical CNT growth modes, i.e. base-growth mode and tip-growth mode. If the particle adheres to the surface of support materials strongly, carbon precipitates from the front of the particle and CNT growth continues with the particle attached on the substrates. In contrast, when interaction between the metal catalyst and the support material is weak, carbon precipitates at the opposite surface of the particles and the growing CNT lifts the particles as it grows. In both cases the critical steps in the CNT growth process are carbon solubility and carbon diffusion through the catalyst particles.

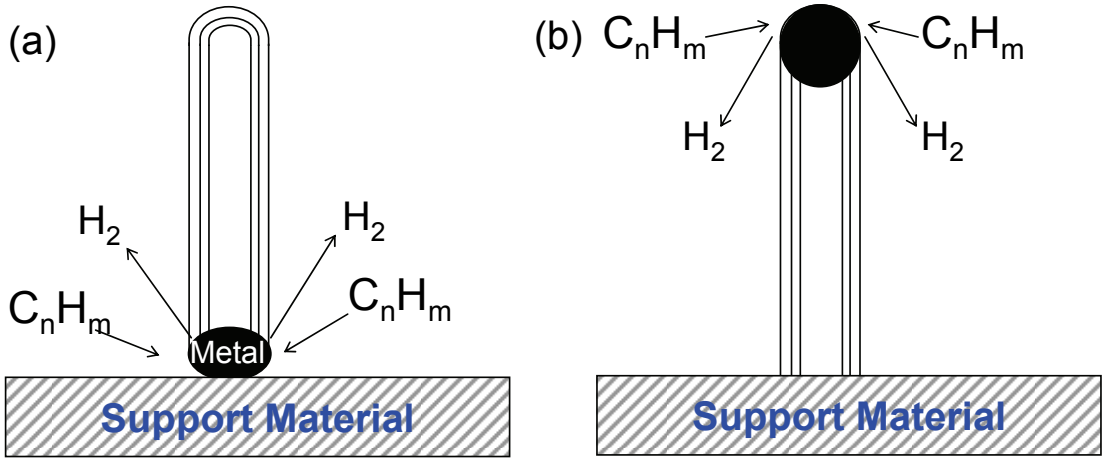

Figure 1.7 Two typical CNT growth modes in CVD: (a) base-growth mode, and (b) tip-growth mode.

1.6 Electrical Properties of Carbon Nanotubes

Electronic properties of CNTs have received the greatest attention in early nanotube research and applications. The nanometer dimensions of CNTs together with the unique electronic structure of a graphene layer make the electrical properties of the one-dimensional structures highly unusual. In addition to the electrical properties, the extremely small size and highly symmetric structure of the nanotubes result in remarkable quantum effects and thermal, mechanical, and optical properties.

Although graphene is a zero band gap semiconductor, initial theoretical calculations have shown that the CNTs can be metals or semiconductors with a size-dependent band gap [13-15, 74], depending very sensitively on the diameter and helicity of the nanotubes. Subsequent experimental measurements confirmed these theoretical predictions [75, 76] and the quantum wire feature of SWNT, SWNT bundles and MWNT. In the theoretical model, only the π orbital is considered, since mixing of $\pi(2p_z)$ and $\sigma(2s,2p_{x,y})$ carbon orbitals caused by the nanotube curvature is small and can be neglected near the Fermi level [13]. The two-dimensional (2D) energy dispersion relations for π bands of graphite, E_{2D}, are expressed using the wave vectors (k_x, k_y)

$$E_{2D}(k_x,k_y) = \pm\gamma_0\{1+4\cos(\frac{\sqrt{3}k_x a}{2})\cos(\frac{k_y a}{2})+4\cos^2(\frac{k_y a}{2})\}^{1/2} \qquad \textbf{Equation 1.2}$$

where γ_0 is the nearest-neighbor overlap integral, and a=0.246 nm. When graphene is rolled over to form a nanotube, the periodic boundary condition, $C_h \cdot k = 2\pi m$, is imposed to eliminate the wave vectors $\boldsymbol{k}$=(k_x, k_y), where m is an integer. In this way, 1D energy bands can be obtained by slicing the 2D energy dispersion relations using the periodic boundary condition. This leads to the following condition at which metallic nanotube properties result

$$(n-m) = 3q \qquad \textbf{Equation 1.3}$$

This suggests that one third of the nanotubes are metallic, while two thirds are semiconducting. The band gap for a semiconducting nanotube is given by

$$E_g = 2d_{cc}\gamma / D \qquad \textbf{Equation 1.4}$$

where d_{cc} is the C-C distance, γ is the nearest-neighbor overlap integral, and D is the nanotube diameter. The band gap of a 1-nm semiconducting nanotube is around 0.7 to 0.9 eV. This relation is in good agreement with STM measurements for SWNTs [16, 17]. The STM measurements also confirm the density of state (DOS) or band structure predicted from the dispersion relation of graphite imposed with tubular periodic boundary condition.

However, the derivation of the dispersion relation of a graphite sheet does not consider the curvature effect or $\sigma - \pi$ rehybridization. Blase *et al.* first recognized that $\sigma - \pi$ rehybridization has a strong effect on the nanotube electronic properties further away from the Fermi level [74]. Rehybridization shifts the π^* states to lower energy, while increasing the energy of the σ^* bands. This effect has been investigated using various approaches, including first principle *ab-initio* calculations [77]. It was found that $\sigma - \pi$ rehybridization can open up a small band gap (~0.02 eV) for smaller (<1.5 nm) nonarmchair metallic tubes. However, this effect is shown to disappear quickly with an increasing in the nanotube diameter.

Experiments show that a single SWNT, a SWNT rope, or a MWNT [78] behaves like a quantum wire due to the geometrical confinement effect on the tube circumference. A SWNT rope or MWNT can be viewed as a parallel assembly of single SWNTs. The conductance for a SWNT, a SWNT rope, or MWNT is given by

$$G = G_0 M = (2e^2 / h)M \qquad \textbf{Equation 1.5}$$

where $G_0=(2e^2/h)=(12.9\ k\Omega)^{-1}$ is quantized conductance, M is an apparent number of conducting channels including electron-electron coupling, intertube coupling effects, and internal channels. M=2 for a perfect ballistic SWNT less than 1 μm long. However, M is

also affected by scattering from defects, impurities, and structural distortions, and coupling with substrates or contact pads. Therefore, the experimentally measured conductance is much lower than the quantized value. For example, the measured resistance for a single SWNT is ~10 kΩ, as compared with the theoretical value of 12.9/2 or 6.45 kΩ. The nature of transport properties determines the fundamental properties such as the amount, location of energy dissipation, and the speed of signal propagation. The measured conductance is determined not only by the intrinsic properties of the tubes, but also by the presence of the scattering sites, such as defects, impurities, structural distortions, tube-tube interaction in a rope, substrate charges, and the nature of tube contacts to the macroscopic electrodes. Therefore, while a single metallic tube ideally has a conductance of $4e^2/h$, a much lower conductance is usually observed.

1.7 Carbon Nanotube Defects

The development of nanoelectronics based on nanotubes is a very promising direction in nanotechnology. The 1D nanotube molecule can conduct electricity at room temperature with essentially no resistance, known as ballistic transport. However, in reality, the CNTs have finite length with defects, which influences the electronic and thermal properties of carbon nanotubes. The possible defective structures can be classified into four main categories: topological defects (introduction of ring sizes other than hexagon), rehybridization of carbon sp^2 and sp^3 orbitals, incomplete bonding defects (such as vacancies and dislocations), and doping with elements other than carbon [79].

1.7.1 Topological Defects

Interesting structural features occur near the ends of the nanotubes from the closure of the graphene cylinders by incorporation of topological defects such as pentagons in the hexagonal carbon lattice. The electrical properties are affected locally in

the nanotube tip regions, while the main body of the nanotube with large aspect ratio of 100-1000 remains unaffected. Complex end structures can result from the way pentagons are distributed near the ends of the nanotube for its closure. Figure 1.8 shows the variations of the density of states along a (10, 10) nanotube capped by a hemispherical C_{240} tip apex containing six pentagons in a five-fold symmetry [80], which indicates that the localized state peak appears sharper and closer to the Fermi level. In principle, a (10, 10) tube is metallic, but, as shown in Figure 1.8, there is a huge increase of density of states near the Fermi energy toward the cap apex. This implies a corresponding enhancement of the field emission current [79]. Different tip apex topologies give rise to peak location in the valence or conduction regions. In the experiments, the tube ends with conical shapes appear more often. Figure 1.9 shows a computed local density of states for a (24, 0) nanotube capped with a conical end [80]. The conical cap reduces the tube diameter from 2 nm (labeled d in Figure 1.9) to 0.8 nm (labeled a). The convexity and concavity at the larger and small ends of this conical cap correspond to the presence of a pentagon and heptagon, respectively.

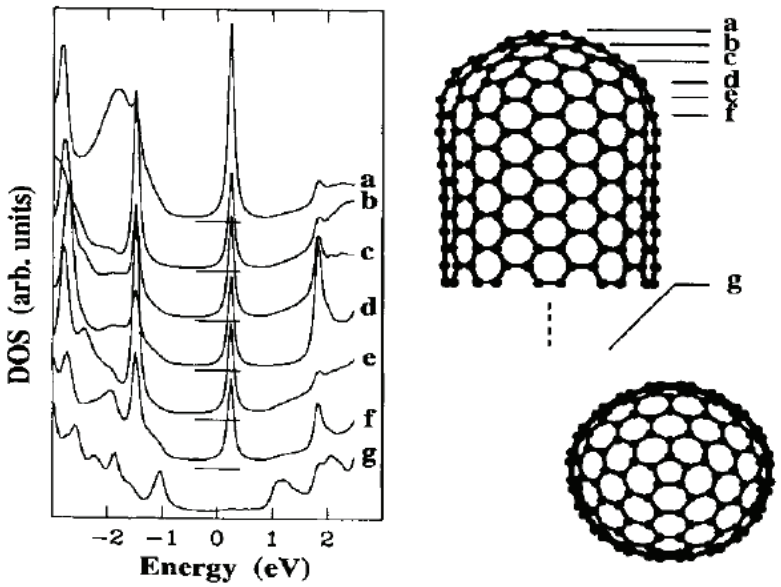

Figure 1.8 Computed tight-binding local density of states along a (10, 10) nanotube capped with half a C_{240} molecule [80].

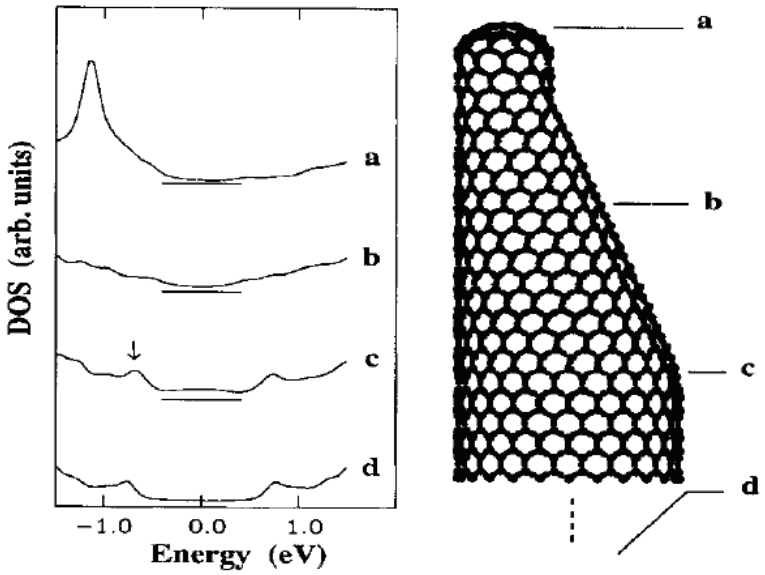

Figure 1.9 Computed tight-binding local density of states along a (24, 10) nanotube capped with a conical end [80].

Nanotube intramolecular junctions, formed by interposing one or multiple topological pentagon-heptagon defects in the hexagonal structure between two nanotube segments of different helicity, were theoretically proposed for their potential in the creation of nanoelectronics devices [81-85]. These carbon-based nanostructures could form molecular-sized metal-semiconductor, metal-metal, or semiconductor-semiconductor junctions. The existence of such atomic-level structures and the measurement of their respective electronic properties have been reported [77, 86]. The pentagon-heptagon pair creates only a small local deformation in the diameter of the nanotube, and may also generate a small change in the helicity, depending on its orientation in the hexagonal network. Figure 1.10 shows the junction using a pentagon-heptagon pair between (8, 0) and (7, 1) nanotubes to join a semiconducting nanotube to a metallic one.

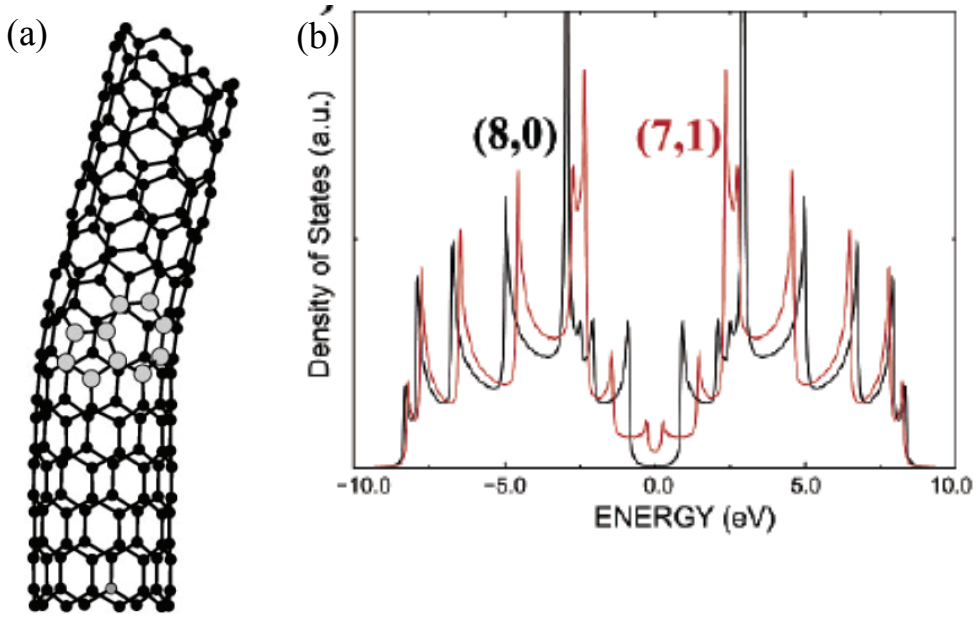

Figure 1.10 (a) Atomic structure of an (8, 0)/(7, 1) intramolecular carbon junction. The large light-grey balls denote the atoms forming the heptagon-pentagon pair. (b) The electron density of states related two perfect (8, 0) and (7, 1) nanotubes [85].

1.7.2 Doping Carbon Nanotubes

Introduction of boron and nitrogen into the carbon lattice leads to changes in the electronic structure of CNTs [87-89]. Carroll et al. studied changes in the electronic structure of MWNTs due to the introduction of boron in the lattice using scanning tunneling spectroscopy [87]. It was found that the doped tubes are metallic with no apparent band gap, in contrast to undoped ones with varying electronic character. Boron-doping of MWNTs results in the addition of acceptor states near the valence band edge. *ab initio* calculations, combined with the tunneling spectroscopy measurements, demonstrate that the changes in the local density of states should be interpreted in terms of nanodomains of dopant islands instead of isolated substitutional species. The local density of states of boron-doped CNTs exhibits strongly localized acceptor states (p-doping), as shown in Figure 1.11. The nitrogen-doped CNTs are also metallic and exhibit strong electron donor states near the Fermi level. The tight binding and *ab initio* calculations show that the pyridine-like N structures are responsible for the metallic

behavior and the prominent features near the Fermi level, as shown in Figure 1.12 [88], in which N rich cavities are formed throughout the predominantly graphitic network. The model consisting of pyridine-like units included in CNTs results in a different electronic behavior. Specifically, the origin of the low-energy electronic states can be observed using tight binding electronic structure calculations of the atomic arrangement, as shown in Figure 1.12. The density of states calculations show prominent donor peaks. The N doping using extended pyridine-type structures localizes the donor state and is responsible for the high intensity π peak, just above the Fermi energy of the original undoped nanotubes.

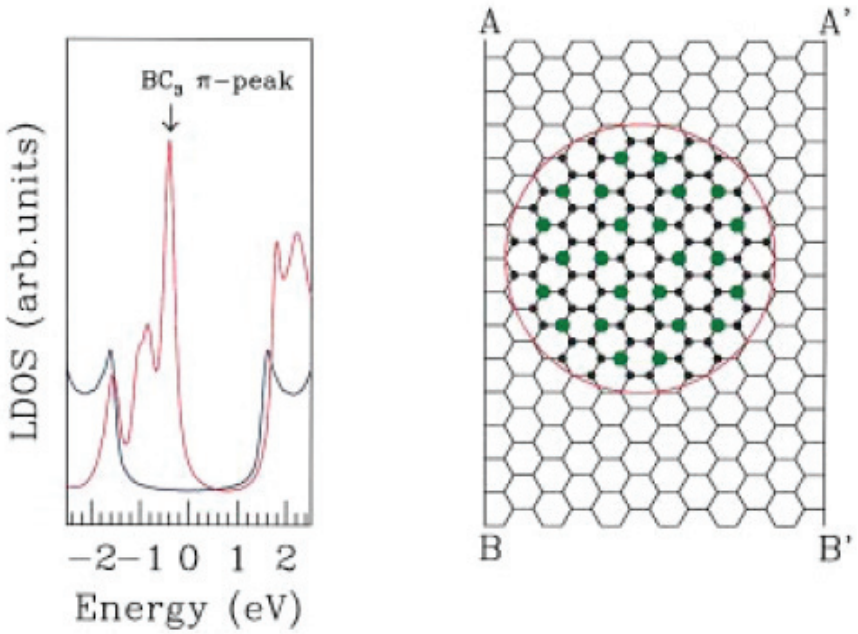

Figure 1.11 Electronic properties of carbon nanotubes doped with boron. Every B atom (Green balls) is bonded to three C atoms [87].

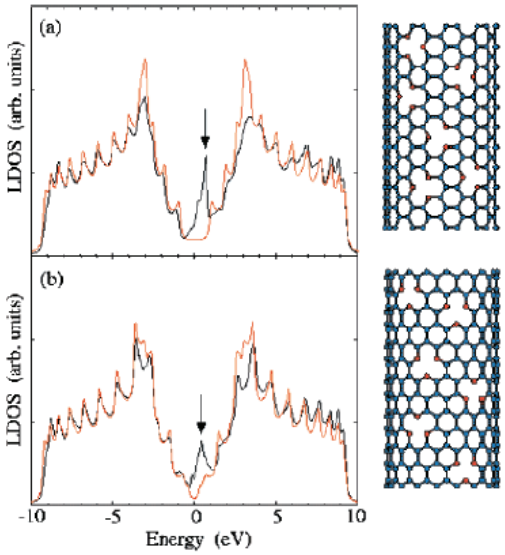

Figure 1.12 Theoretical density of states associated with pyridine-like structure of N-doped (a) (10, 10) armchair and (b) (17, 0) zigzag nanotubes. In both cases, a random but homogeneous doping (N, red balls; C, blue balls) is adopted. The pyridine-like structure of N-doping is responsible for the prominent donor-like features above the Fermi energy. The semiconducting nanotubes become metallic after introducing N in the carbon lattice [88].

1.8 Functionalization of Carbon Nanotubes

As mentioned above, synthesized nanotubes are not ideal structures, but rather contain defects formed during synthesis. An analysis demonstrates that about 5% carbon atoms in a SWNT are localized at defects [90]. The defects in a tube can be divided into four categories, as shown in Figure 1.13. One growth defect encountered frequently is the Stone-Wales defect, comprised of two pairs of five-membered and seven-membered rings, referred to as a 7-5-5-7 defect (Figure 1.14) [91]. A Stone-Wales defect leads to a local deformation of the nanotube sidewall, and thereby introduces increased curvature. The strongest curvature occurs at the interface between the two five-membered rings; as a result, addition reactions are most favored at the carbon-carbon double bonds in this region [92]. Removal of the nanotube caps by strong acids, for example, HNO_3, can result in the decoration of the ends with carboxylate groups [90, 93-95]. Also, the carboxylate groups can be bonded on the defects along the nanotube sidewalls. Typically,

around 1-3% carbon atoms of a SWNT are functionalized as carboxylate groups after a nitric acid treatment [96]. Defects in nanotubes are important in the covalent chemistry of the tubes, because they can serve as anchor groups for further functionalization, or for the covalent attachment of other chemical moieties. Therefore, defects can be utilized as a starting point for the development of covalent chemistries of the nanotubes.

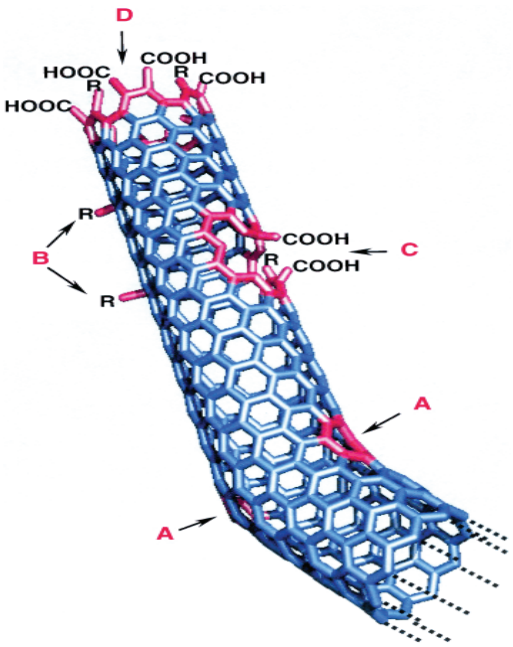

Figure 1.13 Typical defects in a SWNT: (A) Stone-Wales defect, (B) sp^3-hybridized defects (R=H or OH), (C) carbon framework damaged by severe oxidative conditions, leaving a hole lined with –COOH groups, and (D) open end of the nanotube, terminated with –COOH, or other terminal groups such as $–NO_2$, -OH, -H, and =O [97].

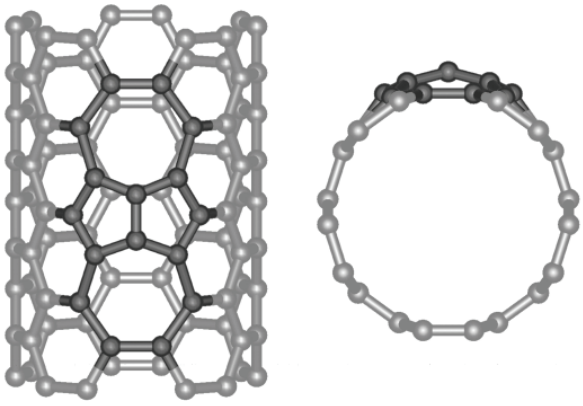

Figure 1.14 Stone-Wales (or 7-5-5-7) defect on the sidewall of a nanotube [91].

Chemical functionalization of the nanotubes offers an additional impetus towards extending their application spectrum. In addition to defect functionalization, other approaches have been developed to functionalize the CNTs including covalent functionalization of the sidewalls, noncovalent exohedral functionalization, and endohedral functionalization (Figure 1.15).

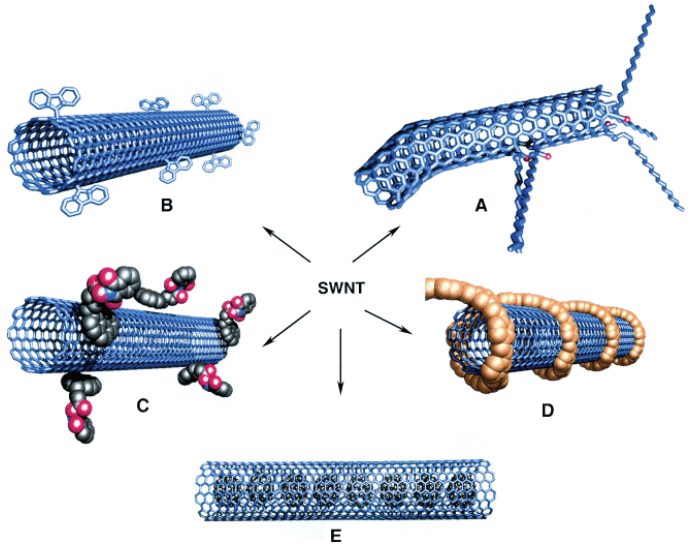

Figure 1.15 Functionalization approaches for CNTs: (A) defect-group functionalization, (B) covalent sidewall functionalization, noncovalent exohedral functionalization with (C) surfactants and (D) polymers, and (E) endohedral functionalization using nanoparticles [97].

1.8.1 Covalent Sidewall Functionalization

CNTs have been fluorinated by elemental fluorine in the temperature range of 50-600 °C [98-103]. Two possible addition patterns, i.e. 1,2-addition and 1,4-addition, have been proposed [104]. However, which pattern (1,2- or 1,4-addition) is more favorable onto the CNT sidewalls is currently unclear. Semiempirical calculations show that 1,4-addition is more stable [104]; on the contrary, density-functional theory (DFT) calculations with periodic boundary conditions on a fluorinated tube predict the 1,2-addition is more energetically stable [105]. But both calculations indicate that the energy difference between the two isomers is quite small, implying both additions may co-exist.

The sidewall carbon atoms attached by F atoms are tetrahedrally coordinated and adopt sp^3 hybridization, which destroys the electronic band structure of metallic or semiconducting CNTs, making the CNTs insulating.

The highest degree of functionalization was estimated to be about C_2F by elemental analysis. However, when the fluorinated SWNTs undergo pyrolysis up to 1000 °C, the tubes were cut into short ones with average length of less than 50 nm [106]. Fluorinated nanotubes were reported to have a moderate solubility (~1 mg/L) in alcohol-based solvents [107]. Treatment of these fluorinated tubes with hydrazine at room temperature causes defluorination reactions [108], whereas elevated temperature annealing is an effective way to recover the nanotubes [109].

Fluorination reactions are very useful because further functionalization or substitution can be accomplished [110]. For example, alkyl groups can replace the fluorine atoms using Grignard [111] or organolithium reagents [112] (Figure 1.16). The alkylated CNTs are soluble in common organic solvents, and can be completely dealkylated upon heating at 500 °C in inert atmospheres. The direct sidewall functionalization with organic groups is possible by reactive species, such as nitrenes, carbenes, and radicals [113, 114].

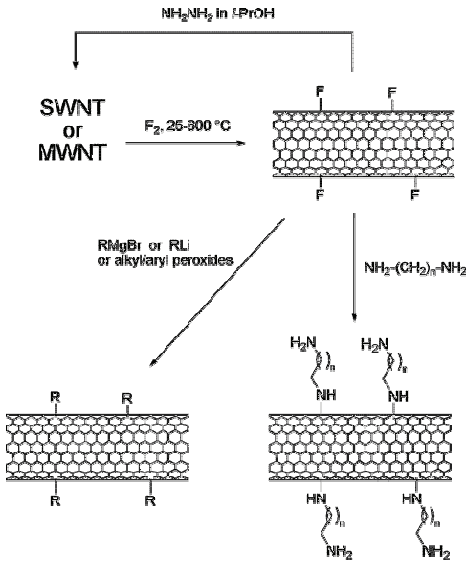

Figure 1.16 Reaction scheme for nanotube fluorination and further derivatization [115].

1.8.2 Noncovalent Exohedral Functionalization

CNTs are difficult to disperse homogeneously in solution without surface treatment due to the formation of strongly held tube bundles. One strategy widely used to exfoliate bundles and prepare individual CNTs is the noncovalent wrapping of the tube sidewalls by various species such as polymers [53, 116-119], polynuclear aromatic compounds [120-124], surfactants [125-128], and biomolecules [129-132]. Noncovalent functionalization of CNTs is very attractive because it offers a nondestructive method for attaching chemical groups on tube sidewalls. The noncovalent interaction is based on van der Waals forces or π-π stacking.

Research on immobilization of biomolecules on tube sidewalls was motivated by the prospects of using nanotubes as new types of biosensor materials [133]. The electronic properties of nanotubes coupled with the specific recognition properties of the immobilized biomolecules could be utilized for miniaturized biosensors. Noncovalent functionalization is a reliable method to immobilize biological molecules onto nanotubes. For example, the bifunctional molecules, 1-pyrenebutanoic acid succinimidyl ester, are adsorbed onto the inherently hydrophobic surfaces of SWNTs in an organic solvent (dimethylformamide, or methanol) (Figure 1.17). The highly aromatic pyrenyl group interacts strongly with the tube sidewalls via a π-π stacking interaction. This leads to attachment of 1-pyrenebutanoic acid succinimidyl ester on the tube sidewalls. The succinimidyl ester groups, which are highly reactive to nucleophilic substitution by primary and secondary amines that exist in abundance on the protein surfaces, form amide bonds for protein immobilization. This technique enables the immobilization of a wide range of biomolecules on the tubes with high specificity and efficiency.

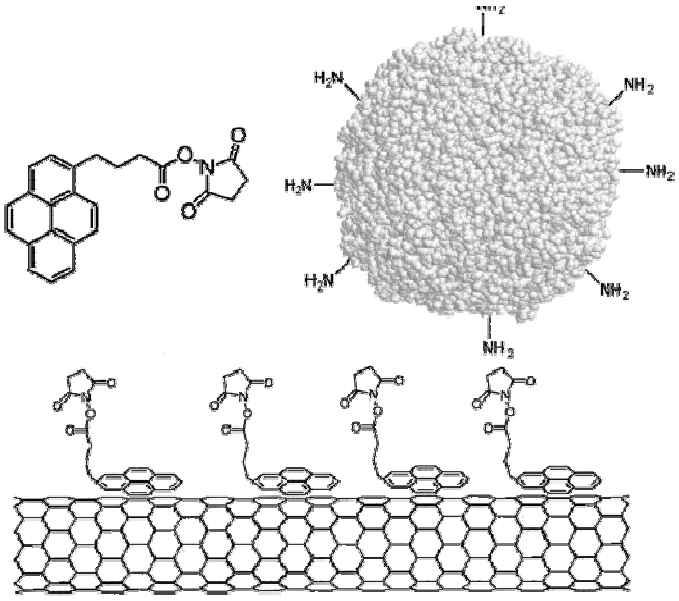

Figure 1.17 Amine groups on a protein react with the anchored succinimidyl ester to form amide bonds for protein immobilization [133].

1.8.3 Endohedral Functionalization

The hollow cavity of CNTs offers space for storage of guest molecules [134, 135], templates for making nanowires [136, 137] or nanochannels for transporting liquids and gases [138, 139]. The first molecule ever encapsulated in the nanotubes is the fullerene C_{60} [140]. Incorporation of C_{60} (formed together with nanotubes by a pulsed laser vaporization method) in nanotubes occurs accidentally during postsynthesis processing of the nanotubes. Fullerenes are the choice for tube filling, as both are structurally related graphitic materials made by similar methods. van der Waals forces combined with the perfect geometrical match of the shape of the fullerene and the interior of the tube provide a highly efficient interaction that can be as high as 3 eV per C_{60}, 50% higher than the cohesive energy of fcc fullerene crystals [141, 142]. This indicates that encapsulation of C_{60} molecules in SWNTs is a spontaneous and irreversible process, provided that the tube diameter is about 0.6 nm wider than the fullerene diameter to allow incorporation of the π-orbitals of the graphitic structures. Other than C_{60}, some higher order carbon

spherical molecules have been reported to fill the tube cavity, such as C_{70}, C_{78}, C_{80}, C_{82}, and C_{84} [143-145]. Also, encapsulation of metallofullerene molecules has also been demonstrated, such as $La_2@C_{80}$ [146], $Gd@C_{82}$ [147], $Sm@C_{82}$ [148], $Dy@C_{82}$ [149], $Ti_2@C_{80}$ [150], $Sc_2@C_{84}$ [151], $Ca@C_{82}$ [152]. Atoms inside fullerenes can be clearly seen as dark spots in microscopy images, whereas the metallofullerenes exhibit an unusual rotational motion inside the confined tube cavity.

In addition to fullerenes, other materials introduced into the tube cavity include pure elements and oxides [153, 154]. Usually incorporation is a two-step process. First, a metallic salt (dissolved in a solvent or in its molten state) diffuses into the tube cavity by capillary force. Then the salt is reduced to the metal form by heat treatment in a hydrogen atmosphere or by photolytic reduction. By this strategy, metals such as Ru [135], Bi [155], Ag [156], Au, Pt, Pd [157], and Ni [158], have been deposited in the tube cavity. Liquid gallium filled CNTs have been reported to behave as nanothermometers by thermal expansion of liquid gallium in the temperature range 50-500 °C in the confined tube cavity [159].

1.9 Challenges and Research Objectives

The ballistic conductivity, high thermal conductivity and mechanical strength of CNTs make them ideal candidates for electrical interconnects in IC packaging and nanoscale devices. CNTs offer the promise of revolutionary improvements in reducing the interconnect pitch size, increasing thermal conductivity, and enhancing system reliability.

However, to utilize these extraordinary properties, several issues related to nanotube growth and assembly must be solved: a) structurally perfect nanotube growth; b) growth of defect-free nanotubes to macroscopic lengths; c) controlled growth of nanotubes at specific locations; d) accurate positioning of CNTs at relatively low

temperature; e) low-temperature synthesis of CNTs below 500°C; and f) improved adhesion of CNTs on substrates. The high resistance of an individual CNT indicates that an array of thousands of parallel CNTs will be necessary for interconnect applications. Although there are many reports about the growth of aligned CNT arrays with high purity, controlled areas and nanotube length, deliberate production of high-aspect-ratio nanotube structures has seldom been reported. High density CNT films/arrays help decrease the electrical resistance. The high CNT growth temperature and poor adhesion of CNTs on substrates have been recognized as a limitation to the immediate implementation of CNTs in microelectronics. One solution to the high growth temperature is to develop low CNT growth temperature process. However, this approach does not seem promising. We propose an alternative way to overcome the high growth temperature and poor adhesion problems. We term this process "CNT transfer technology". In MEMS packaging, the stiction problem is one of the main reasons for the lack of extensive applications. Effective ways to prevent in-use stiction are the use of hydrophobic coatings or the generation of increased surface roughness to reduce solid contact area. A Lotus Effect surface is a good model to satisfy these two needs. However, optimized geometric parameters are needed to design the strategies.

The objectives of this research can be broken into four categories:

- Develop an efficient process for CVD growth of aligned CNT films/arrays with high purity and density. In particular, in-situ opening of CNT ends is emphasized, since the internal CNT walls could be utilized for electrical and thermal conduction.
- Design experiments to establish regimes where diffusion- and kinetics-controlled growth of carbon nanotube films occur.
- Assemble CNTs on different substrates at relatively low temperature and characterize the as-assembled devices electrically and mechanically.

- Explore superhydrophobicity on two-tier (micro- and nano-meter roughness) surfaces to elucidate the roles of micrometer and nanometer roughness for optimized design of surfaces for MEMS stiction prevention.
- Study electrowetting of aligned CNTs to enable assembly of CNTs on copper substrates. The electrowetting strategy may be used to improve CNT-polymer bonding strength.
- Develop high performance CNT/epoxy composites with enhanced CNT/epoxy interfacial properties.

The overall organization and topics addressed in this study are shown in Figure 1.18. In Chapter 2, an efficient CVD method is described to rapidly grow CNTs to a macroscopic length with controllable geometry; by introduction of a trace amount of water into the CVD chamber during CNT growth, in-situ opening of CNTs is realized. In Chapter 3, CNT stack formation is utilized to monitor the CNT growth in diffusion- or kinetics-controlled regions, and the corresponding kinetic expressions are developed and discussed. In Chapter 4, the methodology that we term "CNT transfer process", is described and implemented to assemble aligned CNT films/bundles on substrates at solder reflow temperatures to improve nanotube performance by utilizing their internal walls as a result of the open-ended CNTs, and to assemble CNTs on substrates at low temperature using approaches compatible with current microelectronics fabrication processes. In Chapter 5, CNT architectures are built to explore two-tier (nano- and micro-meter) effects on superhydrophobic surfaces (Lotus Effect); in addition, electrowetting of aligned CNTs is enabled by assembly of CNTs on copper substrates. In Chapter 6, aligned CNT/epoxy composites are prepared with a novel polymer curing method (VFM radiation). VFM curing has been found to be effective in greatly improving the CNT/epoxy interfacial bonding strength. In Chapter 7, the research results in this thesis are summarized and future work for continuing research is recommended.

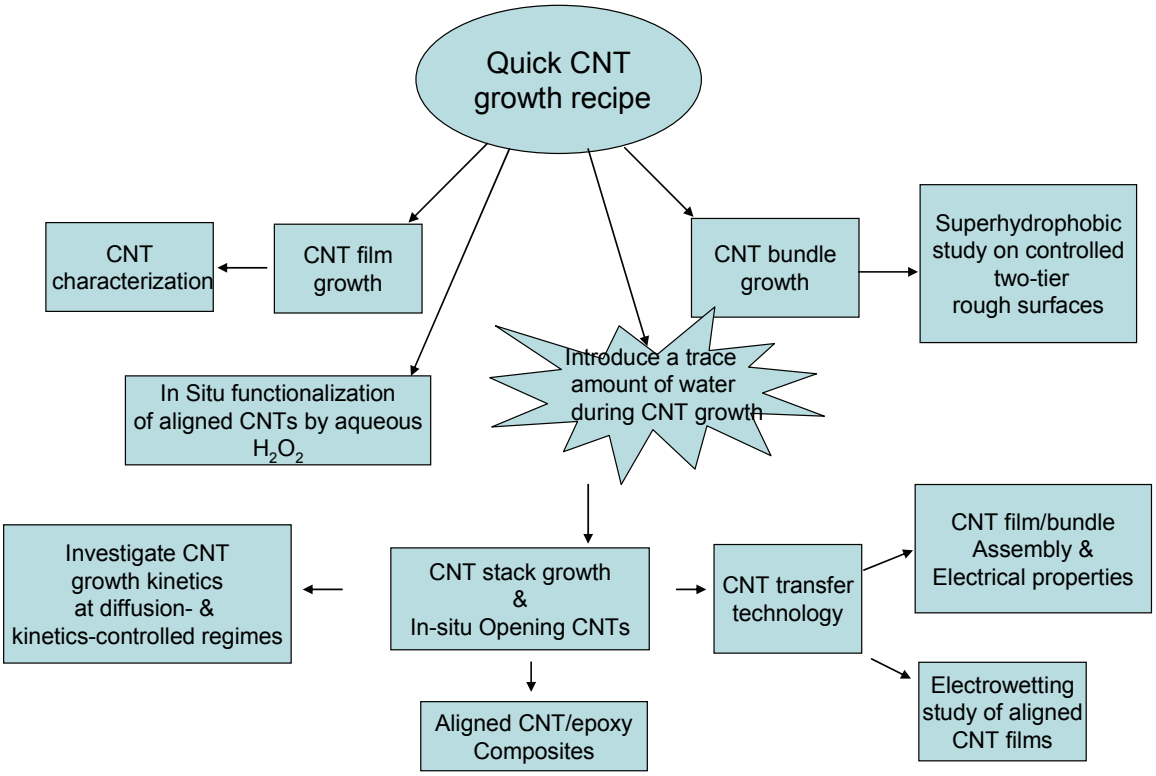

Figure 1.18 Schematic representation of the overall thesis research.

CHAPTER 2

CVD GROWTH OF CARBON NANOTUBE STRUCTURES

Carbon nanotubes (CNTs) have been extensively explored in attempts to take advantage of their unique properties for specific applications [160, 161]. Large-scale, well-aligned carbon nanotube films/arrays are desired because their collective properties could be utilized for fundamental studies and applications, such as field emitter arrays for flat panel displays. In our study, we attempted to develop a simple, but efficient chemical vapor deposition (CVD) method for the growth of high-quality, dense, aligned carbon nanotubes. CVD methods are of particular interest to grow CNTs for electronic device applications, due to the characteristic CNT growth features. This chapter begins with the experimental section (Chapter 2.1), in which procedures for rapid CVD growth of well-aligned CNTs and the characterization techniques are presented. Using these procedures, we demonstrate the growth of well-aligned CNT films (Chapter 2.2) and fine-pitch bundles (Chapter 2.3). Due to the importance of catalyst layers on CNT growth, in Chapter 2.3, detailed investigations are performed on the effects of catalyst film thickness on nanoparticle formation, and the effects of support materials (beneath the catalyst) on CNT growth. During these experiments, we found that if water, a weak oxidant, is introduced into the CVD chamber during CNT growth, the CNT ends can be opened by removing CNT caps. This technique is applied using alternate flow of carbon precursor into the CVD chamber to grow CNT stacks. These results are presented in Chapter 2.5 with a discussion of stack growth mechanisms. In Chapter 2.6, we present an approach to in-situ modification of CNTs. Instead of using water vapor, hydrogen peroxide (H_2O_2) is introduced into the CVD chamber during CNT growth. H_2O_2 can in-situ functionalize CNTs, and the modified CNTs can serve as stabilizing substrates for nanoparticle immobilization and dispersion by providing nucleation sites on the modified CNT walls.

2.1 Experimental

2.1.1 CNT Structure Growth

CNT film growth. Chemical vapor deposition (CVD) was performed in a horizontal alumina tube (3.8 cm diameter; 92 cm long) housed in a Lindberg Blue furnace. The substrates used in this study were (001) silicon wafers coated with SiO_2 (400 nm) by thermal oxidation or plasma-enhanced CVD. The catalyst layers of Al_2O_3 (10 nm)/Fe (1, 2, or 3 nm) were deposited on the silicon wafer by sequential electron-beam evaporation. The wafers were then cut into small samples (1×1 cm^2). In each experiment, the samples were placed in the middle of the CVD tube, the tube evacuated to 50 mTorr and back-filled with argon to atmospheric pressure. A constant argon flow was maintained at 350 sccm (standard cubic centimeters) while the furnace was heated to a temperature between 600 and 800°C. After reaching the desired temperature, hydrogen at 180 sccm and ethylene at 110-150 sccm were admitted to the tube. After a preset deposition time, the hydrogen and ethylene flows were terminated. The furnace tube was cooled to room temperature in the presence of a 350 sccm argon flow.

CNT array growth. Catalyst layers of Al_2O_3 (10 nm)/Fe (1, 2, or 3 nm) were patterned on the silicon wafer by a lift-off process. A schematic of the process is shown in Figure 2.1. A thin layer of photoresist (Shipley 1813) was spin-coated on a silicon substrate and subsequently exposed to UV light and the patterns developed. The catalyst layers of Al_2O_3 /Fe were then deposited onto the substrate by a sequential electron-beam evaporation process. The photoresist was removed by acetone and the wafer was cleaned using acetone, isopropyl alcohol and de-ionized (DI) water rinses. The patterned substrate was placed in the CVD chamber for highly-oriented CNT pillar growth under conditions described in the previous section concerning CNT film growth.

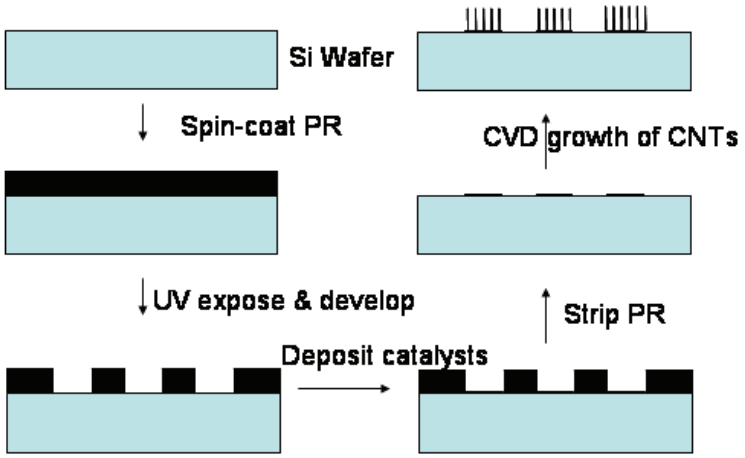

Figure 2.1 Schematic of CNT pillar growth.

Carbon nanotube stack growth. CVD was performed under the conditions described previously for CNT film growth, except that a trace amount of water was introduced into the CVD chamber during nanotube growth. The water vapor concentration in the CVD chamber was controlled by bubbling a small amount of argon gas through the water held at 22 °C. In all experiments, the water concentration was maintained at 750 ppm until the CVD process was terminated. The layered CNT films were obtained by the following sequence. Ethylene flowed into the CVD system for a preset time, after which the flow was terminated; after 5 min of only water, argon and hydrogen flow, ethylene was again introduced for a specific time. The fixed 5 min interval between CNT growth steps was used to selectively etch weakly bonded or amorphous carbon atoms at the interfaces between the nanotubes and catalyst particles by water vapor. This sequence was repeated to obtain the layered CNT films.

In-situ modification of nanotubes. Instead of only bubbling water, a trace amount of oxygen was introduced into the CVD chamber which was controlled by bubbling a small amount of argon through aqueous H_2O_2 (30%). In all experiments, the water concentration in the furnace tube was maintained around 750 ppm until the CVD process was terminated. The layered CNT films were obtained by the following method.

Ethylene was first flowed into the CVD reactor for a preset time. After 5 mins aqueous H_2O_2, argon and hydrogen flow, ethylene was again introduced for a specific time. During the fixed 5 min interval between CNT growth steps, water vapor and a trace amount of O_2 were used to both functionalize the CNT walls and tips and selectively etch weakly bonded or amorphous carbon atoms existing at the interface between the nanotubes and catalyst particles.

2.1.2 Characterization

Samples for transmission electron microscopy (TEM) examinations were prepared by sonicating a trace amount of synthesized carbon nanotubes in methanol for one hour. A few drops of the suspension were placed onto a TEM grid. TEM (JEOL 400EX) analysis was performed at 400 kV. Scanning electron microscopy (SEM) characterization was carried out on a JEOL 1530 equipped with a thermally assisted field emission gun operating at 10 keV. Spatially resolved energy-dispersive spectroscopy (EDS) was used to assess the purity of carbon nanotubes. X-ray Photoelectron Spectroscopy (XPS) was performed using a Physical Electronics (PHI) Model 1600 XPS system equipped with a monochromator; the system used an Al Kα source ($h\nu$ = 1486.8 eV). Ejected photoelectrons were detected by a hemispherical analyzer that provided high sensitivity and resolution. The operating pressure in the sampling chamber was below 5×10^{-9} Torr. All high resolution spectra were collected with a pass energy of 46.95 eV. The step size and time step were 0.025 eV and 100 ms, respectively. Fourier-transform infrared spectroscopy (FTIR, Nicolet, Magna IR 560) was used to study the in-situ functionalized CNTs. The in-situ functionalized CNTs were mixed with dried KBr and pressed to form semi-transparent pellets. The FTIR spectra were collected in the wave number range from 400 to 4000 cm^{-1}.

Two-probe current-voltage measurements of the CNT arrays were performed using an Agilent 4285A Precision LCR Meter. Capacitance-voltage (CV) responses were

measured by an HP semiconductor analyzer at a frequency of 100 kHz. Before the sample measurement, the analyzer was calibrated by touching probes on the two electrodes without CNT arrays on them to exclude the contribution of capacitance from the substrate. The nanotube array solution was placed on a substrate that had pre-patterned Au electrodes. Randomly, the two ends of some CNT arrays contacted electrodes. These samples were mounted on an electrical probe station, and two-terminal resistance measurements were performed by contacting the probes (12 μm tungsten needles) to these electrodes.

2.2 CNT Film Growth

SEM observation of CNT samples grown at 600 °C demonstrated that impurities resembling carbon black were deposited on the substrate as randomly distributed CNTs were formed; these results are shown in Figure 2.2.

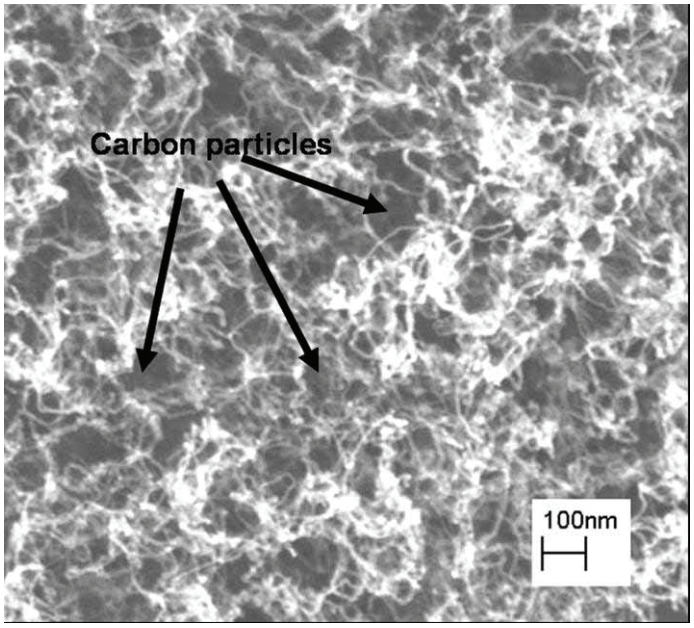

Figure 2.2 SEM image of CNTs grown at 600 °C. No CNT alignment is observed.

When the growth temperature exceeded 650°C, deposition of a black film was observed on the substrate after the samples were taken out of the furnace. Typical SEM images of these samples in a cross-section view are shown in Figure 2.3. Figure 2.3a shows a SEM image of aligned nanotubes grown normal to the substrate at 675 °C. Figures 2.3b-d show the nanotubes synthesized at 700, 750, and 800 °C, respectively. Clearly, aligned carbon nanotubes can be synthesized at temperatures above 650 °C; furthermore, the nanotube growth rate greatly increases with temperature. The average growth rate (μm/min) increases from 6 μm/min at 675°C to 100 μm/min at 800 °C.

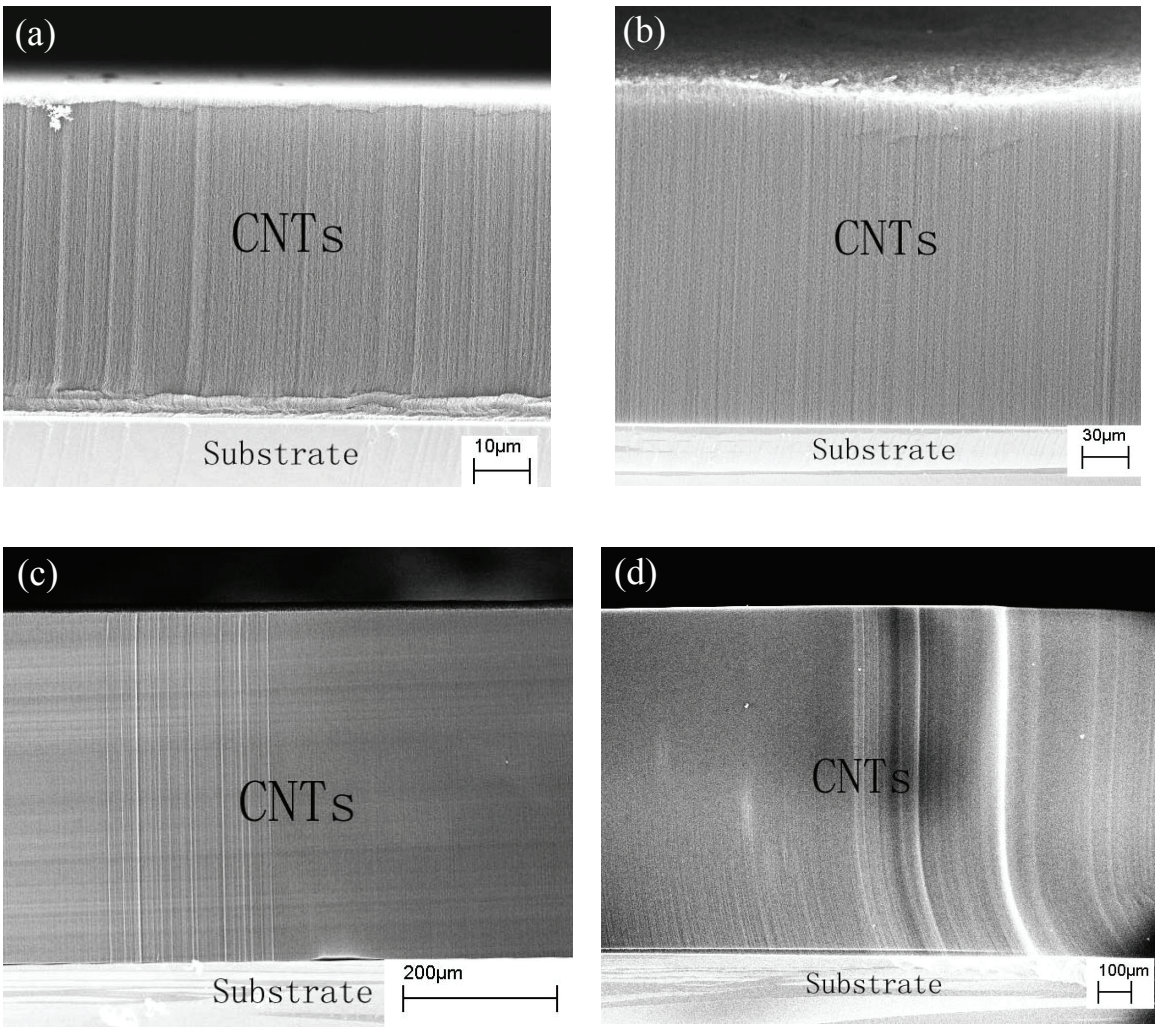

Figure 2.3 SEM images of carbon nanotube films grown at temperatures of (a) 675, (b) 700, (c) 750, (d) 800 °C for 10 min, respectively.

Higher magnification SEM images of the samples shown in Figure 2.4a demonstrate that no iron or carbon particles protrude from the nanotubes; also, it can be seen clearly that the film consists of well-aligned CNTs with high density (estimated above 1000 μm^{-2}). Figure 2.4b shows the TEM image of the CNT bundles after half an hour sonication of the samples. CNT diameters range from 8 to 13 nm, with an average diameter of 10 nm. From high resolution TEM images, it was observed that most of the nanotubes are double-walled (Figure 2.4c) with some 3 to 5 walled nanotubes.

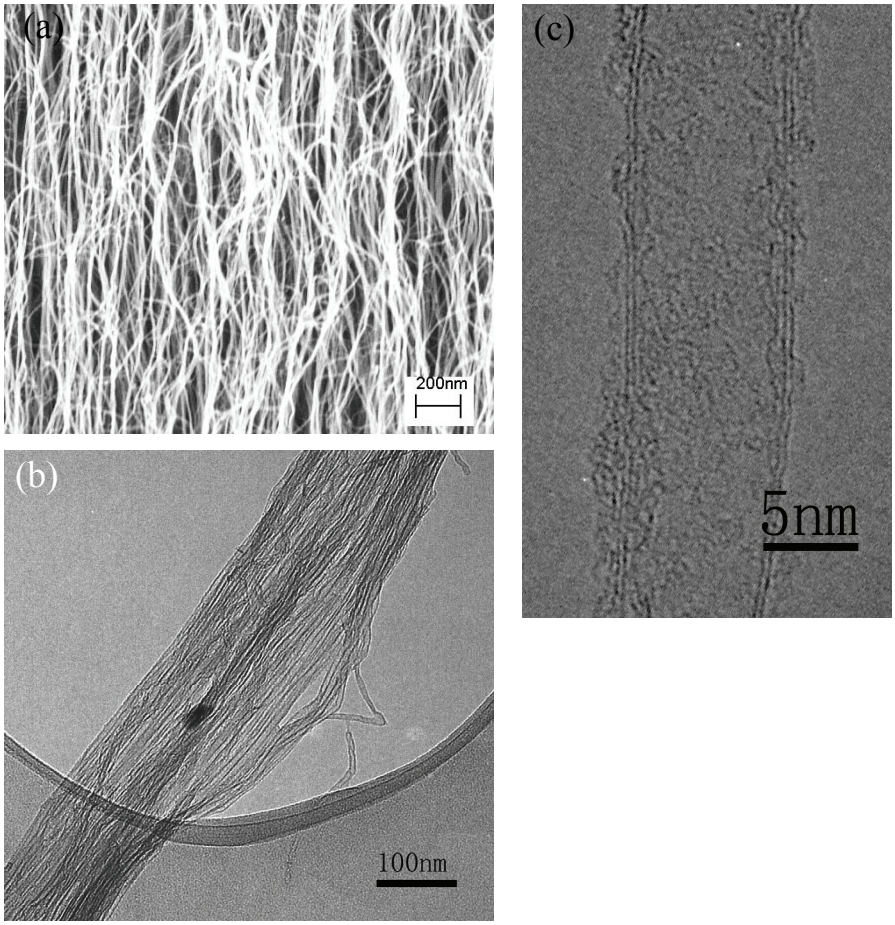

Figure 2.4 (a) High magnification SEM image of nanotube film; (b) TEM image of bundled CNTs; (c) HRTEM image of individual double-walled nanotubes.

2.3 CNT Array Growth

The integration of CNTs for electrical interconnect applications has been reported [162-164]. However, the resistance of a single ballistic SWCNT less than 1 μm long is about 6.5 kΩ with perfect contacts, while ballistic transport in MWCNTs with a resistance of 12.9 kΩ was also reported [165]. The high resistance of an individual CNT indicates that an array of thousands of parallel CNTs will be necessary for interconnect applications. Although there are many reports about the growth of aligned CNT arrays with controlled areas and nanotube length, deliberate production of high-aspect-ratio nanotube structures was seldom reported. In this study, we developed a simple, but efficient CVD method for the growth of aligned carbon nanotube arrays from a small area (<20 μm in diameter) but extending to a very long length (several hundreds of μm) without bending or curling. These high-aspect-ratio nanotube arrays are particularly useful as electrical interconnects or mechanical reinforcing backbones.

2.3.1 Fine-Pitch Nanotube Array Growth

The catalyst islands were patterned on silicon substrates by a lift-off process. These substrates with patterned catalysts were placed into the CVD tube for CNT growth using the procedure described in the experimental section. Aligned CNTs grow readily from the catalyst patterns into well-defined vertical structures, as shown in Figure 2.5, which shows SEM micrographs of CNT arrays with different pattern size, pitch and height. The synthesis conditions for Figures 2.5a and 2.5b are for 3 min at 750^{o}C and 700^{o}C, respectively. The images demonstrate that nearly vertically-aligned CNT pillars are formed on the substrate with minimal entanglement with neighboring CNTs, but the arrays bend at the tips due to gravity if the CNTs are too long. In Figure 2.5a, the height of the CNT arrays reaches 420 μm with an aspect ratio of 32, while in Figure 2.5b the height of the CNT arrays reaches 300 μm with an aspect ratio of 15. Furthermore, the vertical alignment of pillars can be influenced by the array aspect ratio. With a pillar

height <150 μm, no pillar bending was observed. In fact, further studies have demonstrated the CNT pillars maintain vertical growth up to an aspect ratio of 15.

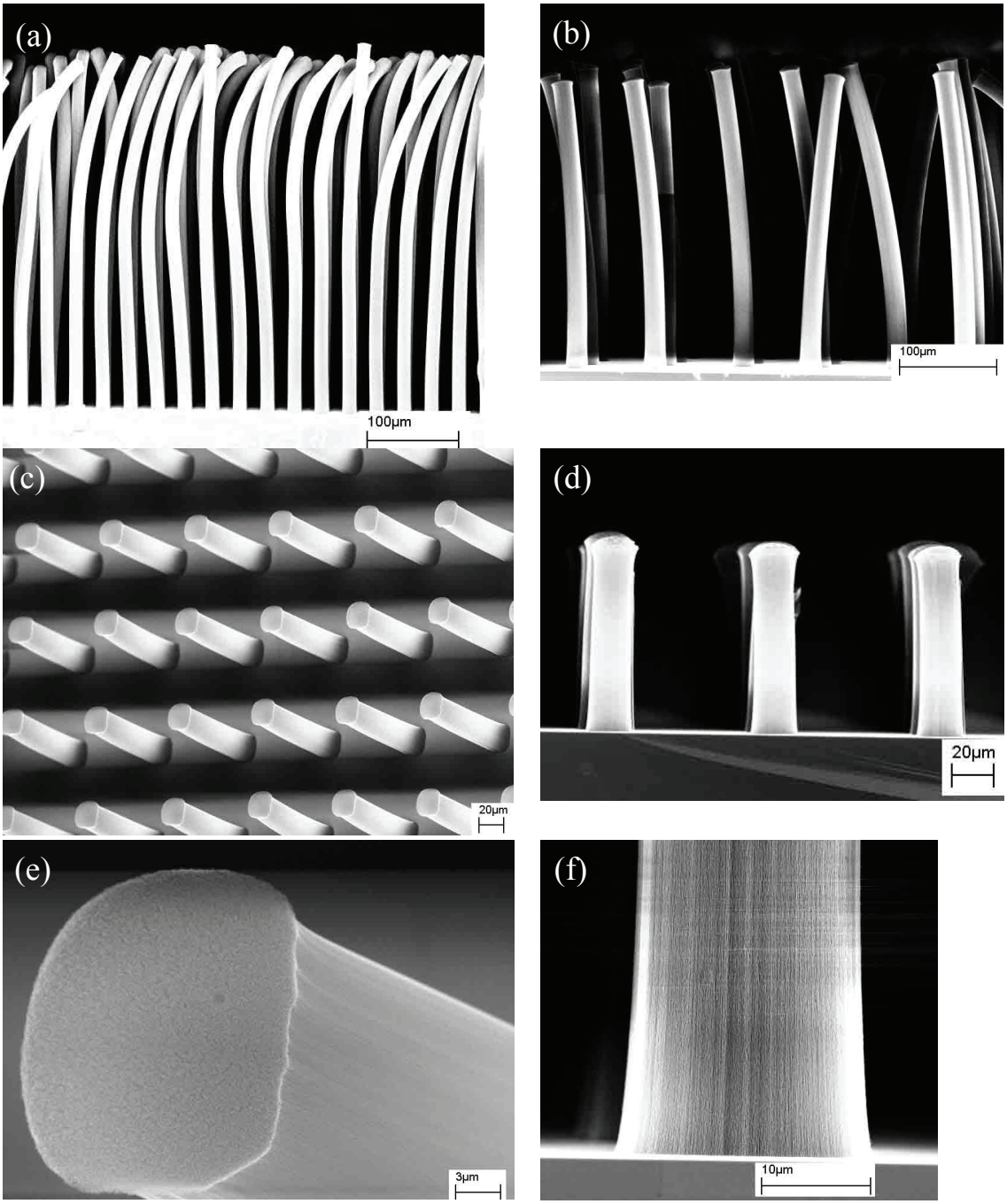

Figure 2.5 SEM micrographs of highly-aligned CNT arrays. (a) SEM image of nanotube arrays synthesized on 12 μm by 12 μm catalyst patterns; (b) SEM image of nanotube arrays synthesized on 20 μm by 20 μm catalyst patterns; (c) SEM image of nanotube arrays synthesized on cylindrical patterns with diameter of 20 μm; (d) side view of the nanotube arrays in (c); (e) enlarged view of a nanotube array tip in (c); (f) enlarged view of a nanotube array root in (d).

Figure 2.5e shows a high magnification SEM image of a nanotube array tip with a diameter of 20 μm. Figure 2.5f shows an enlarged image of the base of a free-standing nanotube array which indicates the well-defined edges of these CNT arrays. These results show that the height and aspect ratios of CNT pillars can satisfy most interconnect applications.

There are two levels of hierarchical alignment structure that exist in this CVD process. The primary alignment is a bundle of densely-packed CNTs to form the CNT pillar (Figure 2.4a). The secondary alignment is the array of CNT pillars on the substrate, where the growth of CNTs is confined within the catalyst patterns. From the microscopic to the macroscopic level, the alignment of CNTs makes possible the novel interconnect structures that can be produced by methods compatible with existing IC fabrication sequences. In Figure 2.4a no carbon or other particles are observed on CNT walls, and the high density of CNT bundles is evident. We estimate that the CNT density could reach 1000 μm^{-2}. EDS examination along the CNT bundles detected no elements except carbon, and HRTEM examination revealed no particles attached on the CNTs walls. These results indicate the high purity of the as-synthesized nanotubes. From HRTEM images, we also know that most of the CNTs synthesized by this CVD method are double-walled or triple-walled with an average diameter of ~10 nm.

It is well-known that the choice of support material and catalyst is one of the key issues for chemical vapor deposition (CVD) growth of nanotubes. In our case, the high-aspect-ratio nanotube arrays are grown by decomposition of ethylene on the Al_2O_3 supported Fe catalyst in a very short time. Aluminum oxide is a good catalyst support for nanotube growth. Without Al_2O_3, we do not obtain high-aspect-ratio nanotube arrays on a flat silicon surface. A detailed discussion of the effects of support materials on the CNT growth is presented in Chapter 2.4.

2.3.2 CNT Growth Mode

As shown in Figure 2.6, the thin Fe film of 2 nm segregated into small islands, after a heat treatment at 700°C or 750°C without ethylene gas introduction or carbon nanotube growth. Island diameters are between 5 and 15 nm, with an average diameter of 10 nm and a pitch (center-to-center spacing between adjacent particles) of ~15 nm. These catalyst islands effectively stimulate the growth of nanotubes in this process. It could be assumed that the nanotubes were grown from each Fe particle, based on the density, size and pitch of the as-synthesized nanotubes. Previous studies suggested that the size of the catalysts could define the diameter of as-grown nanotubes [166, 167], even though the CNTs are not aligned. In our case, it was also observed that the diameter of the as-grown aligned nanotubes is the same as that of the Fe islands, which suggests that the Fe particle size and distribution also determine the aligned CNT diameter and distributions. If the Fe particle size is further decreased, denser CNT arrays can be formed.

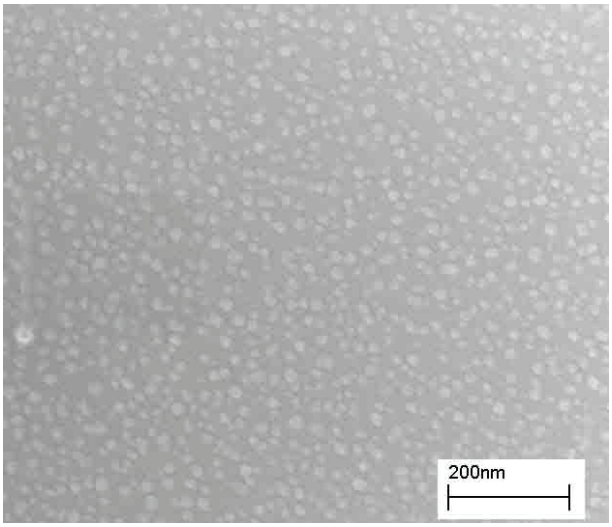

Figure 2.6 Catalyst nanoparticles formed on an Al_2O_3 substrate after a CVD run without ethylene gas or carbon nanotube growth.

XPS survey scans were taken on aligned CNT films prepared by the same CVD procedure except that catalyst material covered the entire substrate. Figure 2.7 clearly indicates that only carbon is detected and the XPS spectrum is identical with that of a

standard graphite sample. These results confirm that the as-synthesized CNTs are highly graphitized and of high purity. EDS studies agree with the XPS spectra in that no elements other than carbon are detected, as shown in Figure 2.8. These data clearly demonstrate the base-growth mechanism for nanotube synthesis by the CVD process. The growth mode also suggests continuous growth of CNTs throughout the entire pillar height, as there are no new catalysts added during the growth process.

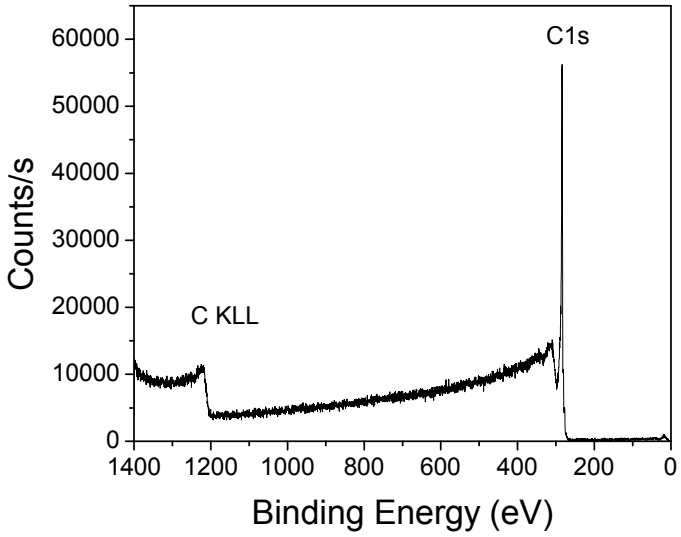

Figure 2.7 XPS survey scan of CNT array surface.

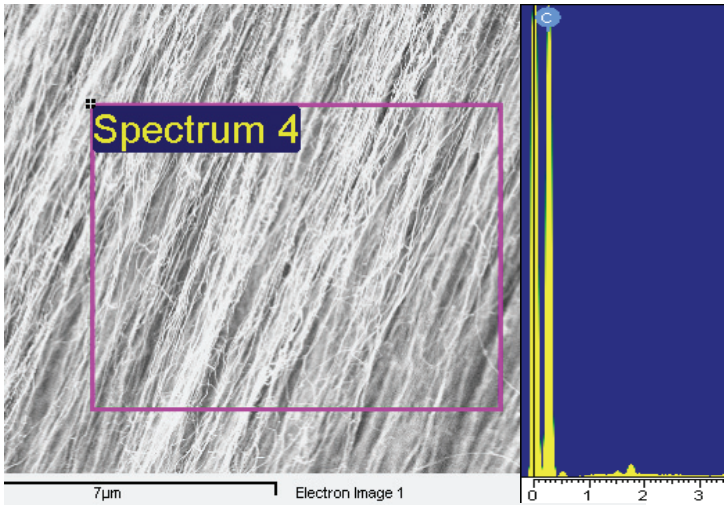

Figure 2.8 EDS analysis of CNTs along the CNT bundles.

To further explore the CNT growth mechanism, the nanotube film was peeled from the substrate as shown in Figure 2.9a. An XPS (Figure 2.9b) survey scan on this substrate indicated that some Fe particles remain on the substrate. Such results clearly demonstrate that the base-growth mechanism is responsible for nanotube growth by this CVD process.

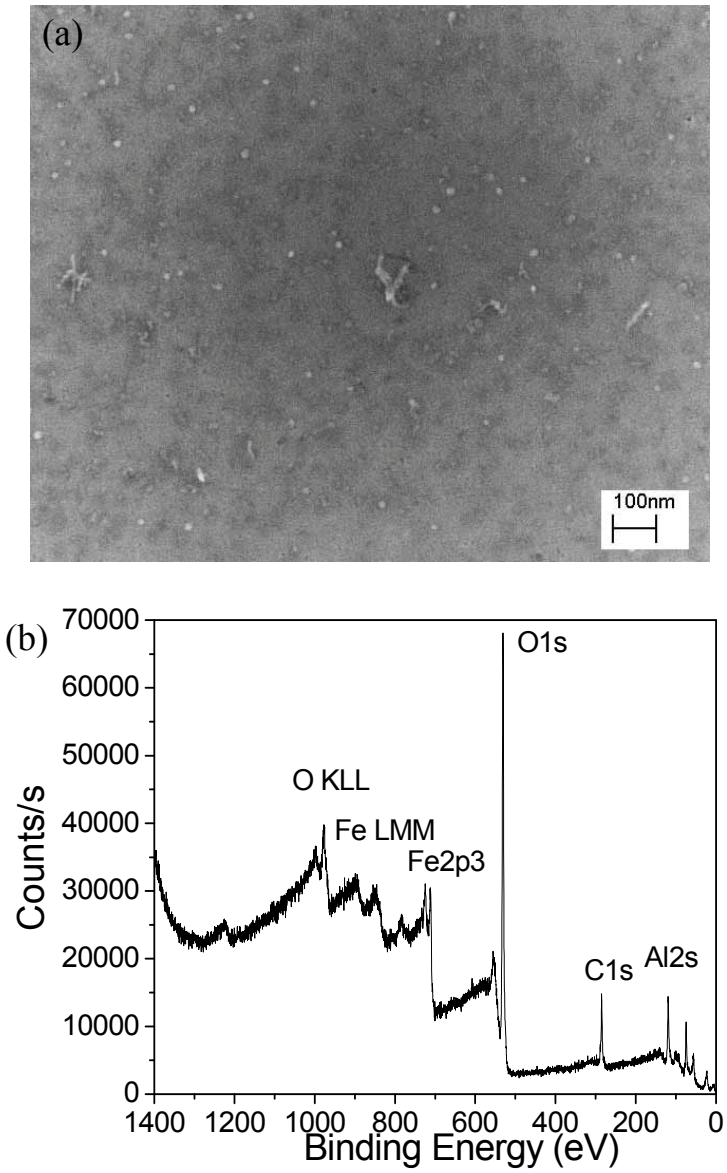

Figure 2.9 (a) High magnification SEM image of the substrate after nanotubes are peeled off; (b) XPS survey scan of the substrate shown in (a).

2.3.3 Electrical Measurements

Figure 2.10 shows an optical micrograph of a nanotube bundle bridging two electrodes. The distance between the two electrodes near the ends of the nanotube bundle is ~215 μm. The measured electrical resistance is ~250 Ω (Figure 2.11a), which corresponds to a resistivity of 0.009 Ω-cm. This resistivity value is similar to those reported previously. For instance, the resistivity of nanotube bundles at 300 K has been reported to be ~0.0065 Ω-cm [168], while resistivities between 8×10^{-4} Ω-cm and 12×10^{-3} Ω-cm have been measured for individual nanotubes [169]. For our measurements, the current-voltage (I-V) characteristics indicate that contact resistance exists. The nearly linear relationship observed between current and voltage is good indication of metallic conductivity. Similarly, except for nanotube defects, the measured high resistance of metallic nanotubes is also due to high contact resistance caused by the unique electronic structure of nanotubes, which gives rise to weak electronic coupling at the Fermi surface [170]. Moreover, in our studies, the probes contacted only the sidewalls of the nanotubes during I-V measurements. As a result, higher electrical resistance is observed, since the electrical resistance in a direction perpendicular to the tube axis is much larger than that parallel to the tube axis [171]. The capacitance of the nanotube bundle was ~2.55 pF as the voltage was scanned from -1 V to 1 V, as shown in Figure 2.11b. Thus, preliminary measurements indicate that the CNT arrays formed by this process are promising for electrical interconnect applications, even though the resistance and capacitance are currently too large for direct CNT interconnect applications.

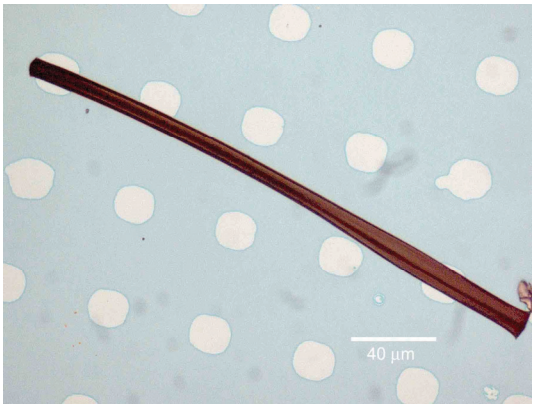

Figure 2.10 Optical micrographs of nanotube bundle of length 215 µm, bridging two electrodes.

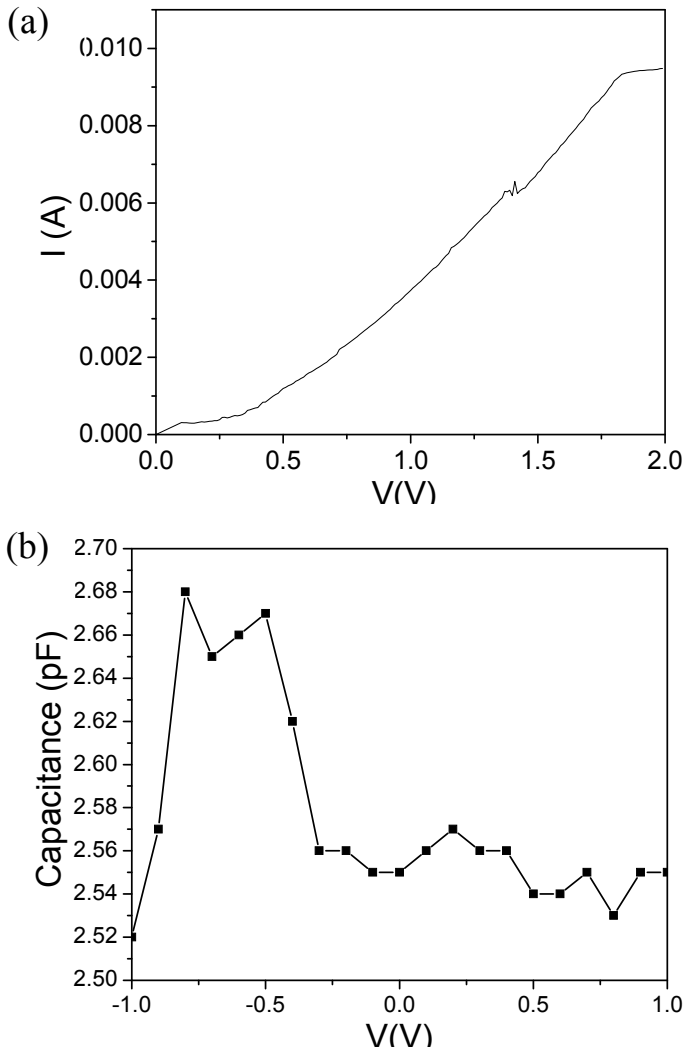

Figure 2.11 (a) IV curve and (b) CV curve of CNT arrays of Figure 2.10.

2.4 Effects of Catalyst Stack on CNT Growth

2.4.1 Effects of Catalyst Film Thickness on Nanoparticle Formation

As mentioned above, the catalyst nanoparticle size and distribution determine the aligned CNT diameter and spatial distributions. In our system, catalyst particles are formed by 'break-up' of the evaporated Fe films as a result of a thermal treatment without admitting ethylene into the CVD system. To investigate the influence of catalyst film thickness on the formation of nanoparticles and thus on the CNT growth, a systematic study is necessary. Catalyst layers of Al_2O_3 (10 nm)/Fe (various thickness) were deposited on a silicon wafer by sequential electron-beam evaporation; Fe films with controlled thickness of 0.6, 1, 1.5, 2, 3, and 4 nm, respectively, were deposited. These substrates were cut into small pieces and introduced into the furnace, and heated to 750 °C in flowing Ar (350 sccm) and H_2 (180 sccm) for 15 min. During this annealing, catalyst Fe islands were formed on the substrates. The size and distribution of Fe islands prior to the CNT growth are consistent with the nanotube diameter and distribution after the growth.

As shown in Figure 2.12, the initially continuous evaporated Fe films were transformed into Fe nanoparticles during the CVD temperature ramping process. The size and distribution of the Fe islands were dependent on the initial thickness of the evaporated Fe. Thicker Fe films (≥3 nm) yield larger Fe islands on average and gave a wide size distribution, while thinner Fe films (<3 nm) result in smaller islands on average with a much narrower size distribution. The catalyst islands produced using 1.5 nm evaporated Fe films have a very uniform size distribution, centered around 17 nm, while the average diameter of islands formed from the 4 nm Fe films is larger than 100 nm, which is too large for CNT growth in our system. Only those Fe nanoparticles with diameter smaller than 20 nm are good for CNT growth in our system, since few nanotubes with a diameter larger than 20 nm were observed.

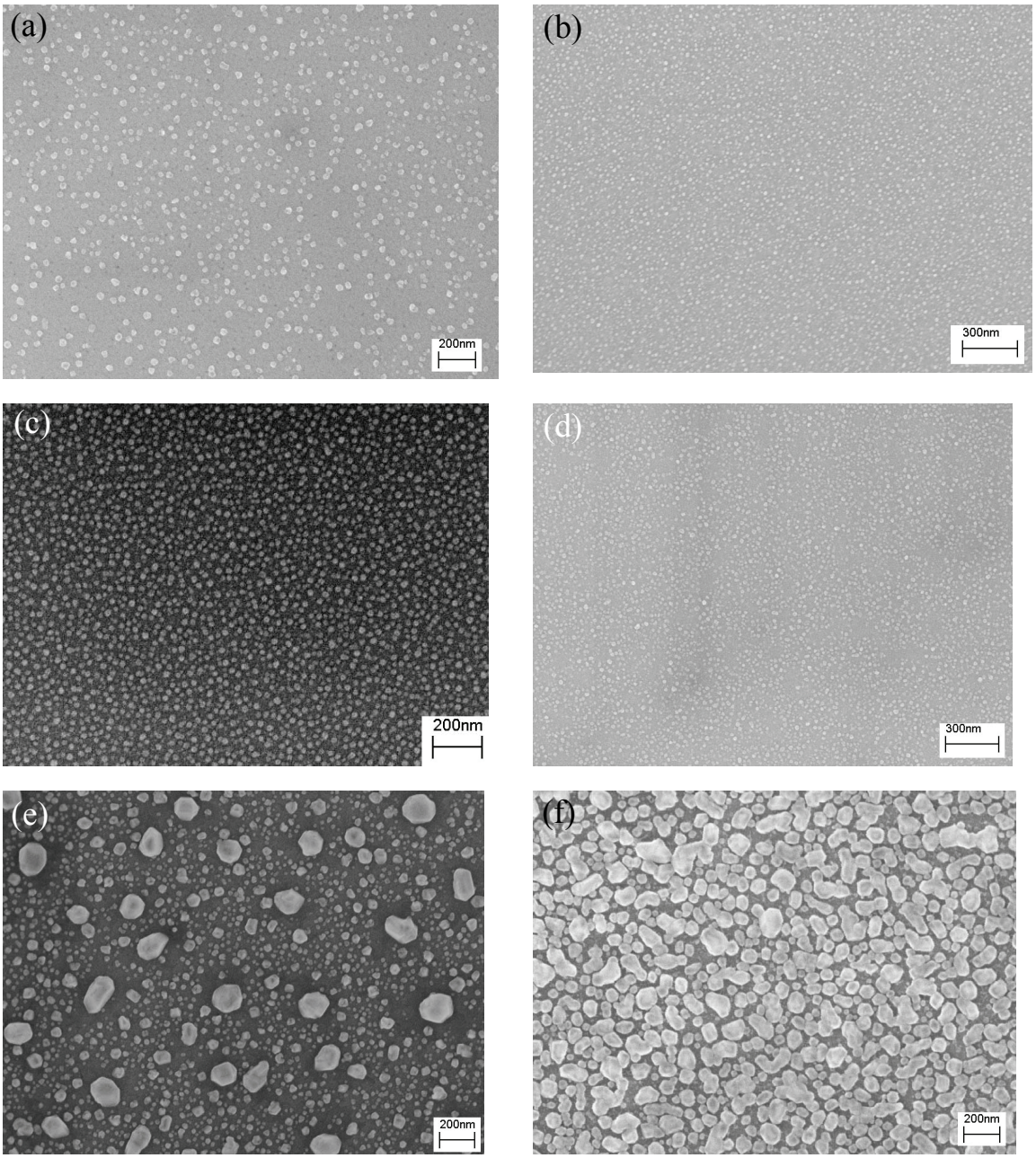

Figure 2.12 SEM images of the Fe islands formed from (a) 0.6, (b) 1, (c) 1.5, (d) 2, (e) 3, and (f) 4 nm thick Fe films.

To illustrate the effect of Fe film thickness on the CNT growth and morphology, the growth of CNTs was implemented on the Fe films with thickness of 0.6, 1, 1.5, 2, and 4 nm, respectively, at 730 °C for 3 min with ethylene (150 sccm) as the carbon source and argon (350 sccm) and hydrogen (180 sccm) as carrier gases Morphologies of the grown CNT films are shown in Figures 2.13-2.17. The alignment of CNTs grown on 0.6,

1, 1.5, 2 and 3 nm Fe films is obvious. In contrast, CNTs grown on the 4 nm Fe films were entangled with each other, as shown in Figure 2.17c. Due to steric hindrance responsible for the aligned CNT growth, a minimum CNT areal density is necessary to form CNT alignment. Thus, the areal Fe nanoparticle (here referred to the appropriate size for CNT growth) density on the substrates is essential, since the CNTs grow from the catalyst nanoparticles. Although the minimum CNT density for achievement of CNT alignment is not defined for thermal CVD, apparently, the CNT areal density of ~11 μm^{-2} is not high enough to maintain the CNT alignment. To our estimation, the CNT areal density should be larger than 100 μm^{-2} to achieve CNT growth alignment.

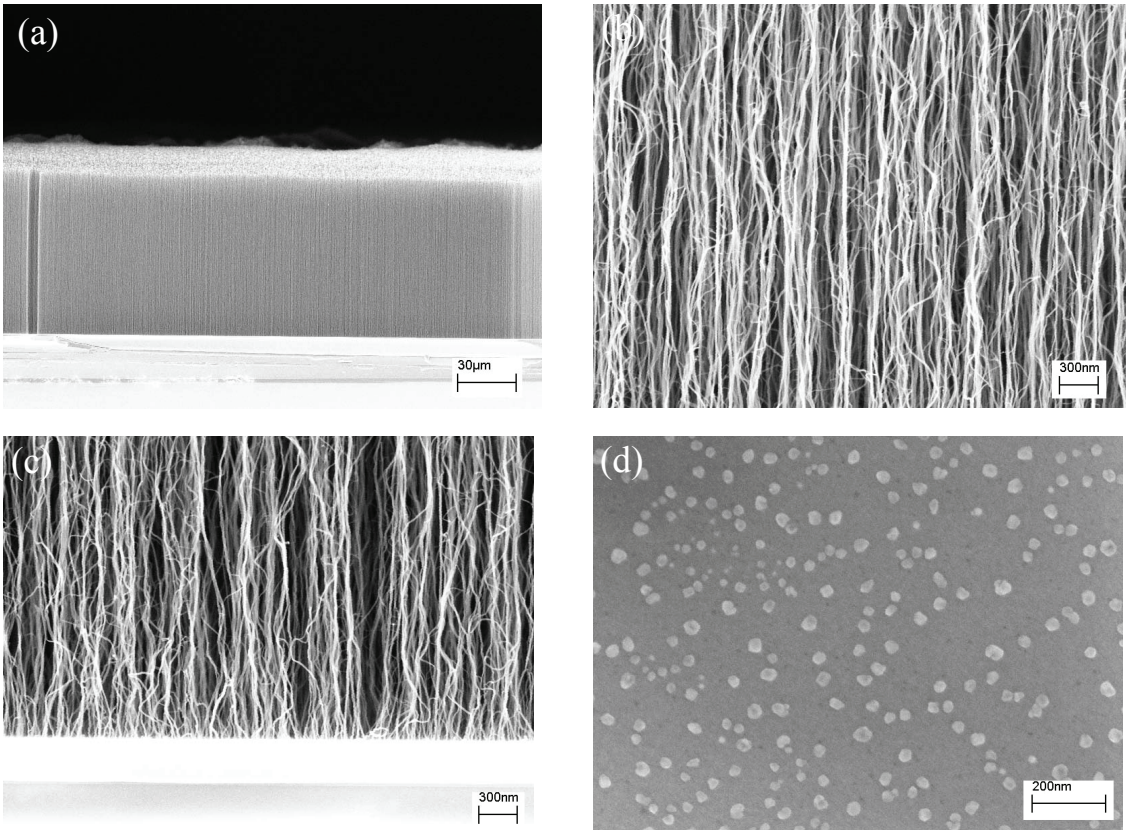

Figure 2.13 (a) SEM image of CNT film grown on 0.6 nm thick Fe film at 730 °C for 3 min; (b) high magnification SEM image of the well-aligned CNTs in (a); (c) SEM images of the CNT-substrate interfaces, and (d) the Fe nanoparticles on the substrate.

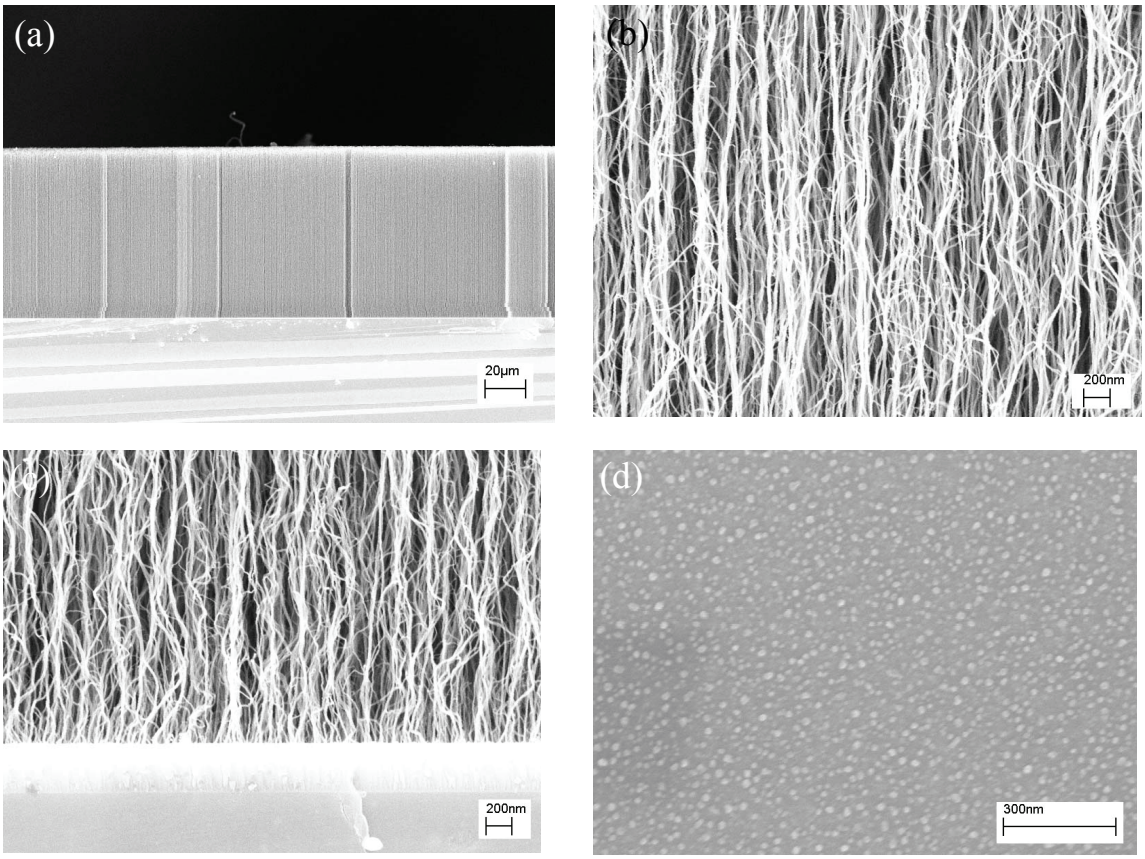

Figure 2.14 (a) SEM image of CNT film grown on 1.0 nm thick Fe film at 730 °C for 3 min; (b) high magnification SEM image of the well-aligned CNTs in (a); SEM images of (c) the CNT-substrate interfaces, and (d) the Fe nanoparticles on the substrate.

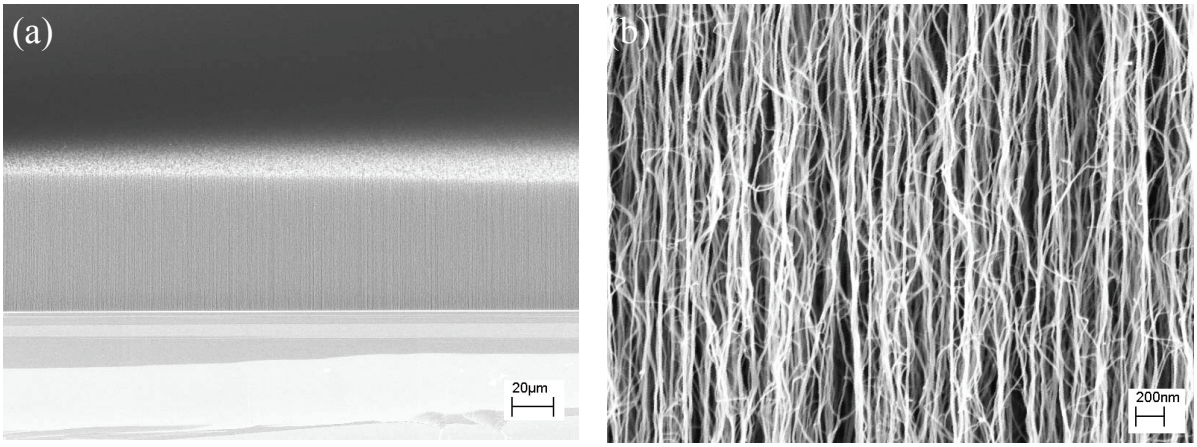

Figure 2.15 (a) SEM image of CNT film grown on 1.5 nm thick Fe film at 730 °C for 3 min; (b) high magnification SEM image of the well-aligned CNTs in (a); (c) SEM images of the CNT-substrate interfaces, and (d) the Fe nanoparticles on the substrate.

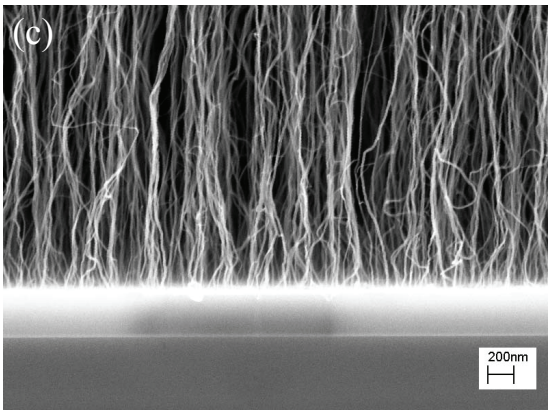

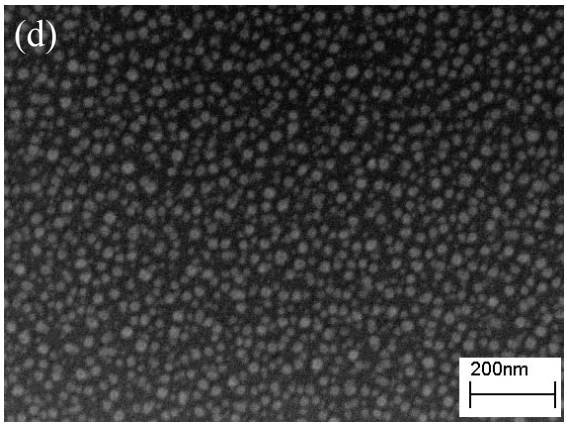

Figure 2.15 Continued.

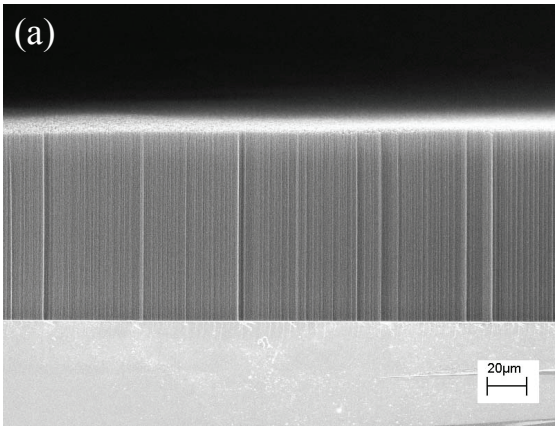

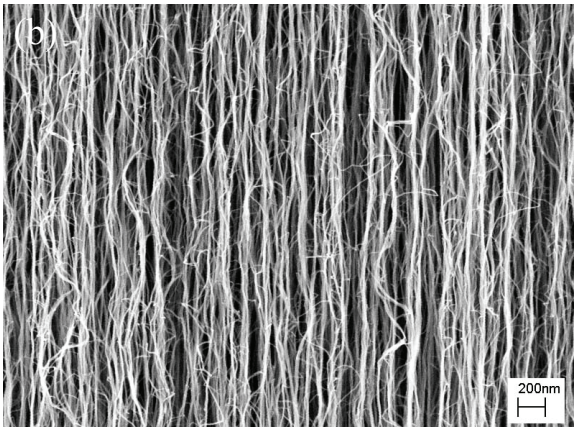

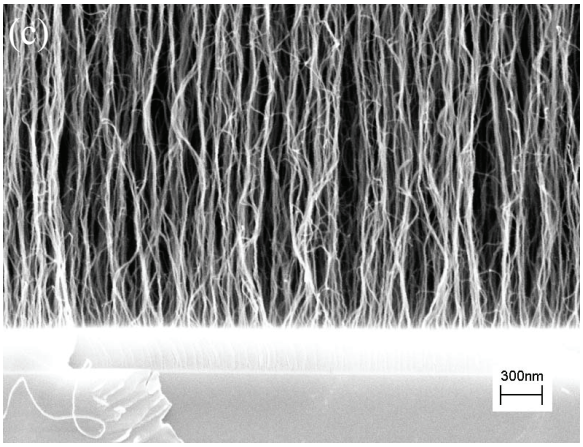

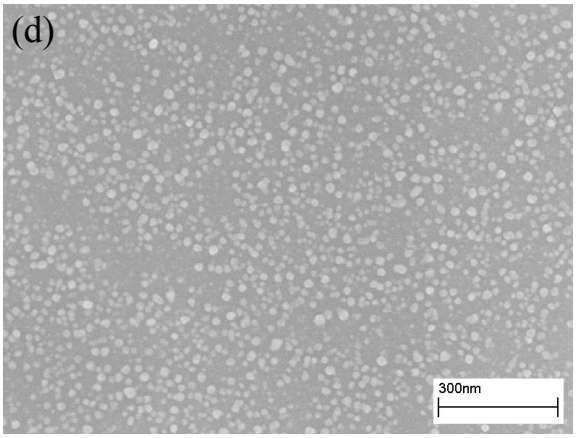

Figure 2.16 (a) SEM image of CNT film grown on 2 nm thick Fe film at 730 °C for 3 min; (b) high magnification SEM image of the well-aligned CNTs in (a); SEM images of (c) the CNT-substrate interfaces, and (d) the Fe nanoparticles on the substrate.

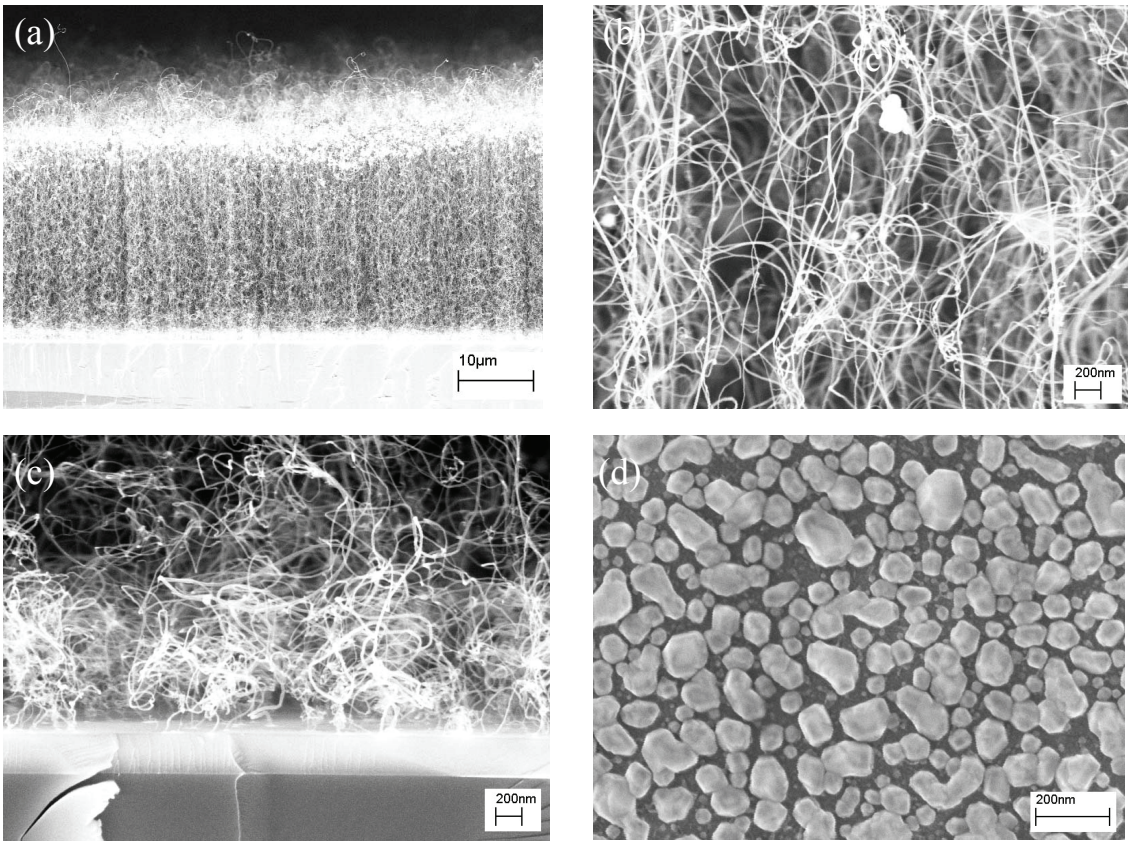

Figure 2.17 (a) SEM image of CNT film grown on 4 nm thick Fe film at 730 °C for 3 min; (b) high magnification SEM image of the well-aligned CNTs in (a); (c) SEM images of the CNT-substrate interfaces, and (d) the Fe nanoparticles on the substrate.

From the SEM images in Figure 2.12, the average size and areal density of catalyst islands formed from evaporated Fe films are summarized in Table 2.1. The areal density of Fe nanoparticles formed from the 2 nm Fe film is the highest.

Table 2.1 Average size and areal density of catalyst islands formed from evaporated Fe films

Film thickness (nm)	0.6	1	1.5	2	3	4
Areal density (μm^{-2})	190	650	750	1200	300	11 (size suitable for CNT growth)
Average size (nm)	25	13	17	14	17	100

2.4.2 Effect of Support Materials on CNT Growth

The peculiar ability of the transition metals such as iron, cobalt, and nickel to catalyze CNT growth is related to their catalytic activity for decomposition of carbon compounds, their ability to form carbides, and the possibility for carbon to diffuse through and over the metals extremely rapidly. In metal catalyzed CNT growth, the first action of the catalyst is to bond the hydrocarbon molecules to the surface. The hydrocarbon is in an adsorbate state, interacting with the catalyst by transferring electron density to the catalyst [172]. This electronic interaction between a 'donor' adsorbate and an 'acceptor' catalyst metal is schematically illustrated in Figure 2.18. Generally, back-donation simultaneously takes place, i.e. electron transfer from the catalyst to the non-occupied antibonding orbitals of the adsorbate molecule. The electronic structure of the adsorbate is then changed in such a way that dissociation of the molecule can occur. The transition metals have un-filled d orbitals and are able to interact with hydrocarbons and show catalytic activity. More precisely, properties contributing to the ability to make and break adsorbate bonds are: (a) the center of the d-bands, (b) the degree of filling of the d-bands, and (c) the coupling matrix element between the adsorbate states and the metal d-states [172]. Therefore, the ability of a metal to catalyze dissociation of a hydrocarbon molecule is closely linked to its electronic structure. This can explain why iron is more efficient than nickel and cobalt in hydrocarbon decomposition [40, 173-175]. Some researchers also demonstrated that an added component can lower the activation energy for dissociation, and thus the growth temperature, by changing the electronic structure of the catalyst [176, 177]. Nevertheless, it is not clear whether differences in electronic structure between different catalyst materials can account for the observed differences in the quality of MWNT in terms of graphitization. In contrast, copper, a non-transition metal with its 3d shell completely filled, was observed to yield only amorphous carbon [178]. Overlap of metal 3d empty orbitals with carbon valence orbitals not only plays a role in the hydrocarbon dissociation process, but is also an essential part in the initial

stage of the CNT growth process, since it allows chemisorption of the carbon cap edges to the catalyst nanoparticle. However, additional studies are needed to determine if and how the unfilled 3d-metal orbitals affect the growth process and thus the graphitization of the entire CNT [179].

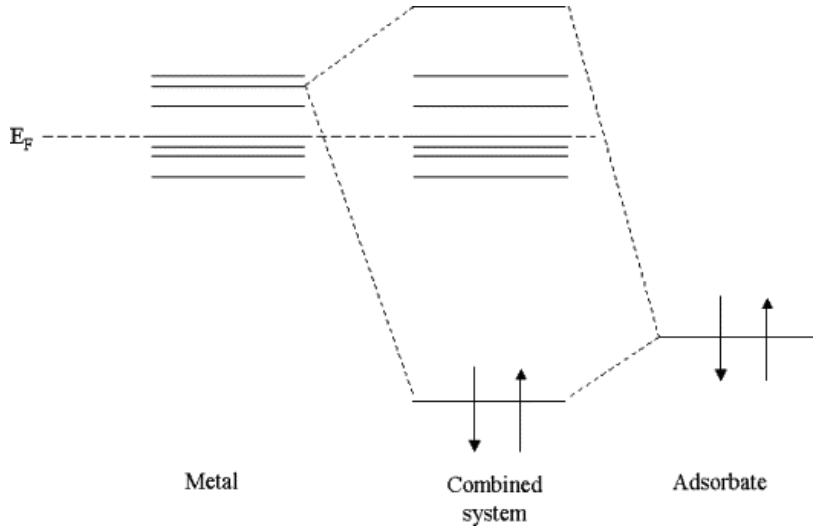

Figure 2.18 Schematic illustration of electronic interactions in chemisorption. A filled orbital on the adsorbate overlaps with an empty orbital on the metal [179].

As noted previously, the additional of negative charges to the catalyst particles can enhance dissociation of the adsorbate by strengthening back donation of electron density into antibonding orbitals of the adsorbate. Thus, a suitable choice of support material beneath the catalysts is essential. Initially, we employ Al_2O_3 as the catalyst support, and compare its effects on CNT growth with a structure wherein only SiO_2 separates the catalyst from the silicon substrate. A 1 nm thick Fe film is e-beam evaporated onto silicon wafers coated with SiO_2 (500 nm)/Al_2O_3 (15 nm) or with SiO_2 (500 nm). The two diced substrates (5 mm×5 mm) are positioned in the middle of the CVD tube and growth of CNTs carried out at 750 °C for 4 min with ethylene as the carbon source, and hydrogen and argon as carrier gases. Figure 2.19 shows SEM images of the as-grown CNTs on the two different substrates; significant differences in CNT growth behavior are observed. In Figure 2.19a, the CNT films attain a height of 267 μm

while in Figure 2.19b the height of the CNT films is only 3.7 μm. These results clearly demonstrate that introduction of the Al_2O_3 support beneath the Fe catalyst increases the CNT growth rate by nearly two orders of magnitude under the same growth conditions. Therefore, direct comparison of the intrinsic kinetics of CNT growth with other studies using different support materials is inappropriate.

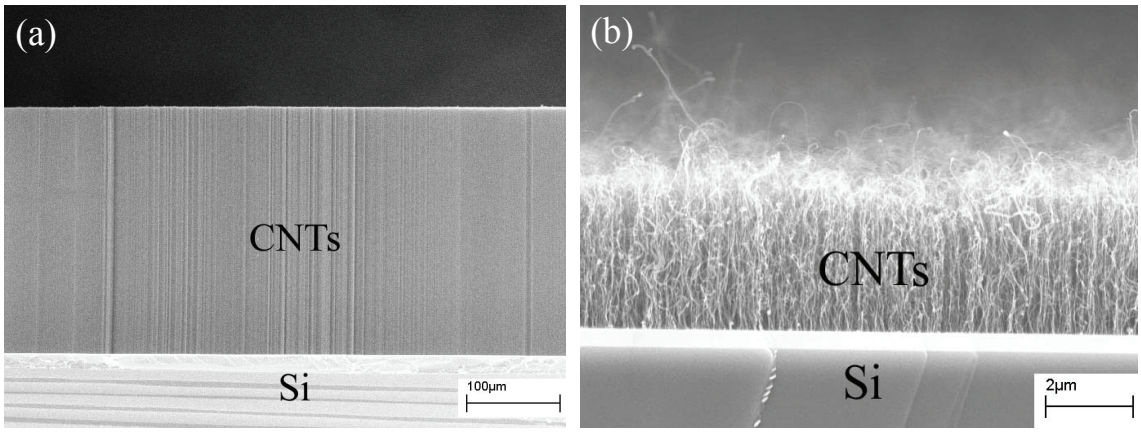

Figure 2.19 SEM images of as-grown CNTs on a substrate coated with (a) SiO_2 (500 nm)/ Al_2O_3 (15 nm) and (b) with only SiO_2 (500 nm).

In the supported metal catalyzed reaction systems, the substrate can interact with catalyst particles both physically and chemically [180-189]. In terms of physical interaction, for example, van der Waals and electrostatic forces, together with the obstruction of catalyst particle movement on the support material surface due to surface roughness, reduce the thermally driven diffusion of metal particles on the support surface. This results in stabilization of the catalyst particle size distribution during CNT growth. In addition to the physical interactions, the support can also interact chemically with the catalyst particles and thus dramatically affect their catalytic activity. If a strong chemical interaction takes place, particle growth is limited due to the decreased particle mobility. 'Strong metal support interactions' (SMSI) may take place between easily reducible metal oxides and transition metals in the presence of hydrogen [189]. The most important

supports such as Al_2O_3 and SiO_2, however, are not easily reduced and thus the interaction via SMSI can be neglected. For support oxides that are not readily reduced, another potentially significant interaction involves the catalyst particle and exposed oxygen anion sites on the support. The anions, with their negative charge, can act as Lewis base sites and thereby donate negative charge to the metal nanoparticles. In a similar manner, the partial negative charges accepted from the oxide can enhance catalytic activity. Al_2O_3 has been generally observed to be a superior support compared to SiO_2. The strong chemical interaction between Al_2O_3 and metal particles has been attributed to either acidic or basic surface groups, since aluminum oxide is an amphoteric material having both acidic and basic sites, which may take part in chemical interactions.

Vander Wal et al. showed the importance of electronic interactions between metal nanoparticle and support on the ability of the metal to decompose adsorbate (hydrocarbons or CO in the case of CNT formation) [56]. Indeed, acquisition of negative charge by the metal catalyst from the substrate can enhance its catalytic activity by strengthening back-donation of electron density into antibonding orbitals of the adsorbate. This electron sharing between catalyst and adsorbate sufficiently weakens the bonding within the adsorbate, resulting in its dissociation. Since dissociation of a hydrocarbon on the metal catalyst is the first step in a widely-accepted mechanism for metal catalyzed CNT growth, the appropriate support material is necessary to enhance CNT grow rate. As seen above, the inclination for electron donation of a surface is linked to its Lewis base character. The strong catalytic activity of copper observed on support media with strong Lewis base sites (CaO and SiO_2) exemplifies this phenomenon [32]. The catalytic activity of a metal is in a first approximation inversely dependent on the filling of its d-band. Bulk copper should therefore be catalytically inactive since its d-shell is completely filled. Nevertheless, upon acquisition of a partial negative charge from the support (acting here as a Lewis base), copper can donate negative charge to the adsorbate. At this point, the catalyst particle acts as a conduit for transferring negative charge to the adsorbate.

The interactions between support surface and metal particles, expressed in terms of interfacial tensions, will determine the shape of the particle. For example, Wright et al. compared the shape of nickel nanoparticles on TiN and on $MoSiO_2$ and found that nickel particles are more spherical on $MoSiO_2$ because of a weaker wetting on $MoSiO_2$ than on TiN [190]. Generally, one can assume that strong metal–support interactions lead to good dispersion of the metal on the support surface. Many researchers ascribed the improved results obtained on Al_2O_3 compared to SiO_2 to the stronger Lewis acidity of the former support [24, 38, 55], yielding a better dispersion of the metal. However, too strong interaction between catalyst and support yields strong wetting and prevents the formation of appropriately shaped catalyst particles for CNT growth. Seidel et al. emphasized that the surface diffusion rate of a specific atom on a substrate depends not only on the substrate nature but also on its roughness [191]. Delzeit et al. also studied the role of the underlayer in the growth of CNTs [192]. The results show that ion-beam sputtering of the underlayer increases its surface roughness, thus providing more active nucleation sites. Surface roughness can therefore hinder surface diffusion of the catalyst and thus its coalescence into large particles.

2.5 CNT Stack Growth

Realization of high-purity CNT growth requires either a novel purification process to remove impurities or defects attached to the CNTs, or the CVD process must be altered to allow in-situ high-purity CNT growth without the need for subsequent purification. Compared to a post-purification process, the strategy of in-situ impurity removal is attractive for efficient and low-cost CNT manufacture. The addition of relatively low reactivity oxidizing agents such as water vapor, into the reaction furnace to remove the amorphous carbon has shown significant promise. Initially, this approach was used to remove amorphous carbon during the synthesis of CNTs [193]. However, the

water content in the growth atmosphere was so high that it damaged the nanotube walls. More recently, addition of controlled amounts of water to the CVD atmosphere have been shown to produce long, dense, vertically-aligned single-walled CNTs [30]. In the current study, we use water addition to obtain a stacked CNT film structure while maintaining high CNT purity. Stacked CNT structures have been fabricated by multi-batch CVD process with a mixture of xylene/ferrocene [194], or by variations of CVD processes with benzene/ferrocene and benzene/cobaltocene [195]. One of their common features is that the catalysts are inevitably incorporated into the CNTs. In our process, a trace amount of water was introduced into CVD chamber during CNT growth to achieve simultaneous purification and opening of the CNT ends. Stacked CNT films have been fabricated with up to 10 layers in one batch; these stacked layers could be easily separated from each other.

2.5.1 CNT Stack Formation and Characterization

CVD was performed in a horizontal alumina tube (3.8 cm diameter; 92 cm long) housed in a Lindberg Blue furnace. The substrates used in this study were (001) silicon wafers coated with SiO_2 (500 nm) by thermal oxidation. The catalyst layers of Al_2O_3 (15 nm)/Fe (3 nm) were formed on the silicon wafer by sequential e-beam evaporation. CVD growth of CNTs was carried out at 775°C with ethylene (150 sccm) as the carbon source, and hydrogen (180 sccm) and argon (350 sccm) as carrier gases. The water vapor concentration in the CVD chamber was controlled by bubbling a small amount of argon gas through water held at 22 °C. The water concentration was measured by Moisture MonitorTM Series 35 (GE Panametrics). in all experiments, the water concentration was maintained at 775 ppm until the CVD process was terminated. The layered CNT films were obtained by the following sequence. Ethylene flowed into the CVD system for a preset time, after which the flow was terminated; after 5 min of only water, argon and

hydrogen flow, ethylene was again introduced for a specific time. The fixed 5 min interval between CNT growth steps was used to selectively etch weakly bonded or amorphous carbon atoms at the interfaces between the nanotubes and catalyst particles by water vapor. This sequence was repeated to obtain the layered CNT films.

Figure 2.20a shows double-layered CNT films fabricated by the following procedure. First, a CNT film was grown for 6.5 min, followed by ethylene flow termination for 5 min with only water etching (argon and hydrogen are still flowing). Subsequently, ethylene is admitted into the system for another 6.5 min. Figure 2.20a demonstrates that a boundary exists between layer 1 and layer 2, which is the interface between layers 1 and 2. The top layer in this structure is easily peeled from the underlying layer. A partially peeled layer is shown in Figure 2.20b, which clearly illustrates the existence of stacked CNT films. Furthermore, the thickness of layer 1 is much greater than layer 2, despite the equal growth time and formation conditions for these two layers. The effect of a 5 min water etching interval during CNT growth was confirmed by growing CNTs continuously for 13 min while introducing water into the growth atmosphere as the process described above; only one thick layer of CNTs was obtained. We therefore performed the following experiments to further investigate the role played by water during the temporary termination of nanotube film growth.

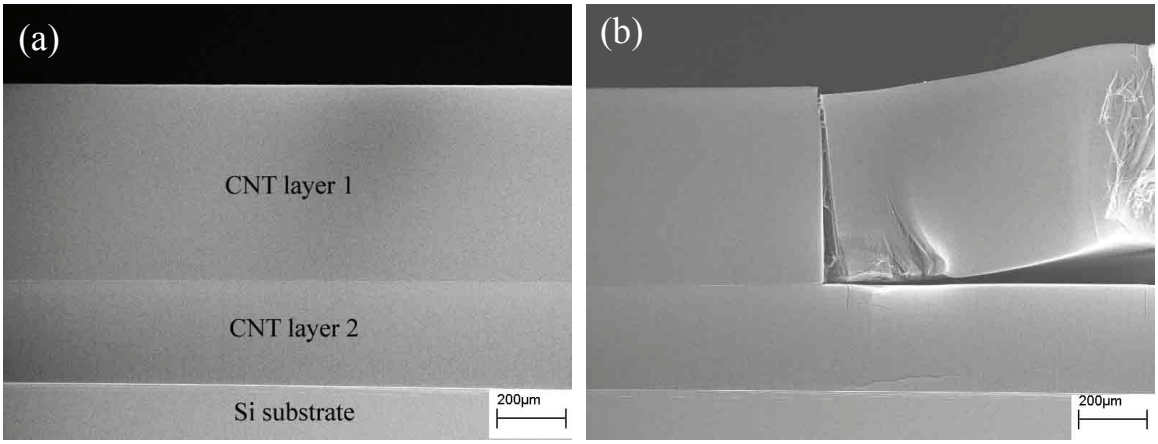

Figure 2.20 Cross-sectional SEM images of (a) double-layered CNT films; (b) partially peeled top layer in (a) to show as-grown double-layered CNT film structure.

XPS and energy dispersive X-ray spectroscopy (EDS) were performed to locate the position of the iron (Fe) catalyst and thereby establish the nanotube growth mode. The top CNT layer (layer 1) was peeled from layer 2. XPS survey scans were performed to identify the species on the top and bottom sides of layer 1, on the top side of layer 2 and on the surface of the substrate after removal (peeling) of layer 2. XPS spectra detect only carbon on the top and bottom sides of layer 1, and on the top side of layer 2, as shown in Figure 2.21a. No iron is detected although XPS scans were performed at ten different locations on each surface examined. Rather, the XPS spectra are identical with that of a standard graphite sample. EDS studies agree with the XPS spectra in that no elements other than carbon were detected. These data indicate that the Fe catalyst remains on the substrate surface. To confirm this conclusion, an XPS survey scan was performed on the silicon substrate after the CNT layers were peeled off; the results are shown in Figure 2.21b. Iron is detected at the substrate surface, confirming that CNT growth occurs by a base-growth mode. This growth mode also suggests continuous growth of CNTs throughout the entire individual layers, since no catalysts were added during the growth process.

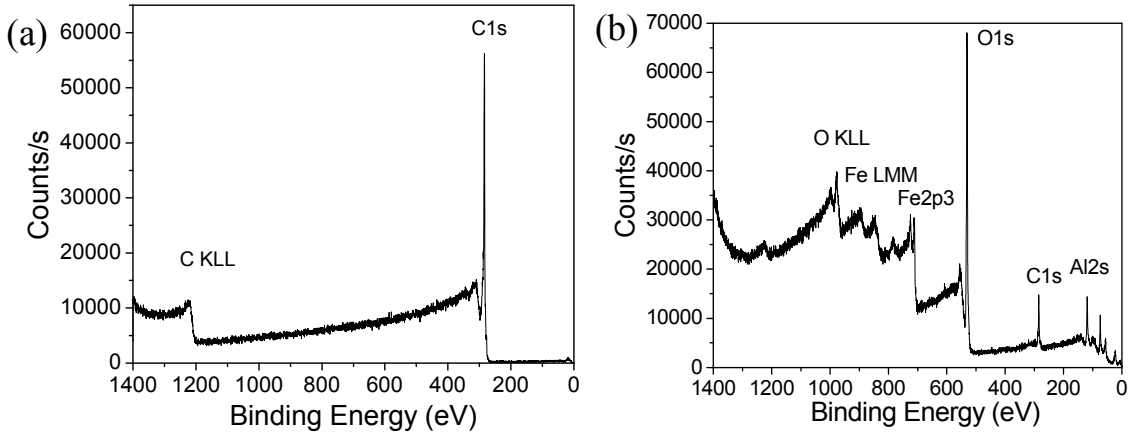

Figure 2.21 XPS survey scan on (a) top and bottom sides of CNT layer 1 and on top side of CNT layer 2; (b) substrate surfaces after removing the CNT layers.

After the ethylene flow is terminated, the 5-min water treatment etches carbon atoms at the interfaces between nanotubes and between nanotubes and the Fe nanoparticles. When the ethylene flow is restarted, a new CNT layer nucleates and grows on the Fe catalyst particles that remain on the substrates. The newly formed CNT layer grows from the catalyst surface and thus moves the previously grown CNT layer upward until the ethylene flow is again terminated. In order to form a new CNT layer, the feed gases and water must diffuse through the existing CNT layer of several hundred microns thickness since a base-growth mode exists.

To further illustrate this particular CNT film growth mode, we changed the ethylene flow time to investigate the growth of a large number of layers. The ethylene flow time was lowered to 45 seconds, while keeping the water etching time (5 min) constant; this sequence was repeated for 10 cycles. Figure 2.22a shows the stacked 10 layer CNT films. Layers 9 and 10 in Figure 2.22a are difficult to discern, due to the very thin layers. Scratching the films with a tweezers indicates the layered structure and the ease with which the different layers are separated from each other (Figure 2.22b). Figure 2.22c is a high magnification SEM image of the interface between adjacent layers, showing density, alignment and height uniformity of individual layers. SEM examinations are used to measure the individual layer thickness; results are plotted in Figure 2.22d. These results show that the thicknesses of layers 9 and 10 are 5 μm and 4 μm, respectively, which indicates increasing mass transfer limitations on CNT growth, which yields the dramatically decreased CNT growth rate. For the growth of these two layers, carbon-containing precursors must diffuse through a 400 μm nanotube layer. At such scales, diffusion control of CNT growth is obvious, since the growth kinetics become diffusion-controlled if the nanotube films are thicker than dozens of microns. Indeed, the CNT thickness grown for a series of layers (inset, Figure 2.22d) is proportional to the square root of time, which indicates a diffusion controlled mode [196].

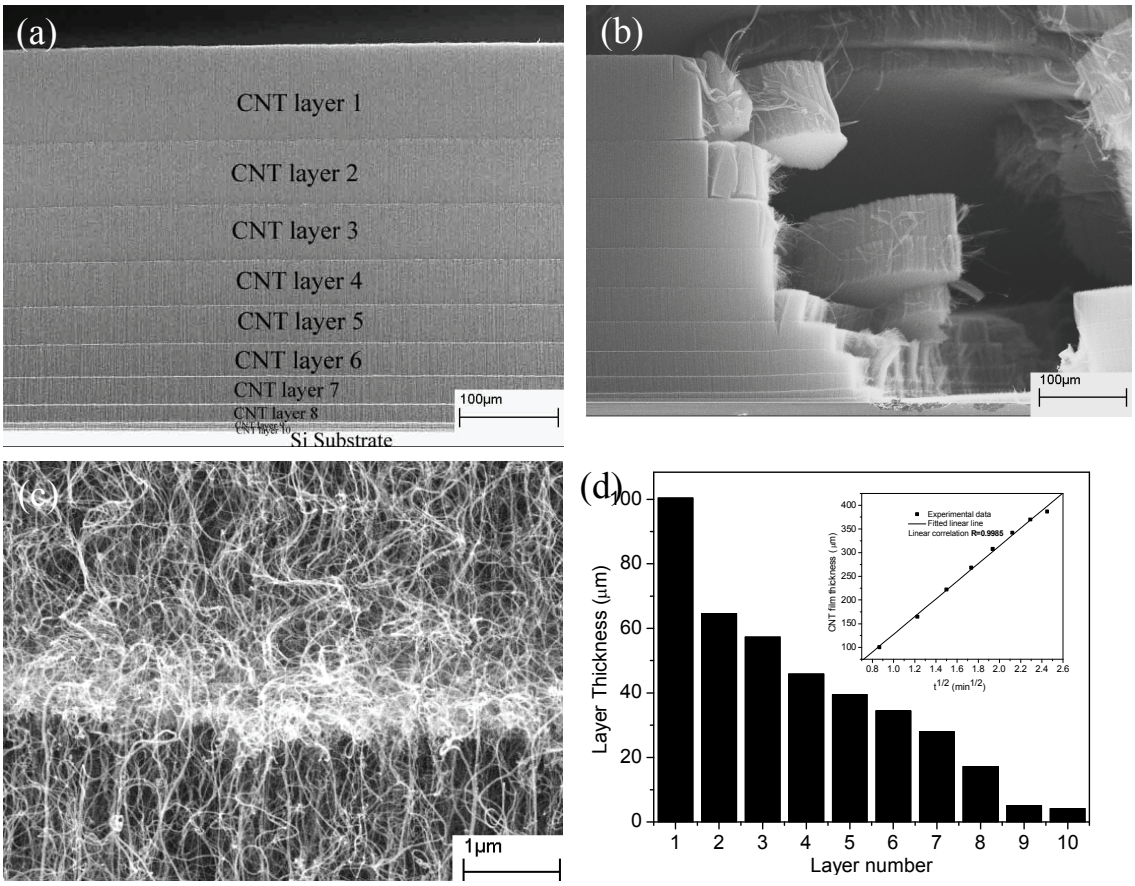

Figure 2.22 Cross-sectional SEM images of (a) 10-layered CNT films; (b) scratched CNT films in (a) to show the layered structures of CNT films; (c) a higher magnification SEM image of the interface between adjacent layers; (d) bar graph to show individual layer thickness of the CNT films in (a). The inset shows the time evolution of CNT film growth. The linear relationship between CNT film thickness and square root of growth time indicates that CNT growth is diffusion controlled under these conditions.

2.5.2 Mechanisms of CNT Stack Formation

We believe that the existence of a small concentration of water vapor etches carbon atoms at the interfaces between nanotubes and Fe catalyst nanoparticles after the ethylene flow is terminated, and this phenomenon can qualitatively explain the formation of stacked CNT films. If this mechanism is correct, then one end of the nanotubes should display an open structure. Indeed, HRTEM shows CNTs with one open end as indicated in Figure 2.23a. In addition, however, the other end of the nanotubes is also opened;

Figure 2.23b shows the opposite (open) end of the same nanotube as in Figure 2.23a. We have examined CNTs from numerous growth runs, with dozens of HRTEM images. Each image has shown open ended structures of the as-grown CNTs. We believe that the relatively small amount of water (775 ppm) etches the ends of the nanotubes because more defect structures and thus high reactivity exist at the ends of the nanotubes, although it may be possible that water vapor also attacks defects along the nanotube walls. However, no wall damage to the nanotubes is evident, as shown in Figure 2.23c. Previous studies utilized much higher concentrations of water (>17%) in the reaction system [193], which apparently causes attack and thus damage of the walls as well as the tube ends. At the ppm water levels investigated in our investigations, nanotube walls do not appear to be etched. Furthermore, under the same growth conditions, water addition increases the CNT growth rate. High magnification SEM studies have demonstrated the absence of particles attached to the nanotube walls when water vapor is used as described above. Also, XPS, SEM, EDS and HRTEM analyses have verified that the as-grown CNTs are of high purity.

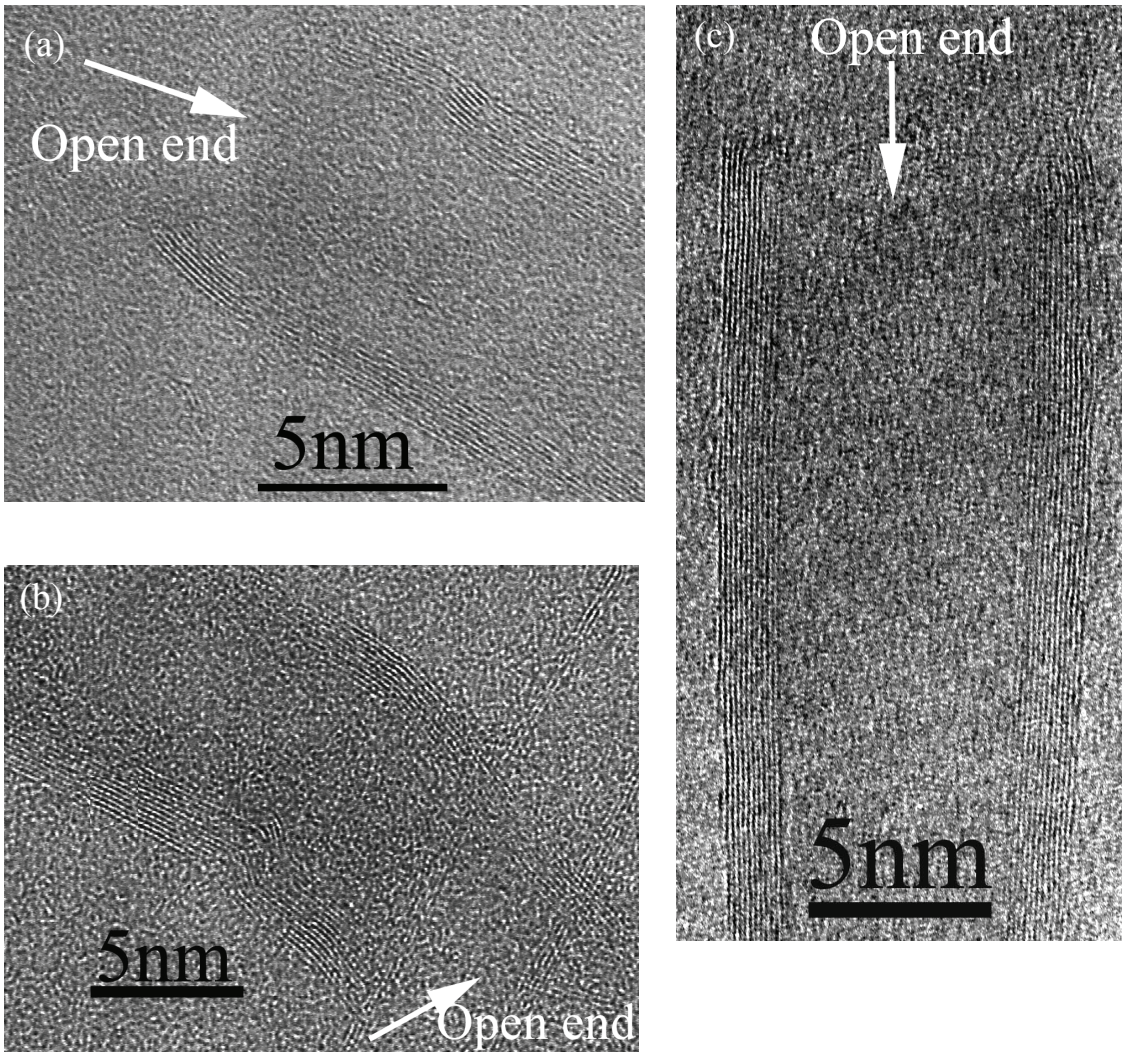

Figure 2.23 (a) and (b) HRTEM images of the two ends of one nanotube, showing that both ends are open; (c) HRTEM image showing that water vapor additions open the nanotube end, while keeping the walls intact.

Based on the above experiments and characterization, a possible mechanism of stacked CNT film growth with open ends can be suggested, as illustrated schematically in Figure 2.24. The deposited Fe thin layer is segregated into nanoparticles upon heat treatment, onto which CNTs grow readily. The catalyst particles interact strongly with the substrate and remain immobilized at the substrate surface during nanotube growth. When ethylene is admitted into the system, nanotubes grow from each catalyst particle and form densely packed nanotube films. After the ethylene feed is terminated, water vapor etches

away the caps of the nanotubes, leaving open-ended nanotubes. The interfaces between CNTs and catalyst particles are also etched away, leaving the CNT films in physical contact with the substrates. However, the nanotube films are still self-supporting due to van der Waals forces between the neighboring nanotubes. The subsequent re-introduction of ethylene causes growth of nanotubes from the original catalyst particles. The oriented growth of additional nanotube film occurs beneath the original layer, thereby shifting the first CNT layer (CNT layer 1) upward until the ethylene flow is again terminated.

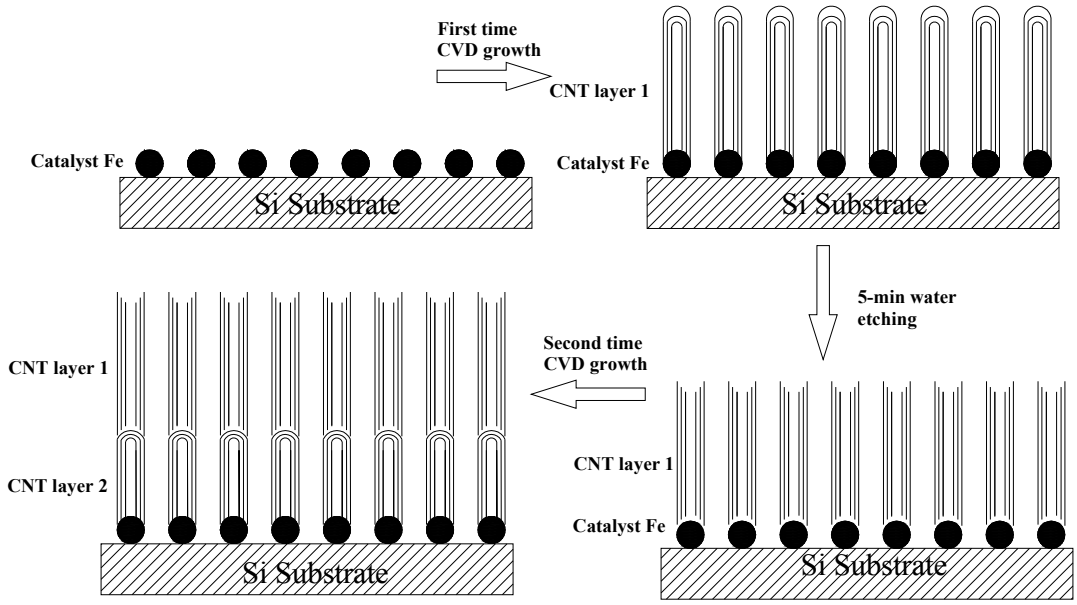

Figure 2.24 Schematic process indicating the growth sequence of double-layered CNT films with open ends.

2.6 In-Situ Functionalization of CNTs

2.6.1 In-situ Functionalization of Aligned CNTs and Characterization

In this study, aqueous H_2O_2 solution (30%) was used as an oxidant, instead of H_2O. Using a similar process sequence as that for CNT stack formation by water etching, CNT stacks were also formed by aqueous H_2O_2 etching. Figure 2.25 shows SEM images of as-synthesized CNT stacks. Four-layered CNT stacks can be obtained by repeating the growth-etching cycle four times, as shown in Figure 2.25a. The CNTs form a dense film with good alignment. No residue particles are observed on the CNT walls, as shown in the high magnification SEM image of aligned CNTs (Figure 2.25b).

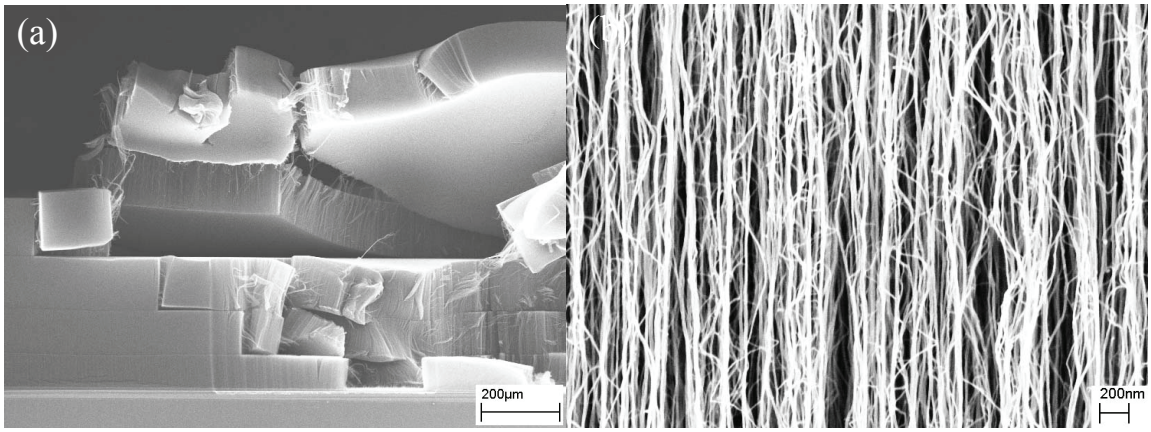

Figure 2.25 (a) Scratched CNT film stacks to show the layered structures of CNT films; (b) high-magnification SEM image of CNTs film grown at 775 ºC.

XPS survey scans were taken on the aligned CNT films grown with the assistance of aqueous H_2O_2, as shown in Figure 2.26a; these spectra clearly indicate the existence of an oxygen peak in addition to the carbon peak. The binding energy of the O1s peak from the CNTs treated by H_2O_2 is ~529.6 eV (Figure 2.26b), which demonstrates that the oxygen is not from the dissociated H_2O, since the binding energy of O1s of H_2O is about 533 eV [197]. The asymmetric C1s peak can be decomposed into six peaks. XPS results clearly show that the CNTs were in-situ functionalized with oxygen functional groups. In contrast, no oxygen was detected by XPS on the CNTs without aqueous H_2O_2 treatment.

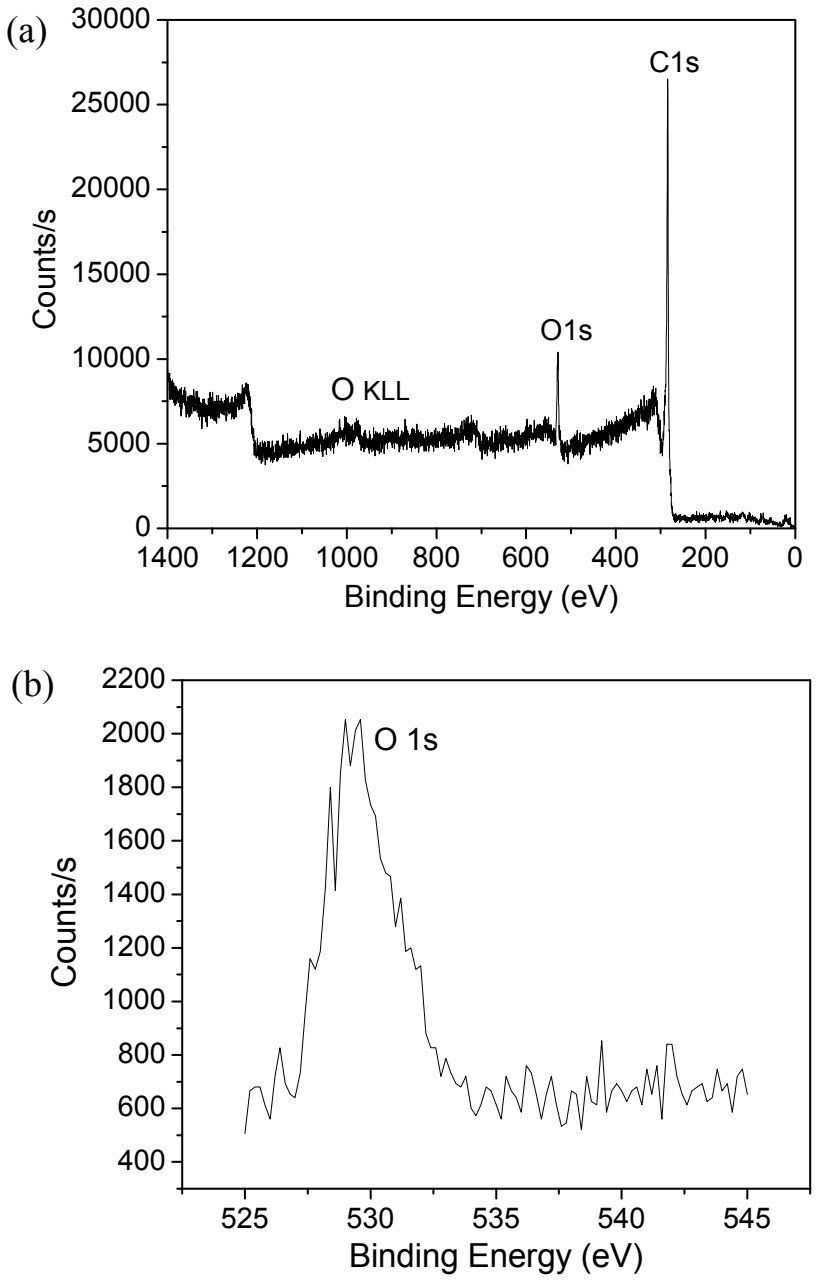

Figure 2.26 (a) XPS survey scan of in-situ functionalized CNTs; (b) O1s spectrum of functionalized CNTs.

Figure 2.27 shows an FTIR spectrum of functionalized CNTs. The peak at 1571 cm^{-1} is assigned to the C=C asymmetric stretching vibration of the graphene sheet. The IR spectrum also shows obvious O-H and C-O-C stretching at 3420 cm^{-1} and 1182 cm^{-1},

respectively. Another weak absorption at 1710 cm^{-1} is assigned to the –COOH stretch. Clearly, this in-situ CNT functionalization method can greatly simplify the CNT functionalization process. Usually, the post treatment (after CNT growth) is quite complicated with low CNT yield, and requires strong oxidants (e.g. HNO_3+H_2SO_4). The in-situ functionalization method can be used to obtain aligned CNTs.

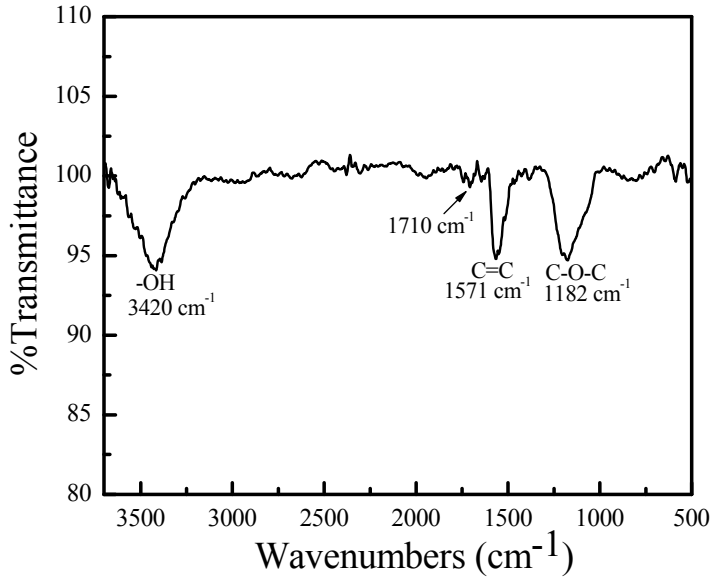

Figure 2.27 FTIR spectrum of functionalized CNTs.

2.6.2 Functionalized CNTs as Stabilizing Substrates for Nanoparticle Synthesis

As noted above, the in-situ functionalized CNTs (f-CNTs) have carboxylic and hydroxyl groups, which may act as nucleation sites for metal ions during a reduction process. Therefore, f-CNTs were used as stabilizing substrates for silver and gold nanoparticles. Silver nanoparticles were synthesized using 0.01 g silver nitrate as the precursor and 0.02 g resorcinol as the reducing agent in 15 ml ethanol in a small vial. 1.0 mg f-CNTs were added into the solution as the stabilizing substrates for the synthesized nanoparticles. Then, this mixture was sonicated for 2 hours in order to disperse the CNTs, as well as to stabilize silver nanoparticles after the precursors were reduced. In a control sample, the un-functionalized CNTs (u-CNTs) were added as stabilizing substrates. Gold

nanoparticles were synthesized from $HAuCl_4$ in a similar manner to that of the silver nanoparticles.

Figure 2.28a is a TEM image of silver nanoparticles synthesized by using 0.02 g resorcinol as reducing agents and 1.0 mg f-CNTs as stabilizing substrates. The silver particle size was less than 5 nm. Figure 2.28a clearly shows that almost all silver nanoparticles grow along the axis of the CNTs; the nanoparticles are lined up to form a stable assembly, which suggests that along the f-CNT walls there are active sites that provide sites for nucleation and growth of silver nanoparticles. By contrast, Figure 2.28b shows the silver nanoparticles synthesized with resorcinol as a reducing agent and u-CNTs as stabilizing substrates. In this case, the silver nanoparticles are larger than 50nm, and randomly mixed with the CNTs without any attachment on CNT walls, indicating no stabilization effects of u-CNTs. Therefore, f-CNTs are much more effective as stabilizing substrates for silver nanoparticle synthesis due to the existence of nucleation sites along CNTs that avoid the agglomeration of nanoparticles during reduction.

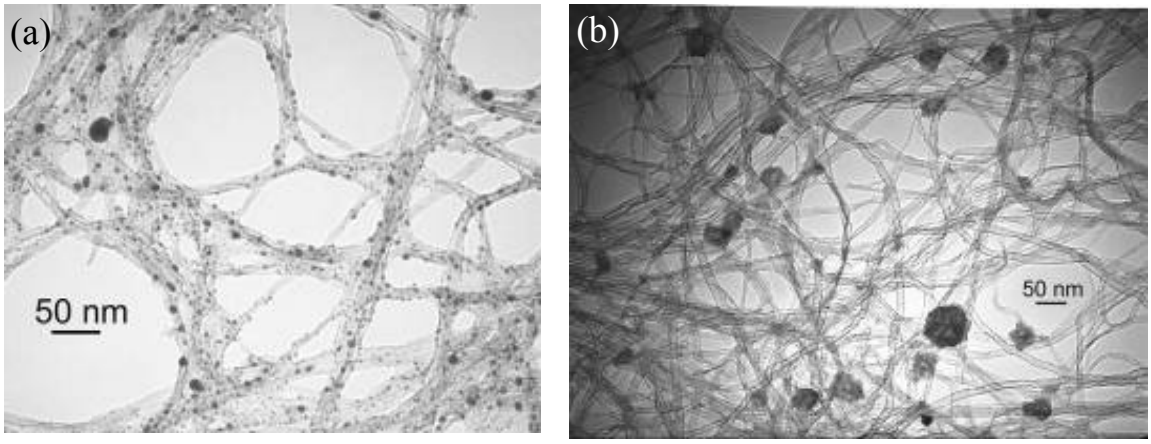

Figure 2.28 TEM images of silver nanoparticles synthesized using (a) f-CNTs and (b) u-CNTs as stabilizing substrates.

The stabilization effects of f-CNTs were further demonstrated by gold nanoparticle synthesis. Figure 2.29a shows a TEM image of gold particles synthesized

using f-CNTs as stabilizing substrates. The particles are well dispersed and attached onto the f-CNT walls; all sizes are less than 5 nm. However, with u-CNTs as stabilizing substrates, the gold nanoparticles formed have a broad size-distribution, from 100 nm to 300 nm (Figure 2.29b). These observations further suggest that on the f-CNT walls, nucleation sites exist that can be used as stabilizing substrates for nanoparticle synthesis.

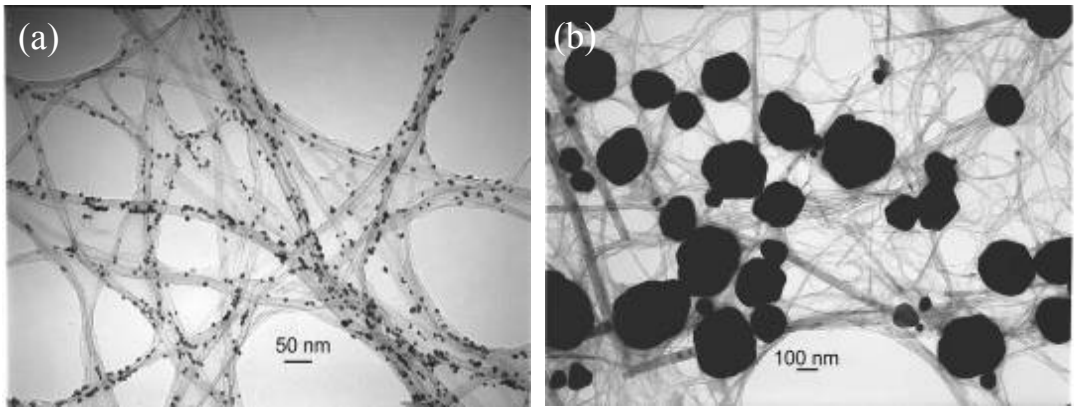

Figure 2.29 TEM images of gold nanoparticles synthesized using (a) f-CNTs and (b) u-CNTs as stabilizing substrates.

An XPS spectrum of Ag nanoparticles stabilized on f-CNTs is shown in Figure 2.30. Two peaks with binding energies of 368.4 and 374.5 eV are observed, corresponding to Ag $3d_{5/2}$ and Ag $3d_{3/2}$, respectively. These are typical values for Ag^0, indicating the formation of Ag nanoparticles on the sidewalls of the f-CNTs.

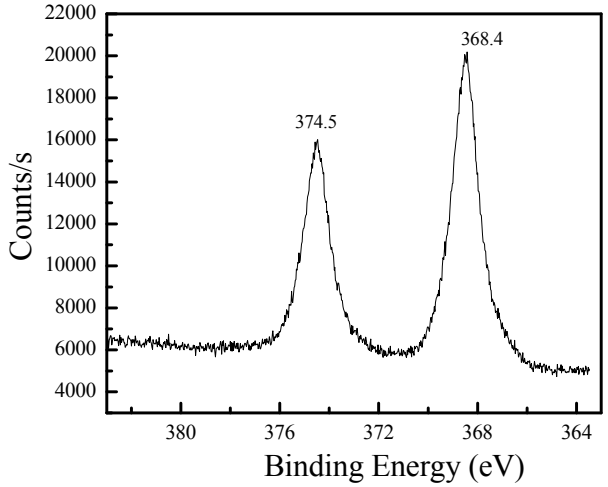

Figure 2.30 XPS spectrum of Ag3d from the as-prepared m-CNTs stabilized Ag nanoparticles in Figure 28a.

2.7 Summary

In this chapter, a CVD process is presented that allows controlled growth of different CNT structures, such as CNT films, bundles, and stacks. At 800 °C, the nanotube films grow at a high average rate of 100 μm/min, and their length can achieve 1 mm in 10 min. The patterned growth of nanotube arrays shows a higher growth rate than that of films, due to the base-growth mode. The Al_2O_3 support enhances the Fe catalyst activity. A controlled amount of water (775 ppm) in the CVD tube during CNT growth appears to etch away the nanotube caps, while keeping the tube walls intact. The as-grown CNTs within individual layers have high purity and open ends. This study has revealed another important role played by water during nanotube growth: opening the nanotubes as well as purifying and removing defects in the nanotubes. This unique process offers a novel and cost-effective way to open the aligned nanotubes. Furthermore, aqueous H_2O_2 introduced into the CVD chamber during CNT growth can in-situ functionalize the aligned CNTs with –OH, C-O-C, and –COOH groups attached to the nanotube walls. These f-CNTs without any post-treatments can be employed as excellent stabilizing substrates for silver and gold nanoparticle synthesis, further confirming the existence of active sites along the nanotube walls. The CVD methods presented in this chapter are simple and straightforward, indicating the potential for application in microelectronic devices and microelectronic device packaging technology.

CHAPTER 3

KINETICS OF CVD CARBON NANOTUBE GROWTH

Among the various CNT synthesis methods, chemical vapor deposition (CVD) approaches are particularly attractive due to specific CNT growth features such as selective spatial growth, large area deposition capability and aligned CNT growth. As a result, the techniques for in-situ observation of CNT growth are desired to understand and optimize CNT growth process. In this chapter, CNT stack growth methods are employed to perform a pseudo in-situ monitor of CNT growth and gain insight into CNT growth kinetics. By varying the growth temperature, it was found that the aligned CNT film growth can be controlled in a diffusion- or kinetics-controlled region. By modeling the nanotube growth at the specific region, the basic parameters that are helpful to optimize the CNT growth process and explore the mechanisms of CNT growth can be deduced, such as gas diffusion mode in the densely-packed nanotube films, activation energy, and reaction order.

3.1 Monitoring of CNT Growth

Numerous efforts have been made to optimize CVD growth by selecting appropriate catalysts, support layers, carbon precursors, flow rates, synthesis temperature and pressure. Also many theories have been proposed to account for observed CNT growth mechanisms [198-200]. Currently, these models focus on the intrinsic CNT growth kinetics, i.e., carbon diffusion into the catalyst nanoparticles and precipitation or formation of graphitic structures when oversaturation occurs. However, the theories have not considered the effect of support materials for the catalysts and thus have not incorporated this parameter into the models. Many reports have shown that the choice of support material is a critical issue for the CVD growth of CNTs [48, 201, 202]. Our

studies in Chapter 2.4.2 demonstrate that selection of appropriate support materials for the catalysts can increase the CNT growth rate by two orders of magnitude.

In-situ monitoring of CNT growth rates would be helpful to optimize the CNT growth process, and explore the mechanisms and kinetics of CNT growth. However, in-situ growth characterization is difficult to implement in a CVD reactor, although certain methodologies have been used to gain information. For example, high-resolution in situ transmission electron microscopy (TEM) has been used to observe the formation of CNTs from methane decomposition over supported nickel nanocrystals [203]. However, the TEM environment is different from that of CVD growth, and TEM only observes CNT growth during the initial stages. Other techniques such as single-slit laser diffractography [204], optical interference [205], and time-resolved reflectivity [200], suffer from inefficiencies when measuring thick (long CNT) films, and from difficulties in data interpretation and nanotube film surface flatness. We are interested in growth of extended CNT films (>100 μm) and wish to explore the time dependence of CNT growth. In Chapter 2.5, we described the formation of carbon nanotube stacks by water-assisted selective etching. In this chapter, we employ that technique to monitor time-resolved CNT growth. Compared to other processes to build CNT stacks, this process can be adjusted to investigate the diffusion of precursor gases in densely-packed CNT films and the CNT growth kinetics in the gas diffusion-controlled regime. This approach also offers a relatively simple method to circumvent the difficulty of investigation of the intrinsic growth kinetics. Indeed, time-resolved CNT growth behavior could be obtained by varying the growth temperature and the ethylene (carbon precursor) ”on” (exposure) time during growth cycles. Furthermore, this process offers a simple way to evaluate the CNT growth behavior from the standpoint of mass transfer of the reaction gases in porous CNT films.

3.2 Diffusion-Controlled CNT Growth Kinetics

3.2.1 Experimental

The catalyst layers of Al_2O_3 (10 nm)/Fe (2 nm) were deposited onto the silicon wafer by sequential e-beam evaporation. CVD growth of CNTs was carried out with ethylene as the carbon source, and hydrogen (180 sccm) and argon (350 sccm) as carrier gases. The water vapor concentration (775 ppm) in the CVD chamber was controlled by bubbling a small amount of argon through water. Layered CNT films were obtained by the following sequence. Ethylene flowed into the CVD reactor for a preset time, after which the flow was terminated; after 5 min of only water, argon and hydrogen flow, ethylene was again introduced for a specific time. In this sequence, water is used to selectively etch weakly bonded carbon atoms that exist at the interface between the CNTs and the catalyst particles during the fixed 5 min interval between CNT growth steps. Scanning electron microscopy (SEM) studies were performed on a JEOL 1530.

3.2.2 Differentiation of Diffusion- or Kinetics-Controlled CNT Growth

Using the above recipe for rapid growth of CNTs, it is possible to explore the growth behavior of thick CNT films. For growth of a single layer CNT film, the CNT growth rate decreases with growth time. However, to establish the time-resolved growth characteristics, in-situ monitoring methods or specific growth marks are needed to track the CNT height at a specific time. By adjusting the ethylene (carbon precursor) cycling times, ethylene exposure times, and growth temperature of this process, we can obtain time-resolved CNT growth behavior. For example, five-layered CNT stacks could be obtained by repeating the growth-etching cycle five times, as shown in Figure 3.1a. Growth conditions for the CNTs shown in Figure 3.1a are 80 sec of ethylene flow followed by 5 min with the ethylene flow terminated in every cycle at 775 °C with ethylene, argon and hydrogen flow rates of 150, 350, and 180 sccm, respectively; the Si/SiO_2 substrate had 2 nm Fe layer deposited onto a 15 nm Al_2O_3 layer. The CNT films

in Figure 3.1a were partially peeled off using tweezers to demonstrate the layered structures of CNT films, as shown in Figure 3.2b. CNT layer 1 is the first nanotube layer grown. For growth of CNT layer 2, ethylene must penetrate CNT layer 1, due to the base or root stack growth mechanism. Growth of CNT layer 3 requires the ethylene to penetrate CNT layer 1 and layer 2; analogous processes must occur as additional stacks are added. Diffusion-controlled CNT growth is evident in the decreasing thickness of each subsequent layer. In our reactor/reaction system, since CNT growth occurs by a base-growth mode, ethylene diffuses to the bottom of the CNT films to allow growth on the Fe nanoparticles. Previous investigations have estimated the CNT density in the films under these growth conditions to be approximately 1200/μm^2 with an average diameter of 15 nm and neighboring CNT distance of 35 nm; thus, the CNT films act as densely-packed nano porous layers which present a diffusion barrier to the ethylene precursor. Due to the thick densely-packed CNT films (>100 μm) plus the rapid CNT growth rate, the CNT growth rate is controlled by ethylene diffusion through an increasing total CNT film thickness. This effect can be seen in Figure 3.1c, which shows the individual layer thicknesses. In the first 80 sec, the CNT film reaches 155 μm; in the second 80 sec, the CNT film grown reaches 140 μm, while the CNT films are 116, 91, and 43 μm, respectively, during the third, fourth and fifth 80 sec growth cycles. Indeed, for a diffusion controlled process, the CNT thickness grown for a series of layers is proportional to the square root of time; this relationship is evident in the inset of Figure 3.1c. When the growth temperature decreases to 725 °C, the CNT growth mode becomes reaction-rate controlled, as shown in Figure 3.1d. The growth conditions for the CNTs in Figure 2d are 80 sec ethylene introduction during each growth/etching cycle at 725 °C; all other conditions remained the same as those for films grown at 775 °C. The image shows that the thickness of the layers is almost the same, except for layer 1, which may be a result of CNT growth latency at the relatively low temperature. The thickness of individual layers is 23.1, 27.7, 27.8, 27.5, 27.5, and 27.5 μm, respectively. If the CNT

growth is reaction rate limited, and we assume a first order rate process, then the individual layer thicknesses should be linear with time. Our experimental results are in agreement with this assumption. Furthermore, for our reactor/reaction system, CNT growth is observed to be reaction rate controlled below 740 °C, and diffusion-controlled when the growth temperature exceeds 740 °C.

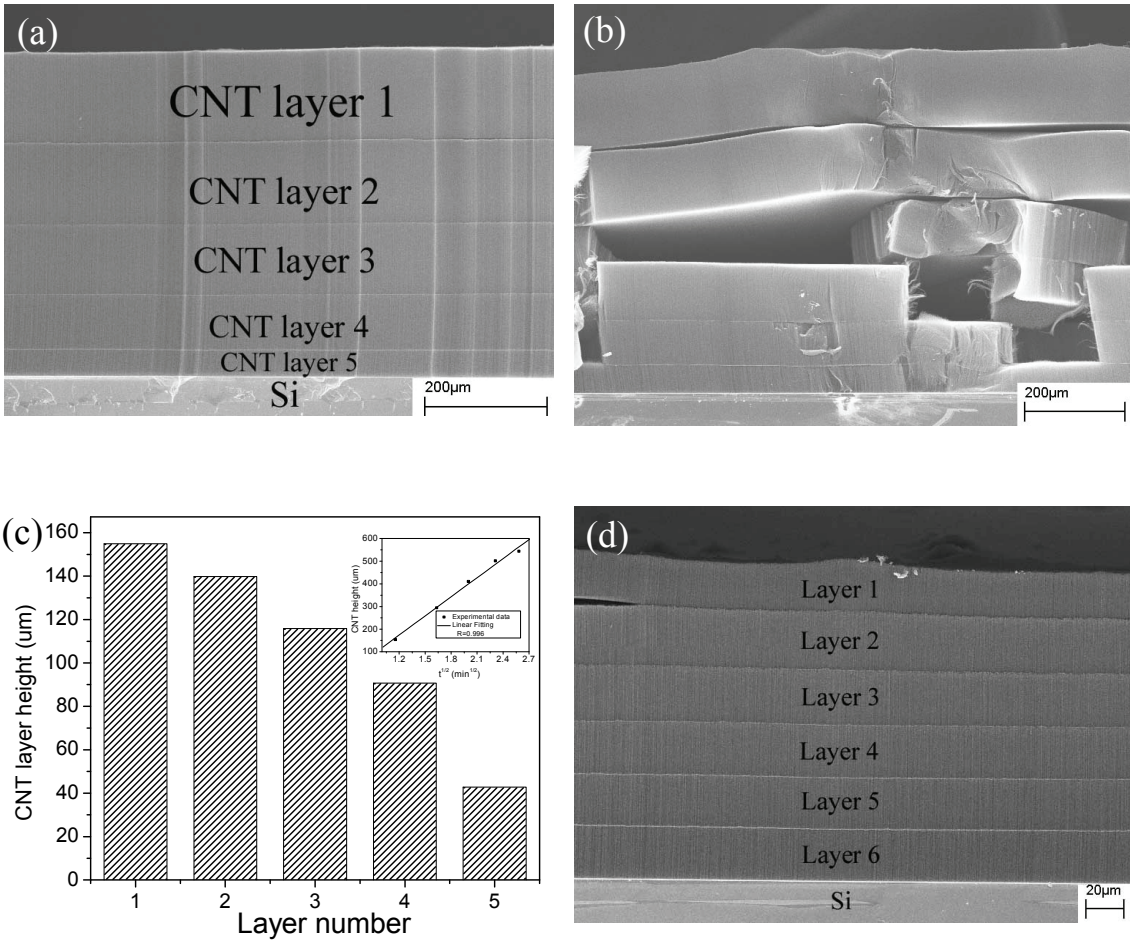

Figure 3.1 (a) Cross-sectional SEM images of 5-layered CNT films; (b) scratched CNT films in (a) to show the layered structures of CNT films; (c) individual layer thickness of the CNT films in (a). The inset in Figure 3.1c shows the linear relationship between CNT film thickness and the square root of growth time, indicating that CNT growth under these conditions is diffusion controlled. (d) Cross-sectional SEM image of 6-layered CNT films grown in a kinetics-controlled region.

3.2.3 Modeling CNT Growth at a Diffusion-Controlled Region

The diffusion-controlled CNT growth provides a means to obtain additional insight into CNT growth behavior and gas diffusion in the densely-packed CNT films. In order for CNT growth to occur, ethylene must reach the Fe catalyst at the base of the CNT, thereby requiring diffusion through increasingly thicker nanotube films, as shown in Figure 3.2. This process is similar to that observed in the thermal oxidation of silicon, which has been studied extensively [196]. As a result, we model CNT growth in an analogous way; detailed theory and models for silicon oxidation have been described previously.

The flux of ethylene across the CNT films is assumed to obey Fick's law, where the flux J is related to any position

$$J = -D\frac{\partial C}{\partial h} \qquad \textbf{Equation 3.1}$$

within the CNT film, D is the diffusion coefficient (μm^2/min) and $\frac{\partial C}{\partial h}$ (mol/μm^3.μm) is the concentration gradient of the ethylene in the CNT films. If it is assumed that the ethylene flux is constant everywhere in the CNT films, i.e. ethylene does not accumulate within the film, then Equation (1) can be simplified to

$$J = -D\frac{C_i - C_0}{h_0} \qquad \textbf{Equation 3.2}$$

where h_0 (μm) is the thickness of the CNT films at a specific time, and Ci (mol/μm^3) and C0 (mol/μm^3) are the ethylene concentrations at the CNT film surface and at the Fe nanoparticle surface, respectively. If we further assume that the growth reaction at the Fe nanoparticle surface is a first order reaction, then the flux of reactant at the interface is

$$J = k_s C_i \qquad \textbf{Equation 3.3}$$

where k_s is the first order rate constant. By eliminating C_i, J becomes

$$J = D\frac{C_0}{h_0 + D/k_s}$$ **Equation 3.4**

The rate of change of CNT film thickness with time is given by the ethylene flux divided by the number of the molecules M (mol/μm^3) of ethylene incorporated into a unit volume of the resulting film:

$$\frac{dh_0}{dt} = \frac{2J}{M} = \frac{DC_0/M}{h_0 + D/k_s}$$ **Equation 3.5**

where 2 means that every ethylene molecule has two carbon atoms.

This differential equation is easily solved using the boundary condition h_0=0 at t=0, which yields

$$h_0 = 0.5\sqrt{A^2 + 4Bt} - 0.5A$$ **Equation 3.6**

where A=2D/k_s and B=4DC_0/M. D is the diffusion coefficient, k_s the first order rate constant, C_0 the ethylene concentrations at the CNT film surface, and M (mol/μm^3) the number of molecules of ethylene incorporated into a unit volume of the resulting film.

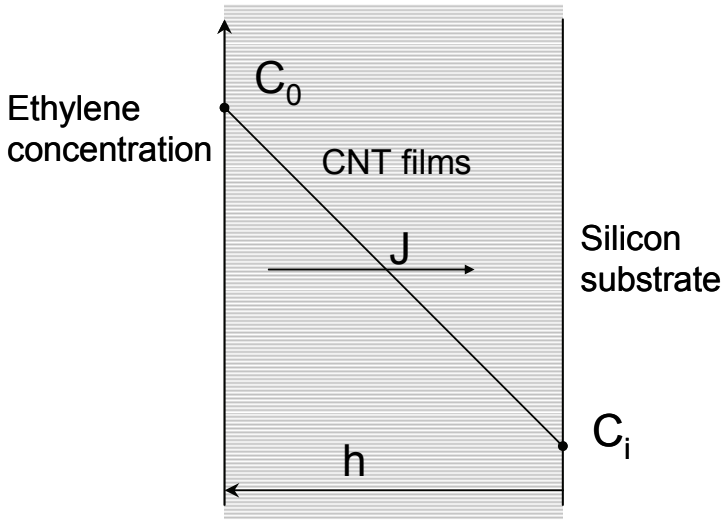

Figure 3.2 Model for CNT growth under diffusion-controlled conditions. h is the thickness of the CNT film at any time t. J is the flux of ethylene diffusing through the film, and C_0 and C_i represent the ethylene concentration at the film surface and film-substrate interface.

To test the validity of this simple model, we have grown CNT stacks for 1 min ethylene flow time in each cycle at various temperatures to investigate the time-evolution behavior of CNT growth; all other conditions are those described in the Experimental section. Figure 3.3 displays experimental CNT film height (thickness) as a function of growth time at different temperatures. A fit of Equation 3.6 to the experimental growth time versus thickness data yields excellent agreement (R^2=0.996) at temperatures of 745, 750, 760 and 770 ºC, as shown by the solid lines in Figure 3.3. We chose the growth temperature to be above 740 ºC to ensure CNT growth within the diffusion-controlled regime. By fitting the model equation to the experimental data, the parabolic rate coefficient B and A can be deduced. From B and A, we can also calculate values for the diffusion coefficient D and rate constant k_s. The results of these calculations at the temperatures investigated are summarized in Table 3.1. The value of C_0 as determined by gas flow rate is 9.566×10^{-18} mol/μm^3; M is obtained experimentally as 1.091×10^{-15} mol/μm^3 (or 6.571×10^{8} molecules/μm^3) from the bulk density (0.0131 g/cm^3) of the as-grown aligned CNT films.

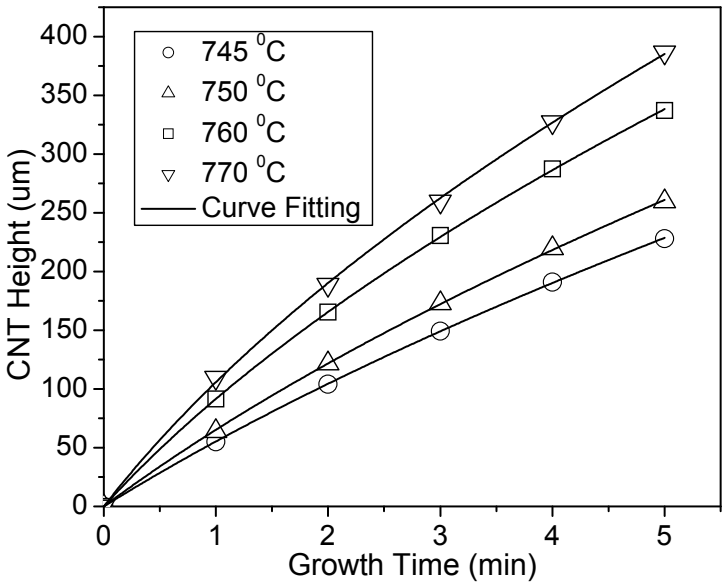

Figure 3.3 CNT height as a function of growth time at different growth temperatures. The solid line indicates a fit of the experimental data to Equation 3.6.

TABLE 3.1 Results summary of parameters at various temperatures

Temperature (K)	B $\times 10^{-4}$ (μm^2/min)	Diffusion Coefficient, D$\times 10^4$ (cm^2/sec)	A (μm)	ks (μm/s)
1018.14	4.56	2.17	768	28.3
1023.14	5.09	2.42	714	33.9
1033.14	6.38	3.03	601	50.5
1043.14	7.90	3.75	552	67.9

3.2.4 Gas Diffusion in Densely-Packed CNT Films

Since the system pressure is uniform in the CVD chamber (p=1 atm), the mass transfer is diffusive in nature and thus may involve ordinary molecular diffusion, Knudsen diffusion and/or surface diffusion in CNT films. However, surface diffusion will occur only when the diffusion gases are adsorbed in a mobile layer [206]; for these studies, we assume that this transport mode is negligible. If the radius (r) of the channel is small relative to the mean free path (λ), the rate of mass transport is governed by collisions with the channel walls. This type of transport is usually referred to as Knudsen diffusion. Qualitatively, Knudsen diffusion dominates when value of r/ λ is less than 0.1 [206, 207]. The mean free path of ethylene is ~181 nm at the same temperature and pressure as our system, as determined from

$$\lambda = \frac{RT}{\sqrt{2}\pi d^2 N_A p} \qquad \textbf{Equation 3.7}$$

where R is the ideal gas constant (8.314 J/mol.K), T is temperature (K), d is molecular diameter (4.163×10^{-10} m for ethylene), N_A is Avogadro's number (6.02×10^{23}/mol), and P is system pressure (101325 Pa). The equivalent diameter of the channels of the CNT films is estimated to be 20 nm by assuming that the diameter and neighboring distance of CNTs are 15 and 35 nm, respectively. Therefore, diffusion apparently occurs in the Knudsen regime, since the ratio of channel radius to the mean free path is less than 0.1.

The effective Knudsen diffusivity may be expressed as [208]

$$D_{A,K} = 97.0r\frac{\varepsilon}{\tau}(\frac{T}{M_A})^{1/2} \qquad \textbf{Equation 3.8}$$

where r is the channel radius, T is temperature, ε porosity of the solid, τ the tortuosity factor, and M_A the molecular weight of component A. We don't know exactly values of ε and τ, but we assume them to be constant due to the same CNT diameter and area distribution density. According to Equation 3.8, the temperature dependence of the Knudsen diffusion coefficient is proportional to $T^{1/2}$; Figure 3.4 shows a plot of diffusion coefficient versus the square root of temperature, indicating a linear relationship between D_A, K and $T^{1/2}$. These results suggest that CNT growth under the conditions investigated in this study, is controlled Knudsen diffusion of gases through the densely-packed CNT films.

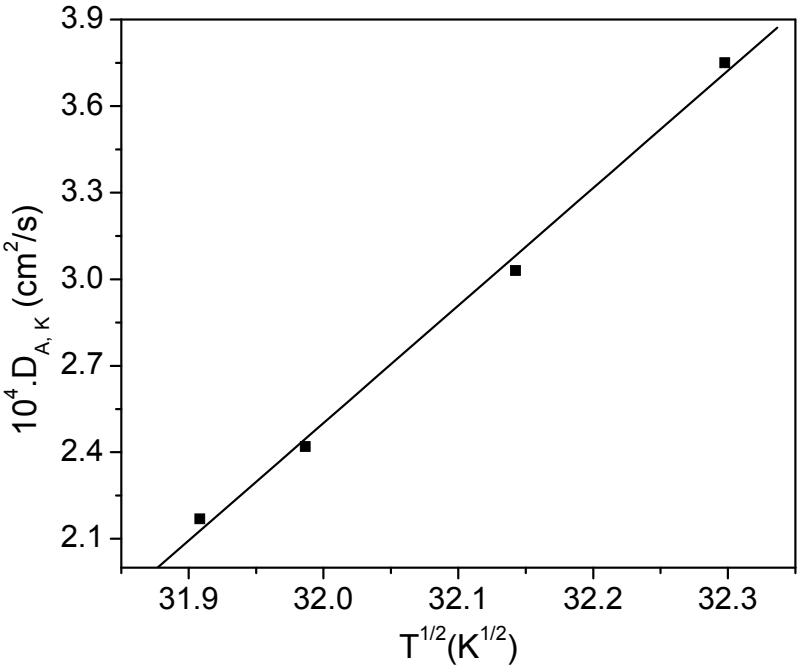

Figure 3.4 Dependence of Knudsen Diffusion Coefficient on temperature.

3.3 Kinetics-Controlled CNT Growth Kinetics

To explore CNT growth kinetics, the time-resolved growth characteristics can be recorded to track the CNT height at a specific time. However, this is commonly performed by dividing the CNT height by growth time to obtain an average growth rate. This method suffers from several limitations. The CNT growth rate may change with time, thereby yielding inaccurate growth kinetics. More importantly, CNT growth at high temperature may be affected by the diffusion of carbon-containing precursors through the CNT films to the catalyst surface, if CNT growth occurs in the base-growth mode. Thus, some fraction of the overall growth kinetics arises from transport (diffusion) effects, rather than from the intrinsic chemical reaction, thus introducing errors into the calculation of order of reactions and activation energies. We invoke a related technique of nanotube formation in the kinetic-controlled regime to explore the activation energy and reaction order. This approach offers a simple way to evaluate the CNT growth behavior and investigate the factors controlling CNT growth, such as catalyst and support materials, without using the growth mark method, which requires special experimental design. Furthermore, this technique provides a unique methodology to investigate the CNT growth during the initial growth stage.

3.3.1 CNT Growth at Kinetics-Controlled Regions

To eliminate mass transport limitations on the reaction rate, growth is performed under conditions for which the CNT growth rate is controlled by the chemical reaction kinetics. This can be achieved by carrying out the CVD process at lower temperatures. In Chapter 3.2, we have shown that the growth reactions at temperatures below 740 °C are kinetic-controlled. In the following experiments, CVD growth of CNTs is performed below 710 °C to ensure that the CNT growth is controlled by reaction kinetics. Using the above recipe for the formation of CNT stacks, it is possible to explore the growth behavior of CNT films.

By adjusting ethylene (carbon precursor) cycling times, ethylene flow rate, and growth temperature of this process, we can observe time-resolved CNT growth behavior. For example, five-layered CNT stacks could be obtained by repeating the growth-etching cycle five times, as shown in Figure 3.5a. Growth conditions for the CNTs shown in Figure 3.5a are 1 min of ethylene flow followed by 5 min with the ethylene flow terminated in every cycle at 690 °C with ethylene, argon and hydrogen flow rates of 150, 350, and 180 sccm, respectively; the Si/SiO_2 substrate had a 2 nm Fe layer deposited onto a 10 nm Al_2O_3 layer. CNT layer 1 is the first nanotube layer grown. For growth of CNT layer 2, ethylene must penetrate CNT layer 1, due to the CNT base growth mechanism. Growth of CNT layer 3 requires the ethylene to penetrate CNT layers 1 and 2; analogous processes must occur as additional stacks are added. The thicknesses of individual CNT layers are 13.7, 17.0, 16.6, 17.0, and 17.0 μm, respectively. Kinetics-controlled CNT growth is evident, in that the individual layer thicknesses are essentially the same, except for layer 1; this discrepancy is likely a result of initial CNT growth latency at the relatively low temperature; this issue will be discussed below. If the CNT growth is reaction rate limited, and the near surface concentration of ethylene is in excess, then the individual layer thicknesses should scale linearly with time.

To further verify that a chemical reaction at the lower temperature is the controlling step in this heterogeneous reaction system, we performed patterned CNT growth by generating catalyst patterns on the substrates using a lift-off process. In this way, catalyst covers only a fraction of the substrate surface, thereby facilitating the transport of ethylene to the catalyst/CNT interface since ethylene does not need to penetrate the increasing CNT film, but can diffuse across the CNT bundle radius. The pattern size is 20 μm with a pitch of 130 μm. CNT pillars grown using this approach are shown in Figure 3.5b. The growth conditions for the CNTs in Figure 3.5b are the same as for those shown in Figure 3.5a. The image demonstrates that vertically aligned CNT pillar stacks were achieved even with a small pattern size. Figure 3.5c is an enlarged

image of the individual pillar stacks shown in Figure 3.5b. The arrows in Figure 3.5c designate the interfaces between adjacent growth segments. The thicknesses of the individual layers are 14.2, 17.4, 16.7, 17.1, and 16.7 μm, respectively. Clearly, the thickness of the corresponding layers is virtually the same; the small variation observed occurs because the growth time is short, and the ethylene flow is initiated and terminated manually. Thus, it is evident that CNT growth under the conditions used in these studies is reaction rate limited and that adjustment of the growth temperature is an effective way to control CNT growth regimes. Figure 3.5d shows a high magnification SEM image of the interface between neighboring CNT film layers. Due to the very high areal density of as-grown CNTs (>1000 μm^{-2}), steric hindrance between CNTs has been assumed to be the main driving force for formation of CNT alignment within a CNT layer [209]; surprisingly, van der Waals forces are able to maintain the alignment of CNT bundles in separate layers. When the growth temperature increases to 700 °C while keeping other conditions constant, the CNT growth mode is still reaction-rate controlled, as shown in Figure 3.5e. The image shows that again, the thickness of the layers is essentially constant, except for layer 1. The thickness of individual layers is 17.3, 23.6, 23.6, 23.1, and 23.0 μm, respectively. Our experimental results are consistent with the assumption of CNT growth in reaction rate controlled regimes at temperature below 710 °C. Using this procedure along with a change in CNT growth temperature or ethylene flow rate, the growth rate at different temperatures can be obtained, which allows determination of the activation energy and reaction order.

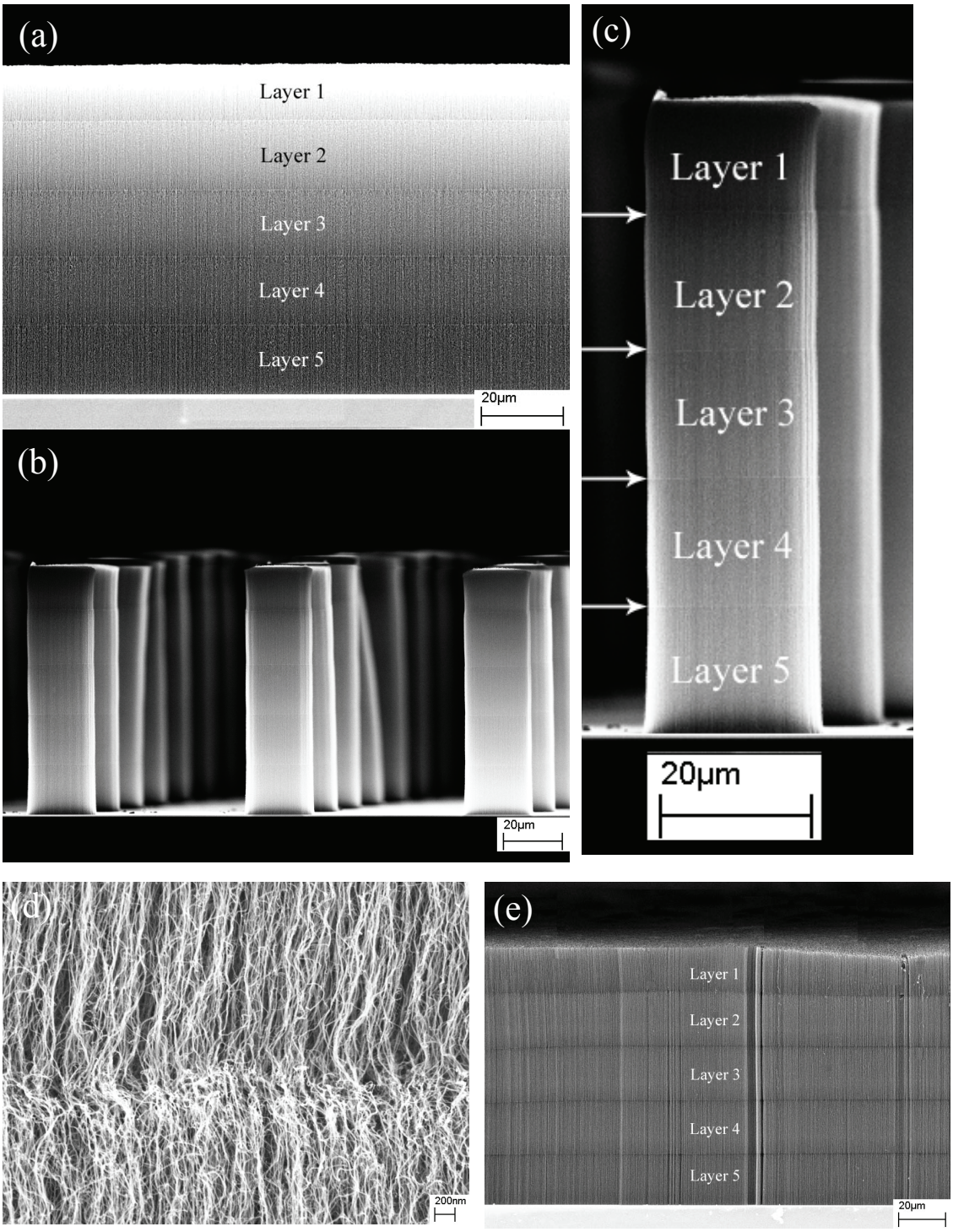

Figure 3.5 SEM images of (a) aligned CNT stacks and (b) CNT pillar stacks grown at 690 °C. (c) High magnification SEM image of CNTS in (b) to indicate the interfaces (designated by arrows). (d) High magnification SEM image of the interface between separated CNT layers. (e) SEM image of aligned CNT stacks grown at 700 °C.

3.3.2 CNT Growth Kinetics

The CNT growth rate can be expressed as

$$r = k[P_{C_2H_4}]^n \qquad \textbf{Equation 3.9}$$

where k is the rate constant, $P_{C_2H_4}$ is the partial pressure of C_2H_4, and n is the reaction order. The rate constant can be written as $k = A\exp(-E_a / RT)$, where A is the frequency factor, Ea is the effective activation energy, R is the gas constant and T is the absolute temperature. According to the above equations, a plot of $\ln r$ versus 1/T should give a straight line with a slope of $-E_a / R$. At a given temperature and in the reaction kinetics-controlled regime, the CNT growth rate can be obtained by measuring the individual layer thickness as a function of ethylene flow time in each cycle. The growth rate value used is an average of the individual layer thicknesses, excluding the first layer. For instance, as described above, the CNT growth rates are 17.0 and 23.4 μm/min at 690 and 700 °C; similarly, the CNT growth rates are 10.1, 12.9, and 27.5 μm/min at 670, 680 and 710 °C, respectively. All growth rates have been measured at an ethylene flow rate of 150 sccm. An Arrhenius plot of these data is shown in Figure 3.6a; a linear fit yields an activation energy of 201.2 kJ/mol. The reaction order is determined by selecting a growth temperature (700 °C), and changing the ethylene flow rate from 75 sccm to 175 sccm. The ethylene partial pressure is calculated by multiplying the ethylene molar ratio (ethylene flow rate divided by total gas flow rate in the CVD process) by the total pressure (101.325 kPa). The resulting growth rates are 8.3, 13.0, 16.5, 23.4 and 28 μm/min with ethylene flow rates of 75, 100, 125, 150, and 175 sccm, respectively. The growth rate dependence on the ethylene partial pressure is plotted in Figure 3.6b; since the growth rate increases linearly with C_2H_4 partial pressure, the reaction is first order.

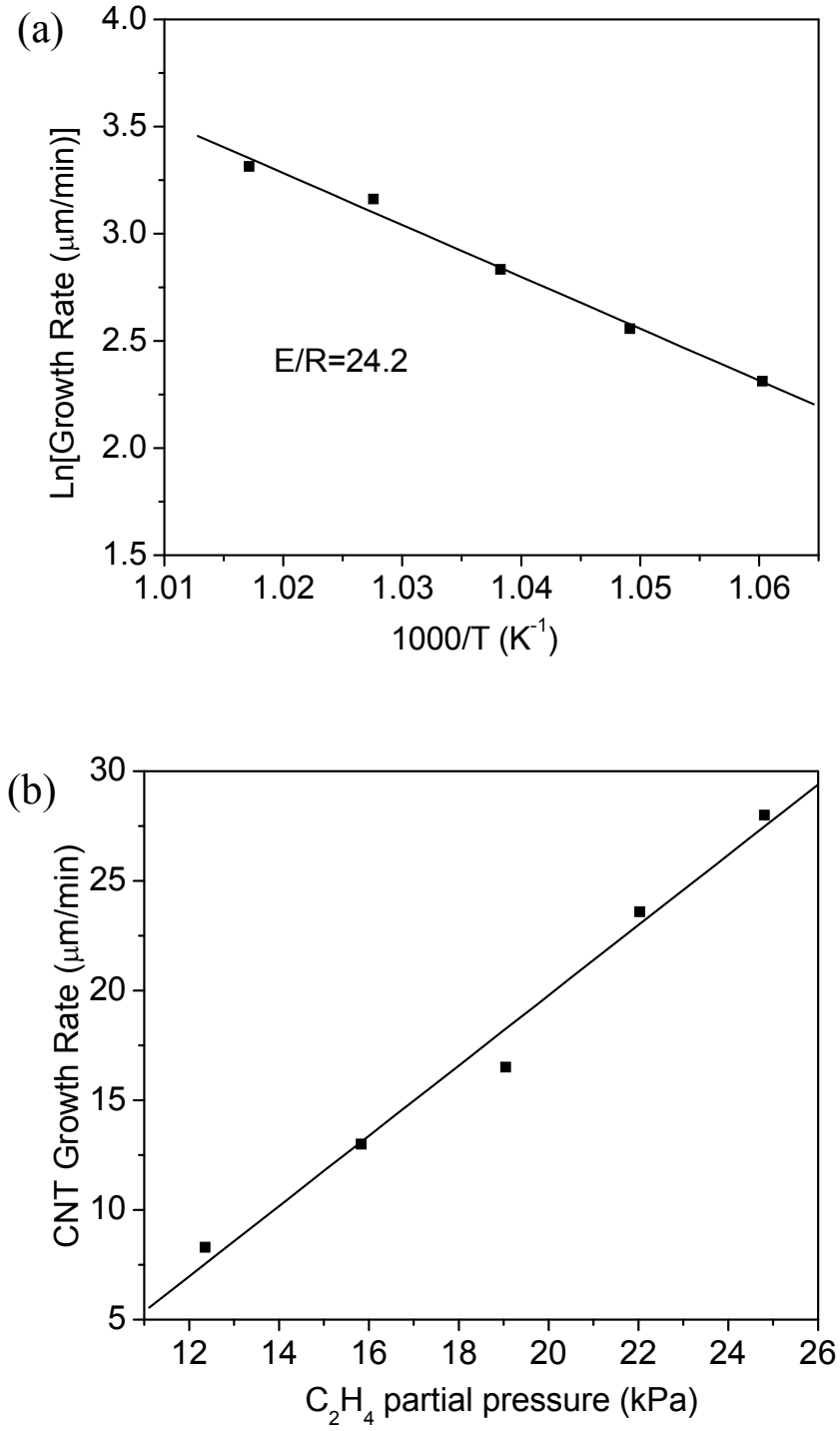

Figure 3.6 (a) CNT growth rate as a function of growth temperature. The solid line is a linear fit of the natural logarithm of the growth rate as a function of the reciprocal of the absolute temperature. (b) CNT growth rate at 700 °C as a function of C_2H_4 partial pressure. Solid squares represent the experimental data.

Analogous to the results observed with temperature variation, where aligned CNTs can be grown only between certain temperature limits, the C_2H_4 flow rate (or partial pressure) must also be within a specified range. If the ethylene flow rate is increased to 200 sccm, the CNT growth rate decreases to 18.2 μm/min. SEM studies of the resulting CNTs reveal that particles attach to CNT walls, and diminished alignment of the CNTs in these films is observed relative to films grown at lower ethylene flow rates. The physical appearance of grown CNT films at 200 sccm relative to that at 150 sccm can be seen clearly by comparison of Figure3.7a to Figure 3.7b.

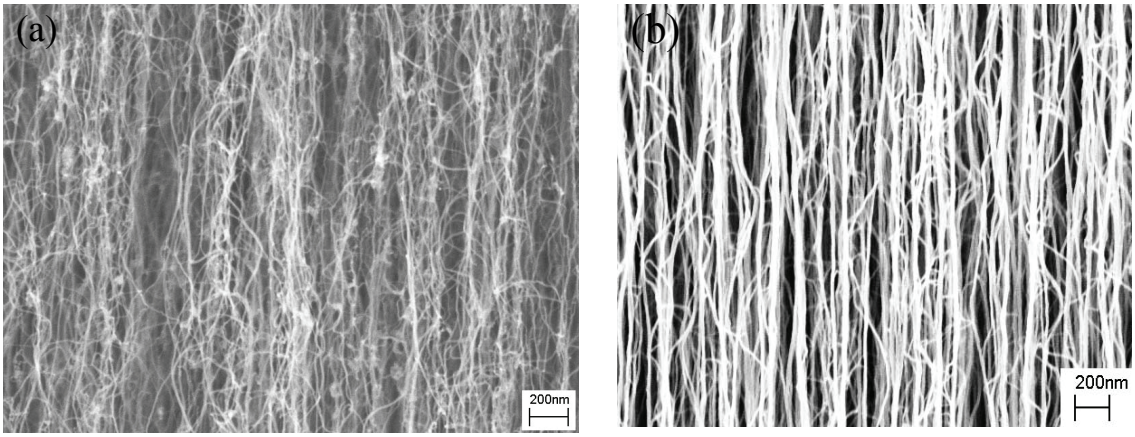

Figure 3.7 High magnification SEM images of CNT films grown at ethylene flow rates of (a) 200 sccm and (b) 150 sccm. Note the degraded quality of the films at 200 sccm.

3.3.3 CNT Growth Latency

As noted above, latency is observed during the initial stage of CNT growth in the kinetics-or reaction rate-controlled regime. In the first minute of CNT growth, the growth rate is lower than that observed during subsequent time periods. Such observations are consistent with the CNT formation process. CNT growth is usually regarded as a dissociation-diffusion-precipitation process, where elemental carbon is formed on the metal (catalyst) particle surfaces followed by diffusion and precipitation in the form of cylindrical graphite; this process requires time to saturate the iron and form iron carbide

on which CNTs grow. With our approach, we can investigate CNT growth during the initial stages while maintaining CNT alignment, by growing CNT stacks at 700 °C with an ethylene flow time of 30 sec during each cycle. Figure 3.8 shows an eight-layer CNT stack formed by repeating the 30 sec cycle eight times. The thicknesses of individual layers are 7.1, 10.1, 13.2, 13.4, 13.0, 12.6, 12.2, and 12.6 μm, respectively. The inset in Figure 3.8 shows a plot of CNT layer thickness versus growth time, indicating that CNT growth reaches steady state in one minute, while CNTs begin growth within 30 sec. The linear relationship between CNT film thickness and growth time clearly demonstrates that CNT growth can be controlled in a kinetics-controlled regime simply by controlling the CNT growth temperature.

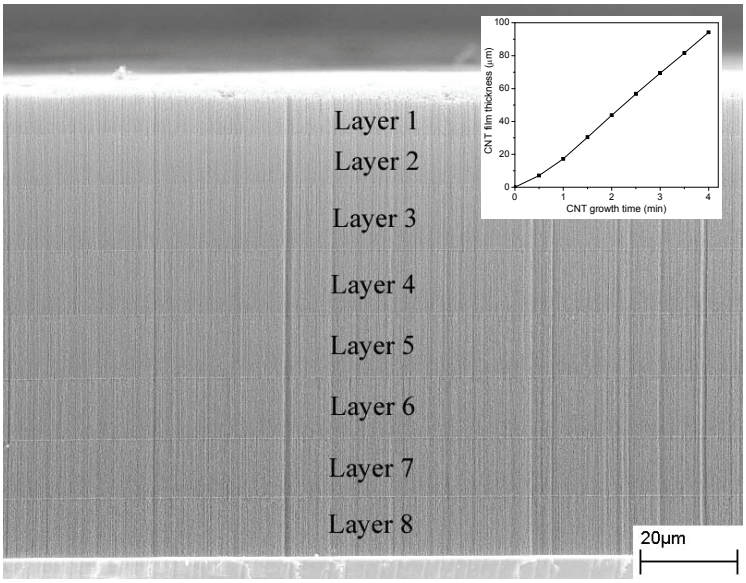

Figure 3.8 Eight layered CNT stacks formed at 700 °C with an ethylene flow time of 30 sec in each cycle. The inset is a plot of CNT layer thickness versus growth time, indicating kinetics-controlled CNT growth in one minute.

3.4 Summary

In this chapter, CNT stack growth methods are employed to perform a pseudo in-situ monitor of CNT growth and gain insight into CNT growth kinetics. By varying the growth temperature and the ethylene introduction time in growth cycles, a parabolic increase of CNT length versus time is obtained, indicating that gas diffusion-controlled kinetics establish the intrinsic CNT growth kinetics. Due to the base growth mode in our reaction/reactor system, the densely-packed, well-aligned CNT films act as porous barrier layers to the diffusion of carbon precursors to the catalyst nanoparticles. By varying CNT growth temperature, a quantitative time-evolution analysis has been performed based on a simple CNT growth model, thereby allowing determination of the mass transfer coefficient in the CNT films. It was found that a simple kinetics model, similar to the thermal oxidation of silicon, can accurately describe the CNT growth behavior. The diffusion of gases in the spaces between densely-packed nanotubes in CNT films is consistent with Knudsen diffusion with a diffusion coefficient on the order of 10^{-4} cm^2/s. These results are important in the modeling of CNT thick film growth and for optimization of the growth parameters.

CNT stack growth methods can also be used to allow pseudo in-situ monitoring of CNT growth in the kinetics-controlled regime. By varying the growth temperature and the ethylene flow rate within growth cycles, the CNT growth was shown to be first order with an activation energy of 201.2 kJ/mol. By deceasing the ethylene flow time in growth cycles, this CNT stack growth technique was used to observe the initial stage of CNT growth. Within one minute, CNT growth reaches steady state. The formation of CNT stacks could be tailored to investigate the effects of factors such as pressure, temperature, flow rate, catalyst support materials, and carbon precursors, on the CNT growth.

CHAPTER 4

ASSEMBLY OF CARBON NANOTUBE STRUCTURES

4.1 Introduction

The simulated properties of carbon nanotubes (CNTs) are extraordinary, such as extremely high thermal conductivity [210], very high electrical conductivities and outstanding mechanical properties [160]. Combined with their one-dimensional molecular structures, CNTs offer many promising applications for future electronic materials and device structures [162, 211]. Growth of aligned CNT arrays with controlled areas and nanotube length is well-known. If open-ended aligned CNT films/arrays can be formed, improved electrical conductance of MWNTs should result, since recent studies have demonstrated that the internal walls of MWNTs can participate in electrical transport, thereby enabling large current-carrying capacity [212]. These considerations imply that multichannel ballistic transport could be achieved if the caps of the CNTs are removed; CNT electrical conductance should therefore be dramatically improved. Such achievements may then allow CNTs to serve as conductive nanowires and thus replace copper and aluminum films used in state-of-the-art circuits; such nanowires are less susceptible to electromigration under high current density than Cu and Al. It is also expected that the hollow cavity of CNTs will allow the wicking of solders, such as Sn/Pb, Sn/Ag/Cu, due to capillary forces. As a result, interconnects of CNTs with metal electrodes by solders should be possible, and the limited wetting of solders on CNT films would be eliminated [213].

For electronic device applications, chemical vapor deposition (CVD) methods are particularly attractive due to characteristic CNT growth features such as selective spatial growth, large area deposition capability and aligned CNT growth. However, the CVD

technique suffers from several drawbacks. One of the main challenges for applying CNTs to circuitry is the high growth temperature (>600°C). Such temperatures are incompatible with microelectronic processes, which are typically, performed below 400-500 °C in back-end-of-line sequences. Another issue is the poor adhesion between CNTs and the substrates, which will result in long term reliability issues and high contact resistance. To fabricate microelectronics devices that incorporate CNT blocks, the CNTs should be selectively positioned and interconnected to other materials such as metal electrodes or bonding pads. The common practices for CNT growth on such substrates involve the deposition catalysts such as Fe or Ni on metal layers such Ti or Ti/Au. Unfortunately, the electrical contact is not necessarily improved, since the catalyst nanoparticles are capped by the nanotubes. To overcome these disadvantages, we propose a methodology that we term "CNT transfer technology", which is enabled by open-ended CNT structures. This Chapter includes the aligned open-ended CNT architecture growth and assembly of carbon nanotube structures using CNT transfer technology.

4.2 In-Situ Opening of CNTs

The nanotubes can be opened by etching away the caps using oxygen [153] and carbon dioxide [214]; however, the nanotube walls are inevitably damaged. As a result, CNT electrical and mechanical properties are degraded. Realization of high-quality open-ended CNT synthesis requires either a novel post-treatment process to open CNTs, or an alteration of the CVD process to allow in-situ high-quality open-ended CNT growth without the need for subsequent processes. In-situ growth of open-ended CNTs is desirable, since it is cost-effective. Our intent is to develop a novel process to open the nanotubes in-situ in order to study the corresponding CNT properties while maintaining CNT film alignment. Toward this end, we developed an in-situ process to open CNTs [215]. In this process, ppm levels of water etch the ends of the nanotubes, due to the

higher concentration of structural defects that exist in the CNT ends. The pentagon structures in the caps result in curvature and correspondingly larger strains and thus higher chemical reactivity compared with unstrained bonds (nanotube walls). Therefore, the nanotube ends are most susceptible to chemical attack by water molecules. This simple process offers a novel way to synthesize aligned open-ended CNT films. The substrates used in this study were (001) silicon wafers coated with SiO_2 (500 nm) by thermal oxidation. The catalyst layers of Al_2O_3 (15 nm)/Fe (3 nm) were formed on the silicon wafer by sequential e-beam evaporation. CVD growth of CNTs was carried out at 775°C with ethylene (150 sccm) as the carbon source, and hydrogen (180 sccm) and argon (350 sccm) as carrier gases. The water vapor concentration in the CVD chamber was controlled by bubbling a small amount of argon gas through water held at 22 °C. Ethylene flowed into the CVD system for a preset time, after which the flow was terminated; it followed by 5 min of only water, argon and hydrogen flow, which was used to selectively etch the nanotube tips and carbon atoms at the interfaces between the nanotubes and catalyst particles. Additional studies have demonstrated that the CNT film height can remain uniform to more than 500 μm if CVD process conditions are adequately controlled. The length uniformity of nanotube films is important for the CNT assembly process described below, since a conformal geometry is required to guarantee that a maximum number of CNT interconnects contact solder that will be placed on the substrates.

4.3 Carbon Nanotube Film Assembly

4.3.1 CNT Transfer Process

To overcome the high CNT growth temperature and poor adhesion that currently plague CNT implementation, we propose a methodology that we term “CNT transfer

technology", which is enabled by open-ended CNT structures. This technique is similar to flip-chip technology as illustrated schematically in Figure 4.1.

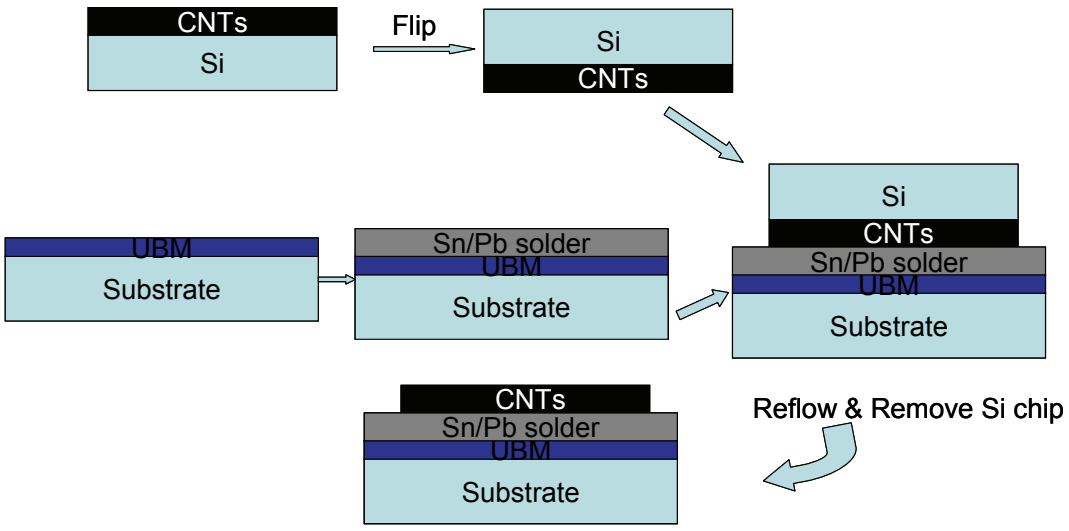

Figure 4.1. Schematic diagram of "CNT transfer technology". UBM: under bump metallization. See the text for detailed explanations.

The substrates can be FR-4 boards coated with copper foil or other materials and modulus, such as heat sinks. To improve the adhesion and wetting of solder on the substrates, the under bump metallization (UBM) layers are sputtered onto the substrate metallization. The eutectic tin-lead paste (100 μm) is then stencil-printed on the UBM. After reflow, the tin-led solder is polished to 30 μm. The silicon substrates with CNTs are flipped and aligned to the corresponding copper substrates, and reflowed in a seven-zone BTU reflow oven at higher temperatures (peak temperature at 270 °C) than those typically used (220 °C) to simultaneously form electrical and mechanical connections. This process is straightforward to implement and offers a strategy for both assembling CNT devices and scaling up a variety of devices fabricated using nanotubes (e.g., flat panel displays). This process could overcome the serious obstacles of integration of CNTs into integrated circuits and microelectronic device packages by offering low process temperatures and improved adhesion of CNTs to the substrates. Figure 4.2a indicates that the entire CNT film (1.5 cm × 1.5 cm) is transferred to the substrate (2.54

cm × 2.54 cm), since no trace amount of CNTs are evident on the silicon chip. This result is in stark contrast to the same process wherein the CNTs are closed-ended, in that only a fraction of the CNT film is transferred to the substrate (shown in Figure 4.2b), indicating that the adhesion of the attached nanotube films is poor. Figure 4.2c is a cross-sectional SEM image of well-aligned open-ended CNT films transferred onto the copper substrate. Any detachment of CNT film from the substrate is not found. Furthermore, the close observations of the interface between CNTs and the solders show that CNTs are well connected by solders, as shown in Figure 4.2d. In addition, upon drop testing, the closed-ended CNT films detached from the substrate, while open-ended CNTs did not. Such observations indicate that the wetting properties of solders on the aligned open-ended CNT film have been improved. We believe that the open channels of nanotubes assist the adhesion between nanotubes and solders due to strong capillary forces that draw solder inside the CNTs. In the molten state, the eutectic tin-lead solder has a similar surface tension as does elemental lead. Indeed, experiments have shown that lead could fill into carbon nanotube cavities by capillary forces, and that the filling at least partially wets the inside surface of the nanotubes. At present, we are not certain if compound formation has occurred by reaction of solder with carbon at the nanotube tips.

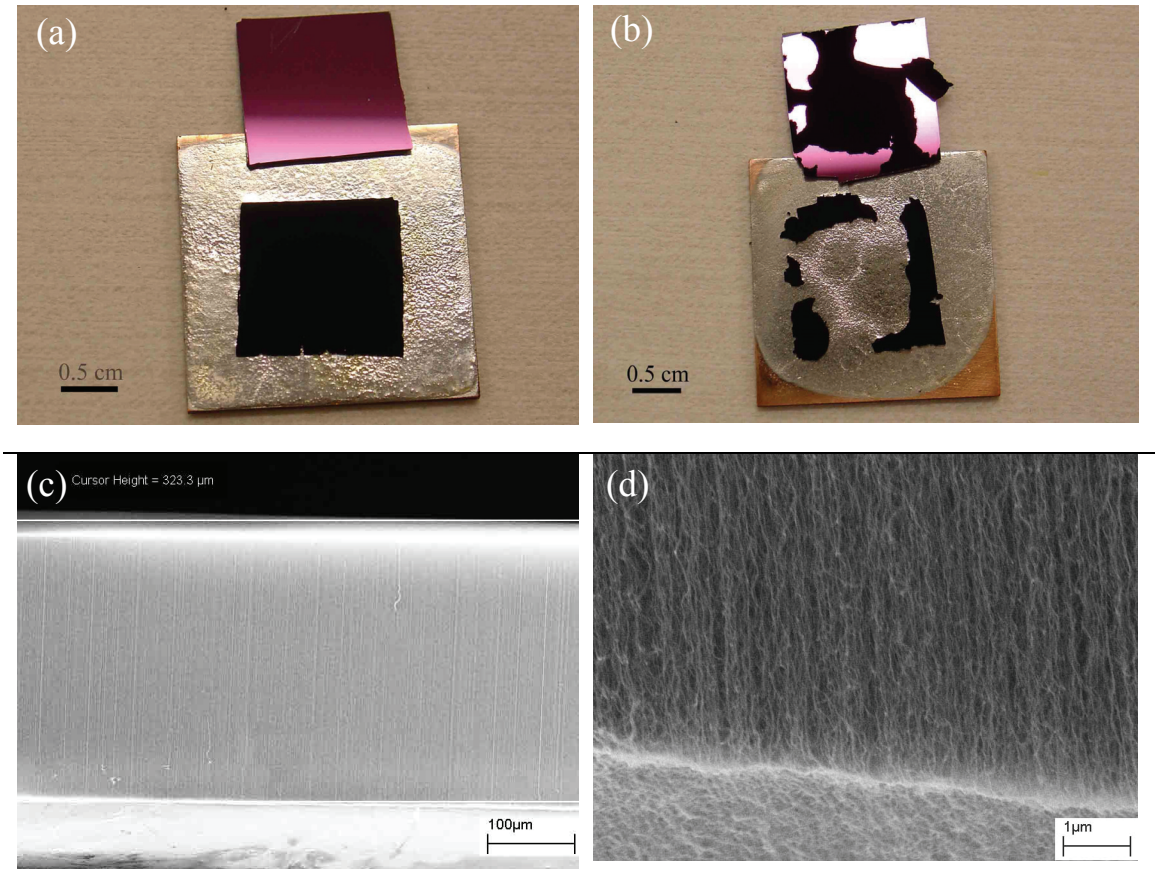

Figure 4.2 (a) Photograph of open-ended CNT film transferred onto the copper substrate coated with eutectic tin-lead solder. The clear silicon chip shows that the CNTs are effectively transferred to the substrate and connected by solder. (b) Photograph of closed-ended CNT film which has only partially transferred onto the copper substrate coated with eutectic tin-lead solder. Most CNTs still remain on the silicon chip, indicating poor wetting properties of solders on the CNT films. (c) A cross-sectional SEM image of well-aligned open-ended CNT films transferred onto the copper substrate. The eutectic tin-lead solder is used to interconnect CNTs and the copper substrate. (d) Side view of the interface between CNTs and solders at angle of 30°.

4.3.2 Field Emission Properties of Assembled CNT Films

To explore the electrical properties of CNTs connected by solders on the copper substrates, field emission characterization of the as-prepared assembly has been performed. The height of the nanotube films is ~323 µm with diameters in the range of 10 to 20 nm. By changing the catalyst thickness, reaction temperature and time, the nanotube film thickness can be controllably varied. We measured the (cathodic) electron emission

from 1.5 cm by 1.5 cm well-aligned open-ended CNT films shown in Figure 4.2a at room temperature and in a vacuum chamber below 10^{-5} Torr. The spacing between the CNT tip and the anode (phosphor-coated ITO glass) was ~180 μm and was maintained by a poly-tetafluoroethylene (PTFE) spacer. The phosphor screen became quite homogeneous over the whole areas when the applied field was 3.0 V/μm, as shown in Figure 4.3a. The measured current density (mA/cm^2) as a function of electric field (V/μm) is shown in Figure 4.3b. A typical turn-on field, which produces a current density of 10 μA/cm^2, is ~1.8 V/μm, while the emission current density of 1 mA/cm^2 requires an applied field of ~2.74 V/μm. The small turn-on field is consistent with literature data of 1.5-2 V/μm observed in CVD-grown dense CNT films [216]. At an electric field of 3.4 V/μm, the assembled CNT field emitters emit a current density of 5 mA/cm^2, which is a remarkably large value considering the distance between cathode and anode. A plot of ln(I/V^2) versus 1/V yields a straight line in a good agreement with the Fowler-Nordheim (FN) expression; this agreement demonstrates that the current originates from field emission (i.e. field emission process) [217, 218]. Furthermore, the quality of fitting to the Fowler-Nordheim expression implies good nanotube/substrate electrical contact [219]. Finally, these observations clearly show an additional advantage to CNT transfer technology: a very small voltage drop can be achieved along CNT/substrate interfaces. The slope of the FN plot can be used to calculate the field enhancement factor β. The Fowler-Nordheim equation can be written as [219]:

$$I = A\frac{1.42\times10^{-6}}{\phi}\beta^2(\frac{V}{d})^2\exp(\frac{10.4}{\sqrt{\phi}})\exp(-\frac{B\phi^{1.5}d}{\beta V}) \qquad \textbf{Equation 4.1}$$

where I is the emission current (A), A the emission areas (m^2), V applied voltage, d the distance between CNT tips and anode (m), ϕ the work function (eV), and B constant (6.44×10^9, VeV$^{-1.5}$m^{-1}). When ln(I/V^2) is plotted versus 1/V, the slope of this linear formulation is given by $-B\phi^{1.5}d/\beta$. Assuming that the work function is 5.0 eV, the

derived field enhancement factor is calculated to be 4540, which is sufficient for application in field emission displays.

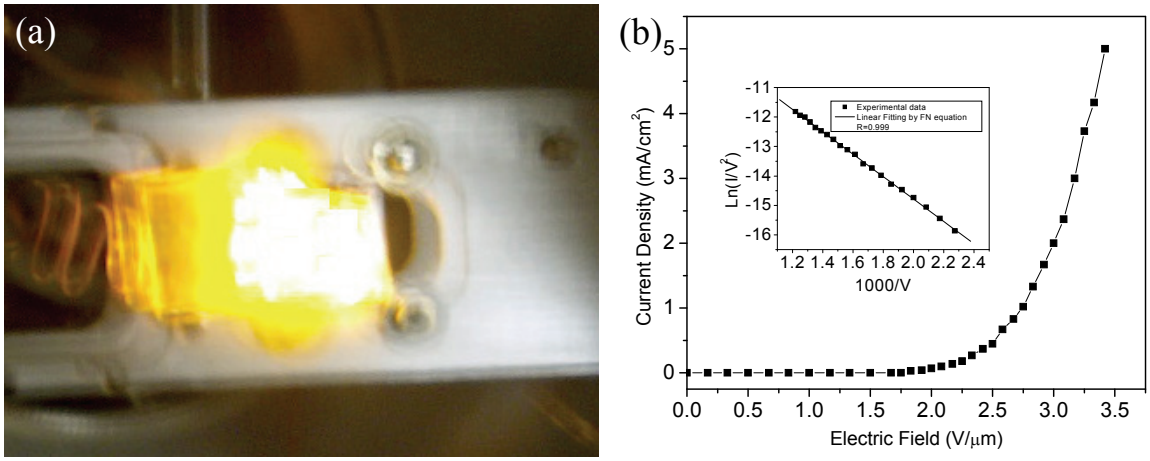

Figure 4.3 (a) Emission pattern of the as-assembled CNTs by applying electrical field of 3.0 V/μm. (b) Field emission measurements of CNT films in (a) at room temperature. The inset shows a Fowler-Nordheim plot, which indicates that the transferred CNTs demonstrate good field emission characteristics.

4.3.3 Electrical Characterization of CNT Assembly

CNT films or stacks were assembled on copper substrates by CNT transfer technology. Figure 4.4a shows that double-layered CNT stacks could also be assembled onto a copper substrate by CNT transfer process; the height of CNT layer 1 and layer 2 is 185 and 223 μm, respectively. The CNT areal density is estimated to be 300 μm^{-2} by counting the number of the catalyst particles formed after a 3 nm Fe film is agglomerated into small islands by heat treatment at 750 °C. Observation of the junctions between the CNT stacks reveal that the CNTs at the interfaces are entangled at a length scale of 200 nm, as shown in Figure 4.4b. However, the individual stacked films are only loosely bound to each other and therefore can be easily peeled apart. By the same process, three-layered CNT stacks can also be assembled onto copper substrates.

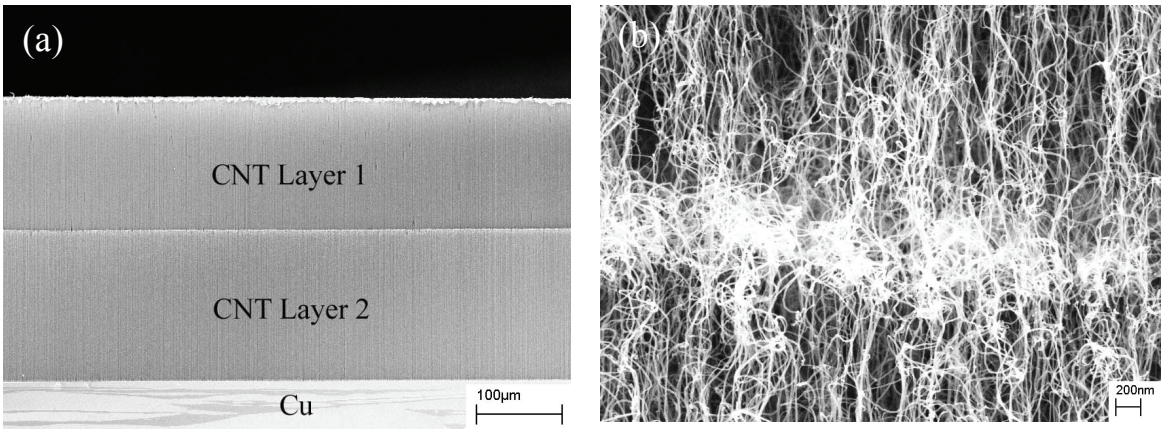

Figure 4.4 (a) Cross-sectional SEM image of well-aligned double-layered CNT stack transferred onto a copper substrate; and (b) CNT stack junctions between two CNT films.

We measured the electrical properties of single-layer CNT film (~180 μm) assembled on copper substrate. The bottom electrodes (Cu) are already suitable for electrical testing, since the CNTs have been connected by Sn-Pb eutectic solder after the reflow process. In order to investigate the performance of the bottom CNT-metal contact, the top electrodes are established by DC-sputtering Ti (20 nm)/Au (400 nm) onto the CNT surfaces through metal masks with openings of 2 mm diameter. Penetration of gold through the densely-packed CNT films is highly improbable. Indeed, SEM examinations of the top electrodes confirm that gold only penetrates into the CNT films ~100 nm. In addition, the CNT film height is ~180 μm; therefore, the two electrodes are separated by the CNTs. To eliminate the resistance contribution from the testing probes and wires, four-probe measurements have been implemented.

Figure 4.5 shows a typical I-V curve of the as-assembled CNT structures measured at room temperature. The I-V curve is linear, suggesting that the electrical transport and the contacts are ohmic. From the I-V curve, the resistance of a compact CNT bundle with diameter 2 mm is 0.0056 Ω. The total resistance can be written as R=R1+R2+R3, where R1 is the resistance of the top electrode-CNT junction resistance, R2 is the resistance of the CNTs, and R3 is the resistance of the CNT-solder junctions. Due to lack of data of the contact resistance between CNTs and solders, we

conservatively estimate the CNT resistivity by neglecting R1 and R3. From the areal density of the as-grown CNTs (300/μm^2), there are ~942 million CNTs in an area of diameter 2 mm. Thus, the 0.0056 Ω resistance corresponds to total resistance of 942 million parallel CNTs. Transmission electron microscscope (TEM) studies have shown that the average CNT diameter is ~10 nm. Therefore, the resistivity of the individual CNTs is estimated to be ~2.3×10^{-4} Ω-cm. This number is consistent with literature reports of CNT resistivity measurements [169]. However, considering the dependence of CNT resistivity on the CNT length [220], this value is very small compared to the resistivity of short CNTs (<10 μm). The measured low resistance of our long CNTs can be attributed to the following considerations. First, good electrical contact between CNTs and solders is formed by the transfer process; achievement of good contacts is a prerequisite for CNT applications in electronic devices. Second, the open-ended CNTs assist electronic transport, since the internal walls of multi-walled CNTs can participate in electron transport. Thus, the electrical conductance of CNTs can be improved by opening CNT ends; in fact, our CVD process produces open-ended CNTs by water selective etching during CNT growth. As a result, each wall of the CNTs is contacted by solder and thus is effectively connected to the electrodes due to the transfer process; this process achieves an end-contact geometry, which offers a generic contact configuration for the study of electrical transport in multi-walled CNTs.

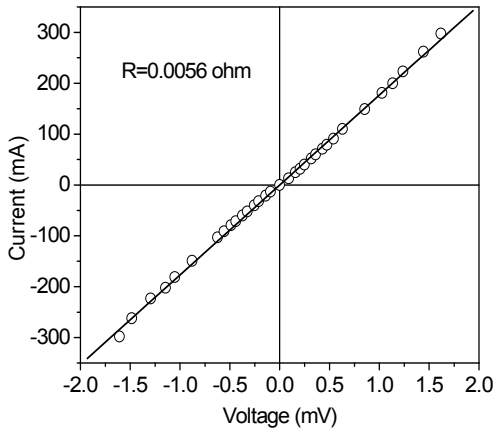

Figure 4.5 I-V curve of the assembled CNTs measured at room temperature.

The electrical transport through the junctions (interfaces) between stacked CNT films is also of interest, since previous studies focused on electrical measurements of junctions made by individual CNTs [221, 222]. By an analogous process to that for the single layer CNT films, the double- and triple-layered CNT films were assembled onto copper substrates. Figure 4.6 shows a typical I-V characteristic of the as-assembled double- and triple-layered CNT stacks measured at room temperature. The linear I-V curves indicate excellent CNT-solder interfacial properties, and ohmic contact behavior between CNT stack junctions. Such behavior is surprising, since as shown in Figure 4.4b, the junctions are composed of nanoscale entanglements or crossed CNTs. The resistance of double-layered CNT stacks is 0.2996 Ω with individual layer heights of 185 and 223 μm, respectively, while the resistance of triple-layered CNT stacks reaches 0.5544 Ω with individual CNT layer heights of 220, 190, 145 μm, respectively. As described above, in a contact area of 0.0314 cm^2, there are ~942 million pairs of entangled CNTs. From comparison of the resistances measured for the single-, double- and three-layered CNT films, the specific contact resistance of the CNT stack junctions is estimated to be 9.01×10^{-3} Ω-cm^2. Thus we estimate the junction resistance of individual entangled CNT pairs to be 2.7×10^{8} Ω, or a conductance G of 3.7 nS; this junction conductance is much lower than the quantum conductance unit of $4e^2/h$ (153.8 μS). Using this value, we can determine the probability of an electron at the junction in one CNT, tunneling through the entangled CNTs into the attached CNT. The measured conductance G corresponds to a transmission probability for the junction of $T_j=G/(4e^2/h)=2.41\times10^{-5}$. Apparently, these junctions are not efficient tunnel contacts. However, we can consider the effect of the distance between individual CNTs in the junction (entangled) region on the transmission probability in order to compare this value with that from previous studies. Previous work has reported $T_j\approx2\times10^{-4}$ for two straight CNTs separated by a van der Waals distance of 0.34 nm; this probability increases to 0.004 only when the mechanical and attractive forces between CNTs and substrate deform the contact region [221]. Due to the CNT

stack formation characteristics in our studies, there should not be strong CNT-substrate (copper) interactions, nor should the CNT contact regions be deformed by external mechanical forces. Also, our CNT junctions are formed by entanglements and close spacing of CNT ends (at the junction region), which differs from previous studies that used the crossing of straight CNTs to measure resistance and conductance [221, 222]. At the CNT ends, more defects, buckles or kinks are expected, which can form intramolecular junctions known to reduce the electrical conductance and decrease the transmission probability [86].

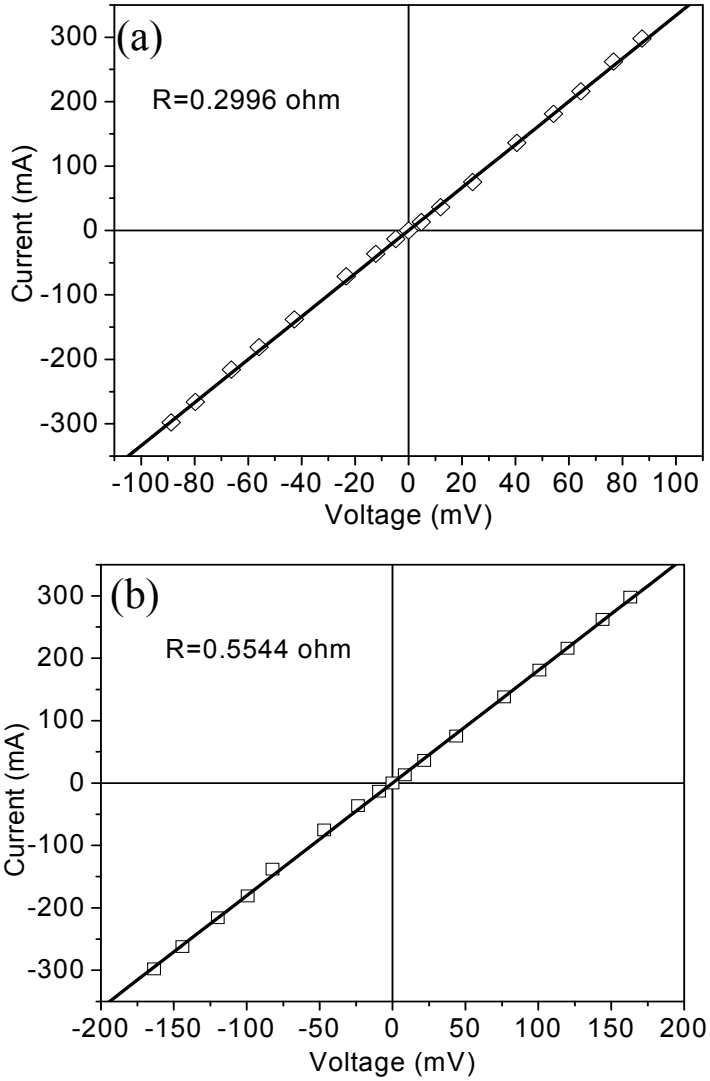

Figure 4.6 I-V curves of the assembled (a) double-layered and (b) three-layered CNT stacks measured at room temperature.

4.4 Assembly of Fine-Pitch CNT Bundles

4.4.1 Fine-Pitch CNT Bundle Growth

By using a lift-off process, a patterned layer of Fe catalyst can be formed on a substrate for the CVD growth of aligned CNT bundles (details in Chapter 2.2). Aligned CNTs grow readily from catalyst patterns into well-defined vertical structures, as shown in Figure 4.7; CNT growth conditions were 730 °C for 3 min. The SEM image demonstrates that essentially vertically-aligned CNT arrays can be formed on a substrate without entanglement with neighboring bundles. The CNT bundles are fine-pitched structures with diameter, aspect-ratio and pitch of 25 μm, 4, and 80 μm, respectively. The ability to grow aligned nanotube arrays with excellent CNT length control indicates that this process should be feasible for electronic device interconnect fabrication.

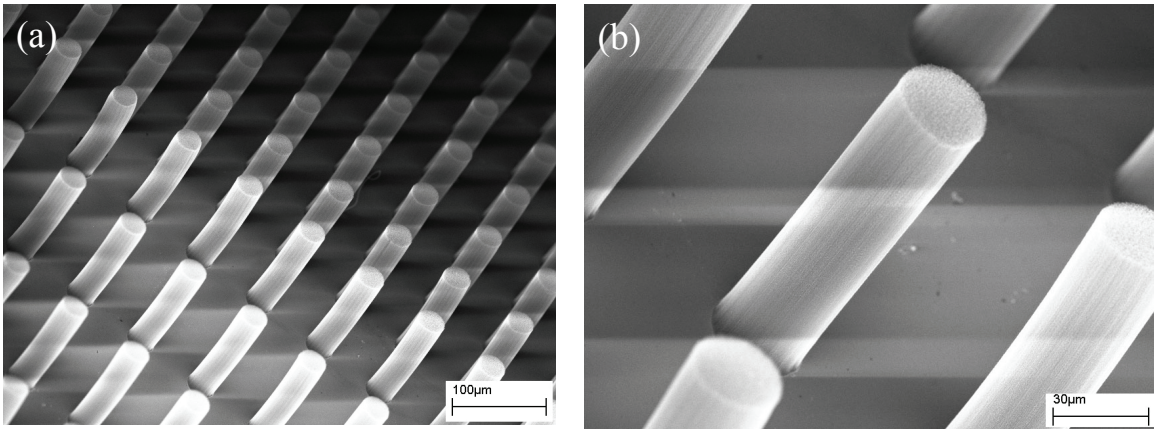

Figure 4.7 (a) SEM image of aligned CNT bundles grown on a silicon substrate with size, aspect ratio, and pitch of 25, 4, and 80 μm, respectively; (b) higher magnification SEM image of (a).

The relatively small amount of water added to the deposition atmosphere and the termination of the ethylene flow at the end of the deposition cycle etches the ends of the nanotubes because a higher number of defects and thus a high reactivity with an oxidant exist at the ends of the nanotubes [215]. Compared to post deposition nitric acid etching,

in-situ water etching of the CNT caps results in less damage to the tubular CNT wall structures [223].

4.4.2 CNT Bundle Assembly by CNT Transfer Process

We use CNT transfer process to assemble CNT bundles onto copper substrates. As shown in Figure 4.8, a eutectic tin-lead paste is stencil-printed on the copper substrate. The silicon substrates with CNT bundles are flipped and aligned to the corresponding copper substrates, and reflowed in a seven-zone BTU reflow oven to simultaneously form electrical and mechanical connections.

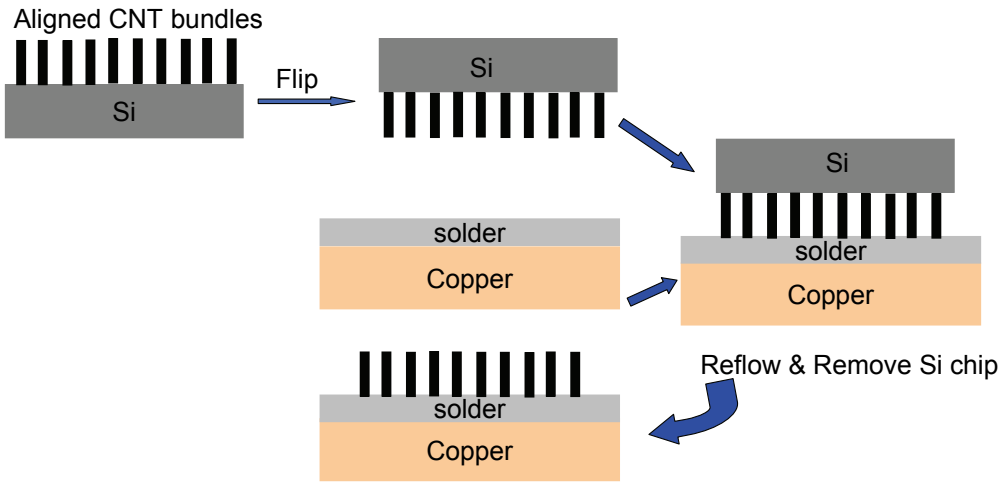

Figure 4.8 Schematic diagram of the "CNT transfer technology" for assembling fine-pitch CNT bundles.

This process can overcome limitations that currently exist in the integration of CNTs into integrated circuits and microelectronic device packages by offering low process temperatures and improved adhesion of CNTs to substrates. Figure 4.9 shows the result of transferring the CNT bundles shown in Figure 4.7 onto a copper substrate. Clearly, the CNT bundle structures remain intact after transfer with respect to the bundle size, aspect ratio, and pitch.

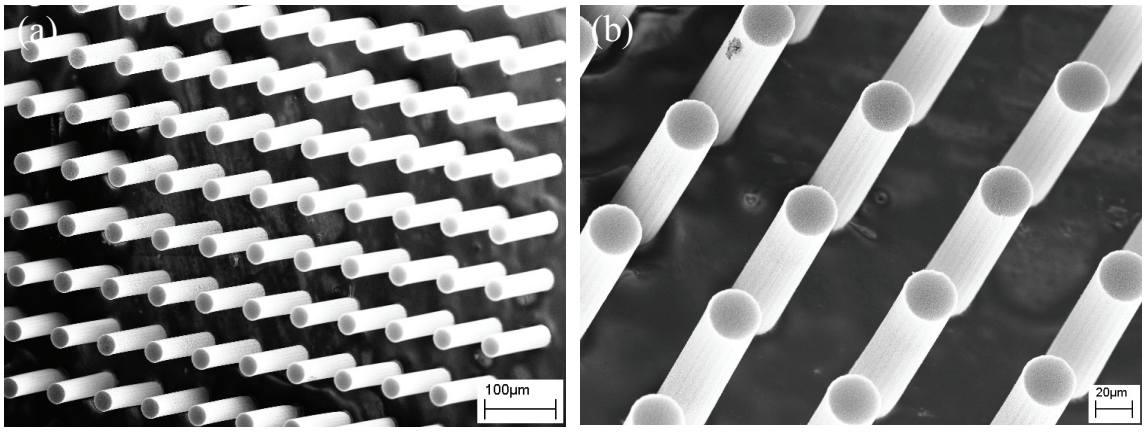

Figure 4.9 (a) SEM image of the CNT bundles in figure 1 transferred onto a copper substrate; (b) an enlarged SEM image showing the assembled CNT bundles on the copper substrate.

For fine-pitch CNT bundle assembly, it should be noted that the amount of flux applied on the solder before reflow process must be well controlled. For effective soldering, solder surfaces must be free from oxide. Flux is used to chemically remove the thin oxide layer from the solder surface to facilitate solder wetting. If an excess of flux is applied, capillary forces cause the flux to diffuse into the CNT bundles during the reflow process, since the flux (an organic reagent) has a lower surface tension than water, and so wets the nanotube walls [224]. This results in bundle shrinkage as the individual nanotubes are drawn closer together, as shown in Figure 4.10. The CNT bundle surfaces show irregular morphologies, although the bundles remain vertically-aligned.

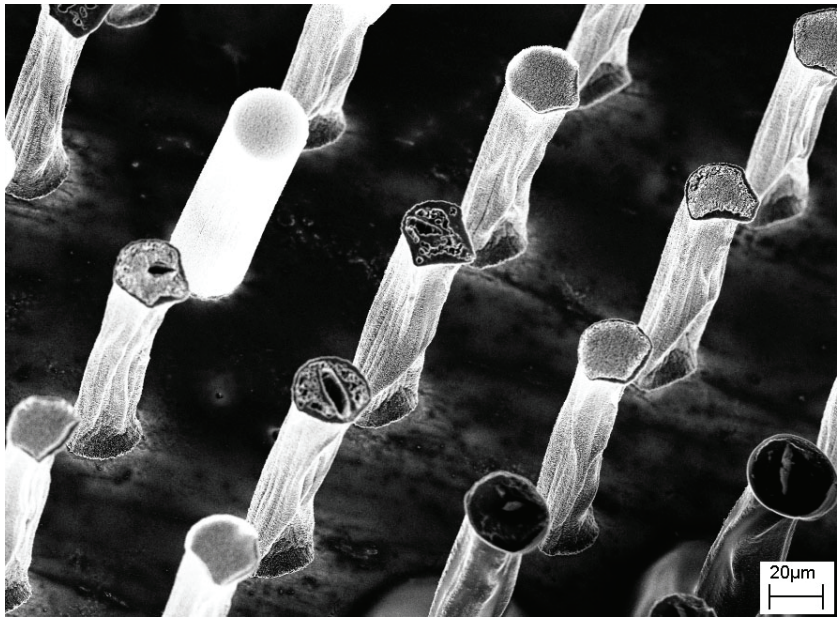

Figure 4.10 Shrinkage of CNT bundles after solder reflow due to capillary forces caused by wetting of the CNT bundles by excess flux.

4.5 CNT/Solder Interfaces

We ascribe the good electrical properties of the CNT assembly to the effective contacts formed by the CNT/solder interfaces. One prerequisite for excellent contacts is that during reflow, the solder should form a strong mechanical bond to the CNTs. To qualitatively demonstrate the bonding strength of the CNTs on a copper substrate that results from the solder reflow process, a section of the assembled CNTs was pulled from the surface using tweezers. Figure 4.11a shows the demarcation between the broken CNTs and the intact and connected ones. When pulled from the substrate, the CNTs break along the axis rather than at the CNT-solder interface, as shown in Figure 4.11b. The high mechanical bonding strength of CNTs on the substrate securely attaches the CNTs and thereby guarantees excellent electrical performance of the entire CNT assembly.

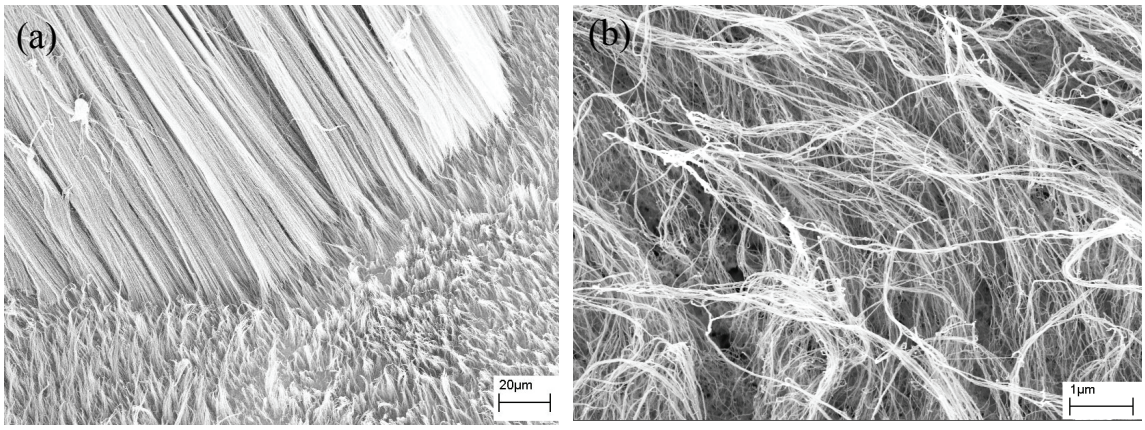

Figure 4.11 (a) A copper substrate on which CNTs were assembled after a portion of the CNTs were pulled from the surface by tweezers; (b) the bottom ends of the broken CNTs that were still anchored on the copper substrate as a result of the solder reflow process.

4.6 Summary

In this Chapter, CNT transfer process was proposed to assemble aligned CNT structures at a low temperature that is compatible with current microelectronics fabrication sequences and technology. The distinctive CNT-transfer-technology features are separation of CNT growth and CNT device assembly. Field emission testing of the as-assembled CNT devices indicates good field emission characteristics, with a field enhancement factor of 4540. The testing results are in agreement with the Fowler-Nordheim expression, which implies good electrical contact between CNTs and solder, and a very small voltage drop across CNT/solder interfaces. We also successfully applied the CNT transfer technology method to assemble fine-pitch CNT bundles with diameter, aspect-ratio and pitch of 25 μm, 4 and 80 μm, respectively, onto a copper substrate. SEM observations indicate that the excellent mechanical bonding strength of solder in contact with the CNTs anchors them securely onto the substrate. Preliminary electrical transport measurements of CNT films, as well as double- and triple-layered CNT stacks assembled onto copper substrates by CNT transfer technology have been performed. The measured resistivity of long CNTs (>150 μm) is ~2.3×10^{-4} Ω-cm. These measurements also

demonstrate that low-resistance ohmic CNT/solder (Sn-Pb) junctions can be formed by a solder reflow process, which offers an effective approach to integrate or assemble CNTs with integrated circuits at low temperatures. These studies also show that CNT stack junctions, formed by entanglement or crossing of CNTs at the interfaces at a length-scale of 400 nm, can form ohmic contacts with a specific contact resistance of 9.01×10^{-3} Ω-cm^2 and a transmission probability (T_j) of 2.41×10^{-5}. Overall, the advantages of CNT transfer technology are embodied in the low process temperature, adhesion improvement and the feasibility of transferring CNTs to different substrates. CNT transfer technology, enabled by open-ended CNTs, shows promising applications for positioning of CNTs on temperature-sensitive substrates, and for the fabrication of field emitters, electrical interconnects, thermal management structures in microelectronics packaging.

CHAPTER 5

WETTING ON CARBON NANOTUBE STRUCTURES

Superhydrophobic surfaces are getting a new attention from academia to industry, due to the broad potential applications of such surfaces. It was known that the surface roughness, stemming from the combined effects of micro- and nano-meter scale surface structures, is necessary for making the superhydrophobic surfaces. However, we still don't know the dependence of contact angle and its hysteresis on the combined effects of micro- and nano-meter scale roughness on superhydrophobicity; such studies will be valuable to design stable superhydrophobic surfaces. In this chapter, we present the method of forming controllable surface roughness, enabled by controlled growth of aligned CNTs, to study the effect of surface geometries on the superhydrophobicity, and to reveal subtle effects of nano-meter scale roughness on the contact angle hysteresis. Then we conducted an initial electrowetting study of aligned CNT film with aim to offer an alternative method to improving wetting of some high surface tension liquids on the low surface energy CNT walls/films.

5.1 Superhydrophobicity

Wettability of solid surfaces with a liquid is of great importance in fundamental research and practical applications of adhesion [225]. Wettability is governed by the surface chemistry of the solid and liquid phases and the geometrical roughness of the solid surface [226]. The roughness of a hydrophobic solid enhances its hydrophobicity [227-233]. The contact angle of water on the flat solids is typically around 100-120°, however, the contact angle of water reaches the values as high as 160-175° if the solid surfaces are rough or microtextured. Thus, surface roughness on a hydrophobic solid can enhance the hydrophobicity relative to that achieved by surface chemistry alone.

Two classical models have been developed to explain this effect. The Wenzel model is described by

$$\cos\theta_W = r\cos\theta_e \qquad \textbf{Equation 5.1}$$

where θ_W and θ_e are the Wenzel apparent contact angle and the Young contact angle, and r is the roughness ratio, defined as the ratio of the actual area of the solid surface to the projected area on the horizontal plane [228]. In this model, the drop wets the entire contact solid surface area, as shown in Figure 5.1a. The Wenzel equation states the apparent contact angle θ_W of the drop on the rough surfaces is related to Young contact angle on the smooth surfaces. A value of $r > 1$ describes the solid roughness. Wenzel equation thus states that wettability is improved by surface roughness for a hydrophilic surface ($\theta_W < \theta_e$ for $\theta_e < 90^o$), but gets worse for a hydrophobic surface ($\theta_W > \theta_e$ for $\theta_e > 90^o$). The other model is the Cassie model [227]. In this scenario, air is trapped beneath the drop, i.e. the water drop does not fill the grooves on the rough surface, as shown in Figure 5.1b. This model can be described as

$$\cos\theta_C = \phi_s\cos\theta_e + \phi_s - 1 \qquad \textbf{Equation 5.2}$$

where θ_C is Cassie apparent contact angle and ϕ_s is the fraction of the projected area of the solid surface that is wetted by the liquid. For a very rough surface, for which ϕ_s tends to be zero, θ_C will tend to be 180°. In the Cassie state, the contact angle hysteresis is low.

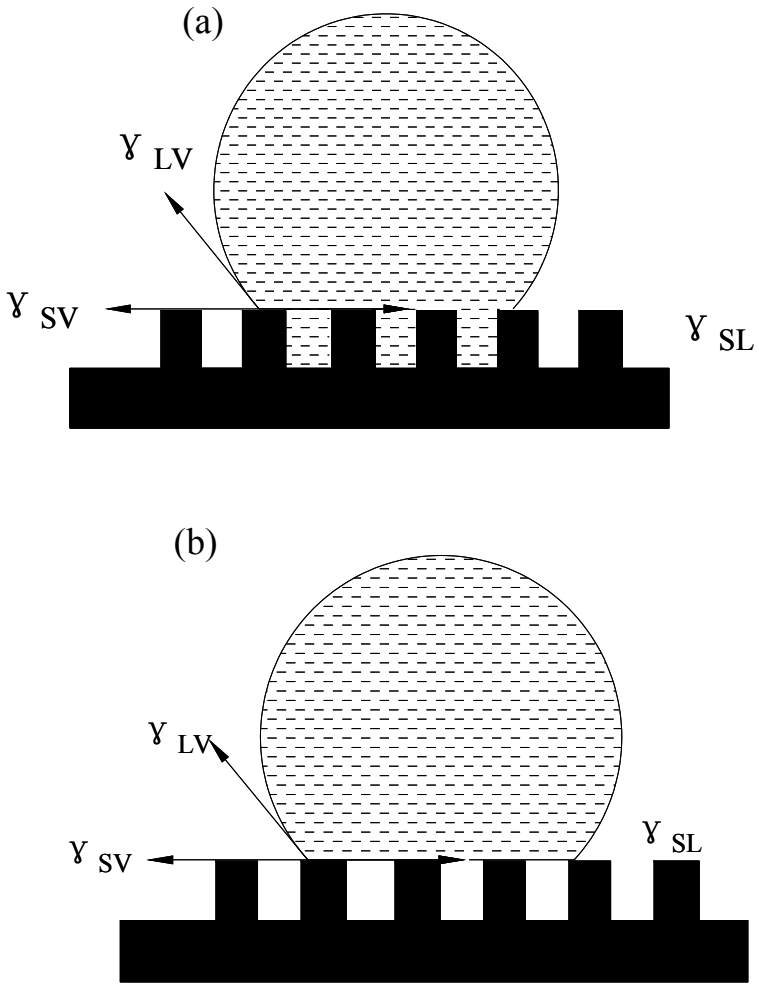

Figure 5.1 Effect of surface roughness on hydrophobicity: (a) homogeneous wetting, and (b) heterogeneous wetting.

5.1.1 Lotus Effect Surfaces

Some plant leaves, e.g. Lotus leaves, demonstrate superhydrophobicity and self-cleaning properties (cleaned by water droplets). Initial studies of this phenomenon revealed that the two-tier roughness (on both the micro- and nano-meter scales, as shown in Figure 5.2), together with its waxy surface chemistry, assists the maintenance of a clean leaf surface [234]. Such leaves are called superhydrophobic, i.e., the water droplets form spheres on such leaves with very little adhesion to the surface, and thus roll off very quickly even at a very mall sliding angle. This recognition is of technical importance for

applications such as medical implants, biological systems, microfluidics, aerospace vehicle coatings, and household commodities [235]. Superhydrophobic surfaces display very high contact angles (>150°) and low contact angle hysteresis (<10°) [230, 231, 236, 237]. These two features are necessary to create so-called self-cleaning surfaces. Water droplets as well as dirt particles only lie on the tips of the surface structures with a roughness on the micro- and nano-meter scales [237]. Therefore, the dirt or contamination particles develop low adhesion forces to such roughness surfaces, and can be removed easily by water droplets. Currently, the self-cleaning characteristics of superhydrophobic surfaces are termed “Lotus Effect”.

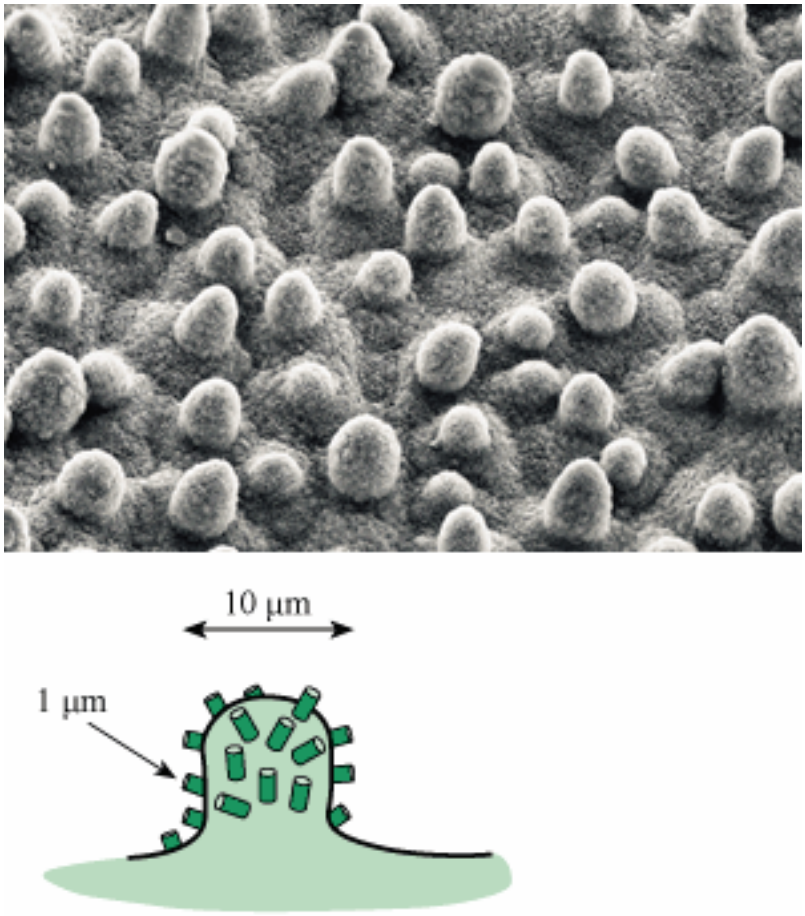

Figure 5.2 Microstructure of the lotus leaf.

5.1.2 Energy Analysis of Droplet on Rough Surfaces

The determination of the equilibrium states of a droplet on a rough surface is a minimization of the Gibbs energy of the system [231]. In the minimization of the Gibbs energy of a drop on a smooth and homogeneous solid surface, the only independent variable is the contact angle. In contrast, the case of a rough surface needs to be described by two independent parameters: the apparent contact angle and ϕ_s (the fraction of the projected area of the solid surface that is wetted by the liquid). In general, the change of the Gibbs energy of the rough solid surface, in which the droplet is on a rough surface, is presented by

$$G = A_{LV}\gamma_{LV} + A_{SL}\gamma_{SL} + A_{SV}\gamma_{SV} - A_{tot}\gamma_{SV} \qquad \textbf{Equation 5.3}$$

where γ_{LV}, γ_{SL}, and γ_{SV} are the interfacial tensions of the liquid/vapor, solid/liquid, and solid/vapor interfaces, respectively, A_{LV}, A_{SL}, and A_{SV} are the interfacial area of the liquid/vapor, solid/liquid, and solid/vapor interfaces, respectively, and A_{tot} is the total area of the rough solid surface before wetting of the liquid. The liquid/vapor interfacial area consists of two parts, the interface of the spherical cap and the liquid/vapor interface within the grooves:

$$A_{LV} = 2\pi R^2(1-\cos\theta) + (1-\phi_s)\pi R^2\sin^2\theta \qquad \textbf{Equation 5.4}$$

where R is the radius of the spherical cap, and θ is the apparent contact angle of the droplet on the rough surface. The solid/liquid interfacial area is given by

$$A_{SL} = r_{\phi_s}\phi_s\pi R^2\sin^2\theta \qquad \textbf{Equation 5.5}$$

where r_{ϕ_s} is the roughness ratio of the wet area. The change of solid/vapor interfacial area, $A_{SV} - A_{tot}$, is given by

$$A_{SV} - A_{tot} = (1-\phi_s)r_{1-\phi_s}\pi R^2\sin^2\theta - r\pi R^2\sin^2\theta \qquad \textbf{Equation 5.6}$$

where $r_{1-\phi_s}$ is the roughness ratio of the unwetted area. Thus the change of the Gibbs energy is expressed by

$$G = [2\pi R^2(1-\cos\theta) + (1-\phi_s)\pi R^2 \sin^2\theta]\gamma_{LV} + (r_{\phi_s}\phi_s \pi R^2 \sin^2\theta)\gamma_{SL} + [(1-\phi_s)r_{1-\phi_s}\pi R^2 \sin^2\theta - r\pi R^2 \sin^2\theta]\gamma_{SV} \quad \textbf{Equation 5.7}$$

The roughness ratios of the wet and unwetted area are correlated by

$$r_{\phi_s}\phi_s + (1-\phi_s)r_{1-\phi_s} = r \quad \textbf{Equation 5.8}$$

By arrangement,

$$\frac{G}{\pi\gamma_{LV}} = R^2[2 - 2\cos\theta - (\phi_s r_{\phi_s}\cos\theta_e + \phi_s - 1)\sin^2\theta] \quad \textbf{Equation 5.9}$$

where $\cos\theta_e = \frac{\gamma_{SV} - \gamma_{SL}}{\gamma_{LV}}$ (Young's equation) **Equation 5.10**

The drop radius is related to its volume by

$$R^2 = (\frac{3V}{\pi})^{2/3}(1-\cos\theta)^{-4/3}(2+\cos\theta)^{-2/3} \quad \textbf{Equation 5.11}$$

Then

$$\frac{G}{\pi^{1/3}\gamma_{LV}(3V)^{2/3}} = (1-\cos\theta)^{-4/3}(2+\cos\theta)^{-2/3}[2 - 2\cos\theta - (\phi_s r_{\phi_s}\cos\theta_e + \phi_s - 1)\sin^2\theta] \quad \textbf{Equation 5.12}$$

Let

$$\mathrm{K}(\theta) = (1-\cos\theta)^2(1-\cos\theta) \quad \textbf{Equation 5.13}$$

$$\Phi(\phi_s) = \phi_s r_{\phi_s}\cos\theta_e + \phi_s - 1 \quad \textbf{Equation 5.14}$$

Then

$$\frac{G}{\pi^{1/3}\gamma_{LV}(3V)^{2/3}} = \mathrm{K}^{-2/3}(\theta)[2 - 2\cos\theta - \Phi(\phi_s)\sin^2\theta] \quad \textbf{Equation 5.15}$$

The equation 5.15 shows the relationship between the Gibbs energy and the droplet contact angle and surface roughness. From thermodynamics point of view, the

final equilibrium state should be such that G is minimized. To get the local extrema, we conduct the first partial derivative:

$$\frac{\partial}{\theta}\left(\frac{G}{\pi^{1/3}\gamma_{LV}(3V)^{2/3}}\right)\Big|_{V,r\phi_s} = -\frac{2}{3}\mathrm{K}^{-5/3}(-3\cos^2\theta\sin\theta + 3\sin\theta)[2 - 2\cos\theta - \Phi\sin^2\theta]$$
$$+ K^{-2/3}(2\sin\theta - 2\Phi\sin\theta\cos\theta)$$
$$= 2K^{-5/3}\sin\theta(\Phi - \cos\theta)(1 - \cos\theta)^2$$

Equation 5.16

To make $\frac{\partial}{\theta}\left(\frac{G}{\pi^{1/3}\gamma_{LV}(3V)^{2/3}}\right)\Big|_{V,r\phi_s} = 0$ **Equation 5.17**

$\cos\theta = 1$ or $\Phi = \cos\theta$, i.e.,

$$\cos\theta = \phi_s r_{\phi_s}\cos\theta_e + \phi_s - 1 \qquad \textbf{Equation 5.18}$$

Since $0 < \theta < \pi$,

only the condition, $\cos\theta = \phi_s r_{\phi_s}\cos\theta_e + \phi_s - 1$, is satisfied to get the local equilibrium state.

In equation 5.18, when $\phi_s = 1$, $r_{\phi_s} = r$, $\cos\theta = r\cos\theta_e$, which corresponds to the Wenzel equation; when $r_{\phi_s} = 1$, $\cos\theta = \phi_s\cos\theta_e + \phi_s - 1$, which corresponds to the Cassie equation.

5.2 Superhydrophobicity Study on Two-Tier Rough Surfaces

Many reports have been published on the fabrication and modeling of superhydrophobic surfaces. For instance, photolithography has been used to pattern a silicon surface to achieve micro-scale surface roughness [238]; in these studies, the silicon surfaces were hydrophobized using silanization reagents. However, photolithography has limitations in the creation of nano-scale features. Specifically, the costs are high if e-beam lithography is utilized. Moreover, it is difficult to create micro-

and nano-scale roughness simultaneously due to the sequential photoresist development and film etching processes required. Plasma etching methods have been used to etch nano-scale roughness onto polymer substrates, although such processes are limited by the need to select an appropriate substrate. In several cases, aligned carbon nanotube (CNT) films were grown to serve as rough surfaces [239, 240]. For example, a stable, superhydrophobic surface was fabricated by the plasma-enhanced deposition of aligned CNTs which were subsequently coated with poly(tetrafluoroethylene) (PTFE) by hot filament CVD [239]. However, the contact angle hysteresis was still large ($\geq 10°$). Also, the effect of micro-scale roughness on contact angle was not established, since the substrate was just a flat CNT film. In addition, many publications report only the static contact angle or the advancing contact angle. A more complete characterization of surface wetting is provided if contact angle hysteresis is measured. Thus, more detailed studies of the dependence of contact angle and its hysteresis on the combined effects of micro- and nano-meter scale roughness on superhydrophobicity are needed; such studies will also allow comparison of experimental results with theoretical predictions and models.

5.2.1 Experimental Design

In this section, we describe the design and novel methods to create two-tier roughness model surfaces in a well-controlled manner. As such, we can compare the superhydrophobicity and contact angle hysteresis of these surfaces with those of micro-scale rough surfaces created by photolithography. A schematic describing surface roughness obtained by the methods investigated in this study is shown in Figure 5.3. Figure 5.3a is a control (silicon) surface fabricated by photolithography; Figure 5.3b is a schematic representation of CNT arrays grown on silicon wafers, which are denoted as model surface I, while Figure 5.3c represents model surface II, where nano-scale roughness exists in the CNT array grooves. The only difference between surfaces I and II

is the nano-scale roughness that exists in the CNT array grooves on surface II. These surfaces are coated with 20 nm fluorocarbon layers that have low surface energy and stabilize the CNT arrays. The unique formation process allows controlled variation in the CNT array size, pitch and height by altering process conditions. As a result, the effects of length scale of the double roughness parameters on hydrophobicity and contact angle hysteresis can be investigated. Also we will discuss the effects of geometric design on the stability of superhydrophobic surfaces.

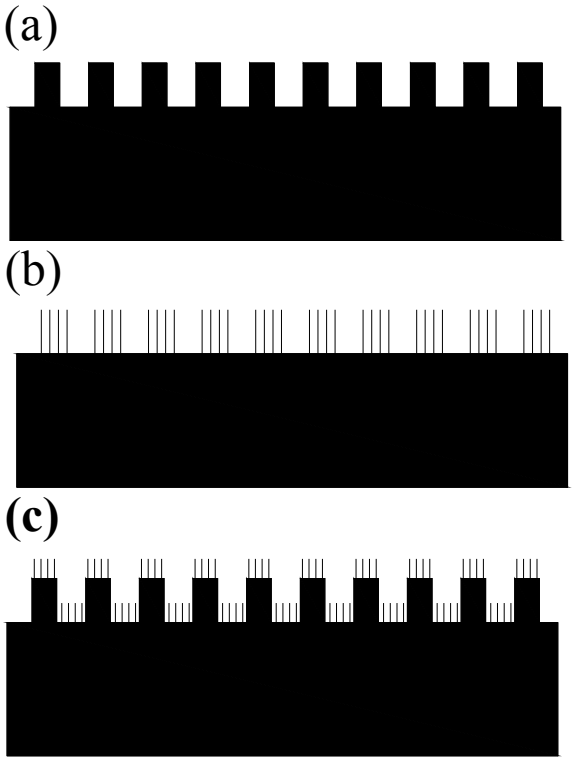

Figure 5.3 Schematic representations of (a) micro-scale roughness created by photolithography; (b) aligned CNT arrays that establish two-tier roughness; (c) aligned CNT films on patterned silicon surfaces.

Deposition of fluorocarbon films. A parallel-plate radio frequency (RF) plasma reactor was used to deposit fluorocarbon films from pentafluoroethane/argon mixtures [241]. RF power was applied to the upper electrode at 13.56 MHz. Substrates were placed on the lower grounded electrode whose temperature was regulated with a Syskon RKC temperature controller. Depositions were performed at a substrate temperature of

110 °C and a constant operating pressure of 1 Torr. Flow rates of pentafluoroethane and argon were 20 and 75 sccm, respectively, for all depositions. XPS spectra were collected using a Physical Electronics (PHI) Model 1600 XPS system equipped with a monochromator; the system used an Al Kα source (hν = 1486.8 eV). Ejected photoelectrons were detected by a hemispherical analyzer that provided high sensitivity and resolution. The operating pressure in the sampling chamber was below 5×10^{-9} Torr. All high resolution spectra were collected with a pass energy of 11.75 eV. The step size and time step were chosen to be 0.025 eV and 100 ms, respectively. XPS analyses of the deposited films indicated that the fluorine-to-carbon (F/C) ratio was ~1.1, suggesting extensive cross-linking in the polymer layer. The deposition time for a 20 nm fluorocarbon film was ~20 seconds.

Preparation of control surfaces. A positive photoresist, AZ4620 (from Clariant Inc), was spin-coated onto a silicon substrate, the photoresist exposed to UV light and developed. An Inductively Coupled Plasma (ICP) reactor using SF6 at 10 mTorr was used to anisotropically etch silicon patterns to the desired depth. Subsequently, the photoresist was stripped in acetone. A 20 nm fluorocarbon film was deposited onto the patterned Si substrate.

Preparation of model surface I. A lift-off process was used to pattern catalyst islands of Al2O3/Fe whose size is the same as that of the silicon array. A thin layer of photoresist (Shipley 1813) was spin-coated onto a silicon substrate coated with SiO_2 (400 nm) formed by thermal oxidation or plasma-enhanced CVD, exposed to UV light and the pattern developed. The catalyst layers of Al_2O_3 /Fe were then deposited onto the substrate by a sequential electron-beam evaporation process. The photoresist was removed with an acetone rinse and the wafer was subsequently cleaned using acetone, isopropyl alcohol and de-ionized (DI) water rinses. Aligned CNT growth by CVD was performed at 700-800 °C with ethylene (110 sccm) as the carbon source. After CNT

growth, a 20 nm fluorocarbon film was deposited over the entire substrate to complete the formation of stable superhydrophobic surfaces.

Preparation of model surface II. First, patterned silicon substrates were fabricated by the procedures described in the preparation of control surfaces. Then aligned CNT films were grown on the entire surface, as described for the preparation of model surface I. Finally, 20 nm fluorocarbon films were deposited over the entire substrate.

Contact angle and hysteresis measurements. Contact angle measurements were performed using a Ramé-Hart telescopic goniometer with a computer-controlled automatic liquid deposition system. Dynamic advancing (θ_{Adv}) and receding angles (θ_{Rec}) were recorded while the probe fluid was added to and withdrawn from the drop, respectively. Contact angles were measured at five different locations on each sample; average values are reported below. The contact angle variability is small (within 1°). Scanning electron microscope (SEM) images were obtained with a JEOL 1530 equipped with a thermally assisted field emission gun operating at 10 keV. The array height of silicon and CNTs on the wafers was measured by SEM on the cross-sectional view.

5.2.2 Fabrication of Two-Tier Rough Surfaces

Two-tier rough model surfaces. Aligned cylindrical CNT arrays grow readily from the catalyst patterns into well-defined vertical structures, as shown in Figure 5.4, which shows representative SEM micrographs of CNT arrays with different pattern size, pitch and height. In Figure 5.4a, the height of the CNT arrays reaches 25 μm with an aspect ratio of 2, while in Figure 5.4c the height of the CNT arrays reaches 90 μm with an aspect ratio of 4.5. The shorter CNT arrays can be much easier to grow, shown in Figure 5.4b. Additional studies have demonstrated that CNT pillars maintain vertical growth up to an aspect ratio of 15. In the present investigations, we control CNT array height to be either ~4.5 μm or 10 μm to allow direct comparison with silicon patterns of similar array

sizes. Figure 5.4d shows a high magnification SEM image of the nanotube array surface, which confirms that the highly entangled CNTs form a nano-scale rough surface.

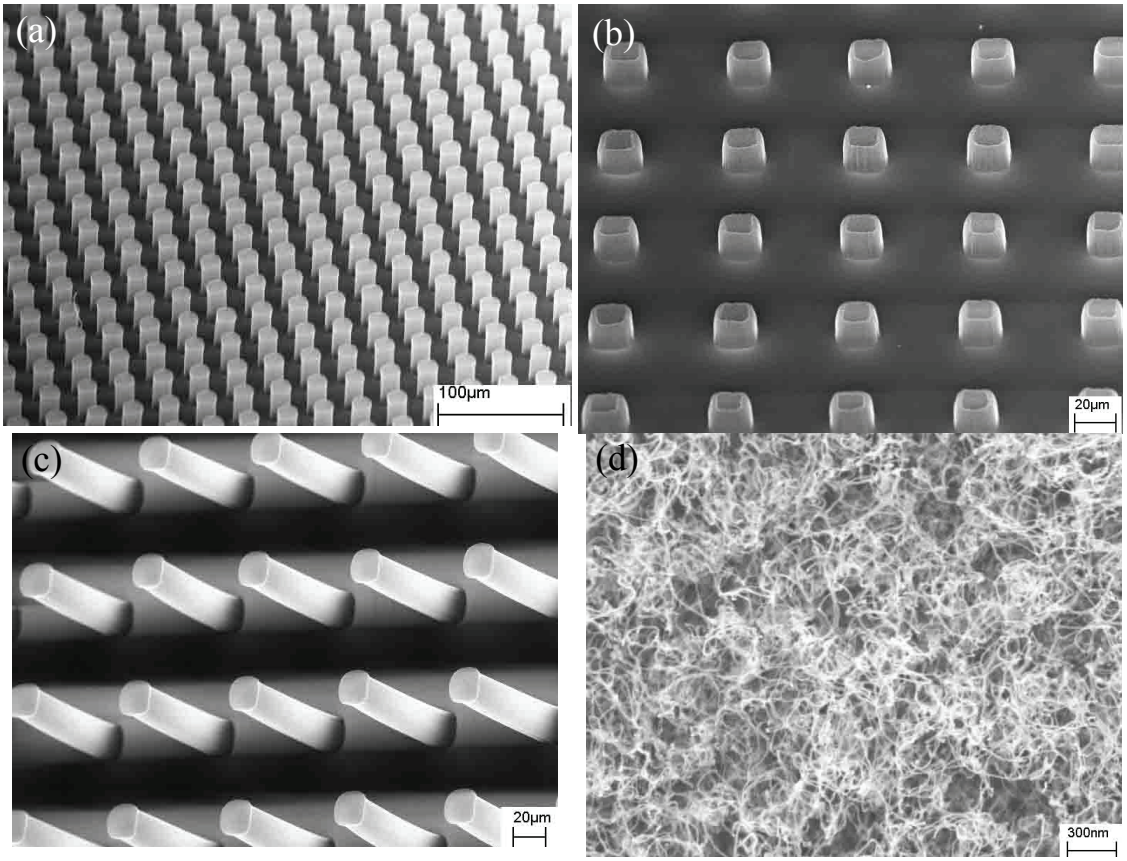

Figure 5.4 Typical SEM images of CNT arrays on silicon substrates: (a) cylindrical CNT arrays with 6 μm radius, 30 μm pitch, and 25 μm height; (b) cylinder CNT arrays with 10 μm radius, 60 μm pitch, and 11 μm height; (c) cylindrical CNTs arrays with 10 μm radius, 60 μm pitch, and 90 μm height; (d) as-grown CNT array surfaces.

Figures 5.5a, b show representative SEM images of model surface II, where the aligned CNT arrays are grown out of CNT films. Figure 5.5a shows the cylindrical CNT arrays with 6.5 μm radius, 60 μm pitch, and 4 μm height above the CNT films, while Figure 5.5b shows cylindrical CNT arrays with 6 μm radius, 30 μm pitch, and 9.5 μm height above the CNT films. Between the CNT arrays are nano-scale structures composed of aligned CNT film surfaces, as shown in Figure 5.4d. For comparison, Figures 5.5c, d show the control surfaces that have been patterned by photolithography

on silicon wafers. The microstructure sizes are the same as those of the CNT arrays, but the surface is flat.

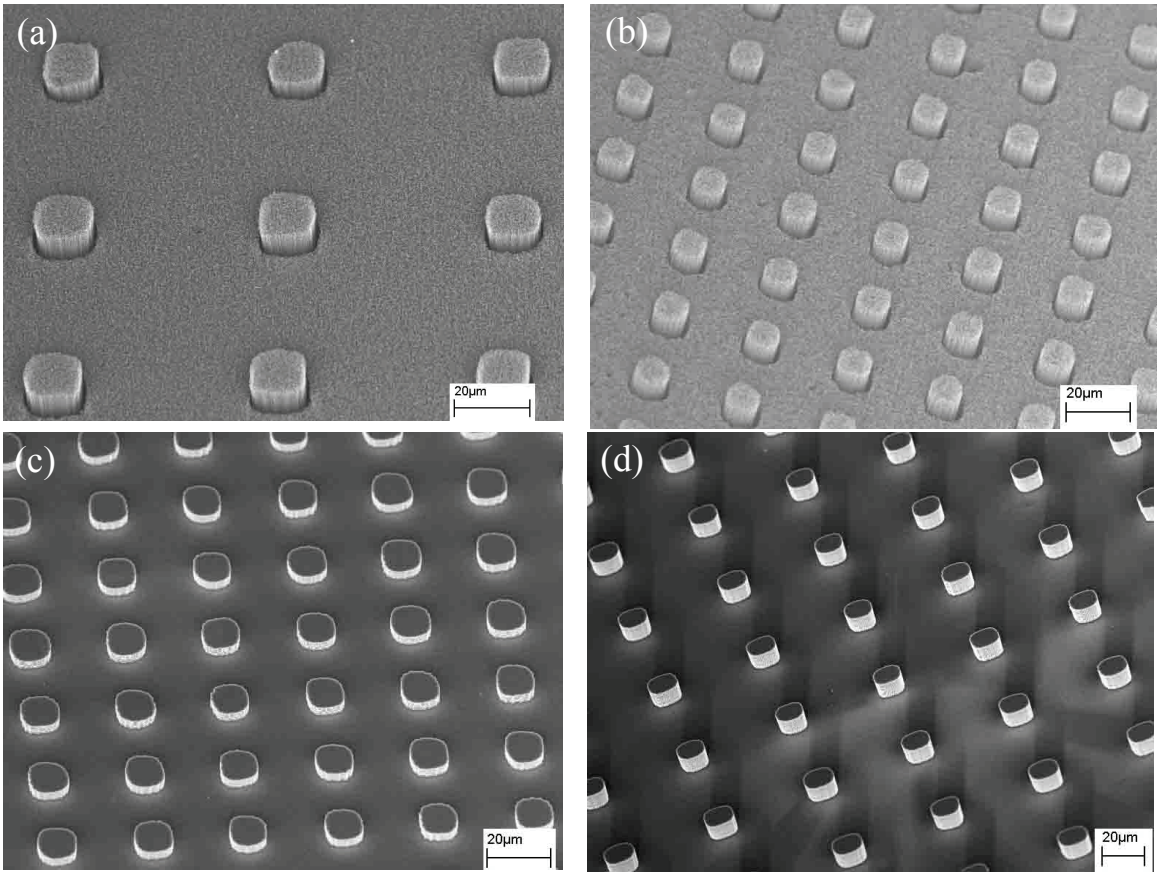

Figure 5.5 SEM images of CNT arrays above aligned CNT films: (a) cylindrical CNT arrays with 6 μm radius,60 μm pitch, and 4 μm height; (b) cylinder CNT arrays with 6 μm radius, 30 μm pitch, and 9.5 μm height. SEM images of cylindrical silicon arrays: (c) Si arrays with 6 μm radius, 30 μm pitch, and 4 μm height; (d) Si arrays with 6 μm radius, 60 μm pitch, and 9.5 μm height.

An important aspect of our CNT growth process is the specific growth mode observed, since the particular growth mode determines the surface morphology. Unlike the tip growth mode obtained by plasma-enhanced hot filament chemical vapor deposition, our CNTs grow by a base-growth mode; that is, the catalyst remains at the substrate surface, while the CNTs grow vertically away from the surface. With this mechanism controlling the growth, the aligned CNT surface is composed of entangled

CNTs, which establishes surface nano-scale roughness. However, on a macroscopic scale, the film is smooth.

5.2.3 Analysis of Contact Angle and Contact Angle Hysteresis

To explore the effect of length-scale on the contact angle and hysteresis, the water droplet contact angle on the three surfaces described schematically by Figure 5.3, have been measured, and the results are shown in Table 5.1, where the advancing and receding contact angles are denoted as θ_{Adv} and θ_{Rec}, respectively. The theoretical contact angle is calculated according to Equation 5.2. The static contact angle θe of water on a smooth silicon wafer coated with fluorocarbon is 109°, while the advancing and receding contact angles of water were measured as 115° and 109°, respectively. ϕ_s is calculated from the following equation:

$$\phi_s = \frac{\pi a^2}{4b^2} \qquad \textbf{Equation 5.19}$$

where a is the array diameter and b is the array pitch as shown by the geometrical array in Figure 5.6. It should be noted that the calculations of ϕ_s for model surfaces I and II do not consider the existence of nano-scale roughness on surfaces. Figure 5.7a shows a high magnification SEM image of a CNT array surface after coating with a 20 nm fluorocarbon film. These experiments demonstrate that water cannot penetrate the treated CNT arrays, although water can easily penetrate the untreated (no fluorocarbon layer) CNT films. The nearly spherical water droplet (Figure 5.7b) confirms that the surface shown in Figure 5.5b is indeed superhydrophobic.

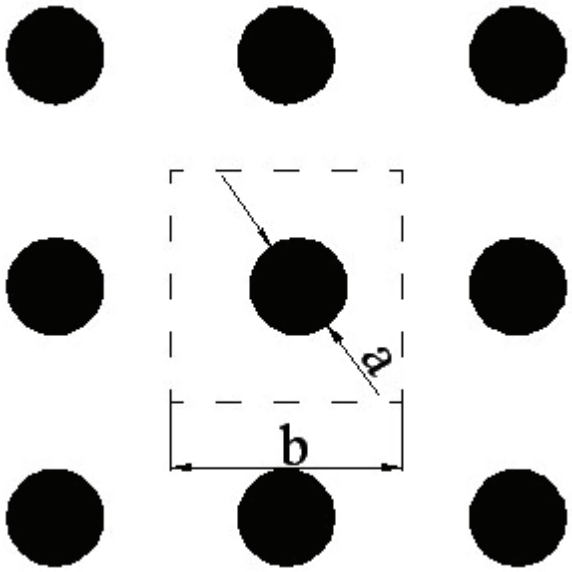

Figure 5.6. Schematic of the top view of the array geometry.

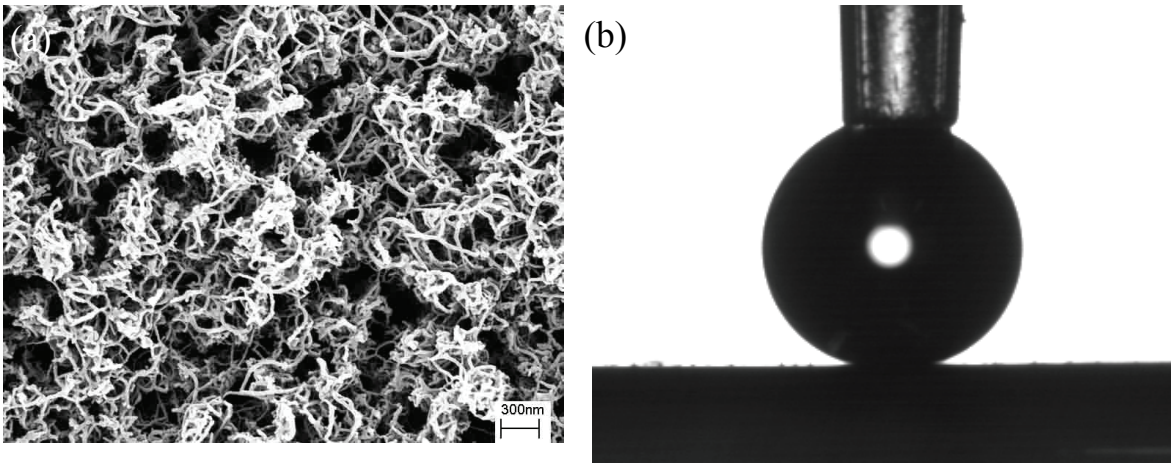

Figure 5.7 (a) high magnification SEM image of CNT array surfaces coated with a 20 nm fluorocarbon film; (b) Shapes of 4 mg water droplets on the surface shown in Figure 5.5b.

Table 5.1 Comparison of water contact angle (CA) on the three types of prepared surfaces

Surfaces	Data point	Geometric dimensions			Experimental results		calculated CA
		h (μm)	a (μm)	b(μm)	θ_{Adv} (deg)	θ_{Rec} (deg)	
Control surfaces	1	4.1	18.7	80	121	111	166
	2		18	60	134	117	162
	3		12	50	163	135	166
	4		12	30	164	156	156
	5	9.5	18.7	80	137	125	166
	6		18	60	165	160	162
	7		12	50	166	162	166
	8		12	30	165	156	156
Model surface I	9	4.6	19.2	80	165	125	165
	10	4.4	18.9	60	165	164	161
	11	4.3	13.7	50	166	166	164
	12	4.8	13.1	30	167	166	154
	13	9.0	19	80	166	166	166
	14	10.5	19.2	60	165	165	161
	15	9.6	12.8	50	168	167	165
	16	10.2	13.3	30	166	165	154
Model surface II	17	4.1	19.5	80	164	163	166
	18		21	60	161	161	160
	19		12	50	166	166	166
	20		12.2	30	166	166	156
	21	9.5	20.2	80	164	164	165
	22		19	60	165	164	161
	23		13	50	168	168	165
	24		12.5	30	167	166	155

Table 5.1 clearly shows that the size, height and spacing (or pitch) of arrays are extremely important to the formation of stable superhydrophobic surfaces. For the control surfaces, when the height of the array is 4.1 μm, the water droplets easily penetrate into the grooves of the arrays and the surface is fully wetted; this situation corresponds to the Wenzel state. However, when the array density is high (a=12 μm, b=30 μm), stable superhydrophobic surfaces can still be formed. When the array height increases to 9.5 μm,

the arrays generally show stable superhydrophobicity. The exception to this statement is the array with a=18.7 μm and b=80 μm (data point 5). We believe that this is due to the large spacing between the arrays. For model surfaces, the contact angle hysteresis is less than 10°, which suggests that stable superhydrophobic surfaces can still be created by the generation of the micro-scale roughness with appropriate geometrical designs. For model surface I, which has nano-scale roughness on the array surfaces, the surface superhydrophobicity is evident: the advancing contact angles are all greater than 160° and the water drops do not collapse when moving forward even on the arrays with a height of only 4.3 μm. If the water droplet decreases its volume, corresponding to the receding contact angle, only on one surface (a=19.2 μm, b=80 μm, data point 9) the droplet collapses to Wenzel state. Introduction of nano-scale roughness on the grooves between the arrays causes the formation of a robust superhydrophobic state as can be seen clearly from the data of model surface II. Even for short array heights (h=4.1 μm), model surface II shows stable superhydrophobicity. The collapse of receding water droplets (data point 9) does not occur, due to the existence of nano-scale roughness on the grooves. The water contact angles on CNT films and flat Si wafers both coated with fluorocarbon are 156° and 109°, respectively. As a result, water cannot easily wet the groove bottom, even when the water droplets move dynamically on the short CNT arrays. The extremely low hysteresis (<1°) indicates that air is trapped beneath the water. The wetting data on model surfaces I and II demonstrate that nano-scale roughness can dramatically decrease the hysteresis and required asperity (in our case, the array) height. Also the nano-scale roughness may stabilize the Cassie state of water droplets on the surface. That is, the nano-scale surface roughness increases the energy barrier for the transition from the Cassie state to the Wenzel state.

To further explore the geometric effects on apparent contact angle, we plot the experimental results with theoretically predicted contact angle as a function of array

geometric parameters. The Wenzel and Cassie equations can be re-formulated to make evident their dependence on the surface geometry. The expressions become

$$\cos\theta_W = (1+\pi\frac{h}{b}\frac{a}{b})\cos\theta_e \qquad \textbf{Equation 5.20}$$

$$\cos\theta_{CB} = \frac{\pi}{4}(1+\cos\theta_e)(\frac{a}{b})^2 - 1 \qquad \textbf{Equation 5.21}$$

where a, b and h are the array diameter, pitch and height, respectively. The roughness factor values are calculated by assuming that the arrays have smooth edges. Figure 5.8 shows the experimental water contact angles on the three surfaces investigated as well as the theoretical (predicted) contact angles as a function of the geometric parameter a/b. For the Cassie state, the contact angle is independent of the array height; however, the Wenzel state is dependent on the array height. For clarity purposes, Figure 5.8 shows only two geometries for the theoretical calculation of Wenzel contact angle: h=4.1 μm, b=80 μm and h=9.5 μm, b=30 μm. Here for calculation of Cassie and Wenzel contact angles, the Young contact angle θ_e is 109°, measured by water droplets on a smooth silicon wafer coated with fluorocarbon.

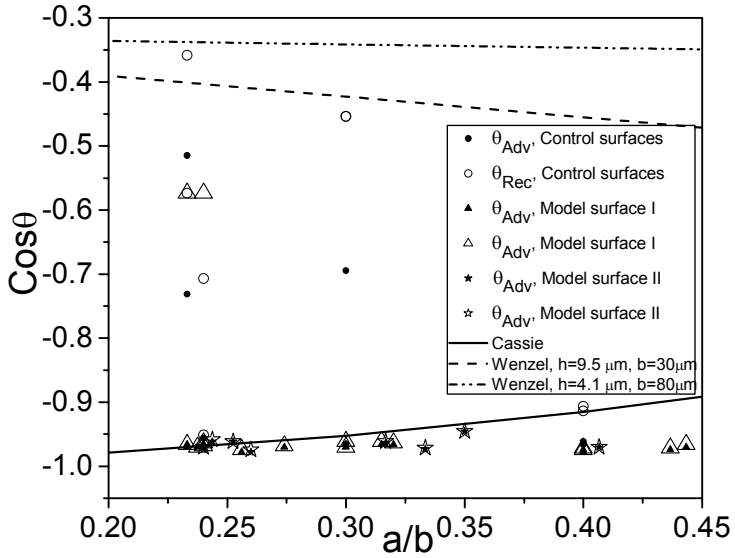

Figure 5.8 Comparison of the experimental water contact angles on the as-prepared surfaces with the predicted contact angles as a function of the geometric parameter a/b. The Wenzel contact angle is theoretically calculated from two cases: h=4.1 μm, b=80 μm and h=9.5 μm, b=30 μm.

Nano-scale roughness on the surfaces does not increase the apparent contact angle as expected. The contact angles are nearly the same for the two-tier roughness surface as for the patterned silicon surfaces, although the hysteresis is greatly reduced. These observations suggest that specific surface geometries exist that establish whether micro- or nano-scale roughness dominates surface wetting behavior; at present, we cannot identify the particular conditions. However, for our studies, the micro-scale roughness dominates the nano-scale roughness, since the micro-scale length is at least 10 μm. We also note that the Cassie equation can accurately predict the contact angle on composite wetting surfaces in most cases. Most experimental observations are in good agreement with predicted values in that the calculated values are essentially the same as the measured advancing contact angles. For the control surfaces with a=12 μm and b=30 μm, the calculated contact angles are very close to the receding contact angles (data points 4, 8). The addition of nano-scale roughness onto the micro-scale roughness may suppress the pinning of water droplets, such that the receding contact angle is similar to the advancing contact angle (data points 12, 16, 20, 24). However, it is still unclear whether Cassie Equation can be used for prediction of the advancing contact angle or the receding contact angle, though this equation was derived for a drop in equilibrium with surfaces, i.e. equilibrium contact angle. Our experimental results indicate that Cassie's formula cannot predict the apparent contact angle accurately if the area density of the arrays is high (a=12 μm and b=30 μm). An increase of array area density signifies an increase of the fraction of solid in contact with the liquid. When the drop recedes on micro-patterned substrates, a thin film of water may be left on the top of the array surfaces [233]. As a result, the increased solid area retains more water on the surfaces as indicated by previous experimental data. These previous studies demonstrate that the contact angle hysteresis is >20°, and this is due to the geometric design: the array pitch is too large or too small. The large pitch design causes the drop to collapse easily into the grooves; the small pitch causes the drop to leave behind a thin layer of water. We find that a ratio of array size to

pitch (a/b) of approximately 0.3~0.4 establishes a stable superhydrophobic surface. However, nano-scale roughness inhibits the water from remaining on the surface, thus decreasing the contact angle hysteresis. Therefore, the addition of nano-scale roughness to surfaces can effectively mitigate the micro-scale design restriction so that robust superhydrophobic surfaces can be obtained.

Finally, we want to discuss briefly the effect of contact angle hysteresis on the surface superhydrophobicity. While the water contact angle has been commonly used as a criterion for the evaluation of surface hydrophobicity, this characteristic alone is insufficient for the evaluation of superhydrophobic surfaces. A surface with high contact angle does not necessarily imply low sliding angles, which is a very important parameter for self-cleaning surfaces. Indeed, an expression has been proposed to describe the importance of contact angle hysteresis in determining hydrophobicty:

$$mg\sin\alpha / w = \gamma_{LV}(\cos\theta_{Rec} - \cos\theta_{Adv}) \qquad \textbf{Equation 5.22}$$

where θ_{Adv} and θ_{Rec} are the advancing and receding contact angles, γ_{LV} is the surface tension of the liquid, g is the force of gravity, and m and w are the mass and width of the droplet. Equation 5.22 clearly shows that the contact hysteresis is an important parameter in determining surface hydrophobicity. During our studies, we have observed that water droplets are unstable on model surface II, where the droplets roll across the surface and do not come to rest on horizontal surfaces until they touch the edges of the surfaces.

5.3 Electrowetting of Aligned CNT Films

One promising application of CNTs is their use as reinforcing fibers in CNT-based composites, especially CNT-polymer composites. However, the fabrication of high performance CNT-polymer composites requires homogeneous dispersion of CNTs and strong interfacial bonding between CNTs and the polymer matrix. The interfacial

interaction depends upon suitable wetting of CNT walls by the surrounding media, unless strong covalent bonds can be formed to the CNTs. Clearly, wettability of solid surfaces with a liquid is of great importance in fundamental research and practical applications of adhesion. Wettability is governed by the surface chemistry of the solid and liquid phases and the geometrical roughness of the solid surface [226]. However, nanotube walls are atomically smooth. Therefore, for acceptable wetting, the polymer solutions or monomers should have low surface tension; this requirement limits the specific CNT-polymer composites that are amenable to particular applications.

Due to the one-dimensional molecular structure of nanotubes, highly anisotropic properties of CNT-polymer composites are expected if the composites contain CNTs that are aligned uniformly in one direction. One approach to achieving this configuration is through the use of high magnetic or electrical fields to align CNTs within the polymer or monomer solution [242, 243]. In addition, it is possible to simultaneously control nanotube alignment and dispersion within the matrix, by infiltrating monomers into pre-aligned CNTs, followed by in situ polymerization [244]. However, the aligned CNT surfaces show superhydrophobic properties, due to fact that the high degree of surface roughness of CNT films amplifies the hydrophobicity of hydrophobic smooth surfaces. Furthermore, the monomer infiltration process is largely driven by the wetting of liquid on the nanotube walls. Thus, enhancement of the wetting of a specific liquid on CNT surfaces is critical for effective formulation of CNT-based composites. For this application, electrowetting is an effective way to decrease the solid-liquid interfacial tension by application of an external voltage across the solid/liquid interface, thereby decreasing the contact angle and enhancing the wetting behavior of the solid without changing surface composition [245, 246]. Recently, electrowetting of liquid mercury to allow penetration into the hollow cavities of individual CNTs has been reported [247]; however, little work has been reported on the electrowetting of aligned CNT films using a liquid with high surface tension. Previous investigations on electrowetting have utilized

primarily smooth/flat electrodes [248, 249], which neglects the effect of surface roughness on the contact angle. With aligned CNTs, electrowetting must occur on a nanoscopically rough surface. In this case, the geometrical structures (surface roughness), in addition to electrical potential, will have an influence on electrowetting behavior. Thus, more detailed studies of the dependence of the contact angle on the electrical potential as well as on the surface roughness are needed. The present work investigates these combined effects and offers a model for electrowetting of rough surfaces.

5.3.1 Experimental

Sessile drop configuration for electrowetting study. Figure 5.9a shows a schematic diagram of the electrowetting experiment. Aligned CNTs were assembled onto copper substrates by a CNT transfer process. Aligned CNT films were grown on silicon substrates by a thermal CVD method with the introduction of a trace amount of water during CVD. Copper substrates were stencil-printed with tin-lead solder. After reflow, the tin-lead solder was polished with SiC papers to a smooth surface. The CNTs were transferred onto the copper substrates, and the solder reflowed in a seven-zone BTU reflow oven at higher temperatures (peak temperature at 270 °C) than those typically used (220 °C) to simultaneously form electrical and mechanical connections. An external voltage was then applied across the two electrodes; the top electrode is a gold wire, while the bottom electrode is the copper substrate. In Figure 5.9a, the droplet shown is DI water or dilute NaCl solution (0.03 M), and γ_{LV}, γ_{SL}, and γ_{SV} are referred to the interfacial tensions of the liquid/vapor, solid/liquid, and solid/vapor interfaces, respectively. Figure 5.9b is a photograph of a 5 μL DI water droplet sitting on the aligned CNT films assembled on the copper substrate via CNT transfer technology. A gold wire has been inserted into the droplet to serve as the top electrode, while another gold wire was soldered to the bottom electrode (copper substrate); this configuration allows the

application of a voltage across the CNT/liquid interface. The size of the copper substrate is 2 cm by 2 cm.

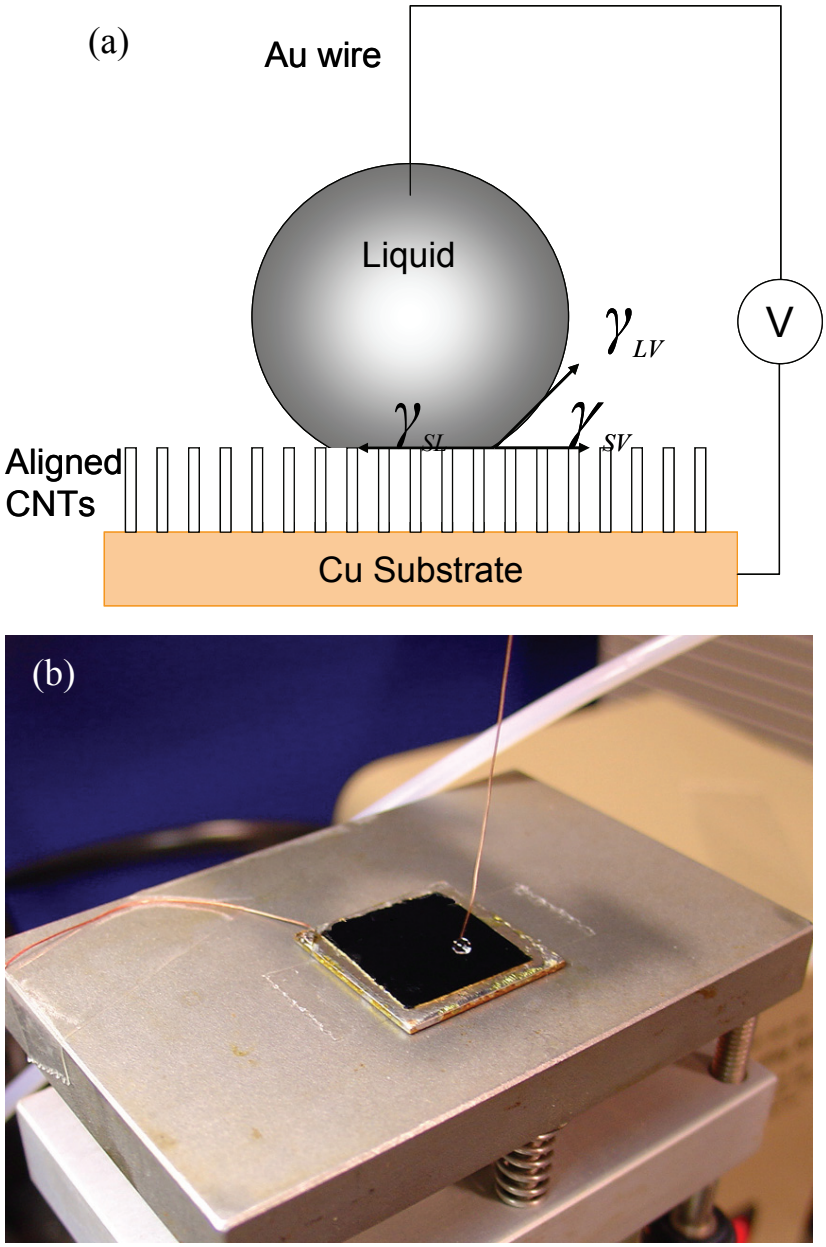

Figure 5.9 (a) Experimental configuration for electrowetting of aligned CNT films, where γ_{LV}, γ_{SL}, and γ_{SV} are the interfacial tensions of the liquid/vapor, solid/liquid, and solid/vapor interfaces, respectively. (b) Photograph of a 5 μL DI water droplet sitting on the aligned CNT films assembled on the copper substrate via CNT transfer technology.

Electrical measurements of the aligned CNT films. The bottom electrode (Cu) serves as an appropriate contact for electrical testing, since the CNTs are connected to the Cu by Sn-Pb eutectic solder after the reflow process. In order to investigate the performance of the bottom CNT-metal contact and CNTs themselves, top electrodes are formed by DC-sputtering Ti (20 nm)/Au (400 nm) layers onto the CNT surfaces through metal shadow masks with openings of 2 mm diameter. Since sputtering is a physical-vapor-deposition process and the sticking coefficient of gold is essentially one, penetration of gold through the densely-packed CNT films is highly improbable. Indeed, SEM examination of the top electrodes confirms that gold penetration into the CNT films is ~100 nm. In addition, the CNT film height is ~180 μm; therefore, the two electrodes are separated by the CNTs. Finally, in order to eliminate the resistance contribution from the testing probes and connecting wires, four-probe measurements have been used. As shown in Figure 5.10, the two probes touch the top electrode, while the other two probes touch the copper substrate.

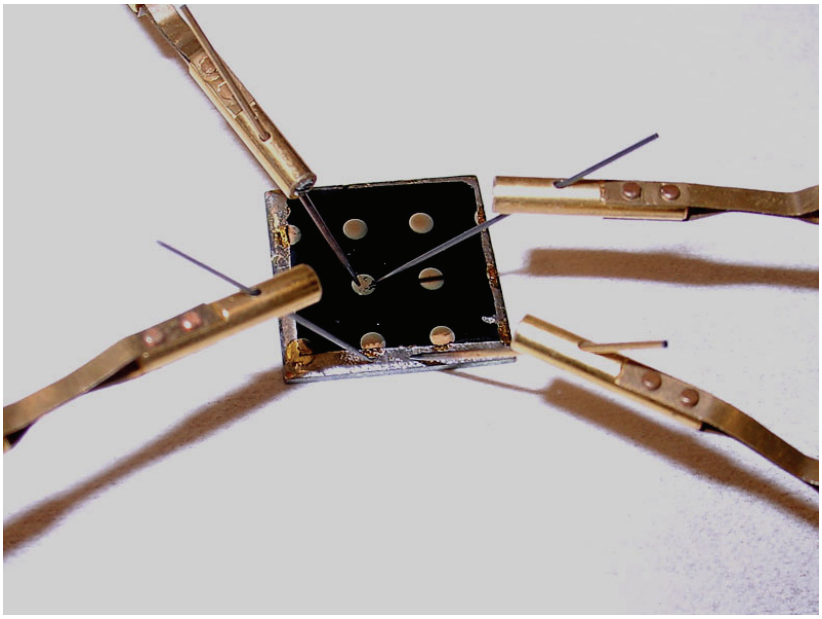

Figure 5.10 Configuration for electrical measurements of the assembled CNT films by four-probe methods.

Contact angle measurements. Contact angle measurements were performed using a Ramé-Hart telescopic goniometer with a computer-controlled automatic liquid dispensing system. The volume of the DI water or dilute NaCl solution (0.03 M) droplets is controlled to be 5 or 10 μL. Dynamic advancing (θ_{Adv}) and receding (θ_{Rec}) contact angles were recorded while probe fluid was added to and withdrawn from the drop, respectively. Scanning electron microscope (SEM) images were obtained with a JEOL 1530 equipped with a thermally assisted field emission gun operating at 10 keV. The array height of CNT films was measured by SEM cross-sections.

In order to examine the alignment and morphology of the assembled CNTs, especially in the tip region, SEM examinations were performed. Figure 5.11a demonstrates excellent alignment of the CNT tips, which generates the CNT surface roughness. The average diameter of the CNTs is ~10 nm with a pitch (center to center) of 30 nm. To qualitatively demonstrate the bonding strength of the CNTs on the copper substrate that results from the solder reflow process, a section of the assembled CNTs was pulled from the surface by tweezers. Figure 5.11b shows the demarcation between the broken CNTs and the intact and connected ones. When pulled from the substrate, the CNTs break along the axis rather than at the CNT-solder interface. The excellent mechanical bonding strength of CNTs on the substrate anchor the CNTs and thereby avoid pull-off and collapse during electrowetting experiments.

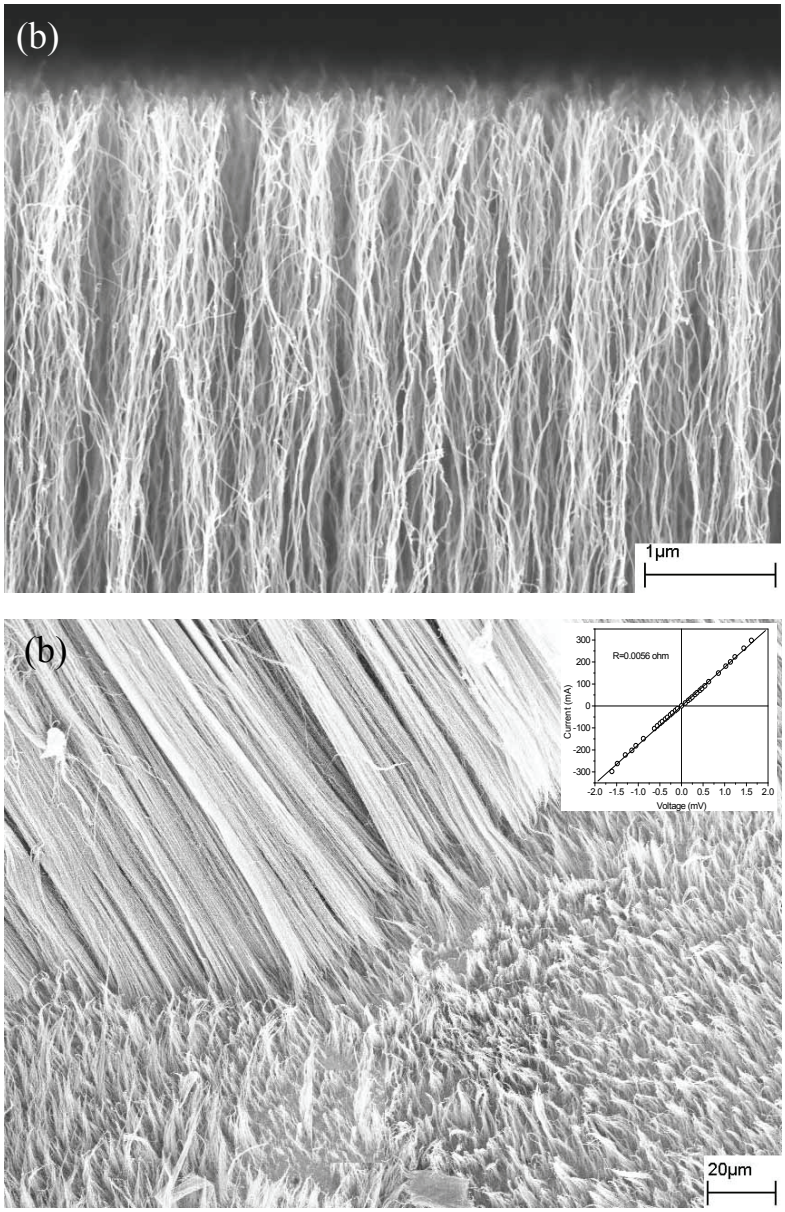

Figure 5.11 (a) Cross-sectional SEM image of the assembled CNT tips. (b) SEM of the copper substrates on which the CNTs were assembled after some CNTs were pulled from the surface by tweezers. The inset in Figure 3b is the linear I-V curve of assembled CNTs measured at room temperature; the I-V relationship indicates the ohmic contact of the CNTs to the copper substrate and the negligible voltage drop along the CNT axis.

In the electrowetting experiments, a potential is applied between the copper substrate and the Au wire inserted into the droplet. In order for electrowetting to occur, sufficient voltage must be applied across the solid/liquid interface to form an electrical double layer. Interfacial tension will therefore be reduced by the accumulation of

electrical charge. To ensure that the electrical potential across the CNTs/droplets is essentially equal to the applied voltage, i.e., the voltage drop along the CNT axis is negligible, we must know the conductivity of the as-grown CNTs. The inset in Figure 5.11b shows a typical I-V curve of as-assembled CNT structures measured at room temperature by a four-probe method. The I-V curve is linear, suggesting that the electrical transport and contacts are ohmic. From the I-V curve, the resistance of a compact CNT bundle with diameter 2 mm is 0.0056 Ω. Since the voltage drop along the CNT axis is apparently negligible, the entire applied voltage is assumed to drop across the CNT/droplet interfaces, creating an electrical double layer in the space between the nanotube tips and the liquid.

5.3.2 Contact Angle Analysis with Applied Voltage

The surfaces of aligned CNTs exhibit superhydrophobic properties with advancing and receding contact angles of 159° and 152°, respectively. The static contact angle is 155° at zero external voltage, as shown in Figure 5.12a, in which the volume of the droplet is 5 μL. By contrast, the contact angle on the flat copper substrate is 76°. After a voltage is applied, the shape of the originally spherical water droplet (Figure 5.12a) is deformed. Figure 5.12 shows the droplet shape evolution of water and 0.03 M NaCl solution on assembled CNT films with an increase of the applied voltage. Figures 5.12b-d show shapes of 5 μL water droplets with an applied voltage of 7.5, 20 and 50 V, respectively, which correspond to contact angles of 142, 128 and 98°, respectively. However, even a small external voltage can actuate the dramatic deformation of a water droplet with a small concentration of salt, since ions present in the electrolyte facilitate the formation of an electrical double layer at the solid/liquid interfaces, thus reducing the solid/liquid interfacial tension [250, 251]. For instance, Figures 5.12e-5.12h show the shapes of 5 μL droplets of aqueous 0.03 M NaCl solution with an applied voltage of 2.5, 5, 6 and 10 V, respectively, which correspond to contact angles of 130, 93, 80 and 50°,

respectively. The contact angle changes abruptly from 155° to 50° upon application of 10 V across the interface. Thus, the superhydrophobic state of aligned CNT films can be changed to a hydrophilic state with the application of low voltage. Figures 5.12i-5.12l show the shapes of 10 μL droplets of aqueous 0.03 M NaCl solution with an applied voltage of 2.5, 5, 6 and 10 V, respectively, corresponding to contact angles of 134, 94, 82, and 52°, respectively. These figures demonstrate that doubling the droplet volume has a minimal effect on electrowetting, at least for the drop sizes investigated in this study.

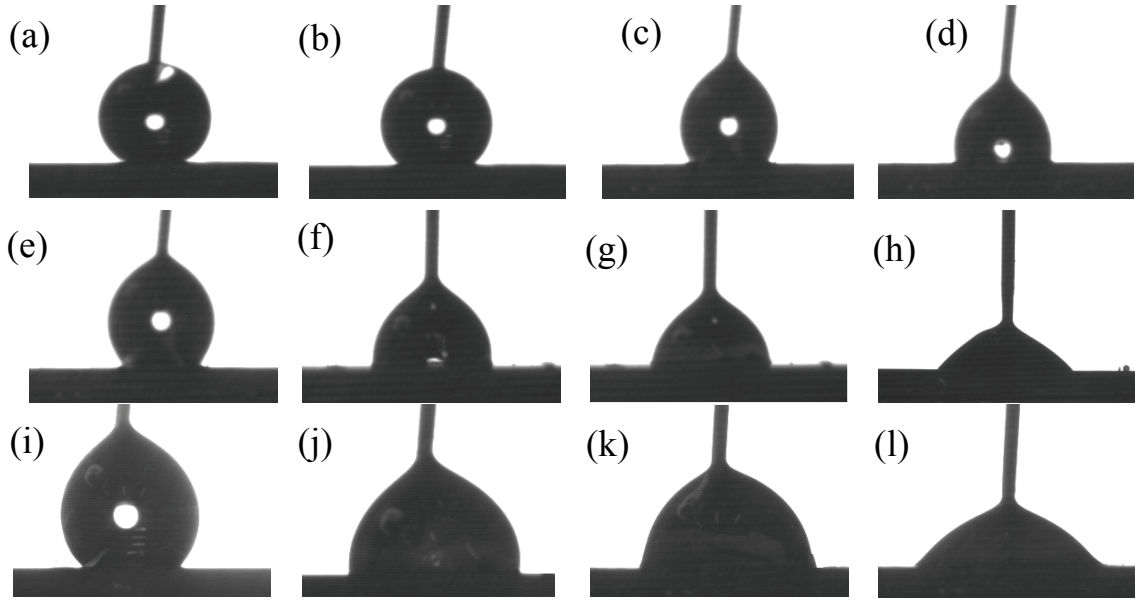

Figure 5.12 Droplet shape evolution of water and 0.03 M NaCl solution on assembled CNT films with an increase of the applied voltage. (a)-(d) Shapes of the 5 μL water droplets with an applied voltage of 0, 7.5, 20 and 50 V, respectively. (e)-(h) Shapes of the 5 μL droplets of aqueous 0.03 M NaCl solution with an applied voltage of 2.5, 5, 6 and 10 V, respectively. (i)-(l) Shapes of the 10 μL droplets of aqueous 0.03 M NaCl solution with an applied voltage of 2.5, 5, 6 and 10 V, respectively.

5.3.3 Contact Angle Saturation

The contact angle of DI water and 0.03 M NaCl water droplets on the assembled aligned CNTs, have been monitored as a function of applied voltage; results are shown in Figure 5.13. With an increase in applied voltage, the droplet contact angle is reduced for

both liquids, indicating that the solid/liquid interfacial tension has decreased, since the contact angle dependence on the applied voltage is entirely due to changes in the solid/liquid interfacial tension while both solid/vapor and vapor/liquid surface tensions are assumed to be potential independent. However, when the voltage reaches a particular value, the contact angle does not decrease further. For instance, the contact angle of DI water on aligned CNTs reaches 98° when the voltage is 30 V; further increases in voltage do not change the contact angle (contact angle saturation). For a 0.03 M NaCl droplet, the contact angle saturates at a voltage of 7.5 V. The exact mechanism that controls this phenomenon is not yet defined, although theories such as zero interfacial tension and charge trapping have been proposed [246, 251, 252]. The electrolyte concentration strongly affects the free energy of electrical double layers, which contributes to the electrical component of the solid/liquid surface energy. In addition, ions within the electrolyte solutions facilitate the formation of the double layer, which exists from the surface of the CNT tips and includes a diffuse region extending to the bulk solution.

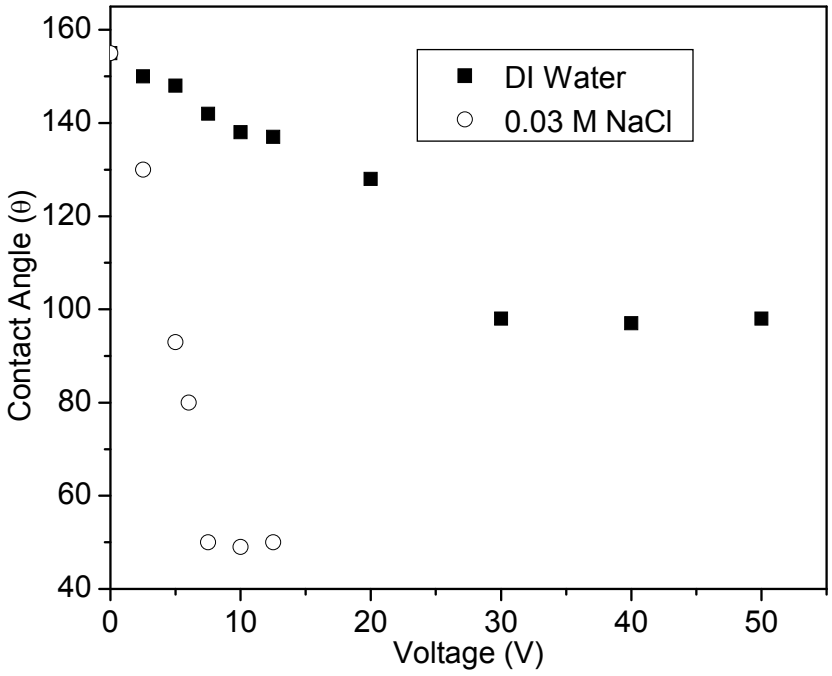

Figure 5.13 Dependence of the contact angle of DI water and 0.03 M NaCl water droplets on applied voltage.

5.3.4 Modeling Electrowetting of Aligned CNT Films

Electrowetting theory assumes that the solid/liquid interfacial tension γ_{SL} is composed of a chemical (potential-independent) component γ_{SL}^{0}, and an electrical (potential-dependent) component γ_{SL}^{V} [225]:

$$\gamma_{SL} = \gamma_{SL}^{0} + \gamma_{SL}^{V} \qquad \textbf{Equation 5.23}$$

The basic equations describing electrowetting are the Lippmann equation

$$(\frac{\partial \gamma_{SL}}{\partial V})_{\mu} = -q \qquad \textbf{Equation 5.24}$$

and the related (derivative) equation

$$(\frac{\partial^2 \gamma_{SL}}{\partial V^2})_{\mu} = -(\frac{\partial q}{\partial V})_{\mu} = -C \qquad \textbf{Equation 5.25}$$

where V is the applied voltage, q is the amount of the charge on the solution side of the solid/liquid interface per unit area, C is the differential capacitance of the double layer, and μ is the chemical potential at constant composition. Integration of Equation 5.25 with the assumption of constant C and combination with Equation 5.23, gives

$$\gamma_{SL} = \gamma_{SL}^{0} - \frac{1}{2} CV^2 \qquad \textbf{Equation 5.26}$$

Thus, Young's equation

$$\gamma_{LV} \cos\theta_0 = \gamma_{SV} - \gamma_{SL}^{0} \qquad \textbf{Equation 5.27}$$

can be modified using Equation 5.26 to give

$$\cos\theta = \frac{\gamma_{SV} - \gamma_{SL}}{\gamma_{LV}} = \cos\theta_0 + \frac{1}{2}\frac{CV^2}{\gamma_{LV}} \qquad \textbf{Equation 5.28}$$

where θ is the contact angle with an applied voltage, γ_{SV} and γ_{SL} are the interfacial tensions of the solid/vapor and solid/liquid interfaces, and θ_0 is the measured contact angle with no applied voltage. However, Young's equation can only describe the contact angle on a flat surface. Hence, Equation 5.28 can only be applied to the electrowetting of liquids on flat surfaces.

CNTs can be regarded as graphitic material. Due to the low surface tension of graphite (~35 mN/m [253]) and the high surface tension of water (72.8 mN/m at 20 °C), the water displays a high contact angle on graphite surfaces. To evaluate the contact angle, a value for the graphite/water surface tension is needed, which can be calculated using [254]

$$\gamma_{SL} = \frac{(\sqrt{\gamma_{SV}} - \sqrt{\gamma_{LV}})^2}{1 - 0.015\sqrt{\gamma_{SV}\gamma_{LV}}} \qquad \textbf{Equation 5.29}$$

Thus, from Young's equation and γ_{SL} =30.3 mN/m, we determine that the water contact angle on a flat graphitic surface is 86.3°. The surface tension of multi-walled CNTs has been shown to be ~27.8 mN/m [255], which results in γ_{SL} =28.2 and thus the water contact angle on flat CNT walls is 90.3°. Due to surface hydrophobicity and the high area density (>1000/μm^2) of CNT films, CNT films form stable superhydrophobic surfaces. Indeed, water droplets are stable (i.e., do not penetrate into the CNTs) when placed on CNT film surfaces. However, in the case of low CNT area density, water easily penetrates into the CNT films; for instance, CNT films with low area density (~10/μm^2) do not form stable hydrophobic surfaces.

In the following derivation, we assume that CNT films wet according to a Cassie model, where air is trapped underneath the water droplets inside the porous CNT films. From Equation 5.2, with θ_C =155° and θ_0 =86° we calculate ϕ_s =0.088. This value is consistent with the surface fraction value estimated from the as-assembled CNT films:

$$\phi_s = \frac{\pi r^2}{d^2} \qquad \textbf{Equation 5.30}$$

where r is the average radius of the CNTs and d is the pitch of the neighboring CNTs. As shown in Figure 5.11a, the nanotubes have an average radius of 5 nm and a pitch of 30 nm, which yields a ϕ_s value of 0.087. After application of low voltages, water droplets penetrate into the CNT films. Equation 5.2 can be modified to

$$\cos\theta_T = r_{\phi_s}\phi_s\cos\theta_0 + \phi_s - 1 \qquad \textbf{Equation 5.18}$$

to describe the wetting transition from the Cassie state to the Wenzel state, where θ_T is the transition contact angle, and r_{ϕ_s} is the roughness ratio of the wetted areas. Since the applied voltage reduces the solid/liquid interfacial tension, we can re-formulate Equation 5.18 to incorporate the dependence of contact angle on electrowetting through the use of Equation 5.28 (θ in Equation 5.28 is equal to θ_0 in Equation 18). This leads to the expression

$$\cos\theta_T = a + bV^2 \qquad \textbf{Equation 5.31}$$

where $a = r_{\phi_s}\phi_s\cos\theta_0 + \phi_s - 1$ and $b = \frac{1}{2}r_{\phi_s}\phi_s\frac{C}{\gamma_{LV}}$. Equation 5.31 can be used to fit the electrowetting data; results are shown in Figure 5.14. Parameters a and b are fitting constants, but determination of accurate values for these parameters is difficult because the value of γ_{ϕ_s} increases as the water droplets penetrate into the CNT films. Therefore, Equation 5.31 is unable to fit the initial data well since γ_{ϕ_s} =1 with no applied voltage. After the application of a voltage, the behavior predicted by Equation 5.31 is consistent with the experimental data, indicating a small variation of r_{ϕ_s} with time. Thus, we can estimate the double layer capacitance between aligned CNT films and DI water with and without the addition of salt. For DI water droplets, a=-0.868 and b=0.0008; for 0.03 M NaCl solution, a=-0.8296 and b=0.02723. With values of 86° and 0.087 for θ_0 and ϕ_s, respectively, the capacitance of aligned CNT films in contact with DI water is 0.017 μF/cm^2, while the capacitance of CNT films with 0.03 M NaCl is 0.311 μF/cm^2. The capacitance values indicate that the capacitance of the electrical double layer is ion concentration dependent, and that the higher capacitance results in higher surface charge density, which is responsible for the reduction of the solid/liquid interfacial tension.

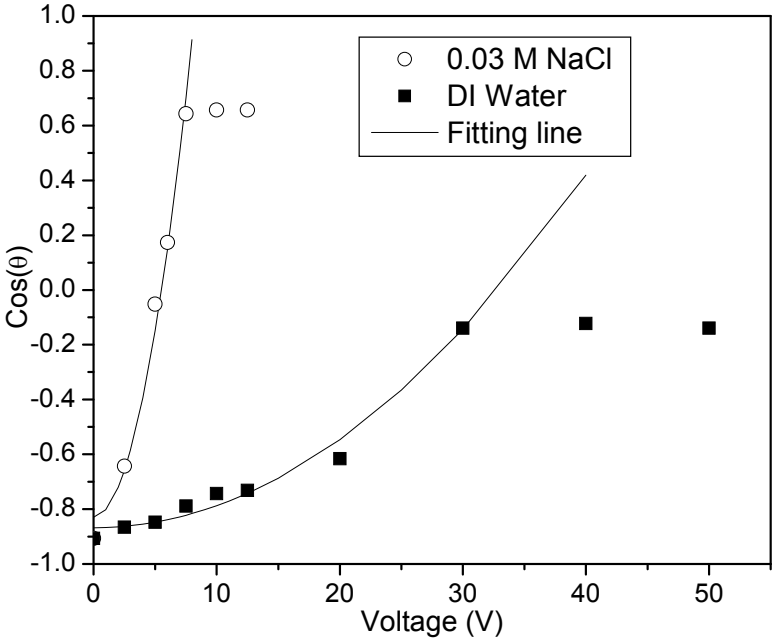

Figure 5.14 Electrowetting data for DI water and 0.03 M NaCl on aligned CNT films; solid lines represent the expression $\cos\theta = a + bV^2$.

Given the assumption that electrowetting only reduces the solid/liquid interfacial intension, the limiting case for Equation 5.28 is

$$\cos\theta_S = \frac{\gamma_{SV}}{\gamma_{LV}} \qquad \textbf{Equation 5.32}$$

where θ_S is the saturated contact angle, and γ_{SL} is zero. Therefore, the contact angle of water on the smooth CNT walls is 61.3° if the value of the CNT surface tension is ~35 mN/m. It has also been suggested that γ_C, the critical surface tension, can replace γ_{SV} [246]. γ_C is a characteristic of the solid surface, defined by the intercept of the horizontal line $\cos\theta = 1$ with the extrapolated straight-line plot of $\cos\theta$ vs. γ_{LV} for different liquids on a specific solid surface. The γ_C of the CNTs was estimated to be in the range of 40-80 mJ/m [256], which yields a contact angle of water less than 56.6°. However, in our case, the zero interfacial theory does not fully account for the dependence of saturation contact angle on the ionic strength. Apparently, the DI water/CNT interfacial tensions are not

reduced to zero even at higher applied voltage. The air ionization theory [257] cannot account for the contact angle saturation on CNTs because the applied voltage is low (<50 V) and thus cannot ionize the air. Indeed, the air ionization theory essentially represents charge equilibrium at the solid/liquid interfaces; that is, the excess charges transport out of the liquid drop via ionized air. In our case, we ascribe the contact angle saturation on the aligned CNTs to charge density saturation. The charges at the solid/liquid interface exert a lateral pressure outwards on the contact line, thus, inducing drop spreading. More charges lead to higher lateral pressure. After the charge density at the solid/liquid interface saturates, the driving force for electrowetting cannot increase further, thus, the contact angle reaches a constant value.

5.4 Summary

In this chapter, we successfully fabricated two model surfaces with two tier scale roughness by controlled growth of CNT arrays followed by coating with fluorocarbon layers formed by plasma polymerization. The CNT array size, pitch and height have been varied to explore geometric effects on surface hydrophobicity. Compared to patterned Si surfaces with similar geometrical sizes, the nano-scale roughness does not significantly increase the apparent water contact angle; thus, the micro-scale roughness determines the apparent water contact angle provided that the micro-scale roughness dominates the nano-scale roughness. The specific criteria that determine which scale dominates and how dominance is achieved are still undefined. However, the introduction of nano-scale roughness can decrease the contact angle hysteresis to less than 1° and improve the stability of superhydrophobic surfaces. Furthermore, nano-scale roughness can also reduce the strict requirements of micro-scale roughness design for superhydrophobic surfaces. The introduction of nano-scale roughness on the groove bottom can decrease the micro-scale array height needed for superhydrophobicity. These results improve the

understanding of the effects of two-tier roughness on superhydrophobicity and offer additional design approaches for stable and robust superhydrophobic surfaces with self-cleaning properties.

Electrowetting of aligned CNT films was investigated by the sessile drop method. Results indicate that even a low concentration of electrolyte (0.03 M NaCl) facilitates the formation of the electrical double layer which is responsible for the reduction of solid/liquid interfacial tension. Electrowetting can greatly reduce the hydrophobicity of aligned CNTs; however, the contact angles of DI water and 0.03 M NaCl droplets saturate at 98° and 50°, respectively. Unlike electrowetting of flat, smooth electrodes, aligned CNT films introduce a geometrical roughness, which affects surface wetting. The contact angle dependence on the external voltage and surface roughness can be described by a modified Cassie or Wenzel equation. From the simplified models, we can extract the capacitance of the electrical double layer formed between aligned CNTs and either DI water or aqueous 0.03 M NaCl solutions: 0.017 and 0.311 $\mu F/cm^2$, respectively. We ascribe the contact angle saturation on the aligned CNTs to charge density saturation. This electrowetting strategy may be invoked to controllably reduce or tailor the interfacial tension between carbon nanotubes (CNTs) and high-surface-tension organic monomers when infiltrating the monomers into pre-aligned nanotube films for preparation of CNT-reinforced composites.

CHAPTER 6

NEGATIVE THERMAL EXPANSION IN ALIGNED CARBON NANOTUBE/EPOXY NANOCOMPOSITES

Due to their extraordinary mechanical properties, carbon nanotubes (CNTs) are considered to be ideal reinforcing fibers in various matrices such as polymers, metals and ceramics. Among them, polymer/CNT composites are under intense investigation due to the good processability characteristics of polymers and the excellent properties of CNTs. However, a number of challenges remain, including enhancement of interfacial bonding strength between nanotubes and the matrix material, and controllable dispersion of CNTs in the matrix. Currently, approaches to improving the interfacial bonding between CNTs and polymers are limited to functionalization of CNTs. In this Chapter, we present an approach to dramatically improving the CNT/epoxy interfacial bonding strength by variable-frequency microwave radiation (VFM) curing of epoxy, instead of conventional thermal heating. The improvement is reflected in the negative thermal expansion of the VFM-cured samples. In one approach, the coefficient of thermal expansion (CTE) of the aligned CNTs/epoxy composites, which is prepared by infiltration of epoxy into the aligned CNTs followed by VFM radiation curing, is -160 ppm/°C, compared to 15 ppm/°C of samples cured by thermal heating. The thermal contraction of the composites is ascribed to the unexpected large negative CTE (<-160 ppm/°C) of the multi-walled CNTs.

6.1 Introduction

Numerous experimental and theoretical studies have revealed that carbon nanotubes (CNTs) have excellent mechanical and physical properties such as high strength, modulus and elasticity [258, 259], high aspect ratio and considerable electrical and thermal conductivity [210] with a wide range of potential applications. One promising application of CNTs is their use as reinforcing fibers in CNT-based composites, especially CNT-polymer composites [260], because such composites may offer improved mechanical strength, high thermal and electrical conductivity as well as unique properties for device applications. There has been significant interest in developing high-performance CNT/polymer nanocomposites [115, 261-264]. However, a number of challenges remain, including enhancement of interfacial bonding strength between nanotubes and the matrix material, and controllable dispersion of CNTs in the matrix. Currently, approaches to improving the interfacial bonding between CNTs and polymers are limited to functionalization of CNTs [265]. The research on CNT/polymer composites are focused on mechanical behavior [266, 267] and thermal conductivity [268, 269]. Few studies to tailor the thermal expansion of such composites by incorporating CNTs into polymer matrices have been reported [270]. Specifically, the CTE of multi-walled CNTs (MWNTs) has not been well-defined due to the lack of experimental and modeling studies on the thermal expansion of MWNTs, although there have been reports on the thermal expansion behavior of single-walled CNTs (SWNTs) [271-273]. Furthermore, the inadequate CNT/polymer interfacial bonding strength results in inefficient load transfer from the polymer matrix to the nanotubes. Thus, the full potential of CNTs for structural reinforcement has not been realized. In this Chapter, we demonstrate that aligned MWNT/epoxy composites cured by VFM radiation display negative thermal expansion in the direction of nanotube alignment. This observation suggests excellent CNT/epoxy interfacial strength, and more importantly, demonstrates an unexpected large thermal contraction of MWNTs. Therefore, in addition to their use as reinforcing fibers,

MWNTs may serve as ideal fillers for tailoring the thermal expansion of composites, since thermal expansion of the matrix can be compensated by a thermal contraction of the fillers.

6.2 Experimental

Our approach to simultaneously controlling the nanotube alignment and dispersion in the polymeric matrix is to infiltrate epoxy into aligned CNT films anchored by double-sided polyimide tape; this process is followed by in-situ polymerization as shown in Figure 6.1. The epoxy resin and hardener used were diglycidyl ether of bisphenol F (Epon 862, Resolution Performance Products) and hexahydro-4-methylphthalic anhydride (HMPA, Lindau Chemicals), respectively. The molar ratio of epoxy to hardener was 1:0.85. The catalyst was 1-cyanoethyl-2-ethyl-4-methylimidazole (2E4MZ-CN, Shikoku Chemicals Crop.). All the chemicals were used as received. The aligned MWNTs were grown on silicon substrates that had been coated with Al_2O_3 (10 nm) and Fe (2 nm) deposited by e-beam evaporation. During nanotube growth, a trace amount of water was introduced into CVD chamber to selectively etch the nanotube caps [215]. CNTs were grown on a 2 nm Fe film, corresponding to a nanotube density of ~1200/μm^2. After growth, the nanotube films were transferred onto double-sided polyimide tape which also acts as an anchor for the nanotubes to prevent nanotube collapse during epoxy infiltration. The CNT/epoxy nanocomposites were subsequently cured by VFM radiation or thermal heating. The thermal expansions of the samples were measured by thermal mechanical analyzer (TMA 2940).

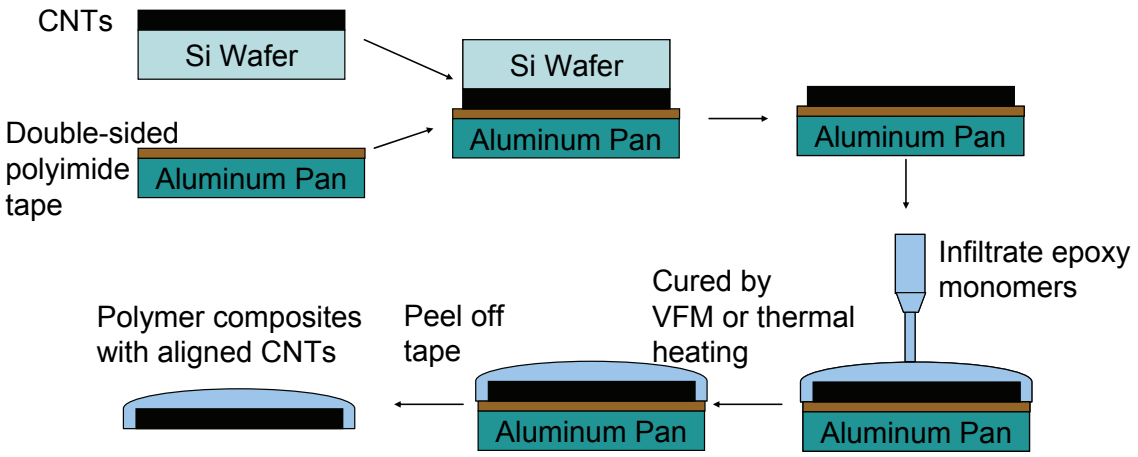

Figure 6.1 Schematic of the CNT-polymer composite preparation process using double-sided polyimide tape as a transferring layer.

6.3 Negative Thermal Expansion of CNT/Epoxy Composites

6.3.1 Verification of Negative Thermal Expansion of CNT/Epoxy Composites

Figure 6.2a shows the thermal expansion behavior of prepared aligned CNT/epoxy nanocomposites cured by VFM. Relative to the CTE of pure epoxy (72 ppm/°C), the aligned CNT/epoxy nanocomposites show a negative thermal expansion with a CTE of -160 ppm/°C below the glass transition temperature (Tg), while above Tg the sample displays thermal expansion. Such results may be due to the large thermal expansion of pure epoxy (~190 ppm/°C) and a reduction of the strong interfacial bonding between CNTs and the epoxy matrix at temperatures above Tg. However, above Tg the presence of aligned CNTs still keeps the CNT/epoxy composite CTE at a value of 67 ppm/°C, which is much lower than that of pure epoxy (190 ppm/°C). We ascribe the thermal contraction of the composites below Tg to the interaction of epoxy with the CNTs and thermal contraction of MWNTs, although other possible explanations for shrinkage of the composites, e.g., incomplete composite curing, may exist. Differential scanning calorimeter (DSC) data of the composite sample do not show exothermic curing

peaks; Tg of the composite is 125 °C, 5 °C higher than the pure epoxy, which indicates that the epoxy is tightly bound to the nanotubes and that the cross-link density of the epoxy is not reduced in the composites reinforced by aligned CNTs.

Two experiments were carried out to further verify the negative thermal expansion behavior of the aligned CNT/epoxy composites cured by VFM. First, the dimension change of the same sample was monitored during thermal cycling. Figure 6.2b shows contraction/expansion of the sample during two thermal cycles. During heating, the sample first undergoes contraction below Tg while above Tg the sample expands. During cooling, the sample reverses this trend and returns to the original thickness, demonstrating that the contraction/expansion process is highly reversible and reproducible during thermal cycling. Along the nanotube axis, a shear stress develops with increasing temperature, because the nanotube CTE is negative but that of the polymeric matrix is positive. Therefore, at certain temperatures, this shear stress at the nanotube/matrix interfaces may be large enough to break the interfacial bonding structure. However, although the sample underwent more than a hundred thermal cycles, no interfacial bonding failure occurred. In the second experiment, we intentionally avoided the complete removal (by polishing) of epoxy above the aligned CNT/epoxy film after VFM curing to prepare heterostructured layers of CNT/epoxy to compare to pure epoxy films. As shown in the inset of Figure 6.2c, the thickness of the CNT/epoxy film is nearly equal to that of a pure epoxy film, with thicknesses of 566 and 576 μm, respectively. In this structure, temperature increases will cause the pure epoxy layer to expand while the CNT/epoxy layer contracts. As a result, the heterostructure should show thermal contraction below Tg, since nearly the same film thickness has been used, and the CNT/epoxy layer has a higher negative CTE than the positive CTE of the epoxy layer under these conditions. Figure 6.2c shows the dimension change of the heterostructured films as a function of temperature. Below and above Tg, the CTEs of the sample are -35 and 110 ppm/°C, respectively, which agrees well with quantitative estimates from film

thicknesses and CTEs of the composites and pure epoxy. Clearly, the above experiments demonstrate a negative thermal expansion of the aligned CNT/epoxy composites cured by VFM radiation below Tg. For comparison, we prepared aligned CNT/epoxy composites but cured these samples by conventional thermal heating while keeping other processing conditions (e.g., catalysts, CNT growth conditions, epoxy) the same. The dimension change of the samples processed in this manner is shown in Figure 6.2d. No thermal contraction was observed from the TMA curve even at temperatures below Tg; below and above Tg, the CTEs of this sample are 17 and 72 ppm/°C, respectively. Although the aligned CNTs can still inhibit expansion of the matrix to some extent, the interfacial strength is not sufficiently high to prevent expansion of the matrix, unlike the result for the samples prepared by VFM curing.

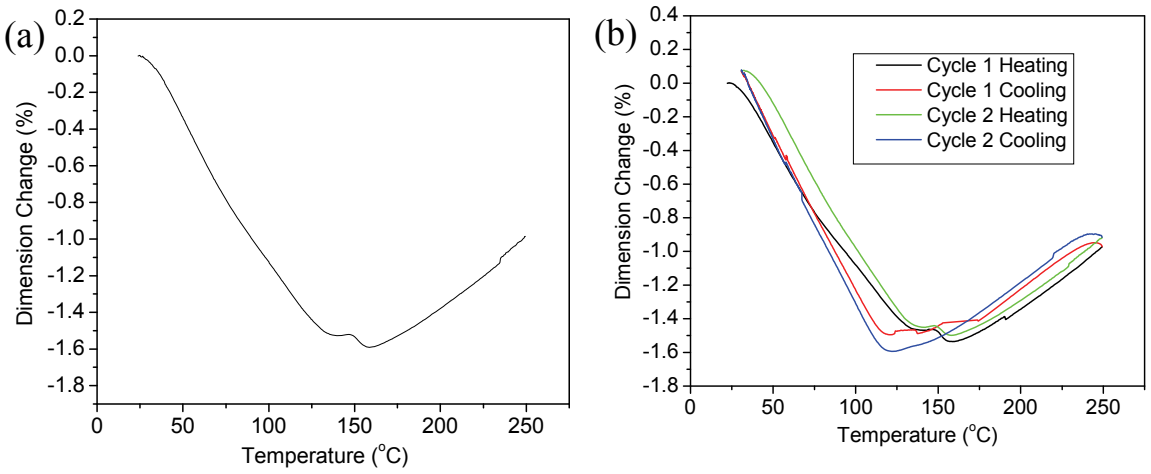

Figure 6.2 Thermal expansion curves of aligned CNT/epoxy composites as a function of temperature. (a) Dimension change of aligned CNT/epoxy nanocompositescured by VFM radiation. (b) Dimension change of the samples under two thermal cycles. (c) Dimension change of heterostructured CNT/epoxy and pure epoxy films with similar film thicknesses. The inset is a photograph of heterostructured CNT/epoxy and pure epoxy films with thicknesses of 566 and 576 μm, respectively. (d) Dimension change of aligned CNT/epoxy nanocomposites cured by thermal heating.

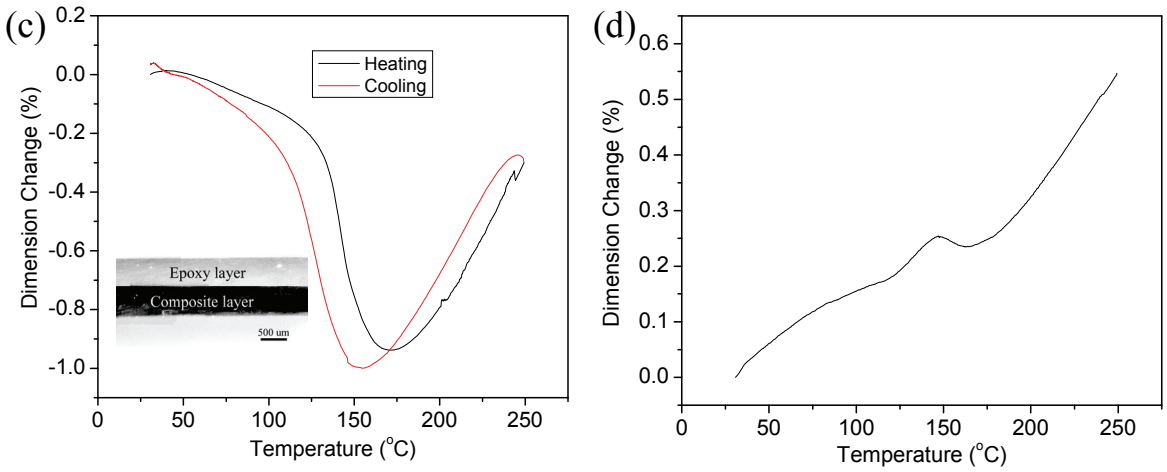

Figure 6.2 Continued.

SEM characterization was conducted in an attempt to observe CNT dispersion and interfacial bonding in the composites. Figure 6.3a is a cross-sectional SEM image along the CNT alignment direction, which shows that the CNTs are well-aligned and dispersed in the matrix. To qualitatively assess the CNT bonding strength in the matrix cured by VFM, SEM was used to observe fractured composite surfaces perpendicular to the CNT alignment direction, as shown in Figure 6.3b. Clearly, only a few short CNTs per μm^2 were displaced from the matrix. In contrast, dozens of long CNTs were pulled out of the matrix cured by thermal heating, as shown in Figure 6.3c. These results suggest that the interface between epoxy and the CNTs in the composites cured by VFM is stronger than the interfaces created by thermal heating. This difference may be due to the heating mechanisms involved in the two curing approaches. For instance, microwave heating of materials occurs as a result of dielectric loss mechanisms [274]. Specifically, microwave curing generates heat within the materials through the bonding structures, thereby affording better control over the solidification behavior of the resin [275]. By varying the frequency of the applied field, VFM can heat dielectric materials rapidly and uniformly and thus eliminate hot spots and arcing associated with conventional fixed frequency microwave. These advantages of VFM radiation promote uniform bonding of

epoxy along the nanotube walls and thereby enhance adhesion of the polymerized epoxy to the array of nanotubes simultaneously. In this way, the load (stress) on the polymer matrix during subsequent heat cycling can be effectively transferred to the nanotubes.

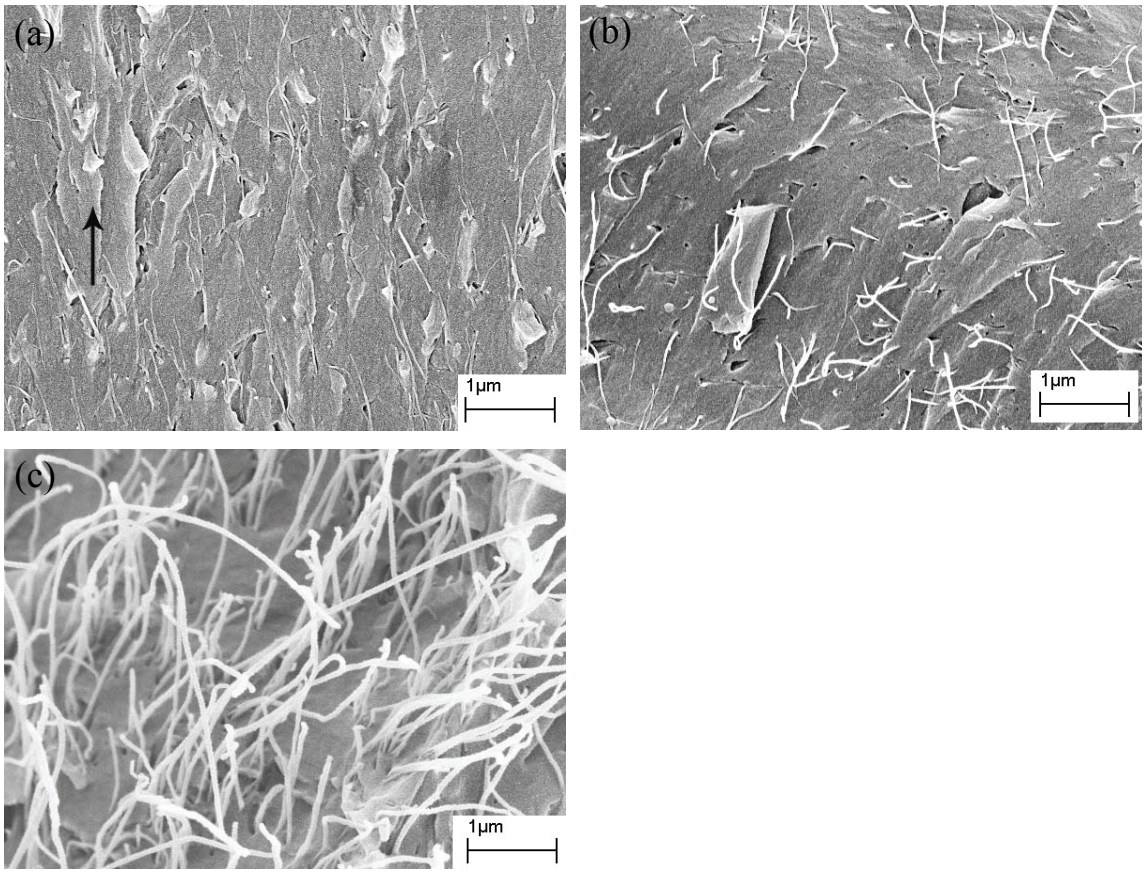

Figure 6.3 (a) Cross-sectional SEM image of aligned CNT/epoxy composites cured by VFM along the direction of CNT alignment shown by the arrow. (b) Fractured surfaces of the composite cured by VFM perpendicular to the CNT alignment direction. (c) Fractured surfaces of the composite cured by thermal heating perpendicular to the CNT alignment direction.

6.3.2 Effects of Nanotube Density in Composites

The well-dispersed and aligned CNTs effectively compensate the thermal expansion of the polymeric matrix via strong interfacial bonding and large interfacial areas. Thus, the CNT density in the matrix will have a significant impact on the thermal expansion behavior of the corresponding composites. To investigate this assumption, aligned CNT/epoxy composites with different CNT densities were prepared. The CNT

density was controlled by the deposited Fe thickness on the substrate, which established the Fe nanoparticle density. In addition to CNTs grown on 2 nm Fe films, CNTs were also grown on 1 and 3 nm thick Fe films. The CNT densities formed on the 1, 2, and 3 nm Fe films are ~650, 1200, and 310 μm^{-2}, respectively, as determined by counting the number of Fe nanoparticles formed on the substrates. In order to ensure reproducibility, three composite samples of each CNT density were prepared, and the dimension change of every sample was measured five times at different sample locations. The experimental results are summarized in Table 6.1.

Table 6.1 Comparison of CTE measurement results from composites with various CNT densities and curing methods.

Fe film thickness	CNT density (μm-2)	CTEs of composites (ppm/°C)			
		Cured by VFM		Cured by thermal heating	
		Below Tg	Above Tg	Below Tg	Above Tg
1	650	-65±5	70±5	33±2	72±5
2	1200	-160±10	65±6	18±2	70±3
3	310	-36±3	73±5	39±2	77±2

Table 6.1 clearly shows that below Tg the CNT density in the polymeric matrix greatly affects the CTEs of the composites cured by VFM. The CTEs vary from -36±3 to -160±10 ppm/°C with CNT density in the matrix increasing from 310 to 1200 μm^{-2}. However, for composites cured by thermal heating, the CTE change is not as obvious, although a somewhat similar trend is observed. Above Tg, the CTEs of composites with the same CNT density cured by VFM or thermal heating display little difference. These results suggest that the interfacial bonding strength degrades due to the polymer chain mobility above Tg. In addition, such observations imply that the interface between the epoxy and the nanotubes as established by VFM or by thermal curing shows similar

properties. Above Tg, the CNT density (at least within our study range) has no obvious effect on the thermal expansion of the composites. However, the CTEs in this study are much lower than that of the pure epoxy. For comparison, we should note that several studies have reported that CTEs above Tg are higher than that of the pure epoxy for randomly mixed CNT/epoxy composites [270, 276].

6.3.3 Enhanced Thermal Conductivity of Nanotube Composites by VFM

We expect that the improvement in CNT/matrix interfaces due to VFM curing favors the thermal conductivity of the composites. The thermal conductivity of the aligned CNT/epoxy composites cured by VFM and thermal heating along the CNT axis was measured by a LFA 447 Nanoflash instrument (Netzsch). To preclude a possible dependence of thermal conductivity on sample thickness, the aligned CNT (grown from 2 nm Fe film)/epoxy composites that were cured by VFM and thermal heating were prepared with thicknesses of 1.04 and 1.08 mm, respectively. The thermal conductivity measurements are shown in Figure 6.5, which clearly indicates that aligned and uniformly distributed CNTs in the polymeric matrix can greatly enhance the thermal conductivity of the composites in the direction of CNT alignment. Moreover, these data demonstrate that improvement of the CNT/epoxy interface results in an enhancement of the thermal conductivity of the composite over the temperature range measured. For instance, at 25 °C the thermal conductivity of the CNT composite cured by thermal heating is 0.52 W/m.K, compared to the pure epoxy with 0.17 W/m.K, which is an enhancement of 205%; the CNT composite cured by VFM displays a thermal conductivity of 0.68 W/m.K, an enhancement of 30% relative to the composite cured by thermal heating.

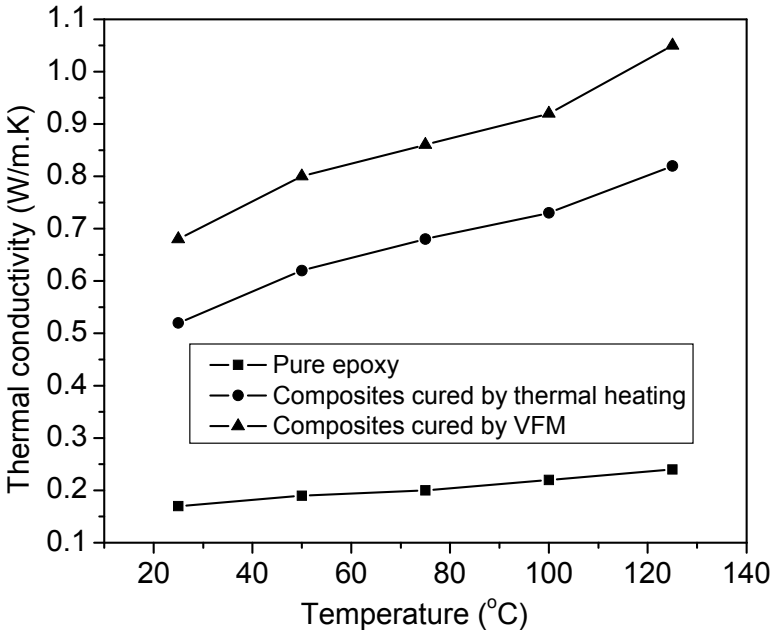

Figure 6.4 Comparison of thermal conductivity of aligned CNT/epoxy composites cured by VFM and thermal heating at different temperatures. The composites were prepared with the same CNT density in the matrix. At 25 °C, the thermal conductivity of the pure epoxy, composites cured by thermal heating, and composites cured by VFM is 0.17, 0.52, 0.68 W/m.K, respectively.

6.4 Summary

CNT/epoxy interfaces can be greatly improved by selection of an appropriate composite curing method. In our study, VFM radiation is employed to cure the aligned CNT/epoxy composites. Compared to composites cured by thermal heating, the VFM-cured composites demonstrate higher CNT/matrix interfacial bonding strength, which is reflected in a negative thermal expansion of the composites. The thermal contraction of the composites is ascribed to the unexpected large thermal contraction of MWNTs (<-160 ppm/°C). The improved CNT/epoxy interface enhances the thermal conductivity of the composites by 26-30%. Thus, in addition to their use as reinforcing fibers for composites, the MWNTs, which serve as highly negative CTE materials, offer much promise as effective fillers to tailor the CTE of polymer/CNT composites.

CHAPTER 7

SUMMARY AND FUTURE WORK

This chapter presents a brief summary of studies performed in this thesis and recommends some directions for future work.

7.1 Summary

Carbon nanotubes (CNTs) display a well-defined quasi one dimensional cylindrical structure with ballistic conductivity, high thermal conductivity and mechanical strength. These features make CNTs ideal candidates for electrical interconnects and thermal management in IC packaging and nanoscale devices. CNTs promise to bring revolutionary improvement in reducing the interconnect pitch size, increasing thermal conductivity, and enhancing system reliability.

This thesis is devoted to the fabrication of carbon nanotube structures for microelectronics packaging applications with an emphasis on fundamental studies of nanotube growth and assembly, wetting of nanotube structures, and nanotube-based composites. A CVD process is developed that allows controlled growth of different CNT structures such as CNT films, bundles, and stacks. In the design of catalyst systems for rapid growth of nanotubes, the Al_2O_3 support enhances the Fe catalyst activity. Results clearly demonstrate that introduction of an Al_2O_3 support beneath the Fe catalyst increases the CNT growth rate by nearly two orders of magnitude under the same growth conditions. At 800 °C, nanotube films grow at a high average rate of 100 μm/min. The patterned growth of nanotube arrays shows a higher growth rate than that of films, due to the base-growth mode. Our study revealed an important role played by water during nanotube growth: opening the nanotubes. During CNT growth, a controlled amount of

water (775 ppm) in the CVD tube can selectively etch and thus remove nanotube caps, while keeping the tube walls intact. This unique process offers a novel and cost-effective way to fabricate aligned nanotubes with open ends. Furthermore, introduction of aqueous H_2O_2 into the CVD chamber during CNT growth can in-situ functionalize the aligned CNTs with –OH, C-O-C, and –COOH groups attached onto nanotube walls. These functionalized CNTs can be employed as excellent stabilizing substrates for silver and gold nanoparticle synthesis without the need for post-treatments.

Kinetics studies of CNT growth are helpful to optimize CNT growth processes and to explore the mechanisms of CNT growth. A novel process was developed to perform allow pseudo in-situ monitoring of CNT growth and gain insight into CNT growth kinetics by formation of CNT stacks. By varying the growth temperature and the ethylene introduction time in growth cycles, a parabolic increase of CNT length versus time is obtained, indicating that gas diffusion-control establishes the intrinsic CNT growth kinetics. Due to the base growth mode in our reaction/reactor system, the densely-packed, well-aligned CNT films act as porous barrier layers to the diffusion of carbon precursors to the catalyst nanoparticles. By varying CNT growth temperature, a quantitative time-evolution analysis has been performed based on a simple CNT growth model, thereby allowing determination of the mass transfer coefficient in the CNT films. A simple kinetics model, similar to that describing the thermal oxidation of silicon, can accurately describe CNT growth behavior. The diffusion of gases in the spaces between densely-packed nanotubes in CNT films is consistent with Knudsen diffusion with a diffusion coefficient on the order of 10^{-4} cm^2/s. At a relatively low temperature, CNT growth occurred in the kinetics-controlled regime; CNT growth was first order with an activation energy of 201.2 kJ/mol. By deceasing the ethylene flow time in growth cycles, this CNT stack growth technique was used to observe the initial stage of CNT growth. Within one minute, CNT growth reaches steady state.

The required high CNT growth temperature remains a challenge for implementation of CNTs into microelectronics manufacturing sequences, since high CNT synthesis temperatures (>600°C) are incompatible with microelectronic processes. However, if the growth temperature is reduced to less than 600 °C, formation of high-quality CNTs with good alignment is not easy to achieve. For direct CNT growth on substrates, the poor mechanical bonding strength at the CNT-substrate interfaces results in long term reliability limitations and high interface thermal resistance. To overcome these challenges, a CNT transfer process was proposed to assemble aligned CNT structures (films, stacks & bundles) at a low temperature compatible with current microelectronics fabrication sequences and technology. The distinctive CNT-transfer-technology developed results from the separation of CNT growth and CNT device assembly. SEM observations indicate that the excellent mechanical bonding strength of solder in contact with CNTs anchors them securely onto a substrate. Field emission testing of the as-assembled CNT devices indicates good field emission characteristics, with a field enhancement factor of 4540. These testing results are in agreement with Fowler-Nordheim tunneling, which implies good electrical contact between CNTs and solder, and a very small voltage drop across CNT/solder interfaces. Preliminary electrical transport measurements of CNT films, as well as double- and triple-layered CNT stacks assembled onto copper substrates by CNT transfer technology have been performed. The measured resistivity of long CNTs (>150 μm) is ~2.3×10^{-4} Ω-cm. These measurements also demonstrate that low-resistance ohmic CNT/solder (Sn-Pb) junctions can be formed by a solder reflow process, which offers an effective approach to integrate or assemble CNTs with integrated circuits at low temperatures. These studies also show that CNT stack junctions, formed by entanglement or crossing of CNTs at interfaces over a length-scale of 400 nm, can form ohmic contacts with a specific contact resistance of 9.01×10^{-3} Ω-cm^2 and a transmission probability (T_j) of 2.41×10^{-5}. Overall, the advantages of CNT

transfer technology are embodied in the low process temperature, adhesion improvement and the feasibility of transferring CNTs to a variety of substrates.

Wettability of nanotube surfaces by liquids is of great importance in fundamental research and practical applications. To study the surface geometric effects on wetting, two model surfaces with two tier scale roughness were fabricated by controlled growth of CNT arrays followed by coating with plasma polymerized fluorocarbon layers. The CNT array size, pitch and height have been varied to explore geometric effects on surface hydrophobicity. Compared to patterned Si surfaces with similar geometrical sizes, the nano-scale roughness does not significantly increase the apparent water contact angle; the micro-scale roughness determines the apparent water contact angle provided that the micro-scale roughness dominates the nano-scale roughness. In addition, introduction of nano-scale roughness can decrease the contact angle hysteresis to less than 1° and improve the stability of superhydrophobic surfaces. Furthermore, nano-scale roughness can also reduce the strict requirements of micro-scale roughness design for superhydrophobic surfaces. Introduction of nano-scale roughness on the groove bottom can decrease the micro-scale array height needed for superhydrophobicity. These results improve the understanding of the effects of two-tier roughness on superhydrophobicity and offer additional design approaches for stable and robust superhydrophobic surfaces with self-cleaning properties.

Due to the hydrophobicity of nanotube structures, electrowetting was investigated to reduce the hydrophobicity of aligned CNTs by controllably reducing or tailoring the interfacial tension between carbon nanotubes (CNTs) and liquids. The contact angles of DI water and 0.03 M NaCl droplets saturate at 98° and 50°, respectively. Unlike electrowetting of flat, smooth electrodes, aligned CNT films introduce a geometrical roughness, which affects surface wetting. The contact angle dependence on external voltage and surface roughness can be described by a modified Cassie or Wenzel equation. From the simplified models, the capacitance of the electrical double layer formed

between aligned CNTs and either DI water or aqueous 0.03 M NaCl solutions can be extracted with a value of 0.017 and 0.311 $\mu F/cm^2$, respectively. Electrowetting can be invoked to facilitate infiltration of high-surface-tension monomers into pre-aligned nanotube films for preparation of CNT-reinforced composites.

Finally, preparation of aligned CNT/epoxy composites was studied to assess potential applications in thermal interface materials (TIMs) and high performance composites. One of the keys to successsul fabrication of such composites is improvement of the stability and strength of CNT/epoxy interfaces. Such improvements can be achieved by selection of an appropriate composite curing method. In our study, variable frequency microwave (VFM) radiation is employed to cure the aligned CNT/epoxy composites. Compared to composites cured by thermal heating, VFM-cured composites demonstrate higher CNT/matrix interfacial bonding strength, which is reflected in a negative thermal expansion of the composites. The observed thermal contraction of the composites is ascribed to the unexpected large thermal contraction of MWNTs (<-160 ppm/°C). Indeed, improved CNT/epoxy interfaces enhance the thermal conductivity of the composites by 26-30%. Thus, in addition to their use as reinforcing fibers for composites, MWNTs, which serve as highly negative CTE materials, offer much promise as effective fillers to tailor the CTE of polymer/CNT composites.

7.2 Future Work

7.2.1 Enhancement of CNT/Substrate Interface Properties through Conductive Molecules

In order to extend the approach that we developed to transfer aligned CNTs to substrates by a solder reflow process, we propose the direct attachment of aligned and in-situ functionalized CNTs onto metal or silicon surfaces by covalent chemical bonding. Figure 7.1 demonstrates the concept of attaching CNTs onto gold surfaces by organic molecule linking. In fact, the targeted substrates should not be limited to gold. In order to accomplish this goal, the following issues need to be investigated:

- In-situ functionalization of aligned CNT tips

In-situ functionalization processes are necessary to attach carboxylic acid or hydroxyl groups at the tips of aligned CNTs. We have shown that aqueous hydrogen peroxide (H_2O_2) can in-situ functionalize CNTs in chapter 2.6. The concentration of H_2O_2 and CNT growth process must be optimized to maximize the functionalization of CNTs at tips.

- Self-assembled monolayer (SAM) treatment of metal and silicon surfaces

Assemblies of SAMs onto metal substrates (Cu, Au and Ag) should be studied. Three types of organosulfur compounds are chosen for metal surfaces: alkanethiols ($HS(CH_2)_nX$), dialkyl disulfides ($X(CH_2)_mS\text{-}S(CH_2)_nX$), and dialkyl sulfides ($X(CH_2)_mS(CH_2)_nX$), where n and m are the number of methylene units and X represents the end group of the alkyl chain (-OH, -COOH) and amine ($-NH_2$). The basic structural characteristics of surface structure, chain organization, and orientation will be explored. The procedures for preparing SAMs (concentration, length of immersion time, solvents, temperature) will be specified. Silanes will be selected to treat silicon surfaces. The chosen SAMs should be conducting and thermally stable at elevated temperatures (~150 °C).

- Covalent chemical bonding of functionalized aligned CNTs onto metal surfaces coated with SAMs

The carboxylic or hydroxyl groups on functionalized CNT tips react with hydroxyl or carboxylic groups on SAM tips by a condensation reaction. The bonding strength, electrical, and thermal properties of CNTs chemically bonded to substrates will be characterized. Specifically, identification of appropriate SAMs (matching different metal surfaces) for chemical bonding of the aligned CNTs with excellent interfacial properties, and determination of fundamental understanding will also be goals.

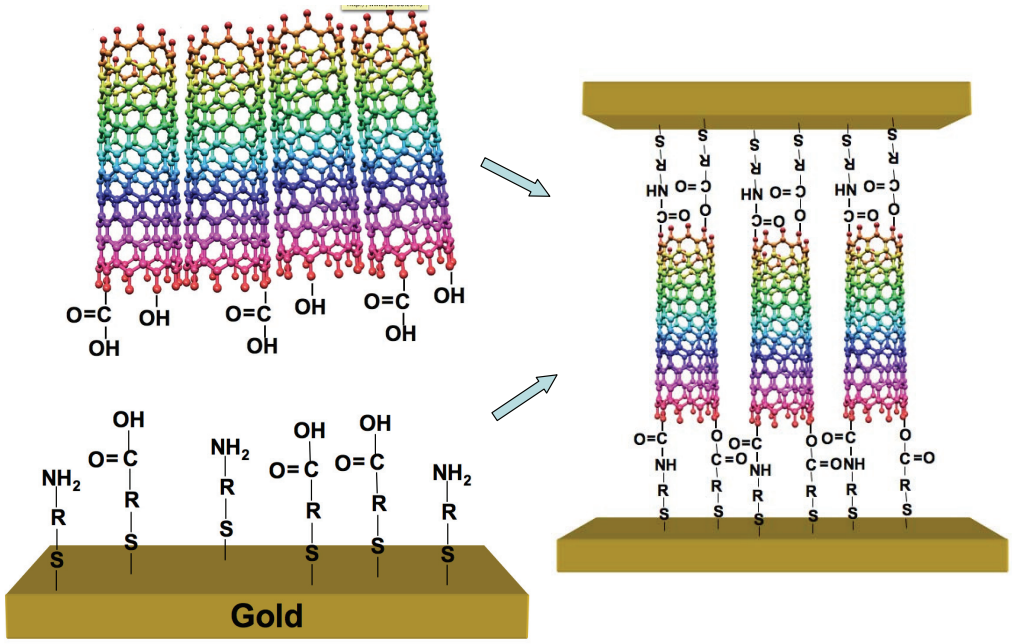

Figure 7.1 Schematic of aligned in-situ functionalized CNTs transferred to surfaces by organic molecules. This process can be applied to assemble CNTs onto other metal or silicon surfaces.

7.2.2 Thermal Characterization of CNT Assembly

Currently, thermal management of microprocessors (~up to 200 W) and high power micro-devices is critical and necessitates advances in power dissipation technology. For thermal management applications, carbon nanotubes (CNTs), due to their unique thermal properties, offer new opportunities in thermal management of microelectronic devices. CNT-based thermal moduli enabled by CNT transfer processes for device thermal management make possible enhanced and directional thermal conductivity along with flexible geometry.

These efforts will focus on improving overall thermal performance of the CNT assembly. For example, the solder layer thickness and material selection will affect the solder/CNT thermal contact resistance. Of course, the quality of aligned CNTs is also key to the overall thermal performance of the assembly. Thermal characterization of the CNT assembly will be conducted by a thermal acoustic method. Figure 7.2 shows a schematic of the experimental configuration for thermal measurement of CNT assemblies [277].

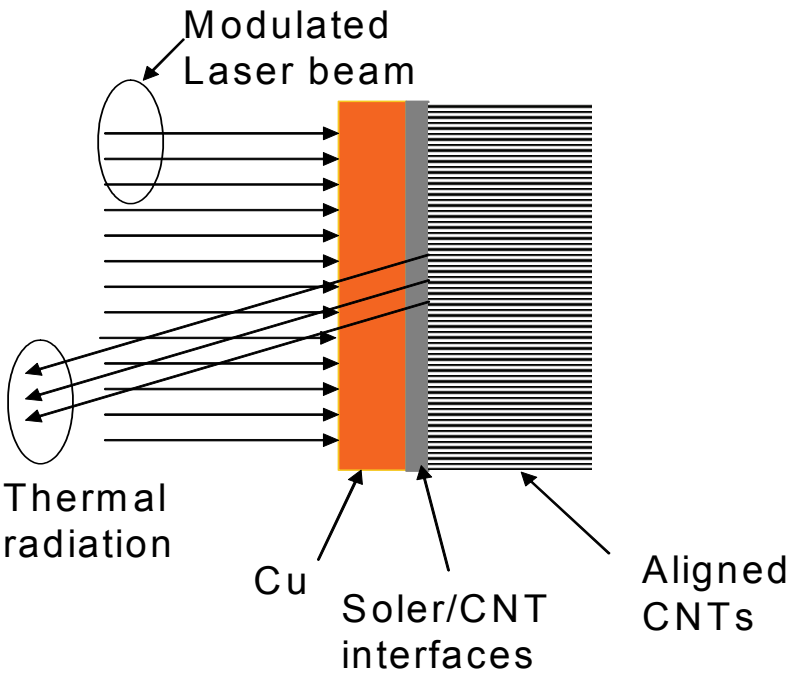

Figure 7.2 Schematic of the experimental configuration for thermal measurements of CNT assemblies [277].

A modulated laser beam is used to irradiate the backside (copper side) of a CNT assembly. The laser beam induces direct heating of the copper plate, generating a periodic temperature variation at the substrate. Thermal conduction along the CNTs causes a temperature variation, which can be sensed by measuring the surface thermal radiation. The phase shift of the surface thermal radiation relative to the laser beam is recorded to determine the sample thermophysical properties. These measurements are performed over a large frequency range. Trial values of unknown properties will be used to compute the theoretical phase shift at each experimental frequency; values will be assigned until the best fit with experimental data is achieved.

7.2.3 Characterization of CNT/Polymer Interfaces in Composites Cured by VFM

In Chapter 6, we demonstrated that CNT/epoxy composites cured by VFM show improved CNT/matrix interfacial bonding strength. VFM radiation both promotes uniform bonding of epoxy along the nanotube walls and enhances adhesion of the polymerized epoxy to the array of nanotubes. Therefore, the load (stress) on the polymer matrix during subsequent heat cycling can be effectively transferred to the nanotubes. Raman spectroscopy has been used to characterize the interfacial properties of aramid/epoxy model composites [278] and randomly mixed CNT/epoxy composites deformed by mechanical bending [279]. Instead of using different micromechanical test methods to induce tensile loading, we can place samples on the Raman sample stage and supply heat to induce a shear stress along the nanotube axis. Changes with increasing temperature will be observed, since the nanotube CTE is negative but the CTE of the polymeric matrix is positive. By determining Raman band shifts with increasing temperature, we can correlate the levels of reinforcement from the nanotubes with the preparation procedures of CNT composites, and thus investigate structure/property relationships in CNT composites cured by thermal heating or VFM radiation.

APPENDIX A

AUTHOR'S AWARDS AND PUBLICATIONS

A.1 Awards

[1] The Intel Best Student Paper Award, 56th Electronic Components and Technology Conference, 2006.

[2] Award of Outstanding Technical Paper, 7th Electronics Packaging Technology Conference, 2005.

[3] Finalist for 14th Motorola/ IEEE CPMT Society Graduate Student Fellowship, 2006.

[4] Advanced Publication Award, MSE, Georgia Institute of Technology, 2006.

[5] Finalist for the 13th Motorola/ IEEE CPMT Society Graduate Student Fellowship, 2005.

A.2 Journal Publications

[1] **L. B. Zhu**, H. J. Jiang, K. S. Moon, H. P. Sun, D. W. Hess, and C. P. Wong, "Negative Thermal Expansion in Aligned Carbon Nanotube/Epoxy Composites", submitted, 2007.

[2] Y. H. Xiu, **L. B. Zhu**, D. W. Hess, and C. P. Wong, "Hierarchical Silicon Etched Structures for Controlled Hydrophobicity/Superhydrophobicity", ***Nano Letters***, accepted.

[3] **L. B. Zhu**, J. W. Xu, F. Xiao, H. J. Jiang, D. W. Hess, and C. P. Wong, "The Growth of Carbon Nanotube Stacks in the Kinetics-controlled Regime", ***Carbon***, 45(2), 344-348, 2007.

[4] H. J. Jiang, **L. B. Zhu**, K. S. Moon, and C. P. Wong, "Low Temperature Carbon Nanotube Film Transfer via Conductive Polymer Composites", ***Nanotechnology***, 18(12), 125203, 2007.

[5] H. J. Jiang, **L. B. Zhu**, K. S. Moon, and C. P. Wong, "The Preparation of Stable Metal Nanoparticles on Carbon Nanotubes Whose Surfaces were Modified During Production", ***Carbon***, 45(3), 655-661, 2007.

[6] Y. H. Xiu, **L. B. Zhu**, D. W. Hess, and C. P. Wong, "Biomimetic Creation of Hierarchical Surface Structures by Combining Colloidal Self-Assembly and Au Sputter Deposition", ***Langmuir***, 22(23), 9676-9681, 2006.

[7] **L. B. Zhu**, J. W. Xu, Y. H. Xiu, Y. Y. Sun, D. W. Hess, and C. P. Wong, "Electrowetting of Aligned Carbon Nanotube Films", ***Journal of Physical Chemistry – B***, 110(32), 15945-15950, 2006.

[8] **L. B. Zhu**, D. W. Hess, and C. P. Wong, "Monitoring Carbon Nanotube Growth by Formation of Nanotube Stacks and Investigation of the Diffusion-Controlled Kinetics", ***Journal of Physical Chemistry – B***, 110(11), 5445-5449, 2006.

[9] **L. B. Zhu**, Y. Y. Sun, Dennis W. Hess, and C. P. Wong, "Well-Aligned Open-Ended Carbon Nanotube Architectures: an Approach for Device Assembly", ***Nano Letters***, 6(2), 243-247, 2006.

[10] **L. B. Zhu**, J. W. Xu, Y. H. Xiu, D. W. Hess, and C. P. Wong, "A Rapid Growth of Aligned Carbon Nanotube Films and High-Aspect-Ratio Arrays", ***Journal of Electronic Materials***, 35(2), 195-199, 2006.

[11] **L. B. Zhu**, J. W. Xu, Y. H. Xiu, Y. Y. Sun, D. W. Hess and C. P. Wong, "Controlled Growth and Electrical Characterization of High-Aspect-Ratio Aligned Carbon Nanotube Arrays", ***Carbon***, 44(2), 253-258, 2006.

[12] **L. B. Zhu**, Y. H. Xiu, D. W. Hess, and C. P. Wong, "Aligned Carbon Nanotube Stacks by Water-Assisted Selective Etching", ***Nano Letters***, 5(12), 2641-2645, 2005.

[13] **L. B. Zhu**, Y. H. Xiu, J. W. Xu, P. A. Tamirisa, D. W. Hess, and C. P. Wong, "Superhydrophobicity on Two-tier Rough Surfaces Fabricated by Controlled Growth of Aligned Carbon Nanotube Arrays Coated with Fluorocarbon", ***Langmuir***, 21(24), 11208-11212, 2005.

REFERENCES

[1] M. S. Dresselhaus, G. Dresselhaus, and P. Avouris, *Carbon nanotubes -- synthesis, structure, properties and applications*. Berlin: Springer-Verlag Berlin Heidelberg, 2001.

[2] M. Inagaki, *New Carbons -- Control of Structure and Functions*. Amsterdam, Netherlands: Elsevier, 2000.

[3] F. P. Bundy, W. A. Bassett, M. S. Weathers, R. J. Hemley, H. K. Mao, and A. F. Goncharov, "The pressure-temperature phase and transformation diagram for carbon; Updated through 1994," *Carbon*, vol. 34, pp. 141-153, 1996.

[4] A. Oberlin, M. Endo, and T. Koyama, "Filamentous Growth of Carbon through Benzene Decomposition," *Journal of Crystal Growth*, vol. 32, pp. 335-349, 1976.

[5] A. Oberlin, M. Endo, and T. Koyama, "High-Resolution Electron-Microscope Observations of Graphitized Carbon-Fibers," *Carbon*, vol. 14, pp. 133-135, 1976.

[6] T. Koyama, Y. Onuma, and M. Endo, "Carbon Fibers Obtained by Thermal-Decomposition of Vaporized Hydrocarbon," *Japanese Journal of Applied Physics*, vol. 11, pp. 445-449, 1972.

[7] M. Endo, T. Koyama, and M. Inagaki, "Preparation and Electronic-Properties of Intercalation Compounds of Graphite Fibers," *Synthetic Metals*, vol. 3, pp. 177-186, 1981.

[8] Lieberma.Ml, C. R. Hills, and C. Miglioni., "Growth of Graphite Filaments," *Carbon*, vol. 9, pp. 633-&, 1971.

[9] S. Iijima, "Helical Microtubules of Graphitic Carbon," *Nature*, vol. 354, pp. 56-58, 1991.

[10] S. Iijima and T. Ichihashi, "Single-Shell Carbon Nanotubes of 1-Nm Diameter," *Nature*, vol. 363, pp. 603-605, 1993.

[11] S. Iijima and T. Ichihashi, "Single-Shell Carbon Nanotubes of 1-Nm Diameter (Vol 363, Pg 603, 1993)," *Nature*, vol. 364, pp. 737-737, 1993.

[12] M. S. Dresselhaus, G. Dresselhaus, and R. Saito, "Carbon-Fibers Based on C-60 and Their Symmetry," *Physical Review B*, vol. 45, pp. 6234-6242, 1992.

[13] R. Saito, M. Fujita, G. Dresselhaus, and M. S. Dresselhaus, "Electronic-Structure of Chiral Graphene Tubules," *Applied Physics Letters*, vol. 60, pp. 2204-2206, 1992.

[14] J. W. Mintmire, B. I. Dunlap, and C. T. White, "Are Fullerene Tubules Metallic," *Physical Review Letters*, vol. 68, pp. 631-634, 1992.

[15] N. Hamada, S. Sawada, and A. Oshiyama, "New One-Dimensional Conductors - Graphitic Microtubules," *Physical Review Letters*, vol. 68, pp. 1579-1581, 1992.

[16] T. W. Odom, J. L. Huang, P. Kim, and C. M. Lieber, "Atomic structure and electronic properties of single-walled carbon nanotubes," *Nature*, vol. 391, pp. 62-64, 1998.

[17] J. W. G. Wildoer, L. C. Venema, A. G. Rinzler, R. E. Smalley, and C. Dekker, "Electronic structure of atomically resolved carbon nanotubes," *Nature*, vol. 391, pp. 59-62, 1998.

[18] M. S. Dresselhaus, G. Dresselhaus, and R. Saito, "Physics of Carbon Nanotubes," *Carbon*, vol. 33, pp. 883-891, 1995.

[19] M. S. Dresselhaus, G. Dresselhaus, A. Jorio, A. G. Souza, and R. Saito, "Raman spectroscopy on isolated single wall carbon nanotubes," *Carbon*, vol. 40, pp. 2043-2061, 2002.

[20] T. W. Ebbesen and P. M. Ajayan, "Large-Scale Synthesis of Carbon Nanotubes," *Nature*, vol. 358, pp. 220-222, 1992.

[21] D. S. Bethune, C. H. Kiang, M. S. Devries, G. Gorman, R. Savoy, J. Vazquez, and R. Beyers, "Cobalt-Catalyzed Growth of Carbon Nanotubes with Single-Atomic-Layerwalls," *Nature*, vol. 363, pp. 605-607, 1993.

[22] A. Thess, R. Lee, P. Nikolaev, H. J. Dai, P. Petit, J. Robert, C. H. Xu, Y. H. Lee, S. G. Kim, A. G. Rinzler, D. T. Colbert, G. E. Scuseria, D. Tomanek, J. E. Fischer, and R. E. Smalley, "Crystalline ropes of metallic carbon nanotubes," *Science*, vol. 273, pp. 483-487, 1996.

[23] J. Liu, A. G. Rinzler, H. J. Dai, J. H. Hafner, R. K. Bradley, P. J. Boul, A. Lu, T. Iverson, K. Shelimov, C. B. Huffman, F. Rodriguez-Macias, Y. S. Shon, T. R. Lee, D. T. Colbert, and R. E. Smalley, "Fullerene pipes," *Science*, vol. 280, pp. 1253-1256, 1998.

[24] M. Su, B. Zheng, and J. Liu, "A scalable CVD method for the synthesis of single-walled carbon nanotubes with high catalyst productivity," *Chemical Physics Letters*, vol. 322, pp. 321-326, 2000.

[25] S. Amelinckx, D. Bernaerts, X. B. Zhang, G. Vantendeloo, and J. Vanlanduyt, "A Structure Model and Growth-Mechanism for Multishell Carbon Nanotubes," *Science*, vol. 267, pp. 1334-1338, 1995.

[26] S. Amelinckx, X. B. Zhang, D. Bernaerts, X. F. Zhang, V. Ivanov, and J. B. Nagy, "A Formation Mechanism for Catalytically Grown Helix-Shaped Graphite Nanotubes," *Science*, vol. 265, pp. 635-639, 1994.

[27] Y. M. Shyu and F. C. N. Hong, "Low-temperature growth and field emission of aligned carbon nanotubes by chemical vapor deposition," *Materials Chemistry and Physics*, vol. 72, pp. 223-227, 2001.

[28] Y. M. Shyu and F. C. N. Hong, "The effects of pre-treatment and catalyst composition on growth of carbon nanofibers at low temperature," *Diamond and Related Materials*, vol. 10, pp. 1241-1245, 2001.

[29] D. Laplaze, L. Alvarez, T. Guillard, J. M. Badie, and G. Flamant, "Carbon nanotubes: dynamics of synthesis processes," *Carbon*, vol. 40, pp. 1621-1634, 2002.

[30] K. Hata, D. N. Futaba, K. Mizuno, T. Namai, M. Yumura, and S. Iijima, "Water-assisted highly efficient synthesis of impurity-free single-waited carbon nanotubes," *Science*, vol. 306, pp. 1362-1364, 2004.

[31] M. J. Kim, N. Nicholas, C. Kittrell, E. Haroz, H. W. Shan, T. J. Wainerdi, S. Lee, H. K. Schmidt, R. E. Smalley, and R. H. Hauge, "Efficient transfer of a VA-SWNT film by a flip-over technique," *Journal of the American Chemical Society*, vol. 128, pp. 9312-9313, 2006.

[32] R. Sen, A. Govindaraj, and C. N. R. Rao, "Carbon nanotubes by the metallocene route," *Chemical Physics Letters*, vol. 267, pp. 276-280, 1997.

[33] Y. Shimizu, T. Sasaki, T. Kodaira, K. Kawaguchi, K. Terashima, and N. Koshizaki, "Fabrication of carbon nanotube assemblies on Ni-Mo substrates mimics law of natural forest growth," *Chemical Physics Letters*, vol. 370, pp. 774-780, 2003.

[34] H. Y. Shang and C. G. Liu, "XPS study of carbon nanotube supported CoMo catalysts.," *Abstracts of Papers of the American Chemical Society*, vol. 227, pp. U230-U230, 2004.

[35] C. J. Lee, S. C. Lyu, H. W. Kim, J. W. Park, H. M. Jung, and J. Park, "Carbon nanotubes produced by tungsten-based catalyst using vapor phase deposition method," *Chemical Physics Letters*, vol. 361, pp. 469-472, 2002.

[36] Y. F. Wang, H. R. Liu, X. X. Xu, Y. Shao, X. W. Cao, S. F. Hu, Y. Y. Liu, and G. X. Lan, "Raman scattering of single-wall carbon nanotubes produced using Y/Ni catalyst," *Spectroscopy and Spectral Analysis*, vol. 22, pp. 580-583, 2002.

[37] S. Seraphin and D. Zhou, "Single-Walled Carbon Nanotubes Produced at High-Yield by Mixed Catalysts," *Applied Physics Letters*, vol. 64, pp. 2087-2089, 1994.

[38] A. M. Cassell, J. A. Raymakers, J. Kong, and H. J. Dai, "Large scale CVD synthesis of single-walled carbon nanotubes," *Journal of Physical Chemistry B*, vol. 103, pp. 6484-6492, 1999.

[39] S. S. Fan, M. G. Chapline, N. R. Franklin, T. W. Tombler, A. M. Cassell, and H. J. Dai, "Self-oriented regular arrays of carbon nanotubes and their field emission properties," *Science*, vol. 283, pp. 512-514, 1999.

[40] J. Kong, A. M. Cassell, and H. J. Dai, "Chemical vapor deposition of methane for single-walled carbon nanotubes," *Chemical Physics Letters*, vol. 292, pp. 567-574, 1998.

[41] A. M. Cassell, S. Verma, L. Delzeit, M. Meyyappan, and J. Han, "Combinatorial optimization of heterogeneous catalysts used in the growth of carbon nanotubes," *Langmuir*, vol. 17, pp. 260-264, 2001.

[42] B. Chen, G. Parker, J. Han, M. Meyyappan, and A. M. Cassell, "Heterogeneous single-walled carbon nanotube catalyst discovery and optimization," *Chemistry of Materials*, vol. 14, pp. 1891-1896, 2002.

[43] V. I. Merkulov, D. H. Lowndes, Y. Y. Wei, G. Eres, and E. Voelkl, "Patterned growth of individual and multiple vertically aligned carbon nanofibers," *Applied Physics Letters*, vol. 76, pp. 3555-3557, 2000.

[44] V. I. Merkulov, M. A. Guillorn, D. H. Lowndes, M. L. Simpson, and E. Voelkl, "Shaping carbon nanostructures by controlling the synthesis process," *Applied Physics Letters*, vol. 79, pp. 1178-1180, 2001.

[45] M. Chhowalla, K. B. K. Teo, C. Ducati, N. L. Rupesinghe, G. A. J. Amaratunga, A. C. Ferrari, D. Roy, J. Robertson, and W. I. Milne, "Growth process conditions of vertically aligned carbon nanotubes using plasma enhanced chemical vapor deposition," *Journal of Applied Physics*, vol. 90, pp. 5308-5317, 2001.

[46] L. Valentini, J. M. Kenny, L. Lozzi, and S. Santucci, "Formation of carbon nanotubes by plasma enhanced chemical vapor deposition: Role of nitrogen and catalyst layer thickness," *Journal of Applied Physics*, vol. 92, pp. 6188-6194, 2002.

[47] Z. F. Ren, Z. P. Huang, D. Z. Wang, J. G. Wen, J. W. Xu, J. H. Wang, L. E. Calvet, J. Chen, J. F. Klemic, and M. A. Reed, "Growth of a single freestanding multiwall carbon nanotube on each nanonickel dot," *Applied Physics Letters*, vol. 75, pp. 1086-1088, 1999.

[48] L. B. Zhu, J. W. Xu, Y. H. Xiu, Y. Y. Sun, D. W. Hess, and C. P. Wong, "Growth and electrical characterization of high-aspect-ratio carbon nanotube arrays," *Carbon*, vol. 44, pp. 253-258, 2006.

[49] R. Sen, A. Govindaraj, and C. N. R. Rao, "Metal-billed and hollow carbon nanotubes obtained by the decomposition of metal-containing free precursor molecules," *Chemistry of Materials*, vol. 9, pp. 2078-2081, 1997.

[50] P. Nikolaev, M. J. Bronikowski, R. K. Bradley, F. Rohmund, D. T. Colbert, K. A. Smith, and R. E. Smalley, "Gas-phase catalytic growth of single-walled carbon nanotubes from carbon monoxide," *Chemical Physics Letters*, vol. 313, pp. 91-97, 1999.

[51] R. Andrews, D. Jacques, A. M. Rao, F. Derbyshire, D. Qian, X. Fan, E. C. Dickey, and J. Chen, "Continuous production of aligned carbon nanotubes: a step closer to commercial realization," *Chemical Physics Letters*, vol. 303, pp. 467-474, 1999.

[52] C. J. Lee, J. Park, and J. A. Yu, "Catalyst effect on carbon nanotubes synthesized by thermal chemical vapor deposition," *Chemical Physics Letters*, vol. 360, pp. 250-255, 2002.

[53] R. Andrews, D. Jacques, D. L. Qian, and T. Rantell, "Multiwall carbon nanotubes: Synthesis and application," *Accounts of Chemical Research*, vol. 35, pp. 1008-1017, 2002.

[54] K. Hernadi, A. Fonseca, J. B. Nagy, D. Bernaerts, and A. A. Lucas, "Fe-catalyzed carbon nanotube formation," *Carbon*, vol. 34, pp. 1249-1257, 1996.

[55] J. F. Colomer, G. Bister, I. Willems, Z. Konya, A. Fonseca, G. Van Tendeloo, and J. B. Nagy, "Synthesis of single-wall carbon nanotubes by catalytic decomposition of hydrocarbons," *Chemical Communications*, pp. 1343-1344, 1999.

[56] R. L. Vander Wal, T. M. Ticich, and V. E. Curtis, "Substrate-support interactions in metal-catalyzed carbon nanofiber growth," *Carbon*, vol. 39, pp. 2277-2289, 2001.

[57] I. Willems, Z. Konya, J. F. Colomer, G. Van Tendeloo, N. Nagaraju, A. Fonseca, and J. B. Nagy, "Control of the outer diameter of thin carbon nanotubes synthesized by catalytic decomposition of hydrocarbons," *Chemical Physics Letters*, vol. 317, pp. 71-76, 2000.

[58] M. Su, Y. Li, B. Maynor, A. Buldum, J. P. Lu, and J. Liu, "Lattice-oriented growth of single-walled carbon nanotubes," *Journal of Physical Chemistry B*, vol. 104, pp. 6505-6508, 2000.

[59] A. Kukovecz, Z. Konya, N. Nagaraju, I. Willems, A. Tamasi, A. Fonseca, J. B. Nagy, and I. Kiricsi, "Catalytic synthesis of carbon nanotubes over Co, Fe and Ni containing conventional and sol-gel silica-aluminas," *Physical Chemistry Chemical Physics*, vol. 2, pp. 3071-3076, 2000.

[60] R. Andrews and M. C. Weisenberger, "Carbon nanotube polymer composites," *Current Opinion in Solid State & Materials Science*, vol. 8, pp. 31-37, 2004.

[61] S. B. Sinnott, R. Andrews, D. Qian, A. M. Rao, Z. Mao, E. C. Dickey, and F. Derbyshire, "Model of carbon nanotube growth through chemical vapor deposition," *Chemical Physics Letters*, vol. 315, pp. 25-30, 1999.

[62] R. T. K. Baker, "Catalytic Growth of Carbon Filaments," *Carbon*, vol. 27, pp. 315-323, 1989.

[63] R. T. K. Baker, M. A. Barber, R. J. Waite, P. S. Harris, and F. S. Feates, "Nucleation and Growth of Carbon Deposits from Nickel Catalyzed Decomposition of Acetylene," *Journal of Catalysis*, vol. 26, pp. 51-&, 1972.

[64] R. T. K. Baker, P. S. Harris, and S. Terry, "Unique Form of Filamentous Carbon," *Nature*, vol. 253, pp. 37-39, 1975.

[65] C. W. Keep, R. T. K. Baker, and J. A. France, "Origin of Filamentous Carbon Formation from Reaction of Propane over Nickel," *Journal of Catalysis*, vol. 47, pp. 232-238, 1977.

[66] N. M. Rodriguez, M. S. Kim, F. Fortin, I. Mochida, and R. T. K. Baker, "Carbon deposition on iron-nickel alloy particles," *Applied Catalysis a-General*, vol. 148, pp. 265-282, 1997.

[67] R. T. Yang and S. J. Doong, "Gas Separation by Pressure Swing Adsorption - a Pore-Diffusion Model for Bulk Separation," *Aiche Journal*, vol. 31, pp. 1829-1842, 1985.

[68] R. T. Yang and K. L. Yang, "Evidence for Temperature-Driven Carbon Diffusion Mechanism of Coke Deposition on Catalysts," *Journal of Catalysis*, vol. 93, pp. 182-185, 1985.

[69] R. T. K. Baker, M. A. Barber, R. J. Waite, P. S. Harris, and F. S. Feates, "Nucleation and Growth of Carbon Deposits from Nickel Catalyzed Decomposition of Acetylene," *Journal of Catalysis*, vol. 26, pp. 51-62, 1972.

[70] R. T. K. Baker, P. S. Harris, R. B. Thomas, and R. J. Waite, "Formation of Filamentous Carbon from Iron, Cobalt and Chromium Catalyzed Decomposition of Acetylene," *Journal of Catalysis*, vol. 30, pp. 86-95, 1973.

[71] J. R. Nielsen and D. L. Trimm, "Mechanisms of Carbon Formation on Nickel-Containing Catalysts," *Journal of Catalysis*, vol. 48, pp. 155-165, 1977.

[72] T. A. Massaro and E. E. Petersen, "Bulk Diffusion of Carbon-14 through Polycrystalline Nickel Foil between 350 and 700 Degrees C," *Journal of Applied Physics*, vol. 42, pp. 5534-&, 1971.

[73] T. Wada, H. Wada, J. F. Elliott, and J. Chipman, "Thermodynamics of Fcc Fe-Ni-C and Ni-C Alloys," *Metallurgical Transactions*, vol. 2, pp. 2199-2208, 1971.

[74] X. Blase, L. X. Benedict, E. L. Shirley, and S. G. Louie, "Hybridization Effects and Metallicity in Small Radius Carbon Nanotubes," *Physical Review Letters*, vol. 72, pp. 1878-1881, 1994.

[75] M. Bockrath, D. H. Cobden, P. L. McEuen, N. G. Chopra, A. Zettl, A. Thess, and R. E. Smalley, "Single-electron transport in ropes of carbon nanotubes," *Science*, vol. 275, pp. 1922-1925, 1997.

[76] S. J. Tans, M. H. Devoret, H. J. Dai, A. Thess, R. E. Smalley, L. J. Geerligs, and C. Dekker, "Individual single-wall carbon nanotubes as quantum wires," *Nature*, vol. 386, pp. 474-477, 1997.

[77] M. Ouyang, J. L. Huang, C. L. Cheung, and C. M. Lieber, "Atomically resolved single-walled carbon nanotube intramolecular junctions," *Science*, vol. 291, pp. 97-100, 2001.

[78] S. Frank, P. Poncharal, Z. L. Wang, and W. A. de Heer, "Carbon nanotube quantum resistors," *Science*, vol. 280, pp. 1744-1746, 1998.

[79] J. C. Charlier, "Defects in carbon nanotubes," *Accounts of Chemical Research*, vol. 35, pp. 1063-1069, 2002.

[80] A. De Vita, J. C. Charlier, X. Blase, and R. Car, "Electronic structure at carbon nanotube tips," *Applied Physics a-Materials Science & Processing*, vol. 68, pp. 283-286, 1999.

[81] P. Lambin, A. Fonseca, J. P. Vigneron, J. B. Nagy, and A. A. Lucas, "Structural and Electronic-Properties of Bent Carbon Nanotubes," *Chemical Physics Letters*, vol. 245, pp. 85-89, 1995.

[82] R. Saito, G. Dresselhaus, and M. S. Dresselhaus, "Tunneling conductance of connected carbon nanotubes," *Physical Review B*, vol. 53, pp. 2044-2050, 1996.

[83] J. C. Charlier, T. W. Ebbesen, and P. Lambin, "Structural and electronic properties of pentagon-heptagon pair defects in carbon nanotubes," *Physical Review B*, vol. 53, pp. 11108-11113, 1996.

[84] J. C. Charlier, P. Lambin, and T. W. Ebbesen, "Electronic properties of carbon nanotubes with polygonized cross sections," *Physical Review B*, vol. 54, pp. R8377-R8380, 1996.

[85] L. Chico, V. H. Crespi, L. X. Benedict, S. G. Louie, and M. L. Cohen, "Pure carbon nanoscale devices: Nanotube heterojunctions," *Physical Review Letters*, vol. 76, pp. 971-974, 1996.

[86] Z. Yao, H. W. C. Postma, L. Balents, and C. Dekker, "Carbon nanotube intramolecular junctions," *Nature*, vol. 402, pp. 273-276, 1999.

[87] D. L. Carroll, P. Redlich, X. Blase, J. C. Charlier, S. Curran, P. M. Ajayan, S. Roth, and M. Ruhle, "Effects of nanodomain formation on the electronic structure of doped carbon nanotubes," *Physical Review Letters*, vol. 81, pp. 2332-2335, 1998.

[88] R. Czerw, M. Terrones, J. C. Charlier, X. Blase, B. Foley, R. Kamalakaran, N. Grobert, H. Terrones, D. Tekleab, P. M. Ajayan, W. Blau, M. Ruhle, and D. L. Carroll, "Identification of electron donor states in N-doped carbon nanotubes," *Nano Letters*, vol. 1, pp. 457-460, 2001.

[89] X. Blase, J. C. Charlier, A. De Vita, R. Car, P. Redlich, M. Terrones, W. K. Hsu, H. Terrones, D. L. Carroll, and P. M. Ajayan, "Boron-mediated growth of long helicity-selected carbon nanotubes," *Physical Review Letters*, vol. 83, pp. 5078-5081, 1999.

[90] D. B. Mawhinney, V. Naumenko, A. Kuznetsova, J. T. Yates, J. Liu, and R. E. Smalley, "Surface defect site density on single walled carbon nanotubes by titration," *Chemical Physics Letters*, vol. 324, pp. 213-216, 2000.

[91] K. Balasubramanian and M. Burghard, "Chemically functionalized carbon nanotubes," *Small*, vol. 1, pp. 180-192, 2005.

[92] J. J. Zhao, H. K. Park, J. Han, and J. P. Lu, "Electronic properties of carbon nanotubes with covalent sidewall functionalization," *Journal of Physical Chemistry B*, vol. 108, pp. 4227-4230, 2004.

[93] J. Chen, M. A. Hamon, H. Hu, Y. S. Chen, A. M. Rao, P. C. Eklund, and R. C. Haddon, "Solution properties of single-walled carbon nanotubes," *Science*, vol. 282, pp. 95-98, 1998.

[94] M. A. Hamon, J. Chen, H. Hu, Y. S. Chen, M. E. Itkis, A. M. Rao, P. C. Eklund, and R. C. Haddon, "Dissolution of single-walled carbon nanotubes," *Advanced Materials*, vol. 11, pp. 834-840, 1999.

[95] M. Monthioux, B. W. Smith, B. Burteaux, A. Claye, J. E. Fischer, and D. E. Luzzi, "Sensitivity of single-wall carbon nanotubes to chemical processing: an electron microscopy investigation," *Carbon*, vol. 39, pp. 1251-1272, 2001.

[96] H. Hu, P. Bhowmik, B. Zhao, M. A. Hamon, M. E. Itkis, and R. C. Haddon, "Determination of the acidic sites of purified single-walled carbon nanotubes by acid-base titration," *Chemical Physics Letters*, vol. 345, pp. 25-28, 2001.

[97] A. Hirsch, "Functionalization of single-walled carbon nanotubes," *Angewandte Chemie-International Edition*, vol. 41, pp. 1853-1859, 2002.

[98] A. V. Okotrub, N. F. Yudanov, A. L. Chuvilin, I. P. Asanov, Y. V. Shubin, L. G. Bulusheva, A. V. Gusel'nikov, and I. S. Fyodorov, "Fluorinated cage multiwall carbon nanoparticles," *Chemical Physics Letters*, vol. 322, pp. 231-236, 2000.

[99] A. Hamwi, H. Alvergnat, S. Bonnamy, and F. Beguin, "Fluorination of carbon nanotubes," *Carbon*, vol. 35, pp. 723-728, 1997.

[100] E. T. Mickelson, C. B. Huffman, A. G. Rinzler, R. E. Smalley, R. H. Hauge, and J. L. Margrave, "Fluorination of single-wall carbon nanotubes," *Chemical Physics Letters*, vol. 296, pp. 188-194, 1998.

[101] H. Touhara and F. Okino, "Property control of carbon materials by fluorination," *Carbon*, vol. 38, pp. 241-267, 2000.

[102] Y. Hattori, K. Kobayashi, S. Kawasaki, F. Okino, K. Yanagiuchi, A. Tsuyoshi, M. Nakayama, K. Nakajima, K. Kimura, and H. Touhara, "Direct thermal fluorination of DLC surfaces," *Carbon*, vol. 36, pp. 1399-1401, 1998.

[103] N. F. Yudanov, A. V. Okotrub, Y. V. Shubin, L. I. Yudanova, L. G. Bulusheva, A. L. Chuvilin, and J. M. Bonard, "Fluorination of arc-produced carbon material containing multiwall nanotubes," *Chemistry of Materials*, vol. 14, pp. 1472-1476, 2002.

[104] K. F. Kelly, I. W. Chiang, E. T. Mickelson, R. H. Hauge, J. L. Margrave, X. Wang, G. E. Scuseria, C. Radloff, and N. J. Halas, "Insight into the mechanism of sidewall functionalization of single-walled nanotubes: an STM study," *Chemical Physics Letters*, vol. 313, pp. 445-450, 1999.

[105] K. N. Kudin, H. F. Bettinger, and G. E. Scuseria, "Fluorinated single-wall carbon nanotubes," *Physical Review B*, vol. 63, pp. 045413, 2001.

[106] Z. Gu, H. Peng, R. H. Hauge, R. E. Smalley, and J. L. Margrave, "Cutting single-wall carbon nanotubes through fluorination," *Nano Letters*, vol. 2, pp. 1009-1013, 2002.

[107] E. T. Mickelson, I. W. Chiang, J. L. Zimmerman, P. J. Boul, J. Lozano, J. Liu, R. E. Smalley, R. H. Hauge, and J. L. Margrave, "Solvation of fluorinated single-wall carbon nanotubes in alcohol solvents," *Journal of Physical Chemistry B*, vol. 103, pp. 4318-4322, 1999.

[108] P. R. Marcoux, J. Schreiber, P. Batail, S. Lefrant, J. Renouard, G. Jacob, D. Albertini, and J. Y. Mevellec, "A spectroscopic study of the fluorination and defluorination reactions on single-walled carbon nanotubes," *Physical Chemistry Chemical Physics*, vol. 4, pp. 2278-2285, 2002.

[109] W. Zhao, C. H. Song, B. Zheng, J. Liu, and T. Viswanathan, "Thermal recovery behavior of fluorinated single-walled carbon nanotubes," *Journal of Physical Chemistry B*, vol. 106, pp. 293-296, 2002.

[110] V. N. Khabashesku, W. E. Billups, and J. L. Margrave, "Fluorination of single-wall carbon nanotubes and subsequent derivatization reactions," *Accounts of Chemical Research*, vol. 35, pp. 1087-1095, 2002.

[111] P. J. Boul, J. Liu, E. T. Mickelson, C. B. Huffman, L. M. Ericson, I. W. Chiang, K. A. Smith, D. T. Colbert, R. H. Hauge, J. L. Margrave, and R. E. Smalley, "Reversible sidewall functionalization of buckytubes," *Chemical Physics Letters*, vol. 310, pp. 367-372, 1999.

[112] R. K. Saini, I. W. Chiang, H. Q. Peng, R. E. Smalley, W. E. Billups, R. H. Hauge, and J. L. Margrave, "Covalent sidewall functionalization of single wall carbon nanotubes," *Journal of the American Chemical Society*, vol. 125, pp. 3617-3621, 2003.

[113] M. Holzinger, O. Vostrowsky, A. Hirsch, F. Hennrich, M. Kappes, R. Weiss, and F. Jellen, "Sidewall functionalization of carbon nanotubes," *Angewandte Chemie-International Edition*, vol. 40, pp. 4002-4005, 2001.

[114] M. Holzinger, J. Abraha, P. Whelan, R. Graupner, L. Ley, F. Hennrich, M. Kappes, and A. Hirsch, "Functionalization of single-walled carbon nanotubes with (R-)oxycarbonyl nitrenes," *Journal of the American Chemical Society*, vol. 125, pp. 8566-8580, 2003.

[115] D. Tasis, N. Tagmatarchis, A. Bianco, and M. Prato, "Chemistry of carbon nanotubes," *Chemical Reviews*, vol. 106, pp. 1105-1136, 2006.

[116] A. Star, Y. Liu, K. Grant, L. Ridvan, J. F. Stoddart, D. W. Steuerman, M. R. Diehl, A. Boukai, and J. R. Heath, "Noncovalent side-wall functionalization of single-walled carbon nanotubes," *Macromolecules*, vol. 36, pp. 553-560, 2003.

[117] S. A. Curran, P. M. Ajayan, W. J. Blau, D. L. Carroll, J. N. Coleman, A. B. Dalton, A. P. Davey, A. Drury, B. McCarthy, S. Maier, and A. Strevens, "A

composite from poly(m-phenylenevinylene-co-2,5-dioctoxy-p-phenylenevinylene) and carbon nanotubes: A novel material for molecular optoelectronics," *Advanced Materials*, vol. 10, pp. 1091-1093, 1998.

[118] A. Star, J. F. Stoddart, D. Steuerman, M. Diehl, A. Boukai, E. W. Wong, X. Yang, S. W. Chung, H. Choi, and J. R. Heath, "Preparation and properties of polymer-wrapped single-walled carbon nanotubes," *Angewandte Chemie-International Edition*, vol. 40, pp. 1721-1725, 2001.

[119] J. N. Coleman, A. B. Dalton, S. Curran, A. Rubio, A. P. Davey, A. Drury, B. McCarthy, B. Lahr, P. M. Ajayan, S. Roth, R. C. Barklie, and W. J. Blau, "Phase separation of carbon nanotubes and turbostratic graphite using a functional organic polymer," *Advanced Materials*, vol. 12, pp. 213-216, 2000.

[120] N. Nakashima, Y. Tomonari, and H. Murakami, "Water-soluble single-walled carbon nanotubes via noncovalent sidewall-functionalization with a pyrene-carrying ammonium ion," *Chemistry Letters*, pp. 638-639, 2002.

[121] J. Zhang, J. K. Lee, Y. Wu, and R. W. Murray, "Photoluminescence and electronic interaction of anthracene derivatives adsorbed on sidewalls of single-walled carbon nanotubes," *Nano Letters*, vol. 3, pp. 403-407, 2003.

[122] K. A. S. Fernando, Y. Lin, W. Wang, S. Kumar, B. Zhou, S. Y. Xie, L. T. Cureton, and Y. P. Sun, "Diminished band-gap transitions of single-walled carbon nanotubes in complexation with aromatic molecules," *Journal of the American Chemical Society*, vol. 126, pp. 10234-10235, 2004.

[123] L. S. Fifield, L. R. Dalton, R. S. Addleman, R. A. Galhotra, M. H. Engelhard, G. E. Fryxell, and C. L. Aardahl, "Noncovalent functionalization of carbon nanotubes with molecular anchors using supercritical fluids," *Journal of Physical Chemistry B*, vol. 108, pp. 8737-8741, 2004.

[124] H. Paloniemi, T. Aaritalo, T. Laiho, H. Liuke, N. Kocharova, K. Haapakka, F. Terzi, R. Seeber, and J. Lukkari, "Water-soluble full-length single-wall carbon nanotube polyelectrolytes: Preparation and characterization," *Journal of Physical Chemistry B*, vol. 109, pp. 8634-8642, 2005.

[125] M. F. Islam, E. Rojas, D. M. Bergey, A. T. Johnson, and A. G. Yodh, "High weight fraction surfactant solubilization of single-wall carbon nanotubes in water," *Nano Letters*, vol. 3, pp. 269-273, 2003.

[126] O. Matarredona, H. Rhoads, Z. R. Li, J. H. Harwell, L. Balzano, and D. E. Resasco, "Dispersion of single-walled carbon nanotubes in aqueous solutions of the anionic surfactant NaDDBS," *Journal of Physical Chemistry B*, vol. 107, pp. 13357-13367, 2003.

[127] V. C. Moore, M. S. Strano, E. H. Haroz, R. H. Hauge, R. E. Smalley, J. Schmidt, and Y. Talmon, "Individually suspended single-walled carbon nanotubes in various surfactants," *Nano Letters*, vol. 3, pp. 1379-1382, 2003.

[128] M. S. Strano, V. C. Moore, M. K. Miller, M. J. Allen, E. H. Haroz, C. Kittrell, R. H. Hauge, and R. E. Smalley, "The role of surfactant adsorption during ultrasonication in the dispersion of single-walled carbon nanotubes," *Journal of Nanoscience and Nanotechnology*, vol. 3, pp. 81-86, 2003.

[129] J. J. Davis, M. L. H. Green, H. A. O. Hill, Y. C. Leung, P. J. Sadler, J. Sloan, A. V. Xavier, and S. C. Tsang, "The immobilisation of proteins in carbon nanotubes," *Inorganica Chimica Acta*, vol. 272, pp. 261-266, 1998.

[130] S. C. Tsang, J. J. Davis, M. L. H. Green, H. Allen, O. Hill, Y. C. Leung, and P. J. Sadler, "Immobilization of Small Proteins in Carbon Nanotubes - High-Resolution Transmission Electron-Microscopy Study and Catalytic Activity," *Journal of the Chemical Society-Chemical Communications*, pp. 1803-1804, 1995.

[131] S. C. Tsang, Z. J. Guo, Y. K. Chen, M. L. H. Green, H. A. O. Hill, T. W. Hambley, and P. J. Sadler, "Immobilization of platinated and iodinated oligonucleotides on carbon nanotubes," *Angewandte Chemie-International Edition in English*, vol. 36, pp. 2198-2200, 1997.

[132] Z. J. Guo, P. J. Sadler, and S. C. Tsang, "Immobilization and visualization of DNA and proteins on carbon nanotubes," *Advanced Materials*, vol. 10, pp. 701-703, 1998.

[133] R. J. Chen, Y. G. Zhan, D. W. Wang, and H. J. Dai, "Noncovalent sidewall functionalization of single-walled carbon nanotubes for protein immobilization," *Journal of the American Chemical Society*, vol. 123, pp. 3838-3839, 2001.

[134] J. Cook, J. Sloan, R. J. R. Heesom, J. Hammer, and M. L. H. Green, "Purification of rhodium-filled carbon nanotubes using reversed micelles," *Chemical Communications*, pp. 2673-2674, 1996.

[135] J. Sloan, J. Hammer, M. Zwiefka-Sibley, and M. L. H. Green, "The opening and filling of single walled carbon nanotubes (SWTs)," *Chemical Communications*, pp. 347-348, 1998.

[136] W. Q. Han, S. S. Fan, Q. Q. Li, and Y. D. Hu, "Synthesis of gallium nitride nanorods through a carbon nanotube-confined reaction," *Science*, vol. 277, pp. 1287-1289, 1997.

[137] K. Matsui, B. K. Pradhan, T. Kyotani, and A. Tomita, "Formation of nickel oxide nanoribbons in the cavity of carbon nanotubes," *Journal of Physical Chemistry B*, vol. 105, pp. 5682-5688, 2001.

[138] J. K. Holt, H. G. Park, Y. M. Wang, M. Stadermann, A. B. Artyukhin, C. P. Grigoropoulos, A. Noy, and O. Bakajin, "Fast mass transport through sub-2-nanometer carbon nanotubes," *Science*, vol. 312, pp. 1034-1037, 2006.

[139] B. C. Regan, S. Aloni, R. O. Ritchie, U. Dahmen, and A. Zettl, "Carbon nanotubes as nanoscale mass conveyors," *Nature*, vol. 428, pp. 924-927, 2004.

[140] B. W. Smith, M. Monthioux, and D. E. Luzzi, "Encapsulated C-60 in carbon nanotubes," *Nature*, vol. 396, pp. 323-324, 1998.

[141] H. Ulbricht, G. Moos, and T. Hertel, "Interaction of C-60 with carbon nanotubes and graphite," *Physical Review Letters*, vol. 90, pp. 095501, 2003.

[142] A. N. Khlobystov, D. A. Britz, and G. A. D. Briggs, "Molecules in carbon nanotubes," *Accounts of Chemical Research*, vol. 38, pp. 901-909, 2005.

[143] H. Kataura, Y. Maniwa, M. Abe, A. Fujiwara, T. Kodama, K. Kikuchi, H. Imahori, Y. Misaki, S. Suzuki, and Y. Achiba, "Optical properties of fullerene and non-fullerene peapods," *Applied Physics a-Materials Science & Processing*, vol. 74, pp. 349-354, 2002.

[144] K. Hirahara, S. Bandow, K. Suenaga, H. Kato, T. Okazaki, H. Shinohara, and S. Iijima, "Electron diffraction study of one-dimensional crystals of fullerenes," *Physical Review B*, vol. 6411, pp. 115420, 2001.

[145] Y. Maniwa, H. Kataura, M. Abe, A. Fujiwara, R. Fujiwara, H. Kira, H. Tou, S. Suzuki, Y. Achiba, E. Nishibori, M. Takata, M. Sakata, and H. Suematsu, "C-70 molecular stumbling inside single-walled carbon nanotubes," *Journal of the Physical Society of Japan*, vol. 72, pp. 45-48, 2003.

[146] B. W. Smith, D. E. Luzzi, and Y. Achiba, "Tumbling atoms and evidence for charge transfer in La-2@C-80@SWNT," *Chemical Physics Letters*, vol. 331, pp. 137-142, 2000.

[147] K. Hirahara, K. Suenaga, S. Bandow, H. Kato, T. Okazaki, H. Shinohara, and S. Iijima, "One-dimensional metallofullerene crystal generated inside single-walled carbon nanotubes," *Physical Review Letters*, vol. 85, pp. 5384-5387, 2000.

[148] T. Okazaki, K. Suenaga, K. Hirahara, S. Bandow, S. Iijima, and H. Shinohara, "Electronic and geometric structures of metallofullerene peapods," *Physica B-Condensed Matter*, vol. 323, pp. 97-99, 2002.

[149] P. W. Chiu, G. Gu, G. T. Kim, G. Philipp, S. Roth, S. F. Yang, and S. Yang, "Temperature-induced change from p to n conduction in metallofullerene nanotube peapods," *Applied Physics Letters*, vol. 79, pp. 3845-3847, 2001.

[150] R. Jaffiol, A. Debarre, C. Julien, D. Nutarelli, P. Tchenio, A. Taninaka, B. Cao, T. Okazaki, and H. Shinohara, "Raman spectroscopy of La-2@C-80 and Ti-2@C-80 dimetallofullerenes," *Physical Review B*, vol. 68, pp. 014105, 2003.

[151] K. Suenaga, T. Okazaki, C. R. Wang, S. Bandow, H. Shinohara, and S. Iijima, "Direct imaging of Sc-2@C-84 molecules encapsulated inside single-wall carbon nanotubes by high resolution electron microscopy with atomic sensitivity," *Physical Review Letters*, vol. 90, pp. 055506, 2003.

[152] A. Gloter, K. Suenaga, H. Kataura, R. Fujii, T. Kodama, H. Nishikawa, I. Ikemoto, K. Kikuchi, S. Suzuki, Y. Achiba, and S. Iijima, "Structural evolutions of carbon nano-peapods under electron microscopic observation," *Chemical Physics Letters*, vol. 390, pp. 462-466, 2004.

[153] P. M. Ajayan, T. W. Ebbesen, T. Ichihashi, S. Iijima, K. Tanigaki, and H. Hiura, "Opening Carbon Nanotubes with Oxygen and Implications for Filling," *Nature*, vol. 362, pp. 522-525, 1993.

[154] P. M. Ajayan and S. Iijima, "Capillarity-Induced Filling of Carbon Nanotubes," *Nature*, vol. 361, pp. 333-334, 1993.

[155] C. H. Kiang, J. S. Choi, T. T. Tran, and A. D. Bacher, "Molecular nanowires of 1 nm diameter from capillary filling of single-walled carbon nanotubes," *Journal of Physical Chemistry B*, vol. 103, pp. 7449-7451, 1999.

[156] Z. L. Zhang, B. Li, Z. J. Shi, Z. N. Gu, Z. Q. Xue, and L. M. Peng, "Filling of single-walled carbon nanotubes with silver," *Journal of Materials Research*, vol. 15, pp. 2658-2661, 2000.

[157] A. Govindaraj, B. C. Satishkumar, M. Nath, and C. N. R. Rao, "Metal nanowires and intercalated metal layers in single-walled carbon nanotube bundles," *Chemistry of Materials*, vol. 12, pp. 202-205, 2000.

[158] J. C. Bao, K. Y. Wang, Z. Xu, H. Zhang, and Z. H. Lu, "A novel nanostructure of nickel nanotubes encapsulated in carbon nanotubes," *Chemical Communications*, pp. 208-209, 2003.

[159] Y. H. Gao and Y. Bando, "Carbon nanothermometer containing gallium - Gallium's macroscopic properties are retained on a miniature scale in this nanodevice.," *Nature*, vol. 415, pp. 599-599, 2002.

[160] P. M. Ajayan, "Nanotubes from carbon," *Chemical Reviews*, vol. 99, pp. 1787-1799, 1999.

[161] H. J. Dai, J. Kong, C. W. Zhou, N. Franklin, T. Tombler, A. Cassell, S. S. Fan, and M. Chapline, "Controlled chemical routes to nanotube architectures, physics, and devices," *Journal of Physical Chemistry B*, vol. 103, pp. 11246-11255, 1999.

[162] F. Kreupl, A. P. Graham, G. S. Duesberg, W. Steinhogl, M. Liebau, E. Unger, and W. Honlein, "Carbon nanotubes in interconnect applications," *Microelectronic Engineering*, vol. 64, pp. 399-408, 2002.

[163] A. Nieuwoudt and Y. Massoud, "On the impact of process variations for carbon nanotube bundles for VLSI interconnect," *IEEE Transactions on Electron Devices*, vol. 54, pp. 446-455, 2007.

[164] Y. Awano, "Carbon nanotube technologies for LSI via interconnects," *Ieice Transactions on Electronics*, vol. E89c, pp. 1499-1503, 2006.

[165] P. L. McEuen, M. S. Fuhrer, and H. K. Park, "Single-walled carbon nanotube electronics," *Ieee Transactions on Nanotechnology*, vol. 1, pp. 78-85, 2002.

[166] C. L. Cheung, A. Kurtz, H. Park, and C. M. Lieber, "Diameter-controlled synthesis of carbon nanotubes," *Journal of Physical Chemistry B*, vol. 106, pp. 2429-2433, 2002.

[167] E. Flahaut, C. Laurent, and A. Peigney, "Catalytic CVD synthesis of double and triple-walled carbon nanotubes by the control of the catalyst preparation," *Carbon*, vol. 43, pp. 375-383, 2005.

[168] S. N. Song, X. K. Wang, R. P. H. Chang, and J. B. Ketterson, "Electronic-Properties of Graphite Nanotubules from Galvanomagnetic Effects," *Physical Review Letters*, vol. 72, pp. 697-700, 1994.

[169] H. J. Dai, E. W. Wong, and C. M. Lieber, "Probing electrical transport in nanomaterials: Conductivity of individual carbon nanotubes," *Science*, vol. 272, pp. 523-526, 1996.

[170] J. Tersoff, "Contact resistance of carbon nanotubes," *Applied Physics Letters*, vol. 74, pp. 2122-2124, 1999.

[171] X. B. Wang, Y. Q. Liu, G. Yu, C. Y. Xu, J. B. Zhang, and D. B. Zhu, "Anisotropic electrical transport properties of aligned carbon nanotube films," *Journal of Physical Chemistry B*, vol. 105, pp. 9422-9425, 2001.

[172] A. Ruban, B. Hammer, P. Stoltze, H. L. Skriver, and J. K. Norskov, "Surface electronic structure and reactivity of transition and noble metals," *Journal of Molecular Catalysis a-Chemical*, vol. 115, pp. 421-429, 1997.

[173] C. Klinke, J. M. Bonard, and K. Kern, "Comparative study of the catalytic growth of patterned carbon nanotube films," *Surface Science*, vol. 492, pp. 195-201, 2001.

[174] A. Fonseca, K. Hernadi, J. B. Nagy, D. Bernaerts, and A. A. Lucas, "Optimization of catalytic production and purification of buckytubes," *Journal of Molecular Catalysis a-Chemical*, vol. 107, pp. 159-168, 1996.

[175] K. Hernadi, A. Fonseca, J. B. Nagy, A. Siska, and I. Kiricsi, "Production of nanotubes by the catalytic decomposition of different carbon-containing compounds," *Applied Catalysis a-General*, vol. 199, pp. 245-255, 2000.

[176] A. R. Harutyunyan, B. K. Pradhan, U. J. Kim, G. G. Chen, and P. C. Eklund, "CVD synthesis of single wall carbon nanotubes under "soft" conditions," *Nano Letters*, vol. 2, pp. 525-530, 2002.

[177] C. J. Lee, J. Park, J. M. Kim, Y. Huh, J. Y. Lee, and K. S. No, "Low-temperature growth of carbon nanotubes by thermal chemical vapor deposition using Pd, Cr, and Pt as co-catalyst," *Chemical Physics Letters*, vol. 327, pp. 277-283, 2000.

[178] V. Ivanov, J. B. Nagy, P. Lambin, A. Lucas, X. B. Zhang, X. F. Zhang, D. Bernaerts, G. Vantendeloo, S. Amelinckx, and J. Vanlanduyt, "The Study of Carbon Nanotubules Produced by Catalytic Method," *Chemical Physics Letters*, vol. 223, pp. 329-335, 1994.

[179] A. C. Dupuis, "The catalyst in the CCVD of carbon nanotubes - a review," *Progress in Materials Science*, vol. 50, pp. 929-961, 2005.

[180] S. C. Fung, S. J. Tauster, R. T. K. Baker, J. A. Horsley, and R. L. Garten, "Properties of Metal-Catalysts Altered by Strongly Interacting Oxide Supports," *Abstracts of Papers of the American Chemical Society*, vol. 179, pp. 94-Coll, 1980.

[181] S. J. Tauster, S. C. Fung, R. L. Garten, R. T. K. Baker, and J. A. Horsley, "Strong Interactions at Metal-Oxide Interfaces," *Abstracts of Papers of the American Chemical Society*, pp. 167-167, 1979.

[182] S. C. Fung, S. J. Tauster, R. T. K. Baker, and R. L. Garten, "Strong Metal-Support Interactions - Group-Viii Noble-Metals Supported on Transition-Metal Oxides," *Abstracts of Papers of the American Chemical Society*, pp. 174-174, 1979.

[183] S. J. Tauster, S. C. Fung, and R. L. Garten, "Strong Metal-Support Interactions - Group-8 Noble-Metals Supported on Tio2," *Journal of the American Chemical Society*, vol. 100, pp. 170-175, 1978.

[184] T. Borowiecki, "Effect of the Support on the Coking of Nickel-Catalysts in Hydrocarbon Steam Reforming," *Reaction Kinetics and Catalysis Letters*, vol. 33, pp. 429-434, 1987.

[185] T. Borowiecki, "Nickel-Catalysts for Steam Reforming of Hydrocarbons - Direct and Indirect Factors Affecting the Coking Rate," *Applied Catalysis*, vol. 31, pp. 207-220, 1987.

[186] I. Yudanov, G. Pacchioni, K. Neyman, and N. Rosch, "Systematic density functional study of the adsorption of transition metal atoms on the MgO(001) surface," *Journal of Physical Chemistry B*, vol. 101, pp. 2786-2792, 1997.

[187] I. V. Yudanov, S. Vent, K. Neyman, G. Pacchioni, and N. Rosch, "Adsorption of Pd atoms and Pd-4 clusters on the MgO(001) surface: A density functional study," *Chemical Physics Letters*, vol. 275, pp. 245-252, 1997.

[188] S. C. Davis and K. J. Klabunde, "Unsupported Small Metal Particles - Preparation, Reactivity, and Characterization," *Chemical Reviews*, vol. 82, pp. 153-208, 1982.

[189] S. J. Tauster, S. C. Fung, R. T. K. Baker, and J. A. Horsley, "Strong-Interactions in Supported-Metal Catalysts," *Science*, vol. 211, pp. 1121-1125, 1981.

[190] A. C. Wright, Y. Xiong, N. Maung, S. J. Eichhorn, and R. J. Young, "The influence of the substrate on the growth of carbon nanotubes from nickel clusters - an investigation using STM, FE-SEM, TEM and Raman spectroscopy," *Materials Science & Engineering C-Biomimetic and Supramolecular Systems*, vol. 23, pp. 279-283, 2003.

[191] R. Seidel, G. S. Duesberg, E. Unger, A. P. Graham, M. Liebau, and F. Kreupl, "Chemical vapor deposition growth of single-walled carbon nanotubes at 600 degrees C and a simple growth model," *Journal of Physical Chemistry B*, vol. 108, pp. 1888-1893, 2004.

[192] L. Delzeit, C. V. Nguyen, B. Chen, R. Stevens, A. Cassell, J. Han, and M. Meyyappan, "Multiwalled carbon nanotubes by chemical vapor deposition using multilayered metal catalysts," *Journal of Physical Chemistry B*, vol. 106, pp. 5629-5635, 2002.

[193] A. Cao, X. F. Zhang, C. L. Xu, J. Liang, D. H. Wu, and B. Q. Wei, "Aligned carbon nanotube growth under oxidative ambient," *Journal of Materials Research*, vol. 16, pp. 3107-3110, 2001.

[194] X. S. Li, A. Y. Cao, Y. J. Jung, R. Vajtai, and P. M. Ajayan, "Bottom-up growth of carbon nanotube multilayers: Unprecedented growth," *Nano Letters*, vol. 5, pp. 1997-2000, 2005.

[195] C. P. Deck and K. S. Vecchio, "Growth of well-aligned carbon nanotube structures in successive layers," *Journal of Physical Chemistry B*, vol. 109, pp. 12353-12357, 2005.

[196] B. E. Deal and A. S. Grove, "General Relationship for Thermal Oxidation of Silicon," *Journal of Applied Physics*, vol. 36, pp. 3770-3778, 1965.

[197] C. D. Wagner, D. A. Zatko, and R. H. Raymond, "Use of the Oxygen Kll Auger Lines in Identification of Surface Chemical-States by Electron-Spectroscopy for Chemical-Analysis," *Analytical Chemistry*, vol. 52, pp. 1445-1451, 1980.

[198] K. Bartsch, K. Biedermann, T. Gemming, and A. Leonhardt, "On the diffusion-controlled growth of multiwalled carbon nanotubes," *Journal of Applied Physics*, vol. 97, pp. 114301, 2005.

[199] O. A. Louchev, T. Laude, Y. Sato, and H. Kanda, "Diffusion-controlled kinetics of carbon nanotube forest growth by chemical vapor deposition," *Journal of Chemical Physics*, vol. 118, pp. 7622-7634, 2003.

[200] A. A. Puretzky, D. B. Geohegan, S. Jesse, I. N. Ivanov, and G. Eres, "In situ measurements and modeling of carbon nanotube array growth kinetics during chemical vapor deposition," *Applied Physics a-Materials Science & Processing*, vol. 81, pp. 223-240, 2005.

[201] H. Hongo, F. Nihey, T. Ichihashi, Y. Ochiai, M. Yudasaka, and S. Iijima, "Support materials based on converted aluminum films for chemical vapor deposition growth of single-wall carbon nanotubes," *Chemical Physics Letters*, vol. 380, pp. 158-164, 2003.

[202] H. Hongo, M. Yudasaka, T. Ichihashi, F. Nihey, and S. Iijima, "Chemical vapor deposition of single-wall carbon nanotubes on iron-film-coated sapphire substrates," *Chemical Physics Letters*, vol. 361, pp. 349-354, 2002.

[203] S. Helveg, C. Lopez-Cartes, J. Sehested, P. L. Hansen, B. S. Clausen, J. R. Rostrup-Nielsen, F. Abild-Pedersen, and J. K. Norskov, "Atomic-scale imaging of carbon nanofibre growth," *Nature*, vol. 427, pp. 426-429, 2004.

[204] L. M. Dell'Acqua-Bellavitis, J. D. Ballard, P. M. Ajayan, and R. W. Siegel, "Kinetics for the synthesis reaction of aligned carbon nanotubes: A study based on in situ diffractography," *Nano Letters*, vol. 4, pp. 1613-1620, 2004.

[205] D. H. Kim, H. S. Jang, C. D. Kim, D. S. Cho, H. S. Yang, H. D. Kang, B. K. Min, and H. R. Lee, "Dynamic growth rate behavior of a carbon nanotube forest characterized by in situ optical growth monitoring," *Nano Letters*, vol. 3, pp. 863-865, 2003.

[206] G. R. Youngquist, "Diffusion and Flow of Gases in Porous Solids," *Industrial and Engineering Chemistry*, vol. 62, pp. 52-63, 1970.

[207] D. S. Scott and F. A. L. Dullien, "Diffusion of Ideal Gases in Capillaries and Porous Solids," *Aiche Journal*, vol. 8, pp. 113-117, 1962.

[208] A. L. Hines and R. N. Maddox, *Mass Transfer: Fundamental and Applications*, 1985.

[209] C. J. Lee, J. Park, Y. Huh, and J. Y. Lee, "Temperature effect on the growth of carbon nanotubes using thermal chemical vapor deposition," *Chemical Physics Letters*, vol. 343, pp. 33-38, 2001.

[210] S. Berber, Y. K. Kwon, and D. Tomanek, "Unusually high thermal conductivity of carbon nanotubes," *Physical Review Letters*, vol. 84, pp. 4613-4616, 2000.

[211] A. P. Graham, G. S. Duesberg, W. Hoenlein, F. Kreupl, M. Liebau, R. Martin, B. Rajasekharan, W. Pamler, R. Seidel, W. Steinhoegl, and E. Unger, "How do carbon nanotubes fit into the semiconductor roadmap?," *Applied Physics a-Materials Science & Processing*, vol. 80, pp. 1141-1151, 2005.

[212] H. J. Li, W. G. Lu, J. J. Li, X. D. Bai, and C. Z. Gu, "Multichannel ballistic transport in multiwall carbon nanotubes," *Physical Review Letters*, vol. 95, pp. 086601, 2005.

[213] E. Dujardin, T. W. Ebbesen, H. Hiura, and K. Tanigaki, "Capillarity and Wetting of Carbon Nanotubes," *Science*, vol. 265, pp. 1850-1852, 1994.

[214] S. C. Tsang, P. J. F. Harris, and M. L. H. Green, "Thinning and Opening of Carbon Nanotubes by Oxidation Using Carbon-Dioxide," *Nature*, vol. 362, pp. 520-522, 1993.

[215] L. B. Zhu, Y. H. Xiu, D. W. Hess, and C. P. Wong, "Aligned carbon nanotube stacks by water-assisted selective etching," *Nano Letters*, vol. 5, pp. 2641-2645, 2005.

[216] W. J. Yu, Y. S. Cho, G. S. Choi, and D. J. Kim, "Patterned carbon nanotube field emitter using the regular array of an anodic aluminium oxide template," *Nanotechnology*, vol. 16, pp. S291-S295, 2005.

[217] J. I. Sohn, S. Lee, Y. H. Song, S. Y. Choi, K. I. Cho, and K. S. Nam, "Patterned selective growth of carbon nanotubes and large field emission from vertically well-aligned carbon nanotube field emitter arrays," *Applied Physics Letters*, vol. 78, pp. 901-903, 2001.

[218] N. de Jonge, "Brightness of carbon nanotube electron sources," *Journal of Applied Physics*, vol. 95, pp. 673-681, 2004.

[219] J. M. Bonard, C. Klinke, K. A. Dean, and B. F. Coll, "Degradation and failure of carbon nanotube field emitters," *Physical Review B*, vol. 67, pp. 115406, 2003.

[220] C. Gomez-Navarro, P. J. De Pablo, J. Gomez-Herrero, B. Biel, F. J. Garcia-Vidal, A. Rubio, and F. Flores, "Tuning the conductance of single-walled carbon nanotubes by ion irradiation in the Anderson localization regime," *Nature Materials*, vol. 4, pp. 534-539, 2005.

[221] M. S. Fuhrer, J. Nygard, L. Shih, M. Forero, Y. G. Yoon, M. S. C. Mazzoni, H. J. Choi, J. Ihm, S. G. Louie, A. Zettl, and P. L. McEuen, "Crossed nanotube junctions," *Science*, vol. 288, pp. 494-497, 2000.

[222] H. W. C. Postma, M. de Jonge, Z. Yao, and C. Dekker, "Electrical transport through carbon nanotube junctions created by mechanical manipulation," *Physical Review B*, vol. 62, pp. 10653-10656, 2000.

[223] G. Tobias, L. D. Shao, C. G. Salzmann, Y. Huh, and M. L. H. Green, "Purification and opening of carbon nanotubes using steam," *Journal of Physical Chemistry B*, vol. 110, pp. 22318-22322, 2006.

[224] A. H. Barber, S. R. Cohen, and H. D. Wagner, "External and internal wetting of carbon nanotubes with organic liquids," *Physical Review B*, vol. 71, pp. 115443, 2005.

[225] A. W. Adamson and A. P. Gast, *Physical Chemistry of Surfaces*. New York: John Wiley & Sons, Inc., 1997.

[226] K. L. Mittal, *Contact angle, wettability and adhesion*: Utrecht, the Netherlands: VSP, 1993.

[227] A. B. D. Cassie, "Contact Angles," *Discussions of the Faraday Society*, vol. 3, pp. 11-16, 1948.

[228] R. N. Wenzel, "Resistance of solid surfaces to wetting by water," *Industrial and Engineering Chemistry*, vol. 28, pp. 988-994, 1936.

[229] E. Nun, M. Oles, and B. Schleich, "Lotus-Effect - Surfaces," *Macromolecular Symposia*, vol. 187, pp. 677-682, 2002.

[230] A. Lafuma and D. Quere, "Superhydrophobic states," *Nature Materials*, vol. 2, pp. 457-460, 2003.

[231] A. Marmur, "Wetting on hydrophobic rough surfaces: To be heterogeneous or not to be?," *Langmuir*, vol. 19, pp. 8343-8348, 2003.

[232] A. Marmur, "Kinetics of penetration into uniform porous media: Testing the equivalent-capillary concept," *Langmuir*, vol. 19, pp. 5956-5959, 2003.

[233] N. A. Patankar, "On the modeling of hydrophobic contact angles on rough surfaces," *Langmuir*, vol. 19, pp. 1249-1253, 2003.

[234] W. Barthlott and C. Neinhuis, "Purity of the sacred lotus, or escape from contamination in biological surfaces," *Planta*, vol. 202, pp. 1-8, 1997.

[235] R. Blossey, "Self-cleaning surfaces - virtual realities," *Nature Materials*, vol. 2, pp. 301-306, 2003.

[236] A. Marmur, "The lotus effect: Superhydrophobicity and metastability," *Langmuir*, vol. 20, pp. 3517-3519, 2004.

[237] R. Furstner, W. Barthlott, C. Neinhuis, and P. Walzel, "Wetting and self-cleaning properties of artificial superhydrophobic surfaces," *Langmuir*, vol. 21, pp. 956-961, 2005.

[238] Z. Yoshimitsu, A. Nakajima, T. Watanabe, and K. Hashimoto, "Effects of surface structure on the hydrophobicity and sliding behavior of water droplets," *Langmuir*, vol. 18, pp. 5818-5822, 2002.

[239] K. K. S. Lau, J. Bico, K. B. K. Teo, M. Chhowalla, G. A. J. Amaratunga, W. I. Milne, G. H. McKinley, and K. K. Gleason, "Superhydrophobic carbon nanotube forests," *Nano Letters*, vol. 3, pp. 1701-1705, 2003.

[240] L. Huang, S. P. Lau, H. Y. Yang, E. S. P. Leong, S. F. Yu, and S. Prawer, "Stable superhydrophobic surface via carbon nanotubes coated with a ZnO thin film," *Journal of Physical Chemistry B*, vol. 109, pp. 7746-7748, 2005.

[241] S. Agraharam, D. W. Hess, P. A. Kohl, and S. A. B. Allen, "Thermal stability of fluorocarbon films deposited from pentafluoroethane/argon plasmas," *Journal of the Electrochemical Society*, vol. 147, pp. 2665-2670, 2000.

[242] T. Kimura, H. Ago, M. Tobita, S. Ohshima, M. Kyotani, and M. Yumura, "Polymer composites of carbon nanotubes aligned by a magnetic field," *Advanced Materials*, vol. 14, pp. 1380-1383, 2002.

[243] C. A. Martin, J. K. W. Sandler, A. H. Windle, M. K. Schwarz, W. Bauhofer, K. Schulte, and M. S. P. Shaffer, "Electric field-induced aligned multi-wall carbon nanotube networks in epoxy composites," *Polymer*, vol. 46, pp. 877-886, 2005.

[244] N. R. Raravikar, L. S. Schadler, A. Vijayaraghavan, Y. P. Zhao, B. Q. Wei, and P. M. Ajayan, "Synthesis and characterization of thickness-aligned carbon nanotube-polymer composite films," *Chemistry of Materials*, vol. 17, pp. 974-983, 2005.

[245] K. H. Kang, "How electrostatic fields change contact angle in electrowetting," *Langmuir*, vol. 18, pp. 10318-10322, 2002.

[246] A. Quinn, R. Sedev, and J. Ralston, "Contact angle saturation in electrowetting," *Journal of Physical Chemistry B*, vol. 109, pp. 6268-6275, 2005.

[247] J. Y. Chen, A. Kutana, C. P. Collier, and K. P. Giapis, "Electrowetting in carbon nanotubes," *Science*, vol. 310, pp. 1480-1483, 2005.

[248] M. Bienia, C. Quilliet, and M. Vallade, "Modification of drop shape controlled by electrowetting," *Langmuir*, vol. 19, pp. 9328-9333, 2003.

[249] C. Decamps and J. De Coninck, "Dynamics of spontaneous spreading under electrowetting conditions," *Langmuir*, vol. 16, pp. 10150-10153, 2000.

[250] M. Vallet, B. Berge, and L. Vovelle, "Electrowetting of water and aqueous solutions on poly(ethylene terephthalate) insulating films," *Polymer*, vol. 37, pp. 2465-2470, 1996.

[251] H. J. J. Verheijen and M. W. J. Prins, "Reversible electrowetting and trapping of charge: Model and experiments," *Langmuir*, vol. 15, pp. 6616-6620, 1999.

[252] V. Peykov, A. Quinn, and J. Ralston, "Electrowetting: a model for contact-angle saturation," *Colloid and Polymer Science*, vol. 278, pp. 789-793, 2000.

[253] I. Morcos, "Surface-Tension of Stress-Annealed Pyrolytic-Graphite," *Journal of Chemical Physics*, vol. 57, pp. 1801-&, 1972.

[254] I. Morcos, "Electrocapillary Phenomena at Stress-Annealed Pyrolytic-Graphite Electrode," *Journal of Physical Chemistry*, vol. 76, pp. 2750-2753, 1972.

[255] A. H. Barber, S. R. Cohen, and H. D. Wagner, "Static and dynamic wetting measurements of single carbon nanotubes," *Physical Review Letters*, vol. 92, pp. 186103, 2004.

[256] E. Dujardin, T. W. Ebbesen, A. Krishnan, and M. M. J. Treacy, "Wetting of single shell carbon nanotubes," *Advanced Materials*, vol. 10, pp. 1472-1475, 1998.

[257] M. Vallet, M. Vallade, and B. Berge, "Limiting phenomena for the spreading of water on polymer films by electrowetting," *European Physical Journal B*, vol. 11, pp. 583-591, 1999.

[258] M. F. Yu, O. Lourie, M. J. Dyer, K. Moloni, T. F. Kelly, and R. S. Ruoff, "Strength and breaking mechanism of multiwalled carbon nanotubes under tensile load," *Science*, vol. 287, pp. 637-640, 2000.

[259] A. Y. Cao, P. L. Dickrell, W. G. Sawyer, M. N. Ghasemi-Nejhad, and P. M. Ajayan, "Super-compressible foamlike carbon nanotube films," *Science*, vol. 310, pp. 1307-1310, 2005.

[260] P. Calvert, "Nanotube composites - A recipe for strength," *Nature*, vol. 399, pp. 210-211, 1999.

[261] M. Moniruzzaman and K. I. Winey, "Polymer nanocomposites containing carbon nanotubes," *Macromolecules*, vol. 39, pp. 5194-5205, 2006.

[262] J. N. Coleman, U. Khan, and Y. K. Gun'ko, "Mechanical reinforcement of polymers using carbon nanotubes," *Advanced Materials*, vol. 18, pp. 689-706, 2006.

[263] V. P. Veedu, A. Y. Cao, X. S. Li, K. G. Ma, C. Soldano, S. Kar, P. M. Ajayan, and M. N. Ghasemi-Nejhad, "Multifunctional composites using reinforced laminae with carbon-nanotube forests," *Nature Materials*, vol. 5, pp. 457-462, 2006.

[264] P. M. Ajayan, L. S. Schadler, C. Giannaris, and A. Rubio, "Single-walled carbon nanotube-polymer composites: Strength and weakness," *Advanced Materials*, vol. 12, pp. 750-753, 2000.

[265] Y. Lin, M. J. Meziani, and P. Sun, "Functionalized carbon nanotubes for polymeric nanocomposites," *Journal of Materials Chemistry*, vol. 17, pp. 1143-1148, 2007.

[266] N. H. Tai, M. K. Yeh, and H. H. Liu, "Enhancement of the mechanical properties of carbon nano tube/phenolic composites using a carbon nanotube network as the reinforcement," *Carbon*, vol. 42, pp. 2774-2777, 2004.

[267] E. T. Thostenson, C. Y. Li, and T. W. Chou, "Nanocomposites in context," *Composites Science and Technology*, vol. 65, pp. 491-516, 2005.

[268] A. P. Yu, M. E. Itkis, E. Bekyarova, and R. C. Haddon, "Effect of single-walled carbon nanotube purity on the thermal conductivity of carbon nanotube-based composites," *Applied Physics Letters*, vol. 89, pp. 133102, 2006.

[269] H. Huang, C. H. Liu, Y. Wu, and S. S. Fan, "Aligned carbon nanotube composite films for thermal management," *Advanced Materials*, vol. 17, pp. 1652-1656, 2005.

[270] S. R. Wang, Z. Y. Liang, P. Gonnet, Y. H. Liao, B. Wang, and C. Zhang, "Effect of nanotube functionalization on the coefficient of thermal expansion of nanocomposites," *Advanced Functional Materials*, vol. 17, pp. 87-92, 2007.

[271] Y. K. Kwon, S. Berber, and D. Tomanek, "Thermal contraction of carbon fullerenes and nanotubes," *Physical Review Letters*, vol. 92, pp. -, 2004.

[272] G. X. Cao, X. Chen, and J. W. Kysar, "Apparent thermal contraction of single-walled carbon nanotubes," *Physical Review B*, vol. 72, pp. 015901, 2005.

[273] Y. Maniwa, R. Fujiwara, H. Kira, H. Tou, H. Kataura, S. Suzuki, Y. Achiba, E. Nishibori, M. Takata, M. Sakata, A. Fujiwara, and H. Suematsu, "Thermal expansion of single-walled carbon nanotube (SWNT) bundles: X-ray diffraction studies," *Physical Review B*, vol. 64, pp. 241402, 2001.

[274] H. J. Jiang, K. S. Moon, Z. Q. Zhang, S. Pothukuchi, and C. P. Wong, "Variable frequency microwave synthesis of silver nanoparticles," *Journal of Nanoparticle Research*, vol. 8, pp. 117-124, 2006.

[275] D. Bogdal, P. Penczek, J. Pielichowski, and A. Prociak, "Microwave assisted synthesis, crosslinking, and processing of polymeric materials," *Liquid Chromatography Ftir Microspectroscopy Microwave Assisted Synthesis*, vol. 163, pp. 193-263, 2003.

[276] C. Y. Wei, D. Srivastava, and K. J. Cho, "Thermal expansion and diffusion coefficients of carbon nanotube-polymer composites," *Nano Letters*, vol. 2, pp. 647-650, 2002.

[278] Y. Xu, Y. Zhang, E. Suhir, and X. Wang, "Thermal properties of carbon nanotube array used for integrated circuit cooling," *Journal of Applied Physics*, vol. 100, pp. 074302, 2006.

[279] M. C. Andrews, D. J. Bannister, and R. J. Young, "The interfacial properties of aramid/epoxy model composites," *Journal of Materials Science*, vol. 31, pp. 3893-3913, 1996.

[280] C. A. Cooper and R. J. Young, "Investigation of structure/properties relationships in particulate composites through the use of Raman spectroscopy " *Journal of Raman Spectroscopy*, vol. 30, pp. 929-938, 1999.

VITA

LINGBO ZHU

Lingbo Zhu was born in November 1976 in Linhai, Zhejiang Province, China. He graduated from Huipu Middle School in 1995 and obtained his B. S. and M. S. in Chemical Engineering from East China University of Science and Technology in 1999 and 2002, respectively. In August 2002, he came to Georgia Institute of Technology to pursue a doctorate in Chemical Engineering under guidance of Dr. C. P. Wong and Dr. Dennis W. Hess. He is receiving his Ph. D in Chemical Engineering in December 2007.